Analysis of Infragravity Frequency Sediment Transport on Macrotidal Beaches

by

Andrew Nicholas Saulter

A thesis submitted to the University of Plymouth
in partial fulfilment for the degree of

Doctor of Philosophy

Institute of Marine Studies
Faculty of Science

January 2000

UNIVERSITY OF PLYMOUTH
Item No. 900 4263293
Date 18 MAY 2000 S
Class No. T 551.35309146 SAU
Contl. No. X 704068078
LIBRARY SERVICES

900426329 3

REFERENCE ONLY

LIBRARY STORE

Analysis of Infragravity Frequency Sediment Transport on Macrotidal Beaches

Andrew Nicholas Saulter

Abstract

Many cross-shore sediment transport models use simple treatments of infragravity frequency (0.005-0.05Hz) processes. For example, infragravity waves have been assumed to provide solely a 'drift velocity' for transport of sediment mobilised by incident frequency waves (0.05-0.5Hz) and be 100% reflected at the shoreline. Furthermore, numerous models calculate broken incident wave heights on the basis of water depth only. This work investigates both the processes underlying infragravity frequency variations in the cross-shore velocity field, and the resulting effect of such variations on sediment suspension and transport.

Data were selected from three beach experiments in order to compare observations from a range of energetic conditions and positions in the nearshore. Experiments conducted on a dissipative beach at Llangennith, and an intermediate beach at Spurn Head, form part of the pre-existing British Beach And Nearshore Dynamics dataset. The third deployment, at a dissipative site at Perranporth (Cornwall), provided new data for analysis. At Llangennith, high swell waves (significant wave height 3m) were observed, and the measurements come from an infragravity wave dominated saturated surf zone. At Perranporth, locally generated wind wave heights were 2m and measurements came from an incident wave dominated saturated surf zone. Conditions at Spurn Head saw swell wave heights of 1.5m, and observations were made in both an incident wave dominated non-saturated surf zone and the incident wave shoaling zone.

Analysis of the data revealed that, in the surf zone, the nature of the infragravity wave field was dependent upon the distribution of energy between higher (>0.02Hz) and lower (<0.02Hz) infragravity frequencies. Lower frequency infragravity waves were found to shoal as free waves, while higher frequency infragravity waves were dissipated near to shore on low gradient beaches. Infragravity wave reflection coefficients showed a dependence on frequency and beach slope (parameterised by the Iribarren number), varied between 50-90% for lower infragravity frequencies, and could be less than 50% for higher infragravity frequencies. Incident wave heights were modulated in the shoaling zone with a 'groupy' form. Modulation was also observed in the surf zone, but in the form of individual large waves occurring at low frequency. In the shoaling zone and very close to shore, non-linear interactions occurred between the incident and infragravity components, and calculated phase values between modulated incident waves and infragravity waves indicated a phase shift from a value of less than 180° in the shoaling zone toward 0° close to shore. However, the two signals were not significantly correlated for much of the surf zone.

High velocities resulting from a combination of the mean, infragravity and incident wave components drove sediment suspension. Large suspension events occurring at infragravity frequencies were correlated with incident wave groupiness in the shoaling zone, and in high energy conditions with infragravity waves near to the swash zone. Such variations in suspension were related not only to velocity magnitude, but the duration for which a threshold for suspension was exceeded. The bed response to forcing also varied during a tide, possibly as a result of changing bed conditions (e.g. due to bedforms). The infragravity contribution to suspension was independent of the magnitude of suspended sediment concentration, and increased from approximately 30% at the breaker line to 90% in an infragravity wave dominated inner surf zone. The contribution of the infragravity component to transport did not show a similar behaviour, due to phase effects, which produced a reversal in the transport direction between higher and lower infragravity frequencies. Comparison of the observations of sediment transport with energetics predictors identified several cases where the observed transport was qualitatively different from the model prediction as a result of sediment transport thresholds being exceeded at, or for, infragravity timescales.

List of Contents

List of figures viii

List of plates xviii

List of tables xviii

List of symbol notation xix

Acknowledgement xxi

Authors Declaration xxii

Page No.

1. Introduction 1

2. Review of nearshore processes

2.1 Nearshore zone incident frequency wave hydrodynamics 8

2.1.1 Incident frequency wave hydrodynamics and a division of the nearshore 8

2.1.2 Incident frequency waves outside the break point 10

2.1.3 Incident frequency waves inside the break point 15

2.1.4 Summary: Incident frequency waves in the nearshore 20

2.2 Infragravity frequency wave hydrodynamics 21

2.2.1 Radiation stress and waves in deep water 21

2.2.2 Infragravity wave release and generation in shallow water 26

2.2.3 Shore normal infragravity waves in the surf zone 29

2.2.4 Edge waves 34

2.2.5. Infragravity wave interaction with morphology and tides 39

2.2.6 Summary: Infragravity waves in the nearshore 42

2.3 Sediment transport 43

2.3.1. Morphology and infragravity waves? 43

2.3.2 Morphology and beach classifications 46

2.3.3 Describing motion of sediment, in response to currents and waves 50

2.3.4 Effects of bedforms 58

2.3.5 Components of transport in the nearshore 61

2.3.6 Summary: Sediment dynamics 65

2.4 Discussion 66

3. Experimental Work

3.1 Selection of experimental data 68

3.2 The B-BAND programme 70

3.2.1 Experiment overview 70

3.2.2 The Llangennith deployment 73

3.2.3 The Spurn Head deployment 77

3.3 The Perranporth field experiment 81

3.3.1 The field site 81

3.3.2 The SLOT system 84

3.3.3 Instruments and Calibration 88

3.3.4 The Perranporth field Deployment 94

3.4 Summary: Experimental work 97

4. Data Processing

4.1 Data details 100

4.2 Time-series analysis 103

4.2.1 Frequency domain analysis 103

4.2.1a The autospectrum 104

4.2.1b The cross-spectrum 106

4.2.1c The bispectrum 109

4.2.2 Time domain cross-correlation 111

4.3 Summary statistics 112

4.3.1 Hydrodynamic parameterisations 112

4.3.2 Sediment suspension and flux 113

4.4 Time-series filtering and reflection analyses 114

4.4.1 Separating the incident and infragravity components 114

4.4.2 Derivation of the incident wave envelope and groupiness factor 118

4.4.3 Reflection coefficient analysis 120

4.4.4 Derivation of incoming and reflected wave time-series 121

4.5 Application of data for a description of processes through the cross-shore 122

4.5.1 'Stationarity' of conditions 122

4.5.2 Wave direction 126

4.6 Summary: Data processing 130

5. Results I, Hydrodynamics 131

5.1 Overview of the hydrodynamics at Llangennith, Spurn Head and Perranporth 132

5.1.1 Basic hydrodynamics 132

5.1.2 Comparison of the three field sites 140

5.1.3 Normalised parameters for a comparison of the data 143

5.2 Nature of the infragravity wave field in the nearshore 149

5.2.1 The infragravity wave field at Llangennith 149

5.2.2 The infragravity wave field at Perranporth 159

5.2.3 The infragravity wave field at Spurn Head 163

5.2.4 Frequency and shoreline gradient dependence for infragravity wave reflection 172

5.2.5 Summary: nature of the infragravity wave field in the nearshore 176

5.3 Modulation of the incident wave field 177

5.3.1 Groupiness in the shoaling and outer surf zones 177

5.3.2 Incident wave modulation in the inner surf zone 183

5.3.3 Summarising variations in *GF* and incident-infragravity wave phase through the nearshore 189

5.4 Incident-infragravity wave phase and interaction through the nearshore 192

5.4.1 Evolution of wave bispectra through the nearshore 192

5.4.2 Incident-infragravity wave interactions 198

5.5 Summary of the low frequency hydrodynamics 203

6. Results II, Sediment Dynamics 206

6.1 Infragravity frequency variations in suspended sediment concentrations 209

6.1.1 Suspension at infragravity frequencies in the shoaling and outer surf zones -Spurn Head data 209

6.1.2 Suspension at infragravity frequencies in the inner surf zone 213

6.1.3 Contribution of the infragravity frequency component to suspension 223

6.1.4 Velocity phase 'asymmetries' in suspension of sediment 226

6.1.5 'Tidal asymmetries' in overall suspended sediment concentration 229
6.1.6 Summary: Infragravity frequency variations in suspension of sediment 238
6.2 Effects of infragravity frequency variations on sediment transport 240
6.2.1 Variations in sediment flux at Llangennith 245
6.2.2 Variations in sediment flux at Perranporth 250
6.2.3 Variations in sediment flux at Spurn Head 255
6.2.4 Summary: Effects of infragravity frequency variations on sediment transport 258
6.3 Infragravity frequency contributions to flux through the nearshore 259
6.4 Summary: Sediment Dynamics 264

7. Discussion of results 266
7.1 Low frequency hydrodynamics in the surf zone 267
7.1.1 Infragravity wave behaviour 268
7.1.2 Incident wave modulation and phase versus infragravity waves 272
7.2 Observations of sediment response to forcing versus an energetics approach 277
7.3 Discussion summary 280

8. Conclusions 282

Appendix I: Summary tables for cross-shore velocity statistics and autospectral analysis 289

References 300

List of figures

Page No.

Figure 1.1 Field data time-series of suspended sediment concentration, instantaneous velocity, and high and low frequency oscillatory components of velocity observed by instruments positioned in the surf zone. 7

Figure 2.1.1 Distribution of (incident wave) hydrodynamic processes across an idealised nearshore. 9

Figure 2.1.2 'Groupy' waves as formed from the combination of two sinusoids. 13

Figure 2.1.3 Variation in skewness and asymmetry between a sinusoidal (Airy) wave form and a shoaled wave. 13

Figure 2.1.4 Real part of a sea surface elevation bispectrum for shoaling waves (with frequency 0.1Hz). 14

Figure 2.1.5 (Theoretical) Change in wave height modulation between deep water, and the outer and inner surf zones. 19

Figure 2.2.1 Idealised deep water wave groups, radiation stresses, and theoretical fluctuations in mean water level. 25

Figure 2.2.2 Schematic of theoretical distribution and generation of infragravity wave energy in the nearshore. 33

Figure 2.2.3 Standing wave surface fluctuations, and underlying current structure (arrows). 33

Figure 2.2.4 Edge wave mode cross-shore surface elevations, plotted in terms of a non-dimensional offshore distance χ (from Holman, 1983). 38

Figure 2.3.1 The Masselink and Short (1993) beach classification scheme. 49

Figure 2.3.2 Turbulent 'burst and sweep' events in a mean current trace (from Heathershaw and Simpson, 1978). 56

Figure 2.3.3 Forces acting upon sediment in a (laminar) fluid flow. 56

Figure 2.3.4 Threshold velocities of combined waves and mean current for waves of period 5 seconds and 15 seconds (from Voulgaris *et al.*, 1995). 57

Figure 2.3.5 Curves predicting bedform type as described from grain size versus velocity (from Van Rijn, 1993). 60
Figure 2.3.6 Sediment transport in relation to wave asymmetry, from Komar (1976). 64
Figure 2.3.7 Transport directions inferred from suspended sediment concentration versus cross-shore velocity (*c-u*) phase. 64

Figure 3.2.1 The B-BAND field sites, situation and profiles (from Russell and Huntley, 1999). 72
Figure 3.2.2 Llangennith beach profiles and description (from Davidson, 1991). 75
Figure 3.2.3 Schematic of the Llangennith field deployment (from Davidson, 1991). 76
Figure 3.2.4 Spurn Head survey results, 23rd April 1991. 79
Figure 3.2.5 Schematic of the Spurn Head instrument array (from Foote, 1994). 80

Figure 3.3.1 The Perranporth beach site. 83
Figure 3.3.2 The SLOT system. 86
Figure 3.3.3 Screen capture of SLOT set-up programme. 86
Figure 3.3.4 Screen capture of spreadsheet format SLOT output file. 87
Figure 3.3.5 Druck 1830 pressure transducer head. 91
Figure 3.3.6 Optical Backscatter Sensor system (from D&A Instruments Manual, 1988). 92
Figure 3.3.7 SLOT 1 OBS calibration curve. 93
Figure 3.3.8 SLOT deployment schematic. 95
Figure 3.3.9 SLOT components deployment.
Figure 3.3.10 Perranporth level survey, 26/3/1998. 96

Figure 3.4.1 Schematic summary of the beach sites at Llangennith, Perranporth and Spurn Head. 98

Figure 4.2.1 95% Confidence limits for cross-spectral phase estimates (from Jenkins and Watts 1968). 108

Figure 4.4.1 Reprocessing of the wave signals. 115

Figure 4.4.2a Sample sea surface elevation spectrum from Llangennith (Storm Day), plus the cut-off frequency used in the elliptical filter. 116
Figure 4.4.2b Sample sea surface elevation spectrum from Spurn Head, plus the cut-off frequency used in the elliptical filter. 116
Figure 4.4.2c Sample sea surface elevation spectrum from Perranporth, plus the cut-off frequency used in the elliptical filter. 116
Figure 4.4.3 Time domain filter used for Llangennith data, red dotted line indicates low pass filter, green line high pass. 117
Figure 4.4.4 Sample time-series and comparison between a frequency domain low pass filter (red), and the results of a zero-phase time domain elliptical filter (green) using the Matlab *filtfilt* routine. 117
Figure 4.4.5 Separation of a) a demeaned η time-series into b) a low frequency (infragravity wave) signal and c) the high frequency (incident wave) plus wave envelope signals. 119

Figure 4.5.1 Example comparisons of sea surface elevation spectra for stationarity test. 124
Figure 4.5.2 Example of a directional wave spectrum, Spurn Head run 20, rig A2. 128
Figure 4.5.3 Corresponding results of run 20 2D and 3D PCA analysis. 128
Figure 4.5.4 Example of a directional wave spectrum, Perranporth run 13. 129

Figure 5.1.1a Distribution of incident wave breaker index versus depth for Llangennith Storm Day and Storm Night tides. 136
Figure 5.1.1b Distribution of incident wave breaker index versus depth for Perranporth. 136
Figure 5.1.1c Distribution of incident wave breaker index and mean current versus depth for Spurn Head. 136
Figure 5.1.2a Distribution of incident and infragravity banded significant wave height versus depth for Llangennith Storm Day and Storm Night tides. 137
Figure 5.1.2b Evolution of η autospectra on ebb tide, Storm Day runs 4,6 and 9. 137
Figure 5.1.2c Evolution of u autospectra on ebb tide, Storm Day runs 4,6 and 9. 137

Figure 5.1.3a Distribution of incident and infragravity banded significant wave height versus depth for Spurn Head. 138
Figure 5.1.3b Evolution of η autospectra on flood tide, Spurn Head rig A2 runs 6 and 23. 138
Figure 5.1.3c Evolution of u autospectra on flood tide, Spurn Head rig A2 bottom EMCM runs 6 and 23. 138
Figure 5.1.4a Distribution of incident and infragravity banded significant wave height versus depth for Perranporth. 139
Figure 5.1.4b Evolution of η autospectra with decreasing depth, Perranporth runs 8,13,17. 139
Figure 5.1.4c Evolution of u autospectra with decreasing depth, Perranporth runs 8,13,17. 139
Figure 5.1.5 Comparison of the (normalised) η spectrum observed during the Storm Day, Spurn Head and Perranporth tides, when depth of water at the instruments was approximately 1m. 142
Figure 5.1.6 Normalised significant (gravity frequency) wave heights versus normalised surf zone position for the Llangennith (Storm Day and Storm Night), Spurn Head and Perranporth datasets. 147
Figure 5.1.7 Ratio of gravity to infragravity frequency wave energy plotted versus normalised surf zone position for the Llangennith (Storm Day and Storm Night), Spurn Head and Perranporth datasets. 147
Figure 5.1.8 Distribution of breaker index values versus energy-distance space for the entire dataset. 148

Figure 5.2.1 Schematic of a Bessel function plotted in frequency-distance space. 155
Figure 5.2.2 Comparison between predicted and observed sea surface elevation (η) spectra, Storm Day run 9. 155
Figure 5.2.3 Comparison between predicted and observed sea surface elevation (η) spectra, Storm Day runs 4 and 6. 155
Figure 5.2.4a Values of R^2 for infragravity frequencies from Storm Day runs. 156
Figure 5.2.4b Values of R^2 for infragravity frequencies from Storm Night runs. 156
Figure 5.2.5 Comparison of Llangennith R^2 values versus depth for frequency bins at 0.01172Hz and 0.02344Hz. 157

Figure 5.2.6a Incoming and reflected (total) infragravity frequency significant wave heights for Storm Day runs. 157
Figure 5.2.6b Incoming and reflected (total) infragravity frequency significant wave heights for Storm Night runs. 157
Figure 5.2.7 Spatial distribution of observed lag times for infragravity wave return from Storm Night runs. 158
Figure 5.2.8 Comparison between predicted and observed sea surface elevation (η) spectra, Perranporth run 13. 160
Figure 5.2.9 Comparison between predicted and observed sea surface elevation (η) spectra, Perranporth run 17. 160
Figure 5.2.10 Values of R^2 for infragravity frequencies from Perranporth runs. 161
Figure 5.2.11 Incoming and reflected η spectra for Perranporth run 2. 162
Figure 5.2.12 Incoming and reflected η spectra for Perranporth run 12. 162
Figure 5.2.13 Incoming and reflected (total) infragravity frequency significant wave heights for Perranporth runs. 162
Figure 5.2.14 Comparison between predicted and observed sea surface elevation (η) spectra, Spurn Head run 23, incident wave shoaling zone. 167
Figure 5.2.15 Comparison between predicted and observed sea surface elevation (η) spectra, Spurn Head run 6, outer surf zone. 167
Figure 5.2.16 Comparison between predicted and observed sea surface elevation (η) spectra, Spurn Head run 4, close to shore. 167
Figure 5.2.17 Spurn Head run 16 cross-spectra for η for A2 versus A1. 168
Figure 5.2.18 Spurn Head R^2 values versus depth for the frequency bins at 0.01172Hz and 0.02372Hz. 169
Figure 5.2.19 Incoming and reflected (total) infragravity frequency significant wave heights for Spurn Head runs. 169
Figure 5.2.20 Incoming and reflected η spectra for Spurn Head run 2, surf zone. 170
Figure 5.2.21 Incoming and reflected η spectra for Spurn Head run 16, shoaling zone. 170
Figure 5.2.22 Spurn Head run 2 cross-spectra for η for A2 versus A1. 171
Figure 5.2.23 Temporal distribution of incoming-reflected wave phase at 0.0195Hz and predicted phase relationship using a reflection point at the shoreline. 171

Figure 5.2.24 Spurn Head runs distribution of reflection coefficient (R) versus Irribarren number. 175

Figure 5.3.1a Foote (1994) 'groupiness factor' plotted versus depth for Spurn Head runs. 180
Figure 5.3.1b List (1991) 'groupiness factor' plotted versus depth for Spurn Head runs. 180
Figure 5.3.2a Spurn Head run 22 time-series for incident and infragravity frequency waves and the incident wave envelope. 181
Figure 5.3.2b Spurn Head run 7 time-series for incident and infragravity frequency waves and the incident wave envelope. 181
Figure 5.3.2c Spurn Head run 1 time-series for incident and infragravity frequency waves and the incident wave envelope. 181
Figure 5.3.3 Spurn Head run 22 cross-spectra for incident wave envelope versus infragravity η. 182
Figure 5.3.4 Correlation between incident wave envelope and incoming infragravity signal for Spurn Head run 22. 182
Figure 5.3.5a List (1991) groupiness factor versus depth for the Llangennith Storm Day and Storm Night tides. 185
Figure 5.3.5b List (1991) groupiness factor versus depth for the Perranporth runs. 185
Figure 5.3.6 Time-series of incident wave signal and corresponding envelope for a) Storm Day run 5, b) Storm Day run 10. 186
Figure 5.3.7a Time-series of wave envelope and infragravity η signal for Storm Day run 5. 187
Figure 5.3.7b Storm Day run 5 spectra for incident wave envelope versus infragravity η. 187
Figure 5.3.8a Time-series of wave envelope and infragravity η signal for Storm Day run 10. 188
Figure 5.3.8b Storm Day run 10 cross-spectra for incident wave envelope versus infragravity η. 188
Figure 5.3.9 List (1991) groupiness factor plotted versus normalised cross-shore distance for the Llangennith, Spurn Head and Perranporth data. 191

Figure 5.3.10 Zero phase cross-correlation values plotted versus normalised cross-shore distance for the Llangennith, Spurn Head and Perranporth data. 191

Figure 5.4.1 η bispectrum (real part) for Spurn Head run 20, shoaling zone. 195
Figure 5.4.2 η bispectrum (real part) for Spurn Head run 8, breaker line. 195
Figure 5.4.3 η bispectrum (real part) for Spurn Head run 4, surf zone. 196
Figure 5.4.4 η bispectrum (real part) for Perranporth run 10, saturated inner surf zone. 196
Figure 5.4.5 η bispectrum (real part) for Storm Day run 2, saturated inner surf zone. 197
Figure 5.4.6 η bispectrum (real part) for Storm Day run 9, saturated inner surf zone. 197
Figure 5.4.7 Cross-shore distribution of incident-infragravity frequency bicoherence values for Storm Day, Spurn Head and Perranporth runs. 201
Figure 5.4.8 Cross-shore distribution of incident-infragravity frequency biphase, for bicoherent interactions between the primary incident frequency and the higher and lower infragravity frequencies. 201
Figure 5.4.9 Bicoherence spectrum for Perranporth run 10, saturated surf zone, depth 2.195m. 202
Figure 5.4.10 Bicoherence spectrum for Perranporth run 1, saturated surf zone, depth 0.468m. 202

Figure 5.5.1 Distribution of breaker index values versus energy-distance space for entire dataset. 205

Figure 6.0.1 Spurn Head run 1-24, lags between bottom (10cm) and middle (25cm) OBS signals. 208

Figure 6.1.1 Spurn Head run 11 c versus u scatterplot and time-series for c, u and incident and infragravity frequency u. 211
Figure 6.1.2 Spurn Head run 8 c versus u scatterplot and time-series for c, u and incident and infragravity frequency u. 212
Figure 6.1.3 Perranporth run 7 c versus u scatterplot and time-series for c, u and incident and infragravity frequency u. 216

Figure 6.1.4 Perranporth run 9 *c* versus *u* scatterplot and time-series for *c*, *u* and incident and infragravity frequency *u*. 217
Figure 6.1.5 Scatterplot of *c* versus cross-shore acceleration for Perranporth run 9. 218
Figure 6.1.6 Perranporth run 1 *c* versus *u* scatterplot and time-series for *c*, *u* and incident and infragravity frequency *u*. 219
Figure 6.1.7 Spurn Head run 1 *c* versus *u* scatterplot and time-series for *c*, *u* and incident and infragravity frequency *u*. 220
Figure 6.1.8 Storm Day run 10 c versus *u* scatterplot and time-series for *c*, *u* and incident and infragravity frequency *u*. 221
Figure 6.1.9 Correlation between c and time-series for the infragravity frequency variations of η, Storm Day run 10. 222
Figure 6.1.10 Correlations between *c* and the infragravity velocity signal for incoming and reflected waves, Storm Day run 10. 222
Figure 6.1.11a Normalised contributions to suspended sediment concentration variance plotted versus normalised cross-shore distance. 225
Figure 6.1.11b Normalised contributions to suspended sediment concentration variance distributed in distance-energy space. 225
Figure 6.1.12 Perranporth run 7 velocity exceedence times, based on a threshold of $0.5ms^{-1}$. 228
Figure 6.1.13 Distribution of 'significant concentration' values for Llangennith runs plotted versus depth. 234
Figure 6.1.14 Distribution of 'significant concentration' values for Spurn Head runs plotted versus depth. 234
Figure 6.1.15 Distribution of 'significant concentration' values for Perranporth runs plotted versus depth. 234
Figure 6.1.16 Distribution of waves with maximum mobility number greater than 50, for Storm Day run 8, Spurn Head run 20 and Perranporth run 9. 235
Figure 6.1.17 Time-series of suspended sediment concentration and mobility number from Spurn Head run 24 235
Figure 6.1.18 Scatterplot of *c* versus *u* for Spurn Head runs 15 (red) and 24 (green). 236
Figure 6.1.19 Distribution of waves with maximum mobility number greater than 50, for Spurn Head runs 15, 20 and 24. 236

Figure 6.1.20 Scatterplot of *c* versus *u* for Perranporth runs 18 (red) and 1 (green). 237

Figure 6.2.1 Normalised bedload moments for B-BAND data used in this analysis, plus Russell and Huntley (1999)'s shape function. 244
Figure 6.2.2 Rescaled sediment fluxes versus normalised cross-shore distance. 244
Figure 6.2.3a Sediment fluxes from Llangennith runs versus normalised cross-shore position. 247
Figure 6.2.3b Temporal variation of mean and oscillatory contributions to sediment flux for Storm Day. 247
Figure 6.2.3c Temporal variation of incident and infragravity frequency oscillatory contributions to sediment flux for Storm Day. 247
Figure 6.2.4 Storm Day run 3 cross-spectra for *c* versus *u*. 248
Figure 6.2.5 Storm Day run 10 cross-spectra for *c* versus *u*. 248
Figure 6.2.6 Comparison between moment terms and fluxes for Storm Day runs. 249
Figure 6.2.7a Sediment fluxes from Perranporth runs versus normalised cross-shore position. 252
Figure 6.2.7b Perranporth temporal distribution of mean and oscillatory sediment fluxes. 252
Figure 6.2.7c Perranporth temporal distribution of incident and infragravity frequency oscillatory sediment fluxes. 252
Figure 6.2.8 Perranporth run 1 cross-spectra for *c* versus *u*. 253
Figure 6.2.9 Perranporth run 9 cross-spectra for *c* versus *u*. 253
Figure 6.2.10 Comparison between moment and (point) fluxes for Perranporth runs. 254
Figure 6.2.11a Sediment fluxes from Spurn Head runs versus depth. 257
Figure 6.2.11b Spurn Head temporal distribution of mean and oscillatory sediment fluxes calculated from bottom sensors on rig A2. 257
Figure 6.2.11c Spurn Head temporal distribution of incident and infragravity frequency oscillatory sediment fluxes calculated from bottom sensors on rig A2. 257

Figure 6.3.1 Contribution to oscillatory flux made by the infragravity component plotted versus normalised cross-shore distance for runs from Storm Day, Storm Night, Perranporth and Spurn Head. 262
Figure 6.3.2 Suspended sediment concentration versus cross-shore velocity co-spectrum for Spurn Head run 1. 262
Figure 6.3.3 Suspended sediment concentration versus cross-shore velocity co-spectrum for Storm Day run 3. 263
Figure 6.3.4 Suspended sediment concentration versus cross-shore velocity co-spectrum for Perranporth run 1. 263
Figure 6.3.5 Suspended sediment concentration versus cross-shore velocity co-spectrum for Storm Day run 10. 263

Figure 7.1.1 Distribution of List (1991) groupiness factor in distance-energy space. The filled symbols indicate where observed incident wave height distributions fit a Rayleigh probability density function. 276
Figure 7.1.2 Comparison between an observed incident wave height distribution, a Rayleigh distribution and a scaled version of Thornton and Guza's (1983) weighted Rayleigh function. Spurn Head run 8, outer surf zone. 276

List of Plates

	Page No.
Plate 3.3.a Example deployment of colocated EMCM and PT.	91
Plate 3.3.b Example deployment of SLOT system (from Egmond-aan-Zee experiment, October 1998).	96

List of tables

	Page No.
Table 3.3.i Calibration values for SLOT 1 OBS.	93
Table 3.4.i Summary of instrument deployments at Llangennith, Spurn Head and Perranporth.	99
Table 4.1.i Thesis dataset run details.	102
Table 4.2.i Autospectra processing details.	108
Table i u statistics for Storm Day, values in ms^{-1}.	289
Table ii u statistics for Storm Night, values in ms^{-1}.	289
Table iii Spurn Head u statistics for bottom EMCM rig A2.	290
Table iv u statistics for Perranporth runs, values in ms^{-1}.	291
Table v Features of the Storm Day η autospectra.	292
Table vi Features of the Storm Day u autospectra.	292
Table vii Features of Storm Day c autospectra.	293
Table viii Features of the Storm Night η autospectra.	293
Table ix Features of the Storm Night u autospectra.	294
Table x Features of Storm Night c autospectra.	294
Table xi Features of Spurn Head rig A2 η autospectra.	295
Table xii Features of Spurn Head rig A2 bottom EMCM u autospectra.	296
Table xiii Features of the Spurn Head rig A2 bottom OBS c autospectra.	297
Table xiv Features of Perranporth η autospectra.	298
Table xv Features of Perranporth u autospectra.	298
Table xvi Features of the Perranporth c autospectra.	299

List of Symbol Notation

a	Wave amplitude (m)
a_0, a_r, b_r	Fourier coefficients
$A_{\infty m}$	Maximum near bottom orbital excursion (m)
$A(f_j)$	Complex Fourier coefficient
$A(t)$	Incident (gravity) frequency wave envelope (m)
$B(f_1,f_2)$	Bispectrum function
$b^2(f_1,f_2)$	Bicoherence estimator
c	Suspended sediment concentration (gl^{-1})
c_g	Wave group speed (ms^{-1})
c_w	Wave celerity (ms^{-1})
c_{nxx}	Discrete time-series cross-correlation function
${c_{bias}}^2$	Biased zero coherence estimator
${c_{unbiased}}^2$	Unbiased zero coherence estimator
C_D	Drag coefficient (dimensionless)
C_0	Reference concentration of sediment at ripple crest (gl^{-1})
C_{12}	Cross-spectral estimator
D	Grain diameter (m)
D_{50}	Median grain diameter (m)
E_g	Incident (gravity) frequency wave energy (m^2)
E_{ig}	Infragravity frequency wave energy (m^2)
EDF	Equivalent degrees of freedom
$Esusp_{ig}$	Infragravity frequency contribution to c spectrum (g^2l^{-2})
$Esusp_{tot}$	Total energy in c spectrum (g^2l^{-2})
f	Wave frequency (Hz)
f_g	Incident (gravity) wave frequency (Hz)
f_i	Infragravity wave frequency (Hz)
f_n	Frequency range for spectral estimates
$f_{N/2}$	Nyquist frequency (Hz)
f_w	Wave friction factor (dimensionless)
$Flux_g$	Incident (gravity) frequency contribution to sediment flux ($kgm^{-2}s^{-1}$)
$Flux_{ig}$	Infragravity frequency contribution to sediment flux ($kgm^{-2}s^{-1}$)
$Flux_{osc}$	Oscillatory components contribution to sediment flux ($kgm^{-2}s^{-1}$)
F_{12}	Phase spectrum
g	Acceleration due to gravity (ms^{-2})
GF	List (1991) groupiness factor
h	Mean water depth (m)
h_b	Water depth at onset of wave breaking (m)
H	Wave height (m)
H_b	Wave height at onset of wave breaking (m)
H_{sig}	Significant wave height (m)
H_{rms}	Root mean square wave height (m)
$I(\omega_p)$	Periodogram function for discrete component frequencies
J_0, Y_0	Zero order Bessel functions
k	Wavenumber ($=2\pi/L$)
k_s	Equivalent bed roughness (m)
K	Number of segments making up spectral estimate
K_{12}	Coherence function
l	Spectrum segment length
L	Wavelength (m)
L_s	Ripple vertical lengthscale (m)
L_∞	Deep water wavelength (m)
L_{12}	Co-spectral estimator

N	Time-series length (sample points)
p	Pressure under waves (Nm^{-2})
p_0	Hydrostatic pressure (Nm^{-2})
$P(f_n)$	Autospectrum function for component frequencies
$P_{12}(f_n)$	Cross-spectrum function for component frequencies
Q_{12}	Quadrature spectral estimator
r^2	Autocorrelation coefficient
r_{xy}	Autocorrelation coefficient for two time-series
Re	Reynolds number
RTR	Relative tidal range
$R^2(f)$	Frequency dependent (squared) reflection coefficient
s	Specific gravity for sediment (dimensionless)
S_{xx}	Radiation stress tensor
t	Time (s)
T	Wave period (s)
TR	Tidal range (m)
u	Cross-shore velocity (x-axis) (ms^{-1})
u_*	Friction velocity at the bed (ms^{-1})
$\hat{U}$	Depth averaged flow (ms^{-1})
$U_{\infty m}$	Maximum free stream wave orbital velocity (ms^{-1})
v	Longshore velocity (y-axis) (ms^{-1})
w	Vertical velocity (z-axis) (ms^{-1})
x	Horizontal cross-shore position (m)
$x(t)$	Arbitrary time-series
z	Vertical position (m)
α	Confidence level
$\beta(f_1,f_2)$	Biphase estimator
$\tan\beta$	Beach slope
Δt	Time-series sampling interval
γ	Wave breaker index
γ_b	Critical wave breaker index
γ_k	Autocovariance function for lag k
γ_{12}	Covariance function
η	Sea surface elevation (m)
η_{in}	Incoming (shoreward directed) wave sea surface elevation (m)
η_{ref}	Reflected wave sea surface elevation (m)
Λ_{12}	Co-spectrum function
Π_{12}	Quadrature spectrum function
θ_{cr}	Critical Shields stress ($kgms^{-2}$)
ρ	Fluid density (kgm^{-3})
ρ_s	Sediment density (kgm^{-3})
σ	Wave angular (radian) frequency ($=2\pi/T$)
τ_0	Bed shear stress (Nm^{-2})
τ_{cr}	Critical bed shear stress (Nm^{-2})
υ	Fluid viscosity (m^2s^{-1})
ω_p	Set of finite component frequencies for periodogram
ω_s	Sediment fall velocity (ms^{-1})
Ω	Dimensionless fall velocity
ξ	Iribarren number
$\Psi(t)$	Mobility number

Acknowledgements

The author would like to thank his two supervisors, Dr. Tim O'Hare and Dr. Paul Russell for their expertise and encouragement during the course of this work. A special mention should also go to Prof. David Huntley, Dr. Mark Davidson and Dr. G. Ruessink for listening, their ideas and suggestions, and not sighing too loudly when I asked stupid questions.

Honours for remaining calm and patient during the teeth gnashing and swearing phases of the project go to my office mate Giovanni Coco and girlfriend Sophie Sim, who have managed to ignore my bad moods in the way that only true friends can. I am also grateful to Darren Stevens for his help with scanning and diagrams and saving my computer from going out of the window on more than one occasion, and Jon Miles and Peter Ganderton, who did all the hard work for the Perranporth experiment.

My family have always supported me, and a special thanks goes to my mum and dad for all they've done for me over the last few years. I feel very lucky to have you as parents.

Finally, cheers to all the friends I've made since coming to Plymouth. In particular my drinking partners, who've reliably informed me over the years that they've kept me out of more trouble than I've got them into. It's been a pleasure...

Author's Declaration

At no time during the registration for the degree of Doctor of Philosophy has the author been registered for any other University award.

This study was financed with the aid of a studentship from the Natural Environment Research Council.

Regular departmental scientific seminars were attended and the author presented work on a number of occasions. The author also attended the UK Oceanography Conference in 1996 and 1998, and the International Conference, Coastal Dynamics '97.

Presentation at Conferences:

Analysis of Infragravity Wave-Driven Sediment Transport on Macrotidal Beaches. Oral presentation at Coastal Dynamics '97, Plymouth.

Mechanisms for Sediment Transport at Infragravity Frequencies in the Surf Zone. Oral presentation at UK Oceanography '98, Southampton.

Signed .....

Date 28/1/2000

Chapter 1: Introduction

Despite the fact that numerous field studies have acknowledged and examined the role of infragravity waves in nearshore sediment transport, modelling approaches have tended to employ relatively simplistic descriptions of low frequency hydrodynamics. Apparently good qualitative cross-shore profile evolution model results have been cited using assumptions such as the incident infragravity wave component being dominated by a single frequency (e.g. Bowen, 1980), or even ignoring the infragravity component altogether (e.g. Dally and Dean, 1984). Similarly, the role of the infragravity component in sediment transport has often been interpreted differently in model design. For example, Bowen (1980) suggested a scheme whereby the infragravity wave velocity acted as a drift velocity for transport of sediment, whereas O'Hare and Huntley (1994) discussed a model in which transport varied through the nearshore as a result of the changing phase between waves in the incident frequency band (which would suspend sediment) and standing infragravity waves (which acted to transport sediment). Models based on a velocity moments approach (e.g. Russell and Huntley, 1999) derive their results from velocity values which include contributions from all the hydrodynamic components (mean, infragravity wave, incident wave).

Consequently, for the purposes of future modelling work it still seems necessary to clarify not only the behaviour of the infragravity wave component in the nearshore, but also its interaction with the other hydrodynamic components. In particular Huntley *et al.* (1993) highlighted the effects of a combination between modulated incident waves and infragravity waves, and concluded that in nearshore modelling the "interactions between long wave motion and other forms of water movement must be included". With this last point in mind, it is worth pointing out that this thesis does not solely discuss infragravity wave driven sediment transport. Instead the work examines infragravity frequency variations in sediment transport and the processes behind them. The difference between these two statements is essential to the subsequent content of the thesis, and so some further clarification will be made over the next few paragraphs.

The term *infragravity* is generally associated with sea surface waves, where the infragravity component of the wave spectrum defines the region of frequency space in the range 0.005-0.05Hz, i.e. periodic motions of between 200 and 20 seconds. The existence of such a component of the wave field was first suggested by Munk (1948), in a presentation to the International Union of Geodesy on the concept of 'beats of the surf'. These were

defined as fluctuations in mean sea level of order 0.01-0.1m at periods of about 2 minutes, and Munk (1948) suggested that these waves were attributable to variations in the height of the surf itself. Tucker (1950) confirmed that these signals existed in the nearshore environment from observation of similar long period oscillations made using a pressure gauge positioned just offshore of a beach at Perranporth, Cornwall. Furthermore, Tucker (1950) demonstrated that these signals lagged those of the incident wave groups by a length of time corresponding to that for propagation into and reflection from the shoreline of a wave as predicted by (linear) shallow water wave theory. This result inferred the existence of long waves associated with surface wave modulations, the energy from which is not dissipated through breaking in the surf zone and therefore is reflected from the beach.

In morphodynamic terms it has been suggested that because nearshore bars have a cross-shore scaling similar to infragravity wave wavelengths, these morphologic features could be somehow associated with these waves (e.g. Short, 1975). For example, following observations that infragravity wave energy will be reflected, rather than dissipated, on a beach (Tucker, 1950; Suhayda, 1974), the formation and maintenance of bars has been linked to the formation of a standing wave structure in the nearshore (e.g. Bowen, 1980). Since within this body of work the intent is to examine the infragravity component of sediment transport in the cross-shore sense, infragravity waves are likely, by definition, to be extremely important. For example, in a high energy dissipative surf zone, infragravity waves may traverse the surf zone, which is a region of dissipation for waves in the *incident* (or *gravity*) frequency band (0.05-0.5Hz), without loss of energy (Bowen and Guza, 1976). Furthermore infragravity wave heights should increase in the shoreward direction, as a result of shoaling, whilst in a saturated surf zone, incident wave heights should be depth limited (Longuet-Higgins, 1970) and will therefore decrease in the shoreward direction. Thus the infragravity waves may well provide the dominant energy for transport close to shore, as was observed by Beach and Sternberg, (1991) and Russell (1993).

However, at this point it is reiterated that the work here examines sediment transport at infragravity frequencies rather than simply infragravity wave associated transport. The difference between the two definitions is that where the latter is seen as sediment flux due to an individual hydrodynamic component, the former will include all low frequency variations in flux caused by the instantaneous velocity field (for example due to groupiness effects of incident waves). This can be illustrated better by the example in figure 1.1, which shows a set of time-series of suspended sediment concentration, instantaneous

velocity and low and high frequency components of velocity. For the run from which these time-series were taken, the instruments were situated inside a saturated surf zone, in a water depth of approximately 0.8m.

An approach to the sediment transport problem such as that described by Dally and Dean (1984) suggests that breaking waves will stir sediment, which will subsequently be transported by the mean current. In a saturated surf zone it is also suggested that wave heights should be uniform at any given point in the cross-shore, since the broken wave heights will be depth limited. Therefore a regular time-series of suspended sediment concentration might be expected if no low frequency components are present. The bottom of the three plots in figure 1.1 shows a high and low passed filter of the cross-shore velocity time-series, which respectively represent the incident and infragravity wave components. Regarding the high passed velocity time-series in figure 1.1, a level of modulation remains present in the (broken) incident wave heights. The time-series of suspended sediment concentration also shows several larger than normal suspension events. Events can be seen at approximately 60, 100 and 230 seconds in the time-series, and the periods separating these events would, if an analogy were drawn with the wave frequency spectrum, put them into the infragravity band. Whilst the first two events appear to be associated with a sharp acceleration due to the passage of a bore front, the largest event at 230 seconds is associated with an offshore directed maximum in velocity magnitude. An examination of the low and high frequency components of velocity shows that this latter velocity maximum is the result of a combination of velocities associated with both an incident frequency wave and an infragravity wave.

In calculating flux of sediment, the phase between observed suspended sediment concentrations and velocity determines transport direction. Correspondingly the suspension events in figure 1.1 at 60 and 100 seconds, which occur during an onshore phase of velocity, will yield an onshore directed transport. The event at 230 seconds will conversely lead to an offshore directed flux. Overall transport from the run will be determined by how the flux associated with these events balance out with the smaller events which occur during the time-series at incident frequencies.

Thus, in terms of predicting flux of sediment, the question posed by large suspension events occurring at low frequencies is: "How these would these modify the type of transport expected, following a model for sediment flux where sediment is suspended by a uniform train of incident frequency waves, and transported by a combination of the mean

and infragravity components?" For example, if suspended sediment-velocity phase is in the opposite sense for the majority of suspension events, when compared with the largest low frequency associated events, transport over a given period of time would be smaller than might be expected. It is therefore important to understand the processes that drive large low frequency suspension events. By simply assuming that suspended sediment concentration will be a function of velocity, the event at 230 seconds in figure 1.1 suggests that the largest suspension events can occur as a product of the coincidence between a large breaker trough and the trough of an infragravity wave. If both the incident and infragravity components of the wave field affect suspension, then it can be argued that in order for such a model to predict events such as those in the example, several hydrodynamic issues must be correctly addressed.

1. Modulation in incident wave heights.
2. Infragravity wave behaviour.
3. The phase relationship between the two components.

It should also be noted that thus far the response of the bed to such forcing has not been considered. Such considerations include whether suspended sediment concentrations are velocity or acceleration driven, and whether the response of the bed is dependent on the direction of the velocity of the overlying fluid.

Considerations of the type listed above, are not general features of current nearshore models. For example, Schoones and Theron (1995) reviewed ten cross-shore profile evolution models with respect to a number of morphodynamic criteria, but also noted the hydrodynamic elements driving the models in each case. It was found that models documented by Shibayama (1984), Nishimura and Sunamura (1986), and Larson (1988) failed to include either a mean (return flow) current or a long wave component. Similarly Dally and Dean (1984), Kriebel and Dean (1984) and Steetzel (1987) ignored the effects of the long wave component. Furthermore, for a number of recent models reviewed by Broker-Hedegaard *et al.* (1992) it was concluded that the understanding of the velocity field in the area around the breakpoint remained poor.

The incorporation of the infragravity component into a hydrodynamic scheme is a particular feature of models by List (1992) and Roelvink (1993). Both of these models solve the shallow water equations for the incident frequency component by linear theory whilst using a second order solution for the infragravity waves, and therefore do not take non-linear interactions between frequencies into account. However, if interactions between the incident and infragravity components do take place, then this will have a direct impact

on the phase relationship between the two components. Furthermore, the models use a description of the breaking incident frequency component which is essentially related to depth, and therefore fails to include any effects of the transmission of groupiness into the saturated part of the surf zone. In this regard, probably a better simulation of the surf zone is likely to be made by Boussinesq models such as those documented by Chen *et al.* (1997), Madsen *et al.* (1997) and Norheim *et al.* (1998). These models allow for interactions between frequencies making up the wave field, and hence follow observed wave spectra rather more closely than those models previously mentioned. In another model, Schaffer (1993) has described a scheme where provision is made for the transmission of a modulated incident frequency wave envelope through the breaker line and into the surf zone. Nonetheless, Boussinesq type models, although encouraging are still seen as being under development in the literature, and as Norheim *et al.* (1998) point out, any deterministic Boussinesq model will be highly computationally intensive.

This last statement illustrates the modeller's major dilemma - that if a model is to be used for a range of scenarios, a balance has to be struck between producing a robust efficient scheme whilst representing physical processes both meaningfully and accurately. Field data such as that presented here, should be a useful tool in such model conception, particularly since data analysis allows the mean, and incident and infragravity oscillatory components of the hydrodynamics and sediment transport to be assessed individually. According to an individual component's behaviour and importance in terms of the overall system, a choice can then be made regarding the level to which accuracy is traded off against convenience in model implementation.

This thesis details such data analysis, with the aim of examining infragravity frequency sediment transport with respect to how this component needs to be represented in cross-shore modelling of beach profiles. The particular issues to be addressed are to find, at least qualitatively and across a range of conditions, the driving mechanisms and effects of high concentration suspension events which occur at low frequencies, and the role played in transport by the infragravity wave component. With this in mind, the approach adopted has been to analyse several datasets, rather than an individual site, in order to attempt to describe more generally the effect of infragravity sediment transport across a range of moderately to highly energetic storm conditions.

To provide a background for the work presented here, chapter 2 presents a literature review describing nearshore processes, with a particular emphasis on the role of the infragravity

component. The field programme, of which two sites are taken from the existing British Beach and Nearshore Dynamics (B-BAND) dataset, is documented in chapter 3, whilst the data and its processing are described in chapter 4. In the following analysis the particular focus will be on the low frequency components of both the hydrodynamics and the resultant sediment dynamics.

Results of the hydrodynamic analysis are described in chapter 5, and aim to examine:

H.1 The evolution of infragravity wave energy through the nearshore, whether these waves are forced or free, and the extent to which infragravity energy may be dissipated.

H.2 Infragravity wave reflection and the possible formation of standing waves.

H.3 The nature of low frequency modulation of incident wave heights through the nearshore.

H.4 The phase relationship between modulated incident and infragravity waves, particularly as a result of any interactions between the two components.

The hydrodynamics results (chapter 5) are discussed further in the context of the sediment dynamics observations, particularly in terms of driving suspension of sediment, in chapter 6. Here the focus will be on:

S.1 Establishing whether sediment suspension is velocity or acceleration driven, and identifying the main hydrodynamic components underlying the largest suspension events at a given point in the cross-shore.

S.2 Examining the contribution to suspension and transport attributable to the infragravity frequency component.

S.3 Identifying cases where a change in the low frequency hydrodynamics results in sediment flux qualitatively different to that expected when assuming a more simplistic scenario.

A discussion of the results and some ideas for future work are presented in chapter 7. The concluding remarks are made in chapter 8.

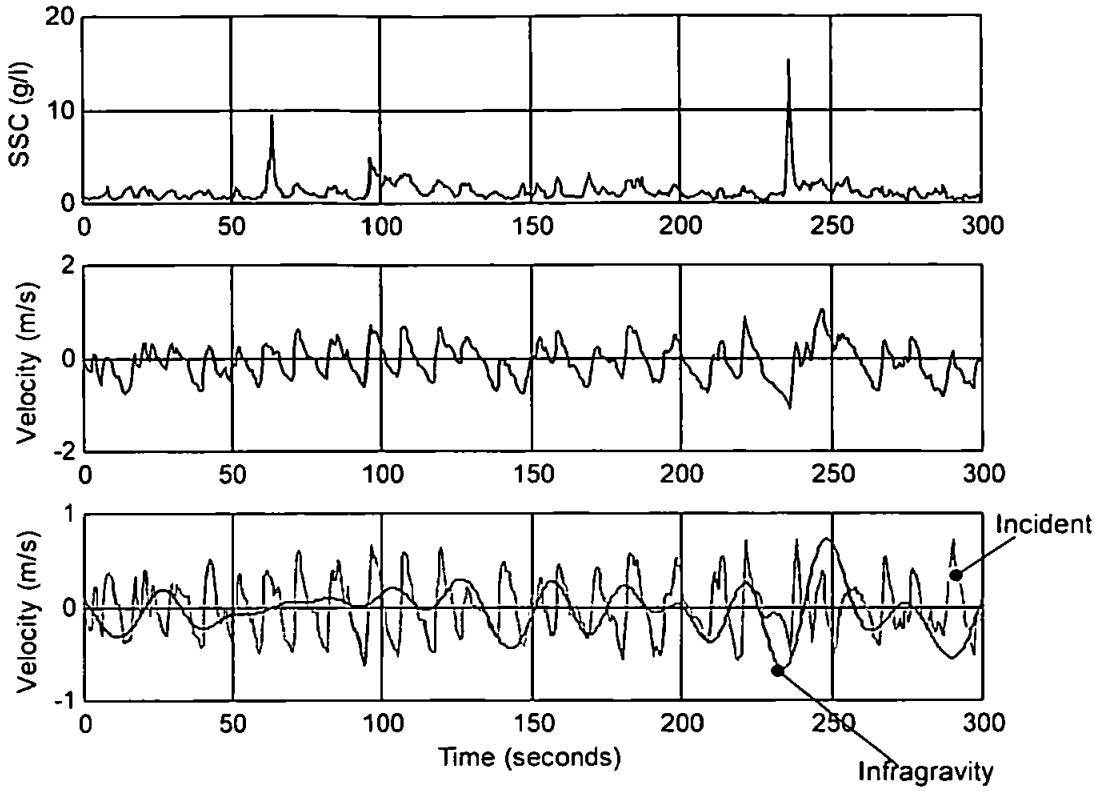

Figure 1.1 Field data time-series of suspended sediment concentration, instantaneous velocity, and high and low frequency oscillatory components of velocity observed by instruments positioned in the surf zone (data taken from experiment at Llangennith beach, South Wales, water depth h=1.06m).

Chapter 2: Review of nearshore processes

For the purposes of this thesis, it is considered that low frequency fluctuations in observed suspended sediment concentrations will result from low frequency modulation of the wave field. Following this assumption, the work first attempts to examine sources of infragravity frequency variation in the hydrodynamics before investigating the sediment dynamics. In the introduction these were identified as modulation of incident frequency wave heights (see section 2.1) and the infragravity wave component itself (see section 2.2).

2.1 Nearshore zone incident frequency wave hydrodynamics

2.1.1 Incident frequency wave hydrodynamics and a division of the nearshore

A discussion of the behaviour of the incident frequency component also allows for a relatively convenient and practical definition and division of the *nearshore zone* to be made. Komar (1998) physically defined the region as an area reaching seawards from the shoreline to just beyond the region of wave breaking. For modelling and engineering purposes this seaward boundary has been more rigorously defined using a depth of closure at which wave effects on sediment transport are deemed negligible (Hallermeier, 1981). Basinski (1989) further noted that by using a visibly observable process such as incident wave behaviour, a logical division of the nearshore zone could be made according to the behaviour of waves within this region. This is because, as the waves enter the nearshore zone, they undergo large changes in celerity, height and steepness, finally leading to dissipation of energy through breaking. In the following discussion, the case is considered of a wave field normally incident onto a plane sloping beach. The nearshore zone may then be divided into four zones (following Basinski, 1989, and extending the three zone definition used by Masselink, 1993, by separating the surf zone into two), according to the incident wave evolution from deep water through to the shoreline (figure 2.1.1).

Using this definition, the nearshore zone consists (from seaward to shoreward) of the

- Wave shoaling zone
- Outer surf zone
- Inner surf zone
- Swash zone.

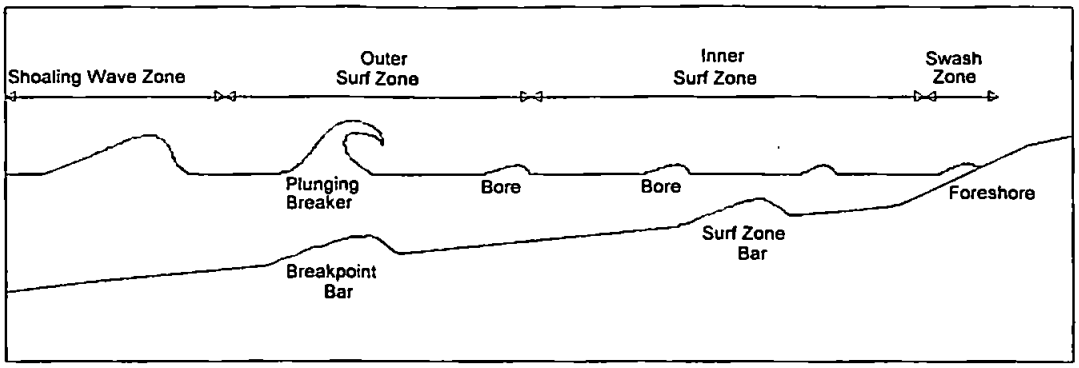

Figure 2.1.1 Distribution of (incident wave) hydrodynamic processes across an idealised nearshore.

2.1.2 Incident frequency waves outside the break point

Waves incident to the nearshore zone will have made a transition from what is defined as deep water to the *shallow water, wave shoaling zone*. Commonly water is considered deep or shallow for waves according to the relationship

$L_\infty/h \leq 2$, deep water, or,

$L_\infty/h \geq 20$, for shallow water,

where L_∞ is the deep water wavelength, and h depth. The waves arriving at the nearshore are generally termed as being in one of two forms. First, swell waves are generated as a product of distant ocean storms, in which strong winds blow for a long duration, and over a large unobstructed area of sea (the fetch). The resulting large swells see 'free' incident frequency waves propagating as modulated groups as a result of wave dispersion. Secondly, localised storms generate wind sea waves, which are generally of a shorter period and wavelength than their swell counterparts, and tend to be more randomly distributed in terms of wave heights. These waves are 'forced' by the wind.

The idea of *groupiness* in unforced deep water swell can be presented simply by making the assumption that deep water waves follow a sinusoidal form. Following this assumption, a monotonic wave train can be described using the expression

$$\eta = a.cos(kx-\sigma t) \tag{2.1}$$

where η is sea surface elevation, a is wave amplitude, k is wavenumber ($=2\pi/L$, L wavelength), and σ is angular frequency ($=2\pi/T$, T is wave period). Wave speed (celerity) may then be defined as $c_w=\sigma/k$. If two wave trains travelling in the same direction, but with different frequencies ($\sigma \pm \Delta\sigma$ respectively) are then superimposed, the resultant is described by

$$\eta = 2a.cos\Delta\sigma t.cos(kx-\sigma t) \tag{2.2}$$

i.e. the original expression is modulated at a period of $T_{group}=\pi/\Delta\sigma$ (e.g. figure 2.1.2, where T=10 seconds and T_{group}=80 seconds). A similar result may also be obtained by considering waves of slightly differing wavenumber. Group speed for such a wave train made up of two monotonic wave trains with similar angular frequencies σ_1 and σ_2, and wavenumbers k_1 and k_2, may then be expressed as

$$c_g = (\sigma_1-\sigma_2)/(k_1-k_2), \tag{2.3}$$

which may be written in terms of the component wave speeds c_1 and c_2

$$c_g = (c_1.c_2)/(c_1+c_2). \tag{2.4}$$

Notably, if the difference between the angular frequencies and wavenumbers is small, then

$$c_g \cong \frac{c}{2}, \tag{2.5}$$

i.e. group speed is approximately half the speed of the component waves in deep water (Kinsman, 1965).

For waves in shallow water, individual wave (phase) speed reduces, tending towards the group speed. Mathematically, following Airy (1845) (linear) wave theory, this gives wave speed in shallow water of

$$c_w = \sqrt{gh}, \tag{2.6}$$

where c_w is wave celerity, and g is acceleration due to gravity. This slowing of the waves gives rise to depth refraction, and consequently wave propagation will tend toward an angle which is normal to the beach face. Since this change in velocity will also lead to a shortening of wavelength and increase in amplitude, shoaling leads to an increase in steepness. Accordingly, wave particle velocities take a more elliptical form.

Two factors, wave 'skewness' and 'asymmetry' (Elgar and Guza, 1985) are used to describe wave shape versus a sinusoidal form in terms of horizontal and vertical symmetry respectively. For example, in the shoaling process a wave would be expected to increase its (positive) skewness as the crest peaks, whilst as the wave pitches forward the steep front face will lead to a negative wave asymmetry (figure 2.1.3).

The skewness and asymmetry descriptors for wave shape were presented mathematically by Doering and Bowen (1995), who parameterised skewness and asymmetry values derived from the wave bispectrum, where the bispectrum describes the wave field component interactions in frequency space. Bispectrum calculation details are given in section 4.4.4, but a brief description of the type of results derived from a bispectral analysis is given now. The calculated bispectrum consists of both real and imaginary parts, and is plotted (using either real, imaginary, bicoherence or biphase values) in a three-dimensional form, where the x-y plane represents frequency space. Peaks in the bispectrum show a strong interaction between frequencies. In interpretation of the bispectrum a notation of $f_1+f_2 \rightarrow f_3$ is used, where f_3 is the sum of the other two frequencies. It is important to point out that this notation does not indicate the direction of energy transfer, i.e. whether energy is transferred to the higher (summed) frequency or the lower (difference) frequency. However, by an examination of whether peaks within the real or imaginary parts of the bispectrum are positive or negative, the direction of transfer of energy can be determined (Wells, 1967).

The behaviour of the real and imaginary parts of the bispectrum was employed by Doering and Bowen (1995) in parameterising changes in wave shape through the nearshore. For example, during wave shoaling, energy from the dominant wave frequency ('primary') cascades to higher harmonics, and in the real part of the bispectrum this will be represented by a positive peak at the primary incident ('gravity') frequency (denoted $B(f_g,f_g)$, e.g. figure 2.1.4). Similarly, in a previous study, Flick *et al.* (1981) noted that in bispectral terms the pitching forward of a wave is represented by a forward phase-shift of the harmonic components relative to the primary. Following this, Doering and Bowen (1995) proposed the skewness parameter based on the real part of the bispectrum, and an asymmetry parameter based on the imaginary part. In the shoaling zone skewness was observed to increase to a maximum at the breakpoint, and then decrease in the surf zone, with increased wave breaking. Waves were also observed to become more asymmetric in the shoaling zone, but this asymmetry was maintained in the surf zone, as waves tend to remain pitched forward when in bore form.

Thus it should be noted that as shoaling occurs, the already tenuous sinusoidal form used to model waves in deep water becomes even less applicable to individual waves, which take on a shape more accurately described by cnoidal theory close to the break point. Furthermore, non-linear interactions occur between the dominant wave frequency and its harmonics and subharmonics in the nearshore zone. The existence of these frequency interactions has led various authors to develop non-linear models for waves in this situation, for example using approaches based around the Boussinesq equations (e.g. Elgar and Guza, 1985, Norheim *et al.* 1998). When considering wave groups however, enough of the convolution properties of the sinusoidal functions used by Airy wave theory appear to hold in the nearshore to allow analysis based on these functions (e.g. Fourier analysis) to be used in studies of nearshore time-series. Indeed, Davidson (1992) found linear theory adequate for characterising surf zone conditions on a natural beach, and use of Fourier techniques to derive wave field spectra has become an established practice used by deep and shallow water oceanographers alike.

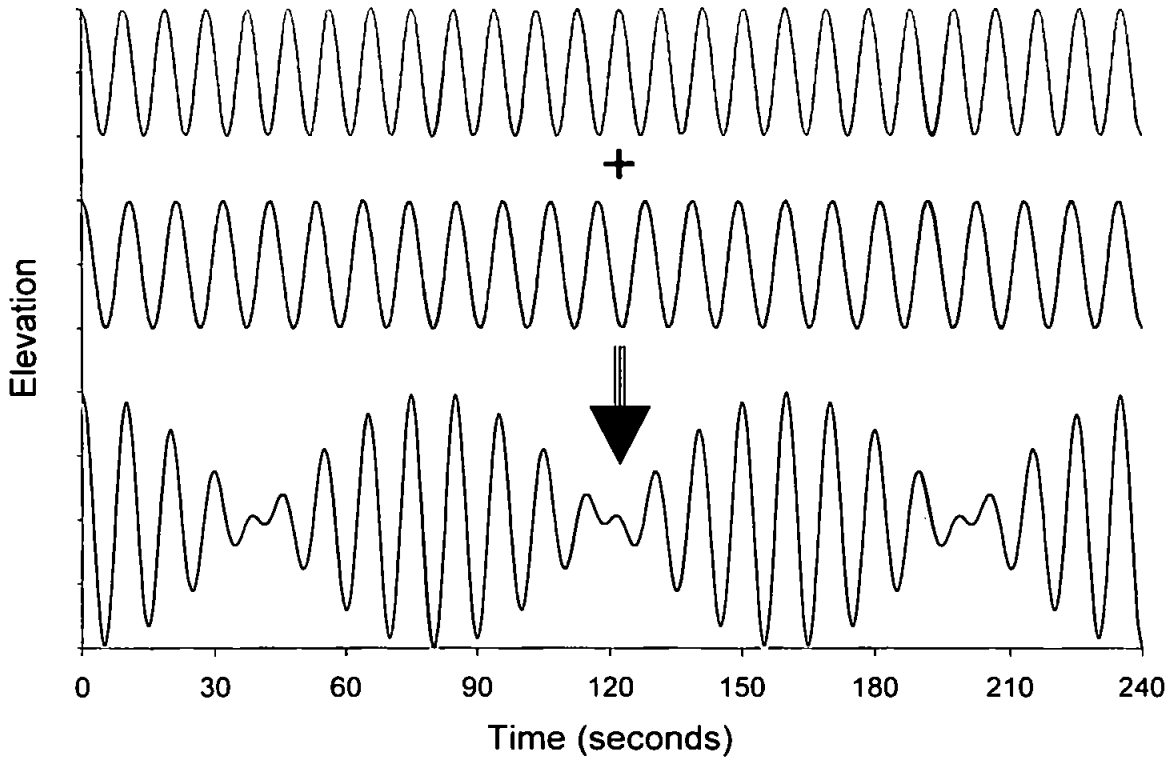

Figure 2.1.2 'Groupy' waves as formed from the combination of two sinusoids. T=10 seconds, T_{group}=80 seconds.

Sinusoidal Waves

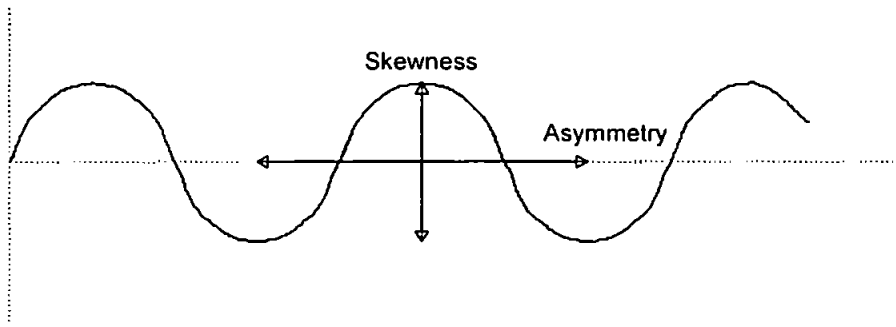

'Shoaled Waves'

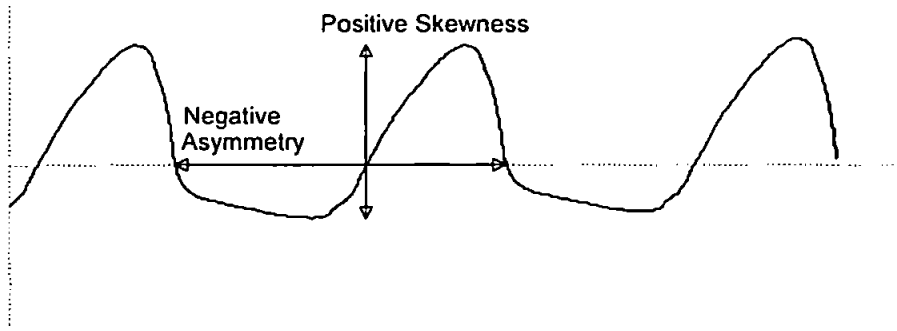

Figure 2.1.3 Variation in skewness and asymmetry between a sinusoidal (Airy) wave form and a shoaled wave.

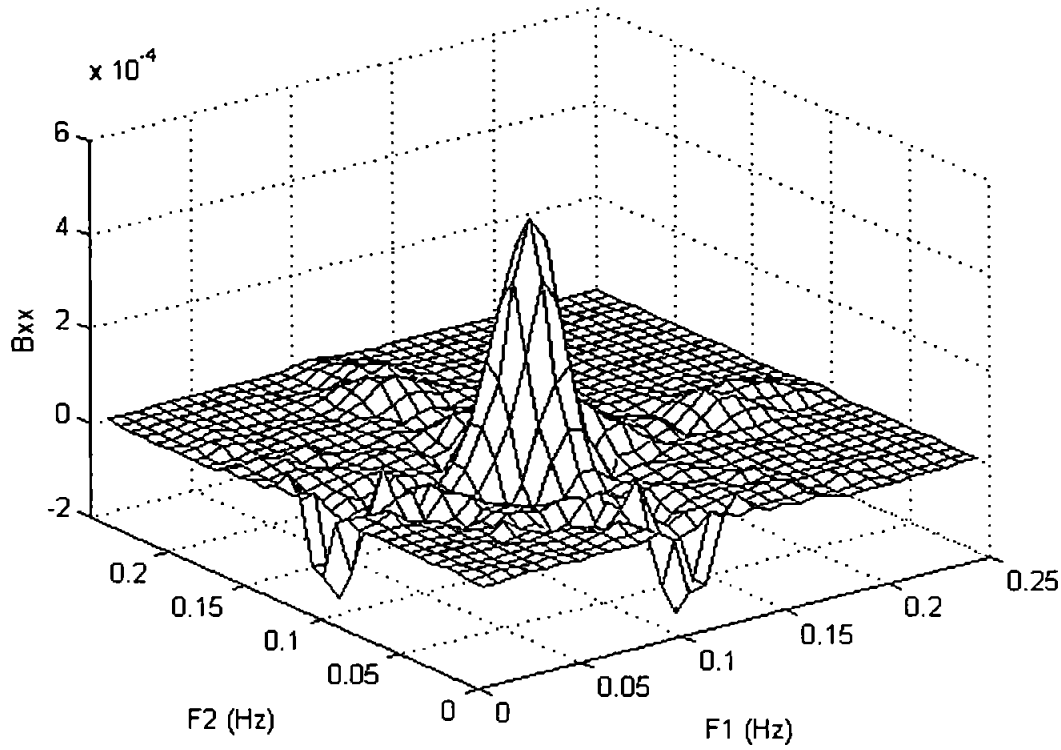

Figure 2.1.4 Real part of a sea surface elevation bispectrum for shoaling waves (with frequency 0.1Hz).

2.1.3 Incident frequency waves inside the break point

In the shoaling zone, incident frequency waves will continue to steepen until finally the wave crest can no longer be supported and the wave breaks. For groupy swell waves wave heights will vary, and therefore breaking may commence, at a varying offshore position dependent upon wave height. This *breaker zone, outer surf zone* region is thus defined by the positions of the onset of breaking for the highest (seaward limit) and lowest (shoreward limit) waves in the incident groups (Symonds *et al.*, 1982). Laboratory research based on solitary waves (Ippen and Kulin, 1954; Kishi and Saeki, 1966) first suggested wave breaking occurring at some critical steepness value, where steepness is defined as the ratio of wave height to wavelength. This led to the derivation of a critical breaker index as a function of wave height H_b and water depth h_b,

$$\gamma_b = \frac{H_b}{h_b}. \tag{2.7}$$

The value of γ_b was found to be variable (usually between 0.78 and 1.3), dependent upon beach profile and wind direction, for periodic waves in the review made by Weggel (1972).

In the breaker zone extremely important dynamic changes in wave form occur, since energy propagated by the waves is released in a violent fashion and is both dissipated through breaking and redistributed to higher and lower harmonics (Doering and Bowen, 1995, Baldock and Swan, 1996). Breaker types can take on four forms according to beach slope and incident wave characteristics. Spilling breaking sees the waves peaking until the wave crest becomes unstable and simply bubbles down the wave face. More spectacularly, plunging breaking finds the crest being thrown forward and downward as an intact mass of water. Surging breakers peak up in a fashion similar to plunging type breakers, but then the base of the wave surges up the beach and the crest collapses. Collapsing breakers (Galvin, 1968) exhibit behaviour somewhere between the plunging and surging types. Komar (1998) noted that these wave types adhere almost to a continuum. In this continuum, spilling breakers tend to be a product of high steepness waves occurring on gently sloping beaches, plunging breakers are associated with intermediate steepness waves on steeper beaches, and surging breakers occur when low steepness waves are incident on extremely steep beaches. For beaches of low to moderate slope, experiencing moderate to high energy conditions, the first two forms are the most commonly observed.

In more analytical terms, Galvin (1968) attempted to predict breaker type based on a dimensionless value derived from deep water wavelength, wave height and beach slope. Galvin's (1968) equations were rearranged by Battjes (1974) to derive deep and shallow water forms of the Iribarren number,

$$\xi_\infty = \frac{\tan\beta}{(H_\infty / L_\infty)^{1/2}}, \tag{2.8}$$

and

$$\xi_b = \frac{\tan\beta}{(H_b / L_\infty)^{1/2}}, \tag{2.9}$$

where $\tan\beta$ is the beach slope, and the subscript ∞ denotes deep water values, with b values at the break point. Following this formulation breaker type is predicted according to

spilling	$\xi_\infty<0.5$	$\xi_b<0.4$
plunging	$0.5<\xi_\infty<3.3$	$0.4<\xi_b<2.0$
surging	$3.3<\xi_\infty$	$2.0<\xi_b$.

These values have been further supported by Okazaki and Sunamura (1991). This relationship between breaker type, wave steepness and beach slope emphasises the importance of wave steepness to the value of the breaker index, and thus Kaminsky and Kraus (1993) derived an empirical formula for γ_b based on the Iribarren number,

$$\gamma_b = 1.20\xi_\infty^{0.27}. \tag{2.10}$$

Following initial breaking, waves in the surf zone transform into a turbulent bore form, and as they propagate toward shore dissipate energy. In the outer surf zone the wave forms will be mixed between as yet unbroken waves and turbulent bores. Consequently the deep water 'groupy' form for the modulation of wave heights may be drastically altered by the onset of breaking (figure 2.1.5). As an extreme case, Schaffer (1993) pointed out that the breaking process could lead to a reversal in the outer surf zone of the wave group form observed in the shoaling zone, as the largest waves break whereas the smallest ones will continue to shoal. Since the breakpoint position for a wave of a given height, and therefore the outer surf zone width, will be dependent upon beach slope, this will have a consequence on the distribution of both wave heights and type (shoaling or breaking) observed at a given point in the outer surf zone. For example on a steep beach waves will remain mostly unbroken until near the shoreline (Baldock *et al.*, 1997).

Thornton and Guza (1983) found that broken wave heights have a distribution which differs from the case where all waves take an unbroken form, as represented by the deep water Rayleigh distribution

$$\mathrm{P}(H) = \frac{2H}{(H_{rms})^2}\exp\left[-\left(\frac{H}{H_{rms}}\right)^2\right], \tag{2.11}$$

where H_{rms} is root mean squared wave height, as validated by Longuet-Higgins (1952). Thornton and Guza (1983) suggested that the breaker heights could be modelled by a distribution based upon the Rayleigh form but where a weighting function was applied using

$$\left(\frac{H_{rms}}{\gamma h}\right)^n\left\{1-\exp\left[-\left(\frac{H}{\gamma h}\right)^2\right]\right\}, \tag{2.12}$$

with n being a coefficient determined from the observations. Thornton and Guza's (1983) values saw γ=0.42 and n=2.

It is notable that the breaker index value used in Thornton and Guza's (1983) weighting function is rather lower than the 0.78 value suggested by Weggel (1972). However, whilst Weggel's (1972) value is deemed applicable to breaking waves, the lower value is considered more appropriate for fully broken waves (bores). For example, Horikawa and Kuo (1966) found that whilst γ_b=0.78 gave a good criterion for initial breaking, an asymptotic decrease in the breaker index occurred within the surf zone as more waves took on a turbulent bore form.

Guza and Thornton (1983) stated that at the value of γ=0.42, wave heights appeared to be governed by water depth and were therefore independent of deep water wave height. Additionally Holman and Sallenger (1985) and Raubenheimer and Guza (1996) have shown that wave heights in this part of the surf zone tend to be independent of offshore wave steepness. This region where breaking wave energy is apparently saturated is defined as the *inner surf zone*. The idea of this region, where breaking wave heights are depth limited has previously provided an important tool for modellers wishing to simplify their description of the surf zone. By making this assumption, wave heights can be described using water depth and a pre-set breaker index. Consequently (and ignoring infragravity wave effects which will be discussed further in the next section), at any given point in a saturated inner surf zone breaker heights will be uniform (figure 2.1.5).

What remains of incident frequency wave energy is considered to be finally dissipated in the *swash zone*. This zone is bounded by the minimum and maximum excursion of waves running-up the shoreface. Whilst at present little is known of the contribution made by this region to sediment transport in the nearshore, numerous studies of wave run-up have been made since Guza and Thornton (1982) produced one of the early papers examining swash (Butt and Russell, 1999). Huntley *et al.* (1977) and Wright *et al.* (1982) found the dominant infragravity components to be visually observable in swash. Interest in this zone has been maintained even on steep beaches, where although individual incident frequency waves can be picked out in run-up time-series, a large amount of energy, in terms of motion of the shoreline, is found at infragravity frequencies (e.g. Baldock *et al.*, 1997).

The model of Madsen *et al.* (1997) has suggested that shoreline motion is dependent upon breaker type, with a lower frequency motion being associated with spilling waves, as opposed to plunging wave conditions where individual waves can be easily picked out in the swash. However, it is worth noting that spilling breakers are more usually associated with beaches of low slope, and are therefore more likely to be observed in conjunction with a saturated surf zone. Since in a saturated surf zone wave heights are deemed to be independent of breaking conditions, then it is likely that the swash in such an instance will show little low frequency variation due to individual incident frequency wave run up. On steeper beaches where plunging breaking occurs, non-saturated conditions may be more likely to occur. Thus the inference of Madsen *et al.*'s (1997) result is more likely a statement on the type of surf zone associated with different breaker type, which is a consequence of beach slope.

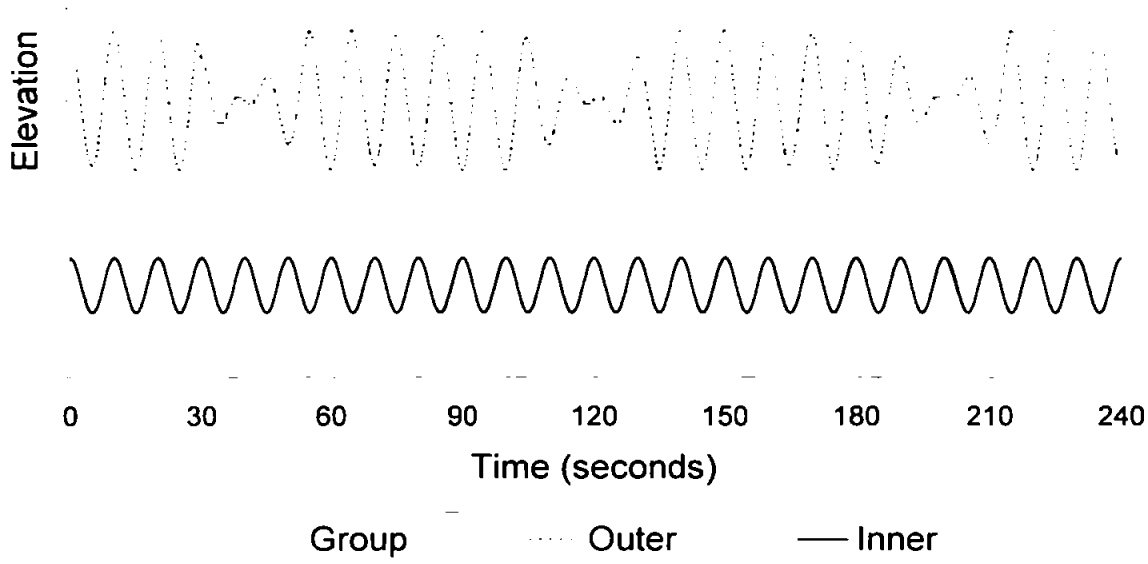

Figure 2.1.5 (Theoretical) Change in wave height modulation between deep water, and the outer and inner surf zones.

2.1.4 Summary: Incident frequency waves in the nearshore

The behaviour of visibly observable incident frequency waves allows the nearshore zone to be conveniently divided into four further regions. Furthest offshore, in the wave shoaling zone wave height and steepness increases as depth decreases. At a critical steepness (which can be defined by the breaker index $\gamma=H/h$, e.g. $\gamma=0.78$ for spilling waves) wave breaking will commence, with the highest waves breaking furthest offshore and the smallest waves commencing breaking at some point further onshore. This region defines the time-variant breaker line. Just inside the breakpoint the waves will be a mixture of depth limited bores and unbroken waves; the outer surf zone. As wave breaking increases in the shoreward direction, the breaker index will decrease tending to a value of approximately 0.4 as all waves become broken and their heights will be depth limited. This region of saturated wave breaking is defined as the inner surf zone. Breaking wave energy is finally completely dissipated at the shoreline in the swash zone.

The transformations undergone by waves in these four regions show not only a change in individual wave shape, as can be described by skewness and asymmetry, but also a transformation of the modulation associated with deep water wave groups. In the shoaling zone this modulation is likely to be maximum in terms of the magnitude difference between the largest and smallest wave heights. However, in the outer surf zone the largest waves will have commenced breaking whilst what in deep water were the smallest waves continue to shoal. Theoretically at least, breaking wave heights will tend to be uniform at any given point in the inner surf zone since they are depth limited.

2.2: Infragravity frequency wave hydrodynamics

The previous section introduced the classification of the nearshore solely in terms of the highly visible incident frequency wave component. This component is rapidly dissipated within this region and therefore an increasingly important contribution to the hydrodynamics of the nearshore zone will come from oscillatory components at infragravity frequencies. This next section deals with the generation and behaviour of infragravity waves, firstly in deep water offshore, and then in shallow water with particular reference to beach environments.

2.2.1 Radiation stress and waves in deep water

It was noted in the previous section (2.1.2) that in deep water, waves in the incident frequency band are generated by sea surface interaction with wind. As such, their development is dependent on the strength and duration of wind, along with the distance of unobstructed sea over which the wind blows (fetch). Wave trains propagating away from the generating region will interact to form modulated groups.

Modulated waves such as these will create differences in (water) mass transport between high waves versus that which occurs under lower waves. The differences in momentum flux in this situation were examined mathematically by Longuet-Higgins and Stewart (1962,1964), using the concept of *radiation stress*. Radiation stress is essentially a fluid analogy to 'radiation pressure', which is produced under electromagnetic radiation originating or impinging on a surface. In a fluid medium, radiation stress is defined as the excess flux of momentum due to the presence of waves, where momentum and direction of flux are both vector quantities. Contributions are made to the radiation stress deriving from both wave momentum and the pressure under the waves.

As an example of the calculations made by Longuet-Higgins and Stewart (1962,1964), if a frame of reference is set up such that wave fronts are normal to the x-axis, then the flux of horizontal momentum across a unit area of the vertical plane may be described by

$$p+\rho u^2 \qquad (2.13)$$

where p is the pressure under waves, ρ is the fluid density, and u is the velocity in the x direction. Notable here is that although u may be positive or negative, u^2 will always take a positive value, and hence its average over time will always be $u^2>0$. This expression may

be summed across the plane x=constant, and when applied to the definition for radiation stress (i.e. the excess flux of x directed momentum in the x direction) gives the tensor component S_{xx},

$$S_{xx} = \overline{\int_{-h}^{\zeta}\left(p+\rho u^2\right)\mathrm{d}z} - \int_{-h}^{0} p_0\,\mathrm{d}z\,, \tag{2.14}$$

where ζ is the time-variant sea surface elevation due to waves and p_0 is the hydrostatic pressure. The first term of the equation describes the time-averaged mean value of flux under waves, and the second term the mean flux in the absence of waves.

The radiation stress tensor may then be split into three further components

$$S_{xx} = S_{xx}^{(1)} + S_{xx}^{(2)} + S_{xx}^{(3)}\,, \tag{2.15}$$

where

$$S_{xx}^{(1)} = \overline{\int_{-h}^{\zeta}\rho u^2\,\mathrm{d}z}\,, \qquad S_{xx}^{(2)} = \overline{\int_{-h}^{0}\left(p-p_0\right)\mathrm{d}z}\,, \qquad S_{xx}^{(3)} = \overline{\int_{0}^{\zeta}p\,\mathrm{d}z}\,. \tag{2.16}$$

By assuming the waves to be small, the third term becomes negligible, whilst the first two reduce to

$$S_{xx}^{(1)} = \int_{-h}^{0}\rho\overline{u^2}\,\mathrm{d}z \quad \text{and} \quad S_{xx}^{(2)} = \int_{-h}^{0}\left(-\rho\overline{w^2}\right)\mathrm{d}z\,, \tag{2.17}$$

where u and w are horizontal and vertical velocity. Therefore as the total of the two terms, the radiation stress tensor S_{xx} is related to kinetic energy.

A physical interpretation of the mathematical work by Longuet-Higgins and Stewart (1962) leads to two important results;

i. *radiation stress induced force will be directed into a region of less stress*
ii. *radiation stress is analogous in its behaviour to wave energy.*

Longuet-Higgins and Stewart (1964) applied their results to a modulated wave train propagating in deep water (kh>>1, where k is wavenumber and h depth), by considering the energy density to be varying sinusoidally. Energy density was used rather than the wave group envelope itself, in order to avoid non-linearity. In a wave group, according to the statements above, energy density will reach a maximum under the highest waves in the group and a minimum under the lowest. This behaviour is mirrored by the radiation stress, and thus a divergence of forces will exist under high waves, whilst a convergence occurs under small waves within the groups. In order to preserve continuity water level will therefore be pushed up under small waves, and depressed under the larger ones creating a wave-like disturbance of the mean sea level beneath the wave groups (figure 2.2.1). This

fluctuation of mean water level forced by wave groups is usually described as a *bound long wave* (BLW).

The placement of the BLW in relation to the incident wave groups implies a phase shift of 180° (π radians) between the wave group envelope and infragravity wave signals, i.e. the BLW trough is coincident with the largest waves in a group. This result was also gained by Hasselmann (1962) using second order non-linear theory, and observed in the field by Tucker (1950) and Huntley and Kim (1984). Both field studies used instruments sited just seaward of the surf zone. Propagation of the BLW at group speeds was confirmed in the natural environment by Guza *et al.* (1984). This latter deployment used a series of pressure transducers to overcome the effects of seaward propagating 'free' infragravity waves reflected from the nearshore (mechanisms for which are discussed in subsequent sections) which would affect BLW versus wave group correlation calculations.

The bound long wave described above is forced by wave groups, but free infragravity energy is also observed as part of a naturally occurring wave field. Recent studies have found that infragravity waves in the offshore zone may be easily distinguished as bound or free waves by bispectral analysis (Herbers *et al.*, 1994), since bound waves should have a specific phase and energy relationship compared to the incident band waves. Second order non-linear theory (Hasselmann, 1962) predicted a quadratic energy relationship between incident waves and their BLW. Herbers *et al.* (1994) found a significant level of agreement between this and their observations, although uncertainty inherent in the statistics of bispectra mean that this agreement was observed over the bands as a whole, but not followed at individual frequencies. In terms of total energy however, Herbers *et al.* (1994) found only a secondary contribution being made by the BLW component (approximately 0.1-30%). The ratio of bound to free wave energy increased dramatically with an increase in total energy, and was related to the level of incident wave forcing, i.e. BLW energy increased with an increase in the radiation stress between the largest and smallest waves in a group.

It is worth noting that one of the circumstances where energy differences between large and small incident frequency waves will increase dramatically is during the incident frequency wave shoaling process. Thus for given swell conditions the BLW component should increase in importance with the decreasing depth in the shoreward direction up to the

breakpoint. Ruessink (1998) provides bispectral evidence of bound long wave forcing taking a maximum value just outside of the breaker line.

Free waves making up the remaining offshore energy at infragravity frequencies were considered by Herbers *et al.* (1994) and Elgar *et al.* (1994) to be generated shoreward of their offshore observation point. This was suggested from an examination of spectral wavenumber estimates (Herbers *et al.*, 1994). Additionally, Herbers *et al.* (1995) observed that the energy relationship between incident and free waves was weaker than quadratic. This led to the authors suggestion that a mechanism related to wave breaking (such as that proposed by Symonds *et al.*, 1982, section 2.2.2), which generates further infragravity waves, may be in operation in the nearshore zone in addition to the release of bound long wave energy.

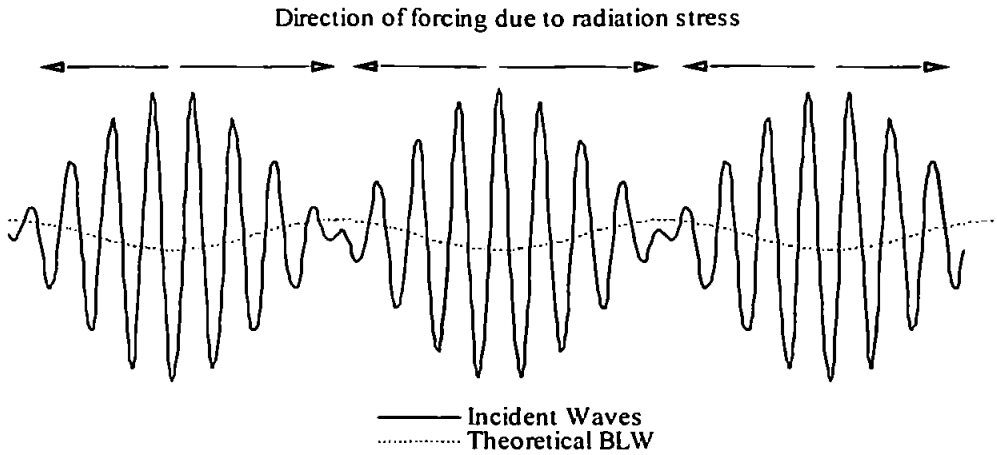

Figure 2.2.1 Idealised deep water wave groups, radiation stresses, and theoretical fluctuations in mean water level

2.2.2 Infragravity wave release and generation in shallow water

Following Longuet-Higgins and Stewart (1964) it is suggested that the wave field propagating toward shore will consist of two components, modulated incident frequency wave groups, and an infragravity wave bound to the groups themselves. The changes undergone by the incident wave groups travelling through the nearshore zone will obviously lead to changes in the radiation stress regime imposed on the water body, and hence cause modifications to the BLW. Outside of the surf zone the analogy between the behaviour of radiation stress and energy, taken from Longuet-Higgins and Stewart (1964), suggests an increase in the forcing of the BLW since an increase in incident wave amplitude through shoaling leads to increasing energy gradients between waves. Correspondingly Elgar and Guza (1985) and Doering and Bowen (1995) saw increasing interaction between primary (incident banded) wave frequencies and the difference frequency associated with the BLW component, suggesting further forcing of the BLW as the waves shoal.

The relative contributions from the two frequency bands to energy spectra have been observed to follow expectations from theory for cases of both locally (Beach and Sternberg, 1991), and long fetch (Russell, 1993) generated waves. Beach and Sternberg (1991) found that in the shoaling zone, incident wave associated peaks dominate spectra, but are flattened out as these energies are cascaded to higher frequencies through shoaling (Elgar and Guza, 1985), or dissipated through wave breaking. Thus more broad banded spectra evolved in the shoreward direction, increasingly dominated by frequencies in the infragravity band.

At the breakpoint it is suggested that as the groupy structure of incident frequency waves is destroyed, the bound wave will be released and subsequently propagates through the surf zone as a free wave (Longuet-Higgins and Stewart, 1964). In the field, Guza and Thornton (1985), List (1987) and Masselink (1995) found in shallow water, a correlation between incident wave and infragravity significant height/velocity values outside of the surf zone. Masselink (1995) further observed a decrease in correlation of these components between this region and the middle of the surf zone, which reached an insignificant level by the inner surf zone. These observations correspond to theory of release of a bound wave with the onset of breaking. However both List (1987) and Masselink (1995) also noted that the phase lag between BLW and wave group envelope was significantly less than 180° (the

value associated with deep water generation of the BLW) in the shoaling zone. This suggested that the bound long waves start to be released from the forcing wave groups prior to the surf zone, or undergo a phase shift through some other mechanism.

Subsequently, in a model study, List (1992) found that a phase lag between the BLW and its associated wave group existed prior to breaking commencing. These observations point to a breakdown of the deep water theory used by Longuet-Higgins and Stewart (1964) for the BLW in shallower water, and this is further indicated by the non-linear triad interactions documented by Elgar and Guza (1985) and Doering and Bowen (1995). Nonetheless, the seemingly contradictory result documented by Ruessink (1998) where bound wave forcing takes a maximum at the breakpoint still has to be borne in mind. Describing these shallow water processes in more detail has led more recent modellers to look toward a more non-linear approach to the hydrodynamic problem in this region, for example using the Boussinesq equations (e.g. Madsen *et al.* 1997).

The radiation stress concept however, remains applicable to other nearshore processes. Since incident wave energy increases during wave shoaling, is dissipated through a shock at the break-point, and then dissipates further toward shore, this suggests that there must also exist a build up of radiation stress seaward of the surf zone toward the break-point, and a decrease in radiation stress through the surf zone itself. If the fluid conserves continuity as for the deep water case, by changing the shape of its surface, then it would be expected that a depression of mean water level would be experienced seaward of the break-point (*set-down*). The trough of the set-down would occur at the breakpoint, and shoreward of this point a rise in sea level would be found through the surf zone and onto the shoreline (*set-up*, Longuet-Higgins and Stewart, 1964). Examining these slopes of mean sea level, Komar (1998) showed that the fluid slope inside the surf zone is proportional to beach slope, according to the set-up relationship

$$\frac{\partial \bar{\eta}}{\partial x} = \left(\frac{1}{1 + 8/3\gamma_b^2} \right) \tan \beta . \tag{2.18}$$

Since γ_b is considered constant for a given breaker type, set-up is therefore independent on offshore wave height. However, since for a plane beach larger waves will break further offshore, hence creating a wider surf zone, the net effect at the shoreline will be larger during more energetic storm events. The slopes of the sea surface described above are driven by currents, which, according to Longuet-Higgins and Stewart (1964), only act in a small layer of the surface of the water body. It was concluded that there must then be a

reaction to this within the water column, which led to the idea of a reverse current at depth, or *undertow*.

In addition to the release of the BLW in the vicinity of the breakpoint, Symonds *et al.* (1982) suggested a further forcing mechanism for infragravity variations operating within the nearshore zone derived from the notion of a 'dynamic set-up'. The mechanism behind this second form of infragravity wave generation comes from the temporal variability of the breakpoint position under groups of modulated waves, and hence the resulting variation of surf zone width. The motion of the breakpoint results in time-varying radiation stress gradients (at wave group periods) occurring in a forcing region defined by the extent of the breaker zone. For weakly modulated bichromatic wave groups this forcing region will follow a weakly sinusoidal motion, but for fully modulated waves should extend all the way to the shoreline, although Madsen *et al.* (1997) noted that this effect might smear breakpoint forcing out.

Symonds *et al.* (1982) found infragravity waves produced at group frequencies and their harmonics, which propagated both shoreward and seaward from the forcing region. Later models incorporating both the BLW and the *break-point forced long wave* (BFLW) (List, 1992, Schaffer, 1993) found varying relative contributions from these two components. List (1992) observed a BFLW component which was secondary in magnitude to, and out of phase with, the BLW in the shoreward propagating wave field. In this instance the phase difference was caused by the lag between BLW and the wave groups produced during the shoaling process. List (1992) further noted that the BFLW, although increasing rapidly after generation, only reached 50% of the BLW amplitude by the shoreline. However, List (1992) also suggested, after a comparison of the model with the flume study of Kostense (1985), that an increase in the beach slope may well lead to a larger relative contribution from the BFLW. Madsen *et al.* (1997) pointed out that the List (1992) model's use of the shallow water equations, which neglect dispersion, may well have led to an overestimation of the BLW component, whilst conversely Schaffer (1993) is likely to have overestimated the BFLW. Whatever the model solutions however, the BFLW component has yet to be satisfactorily resolved through analysis of field time-series. Additionally observations by Okihiro *et al.* (1992), Elgar *et al.* (1992), and Ruessink (1998) were all deemed by the authors to be consistent with low frequency energy being generated almost exclusively by bound waves.

2.2.3 Shore normal infragravity waves in the surf zone

Whatever the generating mechanism, theory suggests that shoreward of the breakpoint free long waves will propagate through the inner surf zone without breaking, be reflected at the shoreline, and then propagate in an offshore direction. A schematic of the distribution of infragravity wave types in the cross-shore is given in figure 2.2.2 and shows that outside of the surf zone, shoreward propagating infragravity waves will theoretically consist solely of the bound long wave component. Inside the surf zone these may be supplemented by breakpoint forced long waves (Symonds *et al.*, 1982). Dependent upon the angle of incidence of these waves both these components may become either trapped in the nearshore as edge waves or be reflected and propagate in the offshore direction (leaky waves). A further offshore directed infragravity wave may also be generated by the breakpoint mechanism.

Ruessink (1998) observed that shoreward of the breakpoint, the free wave component was seen to increase in energy relative to the bound long wave component. This followed the shoreward decrease in interaction between the incident and bound infragravity component, which decreased to near zero as incident wave breaking tended toward saturation, and indicated a release of the bound infragravity component as the wave group structure was destroyed. Whilst the free infragravity waves are expected to shoal further as the water shallows, their lengthscale is such that the waves will not become steep enough to dissipate energy via breaking. Wave steepness versus beach slope may be described using the dimensionless Iribarren number ξ (Iribarren and Nogales, 1949),

$$\xi_\infty = \frac{\tan\beta}{(H_\infty / L_\infty)^{1/2}} . \tag{2.19}$$

Here high values of ξ_∞ correspond to low wave steepness, and hence low dissipation conditions that lead to high reflection. Thus the Iribarren number, or a related 'surf similarity parameter' (ε, Wright and Short, 1983) provides a useful indicator in predicting wave reflection. Examining the equation further, it can be seen that larger values of L_∞ will yield a larger Iribarren number.

Longuet-Higgins and Stewart (1962)'s deep water wave theory suggests that bound infragravity waves propagate at group speed. If it is assumed that this does not alter dramatically in shallower water, then since

$$c_g = L_\infty f , \tag{2.20}$$

where f is frequency, it can be seen that the longest deep water wavelengths (and hence highest values of ξ) are associated with the lowest frequency waves, leading to the idea of a dependence of reflection upon frequency. This has been documented in numerous field studies involving the incident wave component (e.g. Miche, 1951, and more recently Huntley *et al.*, 1995, and Mason *et al.*, 1997). Generally, very large Iribarren numbers are associated with the infragravity component and this has led most modellers to make the important assumption that all infragravity wave energy will be reflected from the shoreline. More recently however, the model of Madsen *et al.* (1997) showed a decrease in the reflection coefficient for higher infragravity frequencies. It was stated that the reason for this lowering in reflection coefficient lay in dissipation of the higher infragravity waves between the observation point and the shoreline prior to reflection. The authors suggested that the reason for dissipation at these frequencies close to shore, whilst little dissipation was associated with the lowest frequencies, could well have been due to a larger dissipative interaction occurring between breaking waves and the infragravity component when the difference between the wave frequencies was reduced.

The reflected free wave component must interact to some extent with incoming waves, with the possibility of the formation of standing waves in the surf zone. Hence it is important to accurately assess not only the reflection coefficient, but also the phase between shoreward directed and reflected waves (Symonds *et al.* 1982). It has been generally assumed (for modelling purposes) that for the infragravity component the reflection point is at the shoreline. Masselink (1995) observed a cross-shore structure of phase angles suggestive of both standing and partially standing waves, but the study also pointed out a disagreement between predicted and observed return travel times for the reflected component in the outgoing infragravity wave signal. Masselink (1995) resolved this difference by applying the (linear) wave propagation model to a reflection point some five metres seaward of the shoreline. Since beach slope at the site was at maximum 0.035, this point would correspond to a water depth of 20cm. Therefore this result is intuitively sensible in suggesting that the reflection point for infragravity waves will not be at the dry shoreline, but in very shallow water extremely close to shore.

Modelling using the shallow water equations for conservation of mass and momentum (e.g. models by Symonds *et al.*, 1982; Howd *et al.*, 1992; List, 1992; Schaffer, 1992, and numerous others) allows for two types of standing wave solution, known as leaky and trapped (edge) waves. The distinction between these two solutions was first recognised by

Ursell (1952). As their names suggest, the solution type depends upon whether the waves will be allowed to propagate offshore, or whether any refractive trapping of the waves within the nearshore will occur. In the case of shore normal waves propagating onto a plane beach the leaky mode solution, initially described for tides by Lamb (1932) and confirmed as a nearshore solution for waves by Friedrichs (1948), might be expected. This type of solution has been employed in two-dimensional models such as those of Symonds *et al.* (1982), and List (1992).

For formation of a standing, or partially standing leaky mode wave, again the simplest description of this process comes from the consideration of two waves of sinusoidal form. In this simple example the waves are identical in amplitude a and frequency σ, but not for direction of propagation as defined by wavenumber k. If these waves are superposed, then surface elevation η may be expressed as

$$\eta = 2a.\cos kx.\cos \sigma t. \tag{2.21}$$

This is the form of a sinusoidal standing wave (figure 2.2.3), assuming wave propagation over a flat bed, and full reflection from a vertical reflector. Examining equation 2.21 in terms of the sea surface elevation, when

$$kx = \frac{(2n+1)\pi}{2}, \tag{2.22}$$

where x is distance from the reflection point and n is an integer, surface elevation will not vary over time. Such points are known as nodes. Conversely, points of maximum variation in elevation (antinodes) are also described, occurring when $kx=n\pi$. Nodal and antinodal points have corresponding maxima and zero variation respectively in the water column velocity field. One important respect in which the leaky mode solution differs from this simple standing wave is that, due to wave shoaling effects, such a wave will decay exponentially through the cross-shore in the seaward direction. Hence, infragravity wave energy is capable of dominating the wave field in the inner surf zone, but may be far less important further seaward.

In the natural environment infragravity wave frequencies will be broad banded, and of variable height. Hence the degree to which a standing wave will form may be dependent upon the phase relationship between incoming and reflected waves and their respective magnitudes. Formation of a fully standing wave as above is seen to be dependent on incoming waves taking a regular form. However, non-regular waves may give rise to partially standing structures. In a numerical model study O'Hare (1994) noted formation of

relatively stable structures of nodes and antinodes in the cross-shore after an order of ten or so (non-regular) wave groups.

Compilation of field evidence for reflection of shore-normal propagating infragravity waves requires a comparatively rare set of coinciding conditions of swell and morphology, but a seminal example was provided by Suhayda (1974). The study targeted a planar beach environment where a leaky mode type of solution would be most applicable, and succeeded in observing coherent cross-spectra between offshore and shoreline gauges with corresponding 0° or 180° phase indicative of standing waves. Suhayda (1974) also cited a good comparison between this data and a leaky mode model (Munk, 1964) versus a poor one with edge wave theory (see section 2.2.4) in order to justify the choice of a leaky solution. Huntley *et al.* (1981) pointed out that in the field both edge wave and leaky mode waves can coexist. The ratio between the two types of energy is liable to be dependent upon the incident wave direction. For example, Howd *et al.* (1991) found leaky wave energy to be dominant in a field study where the incident wave direction was shore normal.

Whilst infragravity wave energy is generally assumed to be free in the surf zone, it has been proposed that infragravity wave induced variations in depth will affect breaker height (List, 1991; Nelson and Gonsalves, 1992). This would imply that some level of modulation for breaker height time-series will be observed even in a saturated surf zone, and data showing this effect was gathered by Nelson and Gonsalves (1992). This element of interaction between the two wave components has been incorporated into models conceived by both Schaffer (1993) and Madsen *et al.* (1997). Nonetheless, modulations of breaker height in this region of the surf zone seem to have little effect on the value of the (time-series averaged) breaker index. For example, Raubenheimer and Guza (1996) found a range in their breaker index estimates of less than 20%, and noted that it was extremely difficult to establish a causal link between infragravity waves and variations in breaker height. Possibly a more important interaction between the infragravity and incident waves has been simulated at the swash zone by Madsen *et al.* (1997), who saw infragravity waves causing varying velocities of the incident waves running up the beach. This would be likely to further increase the infragravity component within the shoreline motion signal.

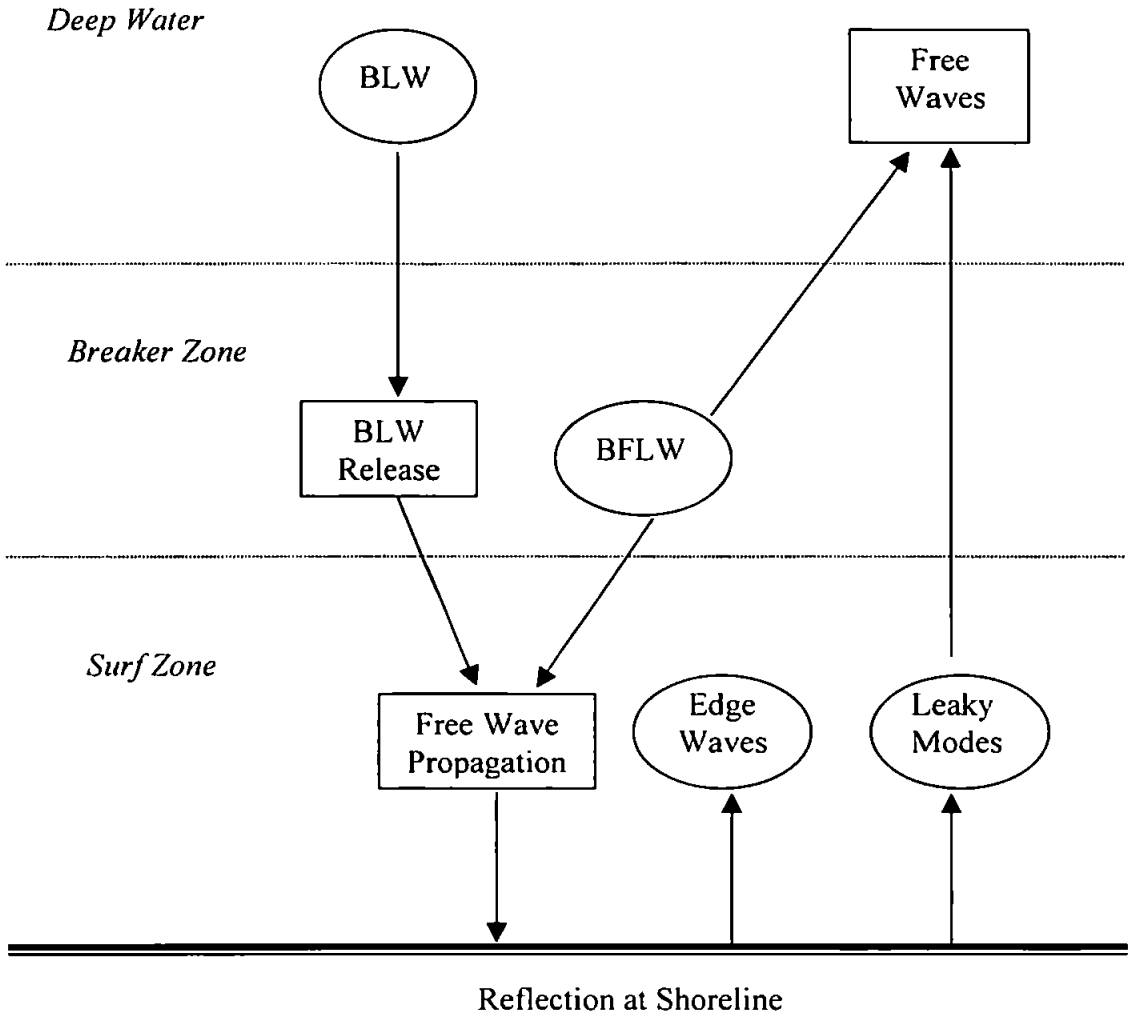

Figure 2.2.2 Schematic of theoretical distribution and generation of infragravity wave energy in the nearshore.

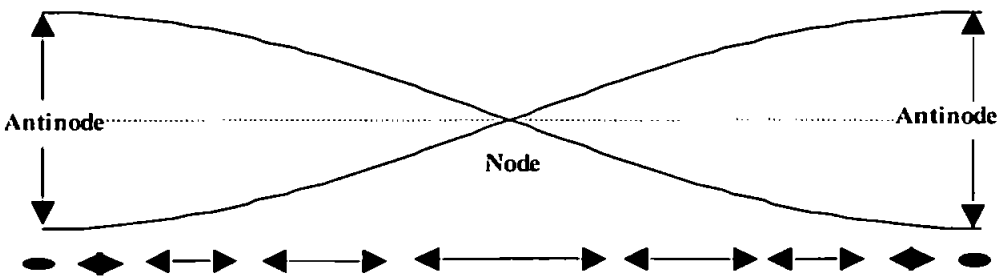

Figure 2.2.3 Standing wave surface fluctuations, and underlying current structure (arrows).

2.2.4 Edge waves

Radiation stress theory applying to set-up/set-down in the two-dimensional case also has implications if some longshore variability is introduced into the beach system. As an example, the break point position may be of a variable distance offshore in a plane parallel to the beach. This can often occur as a result of three-dimensional variations in a bar, which will lead to alongshore variations in the offshore distance of the break point. Applying a radiation stress argument to this behaviour, an alongshore variation in set-up is implied. This leads to a gradient driving flow alongshore, and ultimately, due to an imbalance of momentum, offshore in the form of a rip-current. Alternatively, if waves are obliquely incident to a plane beach, then the shoreward set-up current will have an alongshore component, and thus a wave driven longshore current will be established (e.g. Longuet-Higgins and Stewart, 1964; Deigaard, 1993). Similarly, where two progressive shallow water waves approach the shore obliquely, a temporally modulated forcing zone is set up, and resonant low frequency energy trapped in the nearshore will take a form best described by an edge wave solution (Lippmann *et al.*, 1997). Under such modulated conditions Lippmann *et al.*(1997) found a timescale for full formation of the edge waves (and also for wave half-life) of the order of tens of edge wave periods. Edge waves exhibit a cross-shore as well as longshore structure, and hence it is necessary to consider whether infragravity energy follows a leaky or edge wave solution when examining the cross-shore distribution of infragravity wave energy (as for example in section 5.2).

Edge waves are confined to the shoreline, and by definition are standing in the cross-shore following an exponential decay in the seaward direction (figure 2.2.4). However, they take a periodic form in the alongshore, and may be either progressive or standing. To give an idea of scale, an infragravity edge wave with a period of approximately 100 seconds will have a wavelength of approximately 300m for its dominant mode on a shallow bottom slope of $\tan\beta$=0.02 (Schaffer and Jonsson, 1992). A general solution for edge waves was devised by Ursell (1952), and leads to the relationship

$$\sigma^2 = gk.\sin[(2n+1).\tan\beta] \qquad (2.23)$$

where σ is the angular frequency, k is wavenumber, g acceleration due to gravity, and $\tan\beta$ is the beach slope. n is an integer, and must satisfy the relationship

$$(2n+1).\tan\beta \leq \pi/2. \qquad (2.24)$$

Therefore the solution describes a finite number of discrete edge wave modes for a given frequency. Furthermore, since $\cos(2n+1).\tan\beta \geq 0$ exponential growth of the waves in the

seaward direction is ruled out (Schaffer and Jonsson, 1992), and thus the waves are 'trapped' at the shoreline. From the above it can be seen that a decrease in beach slope will increase the number of edge wave modes allowed. Higher modes will produce cross-shore standing waves similar in structure to leaky mode solutions (Guza and Thornton, 1985). Angular frequency σ is also limited according to $\sigma_{cutoff}^2=gk$ and the maximum value that can be taken is known as the cut-off frequency (σ_{cutoff}).

An approximate solution applicable to shallow water was made by Eckart (1951) yielding the dispersion relation

$$\sigma^2=gk(2n+1).tan\beta \tag{2.25}$$

and corresponding surface elevation

$$\eta=e^{-x/2}L_n(x) \tag{2.26}$$

where $L_n(x)$ is the Laguerre polynomial of order n, operating on variable x, which represents cross-shore distance. It should be noted that Eckart's (1951) solution does not predict the cut-off frequency obtained by Ursell's (1952) general theory. This shallow water approximation was considered by Schaffer and Jonsson (1992) to be an accurate solution only on beaches of slope $\tan\beta<0.2$, where high amounts of energy are dissipated through breaking. For steeper beaches they deemed a refraction theory (geometric optics) approach obtained the most applicable result.

Correspondingly, in field studies, oblique waves have been found to be specularly reflected at the shoreline, and significant amounts of energy propagating at large angles to the shore become trapped in the nearshore as predicted by Snell's Law (Herbers *et al.* 1995). This refractive trapping was implied by an observation made offshore of the surf zone of a lower than expected ratio of seaward to shoreward propagating energy, which suggested edge wave structures occurring across and along the nearshore. Low mode progressive waves were presented from analysis of an alongshore current meter array by Huntley *et al.* (1981). The energy was seen to form several 'dispersion ridges' in frequency-wavenumber space which were dominated by a single mode zero or 1 wave, although direction of wave propagation in the alongshore was equally divided. In the study described by Howd *et al.* (1991) these low modes were also seen to dominate the alongshore oscillatory component for all angles of wave incidence.

Howd *et al.* (1991) also noted changes in cross-shore velocity (u) fluctuations for an array of incident wave angles, such that as the incident angle with respect to the shore-normal

increased, the variance in u was seen to decrease and take on a structure suggestive of high mode edge waves. Inference of edge wave mode number was made when these cross-shore observations were compared with the predicted character of cross-shore energy decrease accorded to modelled modes for the dominant frequency. This method was also employed by Bauer and Greenwood (1990), who identified a mode 3 edge wave in their results. Bauer and Greenwood (1990) argued that the wave observed in this instance, was an edge wave, rather than a standing leaky wave, from observations of phase between longshore and cross-shore current measurements.

Interactions may occur between edge waves of different mode, through 'phase coupling' as was pointed out by Holman and Bowen (1982). Considering a linear combination of two edge wave modes, Holman and Bowen (1982) suggested that a wave motion would be derived which consisted of a simple progressive wave, with an amplitude proportional to the difference between the two component waves, and a longshore amplitude modulated progressive wave, with a wavenumber the average of the two component wavenumbers. The longshore modulation of this second wave should have fixed nodes and antinodes, and a wavenumber equal to the average of the difference of the two component wavenumbers. Hence in this study a complicated three-dimensional wave structure was derived from a simple combination of two waves.

Evidence for such phase coupling between edge waves was found in the cross-shore direction by Huntley (1988). Once again low mode (mode zero) waves dominated a broad range of infragravity frequencies, but a degree of interaction was noted between the mode zero and higher mode waves for those observed resonant frequencies in the mid-high infragravity band.

The dispersion relationships described above may also be modified by the presence of a longshore current (Howd *et al.,* 1992, Schonfeldt, 1995). The magnitude of change to modular wavenumber $|k|$ was considered by Howd *et al.* (1992) to be a function of both cross-shore position and magnitude of the longshore current velocity maximum. The authors suggested that this modification would have a maximum for intermediate frequencies in the infragravity range, but that this would occur at a lower or higher frequency dependent on whether the waves are propagating with or against the current respectively. The frequency at which the $|k|$ maximum occurred was seen by Howd *et al.* (1992) to increase with increasing mode number. The effect on cross-shore wave structure

of these changes in $|k|$ was to increase/decrease cross-shore scale for decreasing/increasing $|k|$ respectively, hence causing a shift in the position of cross-shore nodes and antinodes. Howd *et al.* (1992) also suggested that the amplitude of antinode oscillation would be modified by the presence of a longshore current.

Variances in longshore current shear were also observed by Howd *et al.* (1991) which made up to approximately one-third of the total oscillatory contribution to current. It was suggested that these variances might be due to shear waves, as was also hypothesized by Oltman-Shay and Howd (1989). These waves fall into frequency-wavenumber space at *far infragravity* frequencies (<0.01Hz), but have wavelengths almost an order of magnitude smaller than same frequency edge wave modes. Unlike the waves previously discussed which are restored by gravity, it is believed that shear waves have a restoring force based on conservation of vorticity within the longshore current. Oltman-Shay and Howd (1989) found such components to be dynamically tied to longshore currents, and observed a positive correlation between direction of shear wave propagation and that of the longshore current.

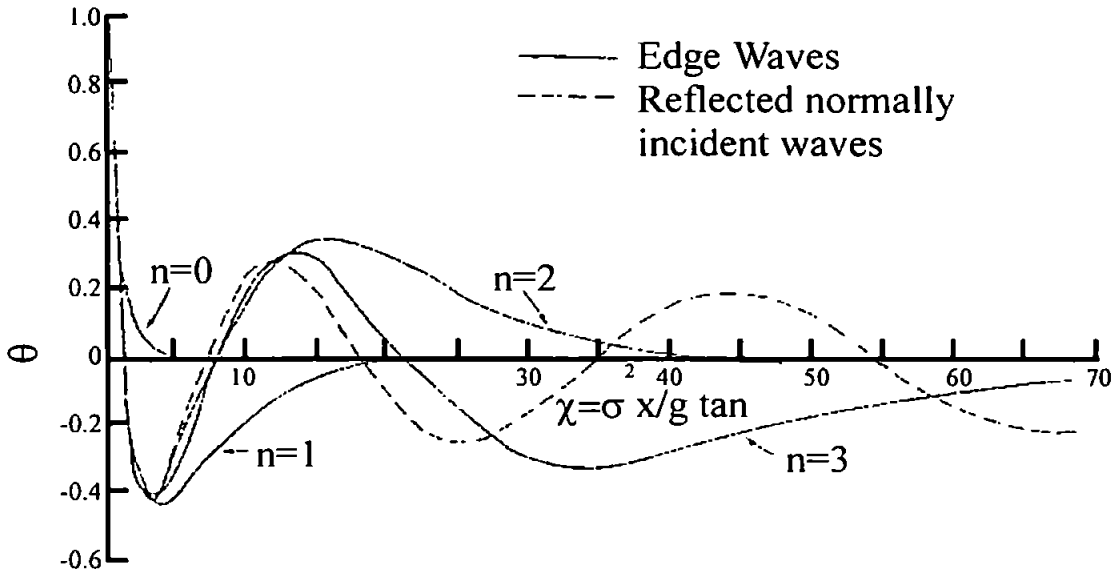

Figure 2.2.4 Edge wave mode cross-shore surface elevations, plotted in terms of a non-dimensional offshore distance χ (from Holman, 1983).

2.2.5 Infragravity wave interactions with morphology and tides

One of the motivating problems behind infragravity wave research has been to establish if any relationship exists between waves in this frequency band and naturally occurring features in morphology, such as sandbar systems. The details of transport are discussed in a later section, but the fact that observed sandbars and infragravity waves are of the same length scale, and the theoretical cross-shore current structure under standing waves, which implies scouring at nodal points and deposition at antinodes, hints at a connection. However for sandbars to be maintained by such a mechanism, forcing of infragravity waves at a specific 'favoured' frequency may be required, in conditions where the incident wave energy will be broad banded. Symonds and Bowen (1984) obtained resonant conditions for a standing long wave with its antinode occurring at the bar crest, using the infragravity BFLW from the Symonds *et al.* (1982) model. This result suggested that a bar may be capable of favouring certain frequencies in order to maintain itself as was also suggested by Kirby *et al.*, 1981. However the broad-bandedness of natural wave fields (which may include highly energetic BLWs of a frequency different to that favoured by the bar) in comparison to the model inputs, and the fact that no mechanism for initial bar establishment was evident in the model, weigh against this theory.

Schonfeldt (1995) demonstrated that a longshore current can reinforce trapping of any high mode edge waves propagating with the current onto a bar system. In this situation a frequency range existed where wave phase velocity was independent of frequency, and as this independence increased the wave became more bound to the bar crest, whilst its amplitude over the bar increased through resonance. Thus resonant frequencies have been theoretically established from far more broad-banded wave fields than used by Symonds and Bowen (1984).

Ruessink (1998) pointed out that the best way of establishing whether bars force a resonant frequency comes from an investigation of the swash, where all waves are expected to have an antinode (e.g. Sallenger and Holman, 1987). Both Sallenger and Holman (1987), and Aagaard (1990), addressed morphologic forcing of resonant frequencies for high energy (swell and fetch limited respectively) storm events. However, neither work provided evidence that such forcing occurs. Although Sallenger and Holman (1987) found resonant conditions, with the dominant frequency possessing a surface antinode at the bar crest on the first day of their storm, as the bar migrated offshore, no further frequencies succeeded

in dominance as this happened. Aagaard (1990) was able to demonstrate an agreement between observed multiple bar positions and dominant edge wave structures, but believed the waves to be a product of interaction with incident waves peculiar to this case, rather than a result of morphologic forcing. Ruessink (1998) described the swash spectrum as possessing no significant peaks, and therefore also found no evidence for a resonant frequency to be forced by his site's bar system.

Little has been hypothesized in terms of interactions between waves and tidal currents in the nearshore environment. However, processes may be modulated temporally on a tidal level. Short (1991) and Masselink (1993) both noted that for beaches of variable slope, tidal range will affect breaker height and type plus surf zone width, with corresponding effects on standing infragravity wave, undertow, and rip current formation, by moving the surf zone over the beach. For beaches of large tidal range the formation of standing infragravity wave structures may be precluded by the rate of change of breaker zone width and/or shoreline position on the flood and ebb. Thus standing waves may only be able to form during slack water periods around low and high tides. Thornton and Kim (1993) presented a model to show that tidally modulated wave breaking, where the modulations arose because breaker heights were hypothesised as depth dependent, was responsible for variations in longshore current generation within the surf zone. This may in turn affect the edge wave-longshore current interactions suggested by Howd *et al.* (1992) and Schaffer (1995). Outside of the surf zone Thornton and Kim (1993) also saw longshore current as being dominantly tidally driven.

Tidal modulation of infragravity wave energies was examined in the field by Okihiro and Guza (1995), and was found to be of variable influence over the band frequencies during the observation period. Far infragravity frequencies ($0.004<0.01$Hz) were seemingly unaffected, but some asymmetric modulations of energy were noted for higher frequencies in the band ($0.01<f<0.04$Hz), including an approximate five-fold increase between low and high tides at one site. A satisfactory explanation for these variations was not found, although one possibility was a variation in surf zone width through the tidal cycle, which could vary both the forcing region for a BFLW and release of any bound infragravity component. This may fall in line with a model such as that produced by List (1992), which incorporates both BLW and breakpoint forced waves, and produces a reflected signal. Here the levels of infragravity standing wave energy attained in the model are based on phase between the components, which to some extent is determined by surf zone width. A tidal

signature is also found in the variance of breaker height and longshore current as observed by Thornton and Kim (1993), and this could also affect infragravity wave forcing prior to release in the surf zone.

2.2.6 Summary: Infragravity waves in the nearshore

Deep water bound long waves may remain forced by wave groups up to the breaker line but have already begun to detach themselves from the wave group structure in the shoaling zone. At the breaker line infragravity energy is released, and propagates through the surf zone as free waves. It has also been suggested (Symonds *et al.*, 1982) that infragravity waves may be generated at the breaker line as a result of the dynamic set-up induced by time variation of the breakpoint position. Since wave heights are small and wavelengths long, little energy is dissipated in the surf zone and hence the waves shoal in the shoreward direction in this region. Thus infragravity wave energy will become increasingly important in terms of the overall wave energy near to shore, but will also be reflected from the shoreline. Whether the reflected signal is transmitted offshore from the surf zone (leaky mode), or becomes trapped in the nearshore as an edge wave will be largely dependent upon how near to shore normal the incident wave direction was.

Because of the high Iribarren numbers associated with infragravity waves it is generally assumed that near total reflection of wave energy at these frequencies will occur. However, the recent model study of Madsen *et al.* (1997) suggests that some level of dissipation of higher infragravity frequency energy may occur near to shore due to interactions between waves at these frequencies and the breakers. The interaction between incoming and reflected waves leads to the possibility of the formation of standing or partially-standing wave structures forming through the nearshore. This will be dependent upon both the magnitude of the incoming and outgoing components and their respective phases.

It has also been suggested that depth variations in the inner surf zone, caused by infragravity wave presence, may be responsible for inducing a level of modulation in the depth limited breaker heights (Nelson and Gonsalves, 1992). However, this link is difficult to prove and the presence of an energetic infragravity wave component does not seem to affect time-averaged breaker index values (Raubenheimer and Guza, 1996).

2.3: Sediment transport

2.3.1 Morphology and infragravity waves?

The hydrodynamic components discussed in the previous sections provide an input of energy into the nearshore morphodynamic system. This has the likely effect of deforming the seabed, and ultimately may result in changes of local beach topography. One of the early motivations for infragravity wave study was in relating the distribution of energy at these frequencies to the processes of erosion and deposition involved in the formation and maintenance of barred profiles. Using an approach based simply on the effects of breaking waves and transport by mean currents (e.g. Dally and Dean, 1984), it was initially believed that bars could be formed at the breakpoint, since at this point the mean current is near zero, and changes direction from offshore inside the surf zone, to onshore in the shoaling zone (Dyhr-Neilsen and Sorensen, 1970). However, Sallenger and Howd (1989) pointed out large differences in scale between surf zone width and a bar formed and maintained during the storm event that they observed.

In other studies where conditions were also highly energetic, bars have similarly been observed to have cross-shore length scales more readily associated with infragravity wave wavelengths (e.g. Lippman and Holman, 1990). Short (1975) demonstrated that the location of bar positions within a multiple bar system could be linked to the positions of nodes or antinodes within a standing wave envelope. In this case, the infragravity waves are seen as providing a drift velocity for the transport of sediment. Thus scour (and the bar trough) would occur at the drift velocity convergence, in coincidence with a velocity antinode. Conversely, deposition occurs at the velocity node, leading to a bar crest at this point. Such a theory however would require an as yet unproven resonance of the standing waves occurring at specific frequencies (within the naturally broad band infragravity spectra) over long periods of time for a bar to be formed. Holman and Bowen (1982) nonetheless extended this theory to a three-dimensional case in their mathematical model, using narrow banded input waves. Their results produced both a two-dimensional longshore bar, and a rhythmic barred morphology by virtue of the current pattern generated by varying degrees of the level of coupling between low mode edge waves.

With the weakness of requiring resonant interactions for bar formation that is part of the above argument in mind, O'Hare and Huntley (1994) suggested an alternative hypothesis

where infragravity wave drift velocities act to transport sediment along with the mean current, whilst incident waves mobilize sediment. Here the infragravity onshore and offshore phases of velocity simply supplement or oppose the mean flows induced by wave set-up. O'Hare and Huntley (1993) generated barred morphologies by considering zones of deposition and erosion arising from the current patterns generated by the incident-infragravity wave model of List (1992). In this study, the bars, the first of which was always found in the inner surf zone, formed just offshore of the infragravity wave elevation nodes, and the separation between node and bar increased with increasing distance offshore. With the exception of the inner surf zone bar, bar location in this model was found to be strongly dependent on the period of incoming waves, and hence still required a dominant infragravity frequency similar to the standing wave theory. However, the authors considered this model as providing a more plausible mechanism for transport, firstly since the currents involved were of higher magnitude than those produced solely by standing waves under the same conditions, and also once a standing or partially standing wave was formed were effective immediately. The further work of O'Hare (1994) suggested that, even for random input waves, transport patterns would still form when averaged over a number of wave groups, and hence that a over a certain time period a beach would tend to a certain morphology.

The models cited thus far have used an assumption that the incident frequency waves provide a stirring effect for sediment whilst the low frequency and mean components transport sediment. An alternative to this is provided by the energetics approach, first conceived by Bagnold (1963,1966), and subsequently applied to a beach environment by Bailard (1981). Energetics models are based upon the idea of sediment being mobilised by the instantaneous velocity applied to the bed, and as a result transport direction and magnitude over a given period is described according to a power of the time-averaged velocity (the *velocity moment*). Russell and Huntley (1999) derived a (normalised) velocity moments 'shape function' from the results of a number of field experiments, where wave conditions varied considerably. The resulting function showed a good quadratic fit to the data, and showed a convergence of transport at the breakpoint, suggesting that a bar could form at this point.

In all of the previously mentioned models, seemingly realistic morphologies can be inferred from slightly different appraisals of beach response to hydrodynamic components. Yet the majority of such studies are purely qualitative, in that zones of deposition and erosion are

inferred from current patterns. Most cases neglect the type of sediment motion likely to occur under the hydrodynamic conditions generated (i.e. bedload and/or suspended load), the existence and effects of bedforms, and effects of turbulence on the vertical distribution of sediment. In fact the mechanics behind sediment motion in the nearshore have generally lagged the hydrodynamic components in terms of our knowledge of the relevant processes and their appropriate application in models, as was acknowledged by the Nearshore Processes Workshop (1990). Largely this has been due to the difficulties of making appropriate measurements of bed response in a region as potentially energetic as the nearshore. Nonetheless it is recognised that the mechanisms of, and components driving, sediment suspension must be described accurately in order for such models to be fully predictive. Works such as this thesis, which analyses the role of a particular component of the sediment transport problem, are intended to aid in the conception of models which produce not only accurate results, but are correct on a process level.

2.3.2 Morphology and beach classifications

In order to compare results gathered from different beach sites, it is necessary to classify various beach types. As will be seen in this subsection, such schemes may also allow certain morphologies to be associated with different hydrodynamic conditions, for example with highly energetic wave fields which are also likely to contain an energetic infragravity component. In the literature, beach classification schemes have sought to describe/predict beach state through mathematically derived criteria. For example the morphologic classification models of Wright and Short (1984), and Lippmann and Holman (1990), which were produced from studies of beaches with small tidal ranges (e.g. Duck, North Carolina, USA for Lippmann and Holman, 1990).

Wright and Short (1984) produced a six-beach classification scheme, based on a dimensionless fall velocity,

$$\Omega = H_b/\omega_s T, \tag{2.27}$$

where the parameters are averages of breaker height (H_b), sediment fall velocity (ω_s), and wave period (T) taken over a timescale large enough to produce changes in the equilibrium beach profile. The various categories of beach states can be loosely thought to describe the beach's effect on incident frequency waves in terms of dissipation of energy. Thus Wright and Short (1984)'s scheme works such that for values of $\Omega<1$ a *reflective* beach state is predicted, whilst when $\Omega>6$ the beach is likely to be *dissipative*. An *intermediate* beach is defined between these two states.

The two year data set of Lippmann and Holman (1990) extended this classification to the following eight-beach model. The beach states are listed in an order running from higher to lower types, as defined by the amount of wave energy required to maintain the profile.

1. *Dissipative*. Unbarred, infragravity scaled surf zone.
2. *Infragravity scaled 2-D bar*. No longshore variability, infragravity scaled.
3. *Non-rhythmic 3-D bar*. Longshore variable, continuous trough, infragravity scaled.
4. *Offshore rhythmic bar*. Longshore rhythmicity, continuous trough, infragravity scaled.
5. *Attached rhythmic bar*. Longshore rhythmicity, discontinuous trough, infragravity scaled.
6. *Non-rhythmic attached bar*. Discontinuous trough, infragravity scaled.

7. *Incident scaled bar*. Little or no longshore variability, may be attached, incident scaled.
8. *Reflective*. Unbarred, incident scaled surf zone.

Again, this classification scheme gives the impression of a continuum of beach states occurring with respect to incident wave energy. At one end of the scale where high wave energy is dissipated, the beach is expected to show a suppressed morphology with either no bar, or a two dimensional bar found in the order of hundreds of metres offshore (infragravity scaled). On more intermediate type beaches bar scaling is still expected to be of an infragravity scale, but shows more longshore variation, and for lower energy states bars may become attached to the shoreline and a bar-rip morphology may develop. In these systems the rip channel forms a natural conduit for transport of water offshore resulting from the mass imbalance produced by a longshore current. Lippmann and Holman (1990) found type 2 the least and type 5 the most stable systems. Storm events tended to cause a jump in state to type 2, followed by a sequential transition through the bar types toward a more stable form as energy decreased. The most reflective beach states 7 and 8 were associated with long periods of low wave energy, when sediment accretion occurred.

In both the Wright and Short (1984) and Lippmann and Holman (1990) schemes a high level of dependence would appear to exist between wave energy and the beach type. Since generally the importance of infragravity energy increases with increasing wave energy, then the beach states most likely associated with periods of high infragravity energy are of the dissipative variety. Lippmann and Holman (1990) also found that where morphology was observed during high energy events (beach states 2 and 3), the bar scaling in the cross-shore took an infragravity associated wavelength.

British beaches, such as those in this study, are macrotidal, and it is also well understood that tidal range is an important factor in morphological change. For example, incident waves will spend more time reworking the beach near to the low water mark than the high water mark, and as a consequence low tide terraces will tend to be of a much lower gradient than the upper beach. These low tide terraces are also more likely to develop a longshore bar-rip morphology. Following Davies (1964) tide ranges have been classified as being micro- (<2m), meso- (2-4m) or macro-tidal (>6m).

Noting that increasing tidal range tends to suppress morphology, Masselink and Short (1993) applied a relative tide range (*RTR*) effect

$$RTR=TR/H_b, \tag{2.28}$$

where *TR* is tidal range, to the dimensionless fall velocity definitions of Wright and Short (1984). This conceptual model classifies beach sites based on these two dimensionless values as follows (see also figure 2.3.1).

1. *Reflective*, $\Omega<2$
    a) $RTR<3$, Fully reflective.
    b) $3<RTR<7$, Steep reflective high tide beach, relatively flat terrace formed at low tide level possibly with rip channels.
    c) $RTR>7$, Wide, uniform, featureless low tide terrace.
2. *Intermediate*, $2<\Omega<5$
    a) $RTR<3$, Rhythmic bar/rip morphology.
    b) $3<RTR<7$, Relatively steep high tide beach, fronted by low gradient middle (intertidal) zone (possibly barred), bar/rip morphology at low tide level.
3. *Dissipative*, $\Omega>5$
    a) $RTR<3$, Subdued longshore bar-trough morphology.
    b) $RTR>3$, Flatter more featureless beach.
4. *Ultra-dissipative*, $\Omega>2$, $RTR>7$, Flat and featureless with very wide intertidal zones.

Again the beach states most likely associated with high levels of infragravity frequency energy are of a dissipative variety in this scheme. It is notable that both high tidal range and the dissipative beach state tend to suppress topographic features such as bars. From this point of view a beach where the prevailing wave conditions are high energy storms is likely to have a relatively simple morphology. Consequently, from a modelling perspective, the incident waves on this type of beach are likely to make a relatively simple transition from shoaling to outer to inner surf zone, without any of the bore to unbroken wave reformation which can occur in the trough of a well developed bar.

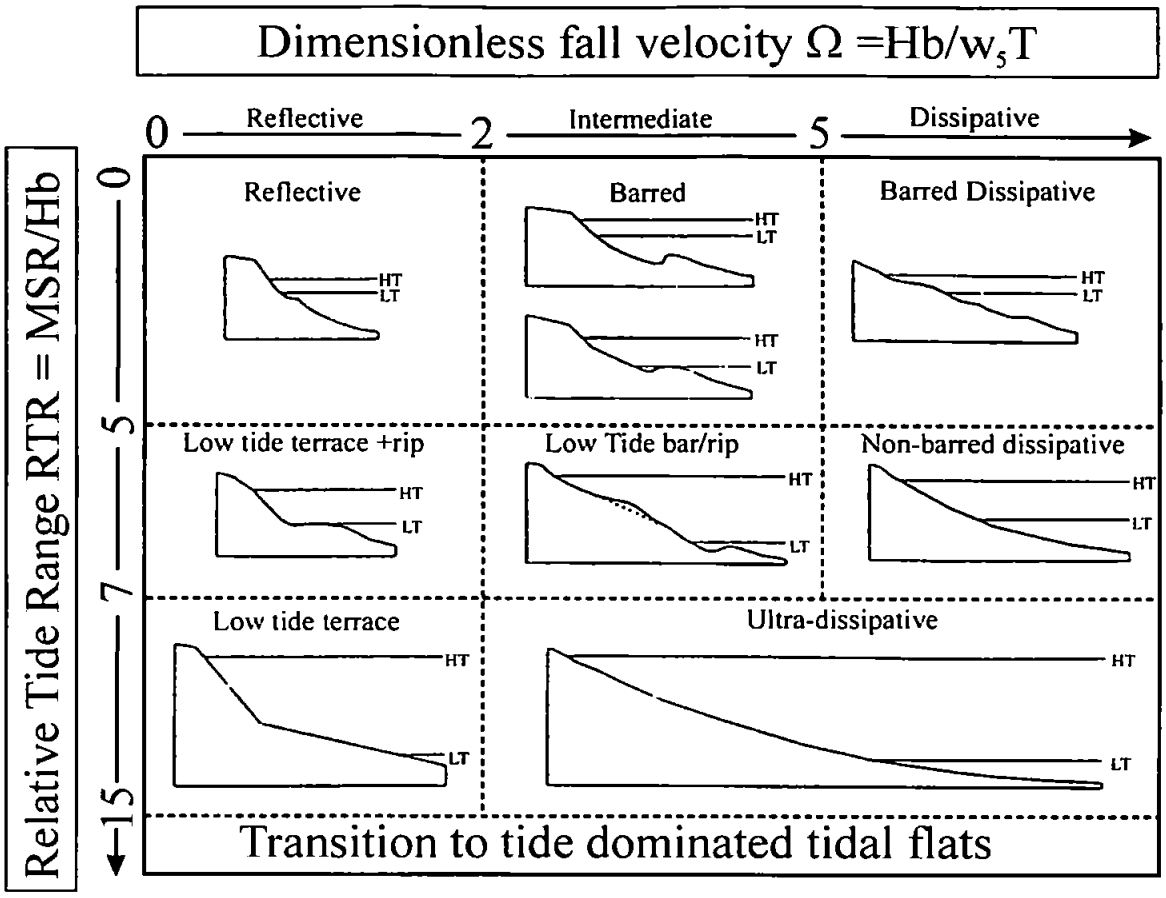

Figure 2.3.1 The Masselink and Short (1993) beach classification scheme.

2.3.3 Describing motion of sediment, in response to currents and waves

Heathershaw (1988) stated that "incipient grain motion (i.e. the beginning of sediment transport) is determined principally by the fluid velocity and the grain size, the position of the grain, sediment composition and packing, and fluid turbulence." He also continued to note the role that may well be played by bedforms (i.e. ripples) in affecting the threshold of sediment movement. Hence any schemes used to determine the onset and type of grain motion will have to be based on variables which describe the above characteristics.

In terms of the type of grain motion induced, a three-category classification (Heathershaw, 1988) is generally used which defines

bedload, where the grains roll or 'saltate' over and above the bed up to two or three grain diameter heights,

suspended load, where the grains are raised above the bed such that they travel freely in the water column many grain diameters from the bed,

washload, where very fine sediments remain in the water column for very long (e.g. tidal) periods.

In the case of the beach environments considered here, the first two modes of transport are considered to be the most common, and sediment type is thought of as non-cohesive. Description of grain size is normally made using a median grain diameter (D_{50}). Relating to this, sediments can be further described by a *settling velocity* (ω_s, e.g. Buller and McManus, 1979). As a general principal from the definition of suspended load, the *friction velocity* (u_*) induced at the bed as a result of waves and current will need to be larger than the settling velocity in order for sediment to be suspended. Indeed both bedload and suspended load transport are considered as a function of velocity, leading to the development of experimentally derived curves describing transport type by comparing friction velocity and grain size (e.g. in reference to mean currents, work by Hjulstrom, 1939). It is believed that qualitatively similar regions of deposition and erosion will occur throughout the nearshore for both bedload and suspended load transport (Foote, 1994). This allows for morphological change to be inferred from the distribution of one type of sediment motion. In the nearshore such evaluations are generally made with respect to the suspended type of transport, as this is rather easier to observe in the field than the bedload component.

The fluid flow at the bed also needs to be described in terms of turbulence, and for suspended load, the vertical structure of velocity. The latter of these sees division of the current boundary layer into a (thin) bed layer, a sublayer, a logarithmic velocity profile layer, and (if the boundary layer is not depth limited) a free stream layer. For the bed layer, the velocity acting upon the bed is more usually stated in terms of a (quadratic) *bed shear stress* (τ_0), which for example may be defined for currents using,

$$\tau_0 = \rho C_D \hat{U}^2, \tag{2.29}$$

where ρ is fluid density, and C_D is a drag coefficient relating to the depth averaged flow $\hat{U}$. For waves a similar expression is used in terms of a maximum bed shear stress,

$$\tau_{0m} = \frac{1}{2}\rho f_w U_{\infty m}^2, \tag{2.30}$$

where f_w is wave friction factor, and $U_{\infty m}$ represents the maximum free stream wave orbital velocity. Shear stresses of this form were related to a critical value for the motion of sediment on a smooth plane bed by Shields (1936), using the relationship

$$\theta_{cr} = \frac{\tau_{cr}}{(\rho_s - \rho)gD}, \tag{2.31}$$

where the critical Shields stress (θ_{cr}) is related to grain diameter D, and ρ_s represents sediment density. This critical stress value then defines a threshold for grain motion.

Turbulence is also necessarily defined for a constant flow, since, as was noted by Heathershaw and Simpson (1978), even in these cases the flow will include small scale 'burst and sweep' events as a combination of variations in the vertical and horizontal components of velocity (figure 2.3.2). Such events are liable to have particular ramifications for the suspended load component, where a lifting force is required to overcome gravity (figure 2.3.3). The current viscous sublayer is described using the *Reynolds number*,

$$Re = \frac{u.D}{\upsilon}, \tag{2.32}$$

where υ defines fluid viscosity. Sternberg (1968) measured critical values of Reynolds numbers in the sea, and produced a classification where flow would be defined as

smooth turbulent for $Re < 5.5$

transitional for $5.5 < Re < 165$

and rough turbulent for $Re > 165$.

The transitional classification is thought of as defining a state where the roughness elements protrude through the sublayer into the flow above. For currents on a flat bed these elements are simply a function of grain size, however for wave motion the *roughness length* will include the scale of bedforms in relation to the range of a wave orbit. In these cases Reynolds number is defined in terms of maximum near bottom orbital excursion,

$$A_{\omega m} = \frac{U_{\omega m}}{\sigma}, \tag{2.33}$$

where σ is wave frequency, such that

$$Re = \frac{A_{\omega m}}{k_s} \tag{2.34}$$

where k_s is the equivalent roughness of the bed as determined by grain and bedform size. Jonsson (1978) and Davies (1983) have both given lower limits for rough turbulent flow under waves. Further turbulence will be seen as an effect of wave breaking in the surf zone, and from collating the evidence of several other studies Svendsen (1987) pointed out that breaker turbulent energy diffuses through the water column and penetrates the bottom boundary layer with little dissipation. Therefore in the surf zone additional turbulent effects which may have an impact on sediment suspension are likely to be present as compared with deeper water. To this end a turbulent diffusion mechanism is used to calculate suspended load in numerous surf zone models, although it has been suggested that broken wave turbulence and boundary layer turbulence terms may be considered separately (Svendsen, 1987, Fredsoe and Deigaard, 1993).

Field study of sediment motion has generally been restricted to suspended load, and in fact reliable and rugged means of measuring suspended sediment concentrations in the surf zone (e.g. acoustic or optical backscatter sensors) have only really become available in the last decade. However, use of vertical and horizontally spaced instrument arrays have enabled field observations to be compared with theory. For example, Hanes and Huntley (1986) and Osborne and Greenwood (1993) examined the vertical distribution of suspended sediment using vertically spaced arrays. One problem with making point measurements of suspended sediment concentration is determining whether sediment is transported to the sensor location by horizontal advection or vertical convection (e.g. by turbulent diffusion). Hanes and Huntley (1986) resolved the two components by examining the lag between sensors of differing heights above the bed, stating that if horizontal advection was the main provider of sediment then the expected lag would be approximately zero, as entrained sediment would be advected to all sensors simultaneously. Studying observations from sensors located just outside of the surf zone these lags were found to

vary as a function of height, and hence the data suggested that vertical motion was generally dominant. Osborne and Greenwood (1993) observed a similar result for sensors not closely located to the bed.

Both studies also observed changes in the dominant oscillatory transport frequency with increasing elevation, from incident wave frequencies at the near bed, to frequencies in the infragravity band higher into the water column. However, both concluded that these low frequency effects at higher elevations above the bed were effects of incident frequency wave groupiness rather than any infragravity waves. Hanes and Huntley (1986) hypothesised that entrainment to the upper levels of the water column is not possible during a single wave cycle, but occurs as a result of a 'pumping action'. In this mechanism, grains are suspended by a wave, but do not completely settle before the next wave arrives; instead sediment mobilised by the first of a set of high waves is suspended further by the subsequent high waves. Thus high levels of suspension at high elevations are seen under the highest waves within groups. For high shear conditions in a water tunnel however, Staub *et al.* (1996), making observations using siphon type suspended load probes, noted that sediment concentration versus height above the bed agreed well with a model assuming a constant turbulent diffusivity.

In terms of cross-shore distribution of sediment suspension, Osborne and Greenwood (1992) noted an order of magnitude increase in sediment transport linked to the onset of breaking, when higher concentrations of sediment were also seen at higher elevations. Within the breaker zone the increase in sediment concentration versus conditions documented further offshore was seen to be particularly significant at infragravity frequencies in both the Osborne and Greenwood (1992) study and that of Russell (1990). On a low gradient beach, Hwang *et al.* (1996) found maxima in measured sediment concentration at the breaker line, which decreased with an almost linear relationship in the shoreward direction. The gradient of this decrease was linked to offshore wave steepness, with the steepest waves causing the largest concentrations at the breakpoint. Similarly Beach and Sternberg (1996) documented plunging type breakers as being associated with the largest concentrations of sediment observed at the breakpoint during their study.

Thus far, waves and unidirectional currents have been considered separately, but when the two components are found together, as is often the case in the nearshore, it is supposed that some interaction effects must take place which will affect sediment motion. Komar (1976)

showed that for waves the threshold velocity for a given grain size would increase corresponding to increasing wave period. Similarly, You (1998) described a relationship, in agreement with the model of Hallermeier (1980), whereby the threshold velocity initially increases with increasing wave period, but then takes a constant value. Conversely, Voulgaris *et al.*, (1995) found that the onset of sediment motion in such oscillatory flows was affected by the relationship between wave period and the underlying current strength. These findings are shown in figure 2.3.4 where lower oscillatory and mean current values are seen to produce sediment transport when the waves have a 15 second period, than when wave period is 5 seconds. This suggests a certain amount of interaction between currents and longer period waves.

These previous studies were carried out as numerical or laboratory experiments, and it could well be that the case is further complicated when it is considered that an infragravity wave component may also be present in instantaneous velocity fields observed in the natural environment. The complexity of this problem makes it difficult to model this behaviour in the sort of beach environment that is discussed in this thesis. Thus, the approaches discussed in section 2.3.1, which used either instantaneous velocity or the incident frequency wave component to mobilise sediment can be viewed as a necessary simplification. A number of field experiments (e.g. Russell 1990) also indicate that in the nearshore the mean current component (e.g. as an undertow) supplements or opposes the oscillatory velocity field, and that the resultant instantaneous velocity mobilises sediment.

Hanes and Huntley (1986) also suggested that the direction of flow is important to sediment entrainment. Events in their study were found to occur at full wave period intervals rather than the half wave interval one would expect if suspension were associated with the onshore and offshore velocity maxima. For this study, outside of the surf zone, the events were correlated with periods of onshore flow. In the shoaling zone, onshore velocities associated with the wave crests are correspondingly stronger than their offshore directed counterparts during the wave trough. Conversely infragravity frequency events where initiation of sediment motion occurred during offshore phases of flow were found by Beach and Sternberg (1988), in data from an array positioned in the surf zone. Beach and Sternberg (1988) also observed that during these events maximum gradients of vertical concentration occurred at, or shortly after, the peak offshore flow. Similarly to Staub *et al.* (1996), Beach and Sternberg (1988) noted high levels of shear, and cited a good comparison between the observed vertical distribution of suspended sediments and a model

using turbulent diffusion as the dominant mechanism in defining the vertical scale of suspension events. It is notable that in a surf zone under high energy conditions, when velocities are large, the dominant wave component is liable to be of an infragravity frequency.

In addition to Beach and Sternberg (1988), Russell (1990) also observed maxima in suspended suspension concentration in association with offshore directed currents in the surf zone. Russell (1990) noted that this effect was most likely due to the offshore directed phase of oscillatory velocity being reinforced by an undertow. In this case the velocity field was further skewed toward the offshore by a highly energetic infragravity wave component, which became increasingly biased in favour of the offshore phase as the waves shoaled close to shore.

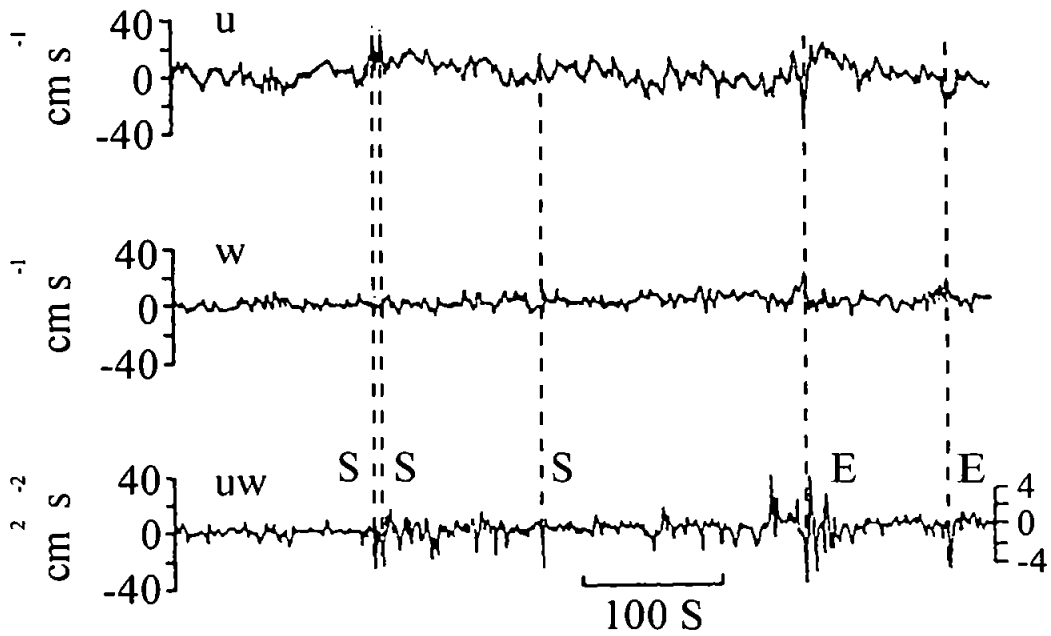

Figure 2.3.2 Turbulent 'burst and sweep' events in a mean current trace (from Heathershaw and Simpson, 1978). In the diagram S denotes sweep events, whilst E denotes ejection or burst events.

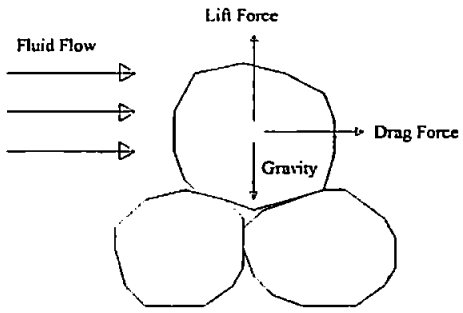

Figure 2.3.3 Forces acting upon sediment in a (laminar) fluid flow.

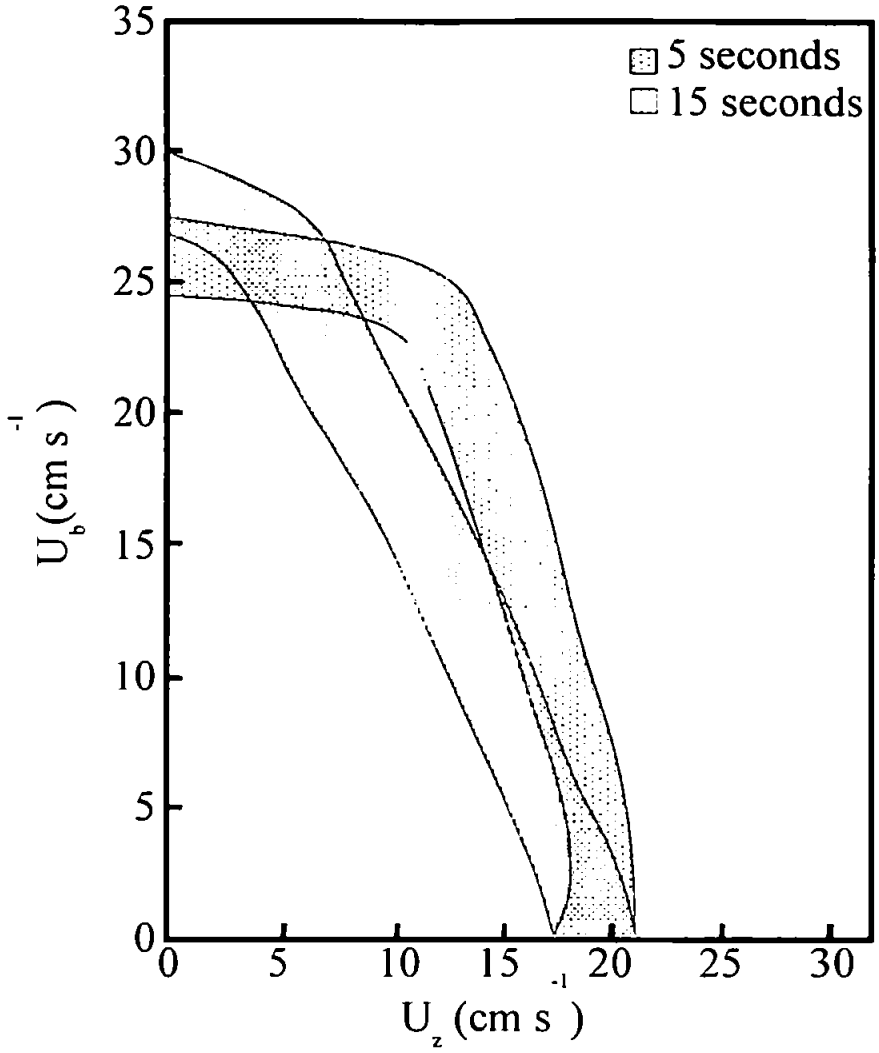

Figure 2.3.4 Threshold velocities of combined waves and mean current for waves of period 5 seconds and 15 seconds (from Voulgaris *et al.*, 1995).

2.3.4 Effects of bedforms

The threshold velocity for sediment entrainment is also affected by the presence of bedforms (i.e. ripples). Such features serve to greatly increase bed roughness, and in breaking up the flow over them produce pressure gradients which add further resistance to flow (*form drag*). Bedforms are classified in terms of a height and wavelength as

ripples: wavelength 0.1-0.5m, height 0.01-0.05m,

megaripples: wavelength 1-5m, height 0.1-0.5m

sandwaves: wavelength 100-500m, height 1-5m.

Thornton *et al.* (1998) made observations of the beach at Duck, North Carolina, and found the first two bedforms in correspondence to mild and storm conditions respectively. In the latter case the megaripples were found in a bar trough whilst the rest of the beach had a planar bed.

The formation of bedforms can be related to velocity magnitude and grain size, as for example in figure 2.3.5, where ripples are seen for velocities of less than $1ms^{-1}$, and grain D_{50} of less than approximately 1.2mm. Under mean current conditions asymmetry in the bedforms is taken as an indication of the dominant direction of the mean flow. Heathershaw (1988) notes however that a rather different type of ripple is formed under oscillatory conditions, where periodic reversal of flow is likely to result in a more symmetrical bedform. Nonetheless it is still suggested that in regions of net sediment transport a more asymmetrical form will be taken by the ripples, in line with the direction of sediment flux.

In oscillatory conditions two different mechanisms of ripple formation are also possible according to the strength of the wave induced current. For weaker flows ripples are likely to be formed by rolling grains (Sleath, 1984), but as the current strength increases, so will ripple height. At a critical height, flow separation at the ripple crest may occur, and sediment from the crest will be set into suspension by vortices ejected from the flow over the bedforms. These vortex ripples will affect sediment transport by providing this second mechanism for sediment suspension. Thus in the presence of vortex ripples, sediment may be suspended in response to velocity maxima from the upstream slope of the ripple, but also suspended from the crest at flow reversal due to vortex shedding. In terms of field observations, this second mechanism can lead to high concentration 'parcels' of sediment being advected past the instruments on the reverse phase of the flow. Therefore the highest

concentrations of sediment will be seen 180° out of phase with velocity field skewness (Trouw *et al.*, 1999).

At higher values of flow still (above approximately $1ms^{-1}$), Reineck and Singh (1980) found that the bed was washed clean of bedforms, and presented a plane surface to flow. The magnitude of suspension events were observed to be increased by such a destruction of a ripple field, as observed by Osborne and Greenwood (1993). Using video observations of the bed, the authors saw the formation of steep asymmetric three dimensional vortex ripples under small shoaling waves, which were then reshaped later in the tide under breaking wave conditions to give a less steep form. This latter period coincided with an increase in the observed values of suspended sediment concentration. Similarly Davidson *et al.* (1993) noted a 'tidal asymmetry' to suspension in their dataset, whereby larger concentrations were observed during the ebb phase of the tide. This was attributed to the destruction of a ripple field that had formed over the high water period.

This transition from ripple field to plane bed was also examined by Hanes *et al.* (1997), who observed rapid deformation and reformation of small ripple fields within an order of a few wave groups. Hanes *et al.* (1997) further related such changes in bed character to mobility number ($\Psi(t)$, Dingler and Inman, 1976), where

$$\Psi(t) = \frac{u^2(t)}{(s-1)gD_{50}}, \tag{2.35}$$

and s is the specific incident of the sediment. Hanes *et al.* (1997) suggested that the behaviour of a sandy bed in terms of generation of ripples under oscillatory flow would follow a model whereby for

$\Psi(t)<50$ ripples would form slowly,

$50<\Psi(t)<150$ ripples would form relatively quickly,

$150<\Psi(t)<240$ ripples would be destroyed by groups of waves which attained such values,

$\Psi(t)>240$ an individual wave could sweep a rippled bed clean.

Again in assuming that the infragravity component will be strongest in association with the highest energy conditions, it is likely that wave conditions corresponding to the highest mobility numbers observed in a saturated surf zone will be dominated by infragravity energy. From this perspective, high levels of infragravity energy may well be coincident with a planar bed.

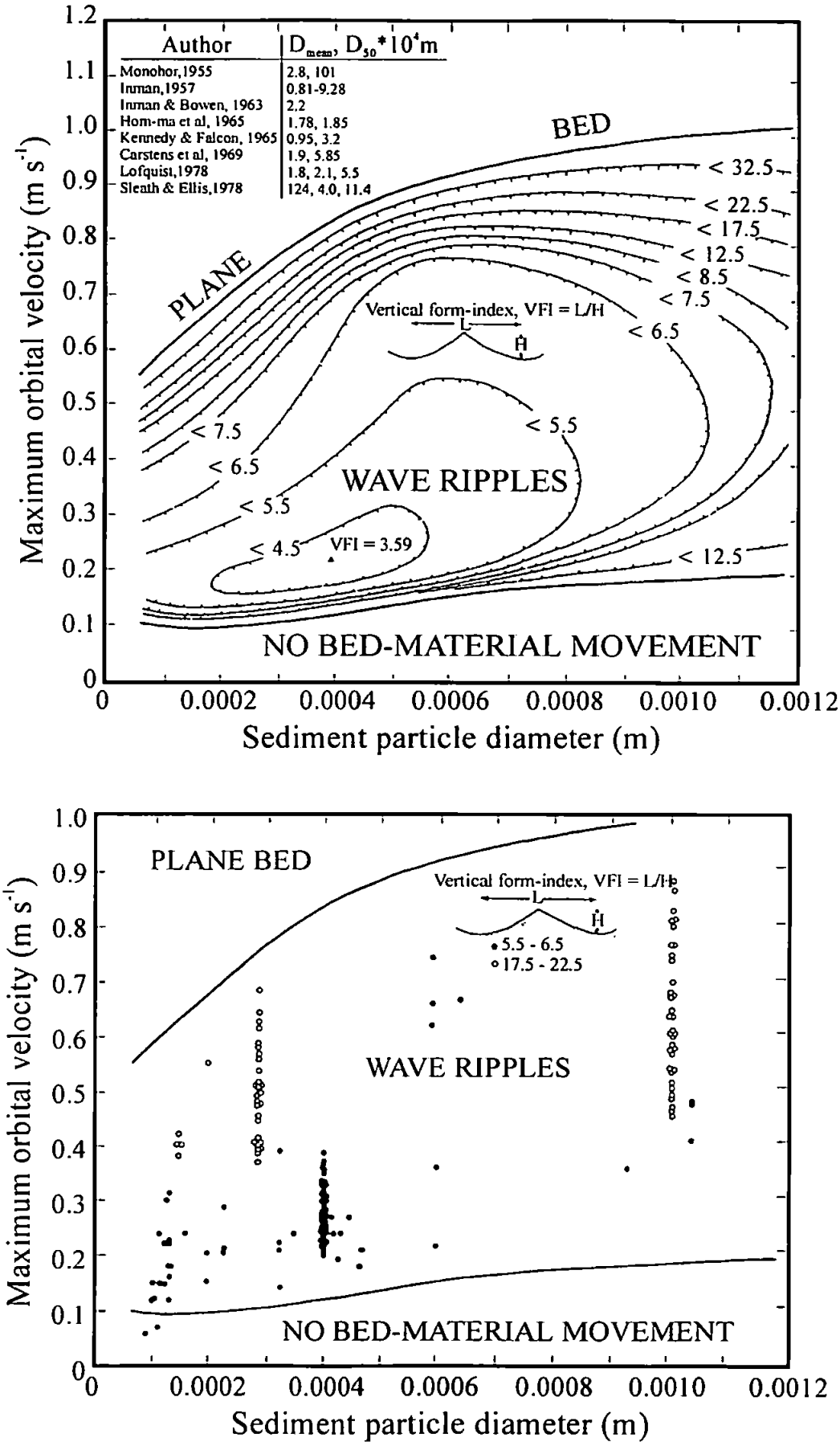

Figure 2.3.5 Curves predicting bedform type as described from grain size versus velocity (from Van Rijn, 1993).

2.3.5 Components of transport in the nearshore

In determining the evolution of beach profile (positions of erosion, accretion and bar formation), the sediment flux budget in this region of the nearshore is considered in terms of zones of erosion and deposition derived from prevailing wave and mean current conditions, with respect to the local tidal and sediment environment. These latter two characteristics will have a major influence on beach morphology. For example, an increasing tidal range is liable to suppress morphology for most of the beach except near the low water line (Masselink and Short, 1993). For given conditions a steeper beach profile is associated with increasing sediment grain size (Heathershaw, 1988). The temporal scales on which beach evolution may be considered vary, for example King (1972) and Short and Aagaard (1993) noted that in a multiple bar system, inner bars may be modified by most wave conditions, whilst outer bars tend to migrate only under moderate or high waves. This would give a result where accretional periods associated with low waves will lead to separation of the bars, and thus a more dissipative beach, whereas moderate/high wave conditions give rise to a more intermediate beach type. Whilst video studies such as that by Lippmann and Holman (1989) have the potential to monitor such long term changes, most field studies (which tend to be of a number of weeks duration only) are only able to discuss processes in terms of a few storm events.

Komar (1976) noted that sediment transport under an individual wave varies as a result of wave skewness. For example in figure 2.3.6 large concentrations of suspended sediment will be transported onshore by the wave crest but for a short period only, whilst lower concentrations will be transported offshore by the trough, but over a longer duration. The balance of these mechanisms will give rise to either an onshore or offshore net flux over a single wave period. The same mechanism will also be affected by grain size on beaches characterised by a mix of sediment. Applying this to the diagram in figure 2.3.6, larger sediments are liable to be transported onshore as suspended load by the more energetic crest, whilst smaller sediments only may be transported offshore by the trough. This would lead to a 'sorting' of sediments seen on beaches where the coarser material tends to be found toward the top of the beach, whilst finer sediments make up the lower part.

Thus spatial evolution of waves, and hence of the velocity field, will lead to a distribution of transport through the nearshore, with corresponding zones of deposition and erosion. Any structure in net transport should then be a resultant of both direction, and volume of

sediment flux for the observed components, where for the oscillatory components transport direction is hypothesised as being a result of phase between suspension events and flow. This led Jaffe *et al.* (1984) to examine sediment flux as a product of observed time-series for suspended sediment concentration and velocity, and furthermore resolve the overall flux into a mean and oscillatory constituent as,

$$\overline{c.u} = \overline{c}.\overline{u} + \overline{c'.u'}\,, \tag{2.36}$$

where the overbar in the above equation describes averaging over wave cycles. The oscillatory term was further divided into an infragravity and incident ('gravity') frequency term by Russell (1990), to give

$$\overline{c.u} = \overline{c}.\overline{u} + \overline{c'.u'}_{\text{grav}} + \overline{c'.u'}_{\text{infrag}}\,. \tag{2.37}$$

These latter terms can be described for oscillatory flow over the frequency domain from the analysis of cospectra between collocated current meters and acoustic or optical backscatter sensors. Davidson *et al.* (1993) pointed out that transport direction is determined by the phase between the suspended sediment and velocity time-series (figure 2.3.7). In cospectral terms the incident frequency wave stirring-infragravity wave transport model, as given in section 2.3.1, assumes that the passage of incident band waves will stimulate suspension events but have a near zero transport component at quadrature phase. In fact, in the field an incident frequency transport component is observed, and is considered a result of orbital velocity asymmetry. The infragravity part of the cospectrum will be determined by infragravity wave asymmetry coupled with the phase between the infragravity waves and periods of sediment suspension.

In the nearshore shoaling wave zone on a planar beach Osborne and Greenwood (1992) found the major transporter to be the wind wave component, leading to flux in the onshore direction, in agreement with earlier observations (Hanes and Huntley, 1986) of suspension associated with an onshore phase of flow. Also noted was a smaller, but still significant cospectral peak indicating offshore transport at an infragravity frequency. This offshore phase of transport was associated with greater than quadrature phase between infragravity wave related current and suspension events.

In the outer surf zone (non-saturated wave breaking), the contributions of both oscillatory components were found to be of the same order of magnitude by Beach and Sternberg (1991), despite wave power spectra still being dominated by peaks at incident frequencies. This was because the major suspension events in this zone were associated with the largest

waves in the incident wave groups. These events led to large offshore transports associated with infragravity components, due to the largest variations in suspension by the incident waves being in phase with an offshore directed infragravity wave velocity. This effect increased the magnitude of the contribution from this part of the frequency domain to the overall cross-spectrum. Beach and Sternberg (1991) also found a phase shift at a single lower infragravity frequency associated with a reversal of the transport direction observed for higher frequencies within the band. A similar reversal of transport at far infragravity frequencies was documented by Aagaard and Greenwood (1994).

Where high energy conditions have been observed, the dominant oscillatory components under saturated breaking in the inner surf zone have been found at infragravity frequencies (e.g. Wright *et al.*, 1982; Beach and Sternberg, 1988; Russell, 1990). Wright *et al.* (1982) assessed the potential contribution to transport at incident and infragravity frequencies, and found an order of magnitude difference in potential transport between the two bands. This was observed in the fluxes measured by both Russell (1990), and Beach and Sternberg (1991). However where Russell (1990) observed a dominant offshore infragravity transport throughout the surf zone, Beach and Sternberg (1991) found the component to be onshore, with the exception once again of a reversed flow at a single far infragravity frequency.

Along with the oscillatory components in the surf zone, Russell (1990) also observed a mean offshore reverse flow (undertow). Similar offshore directed currents observed near the bed were found to provide the dominant mechanism for sediment flux above approximately 0.1m above bed level by Huntley and Hanes (1987), Osborne and Greenwood (1992), and Davidson *et al.* (1993). When considered alongside the oscillatory components, this leads to the result presented in Russell (1993) that the surf zone sees large offshore net flux of sediment due to dominant infragravity oscillatory, and mean current components. However, the inner surf zone of Beach and Sternberg (1991) showed only a very small net transport since these two dominant mechanisms were in opposition.

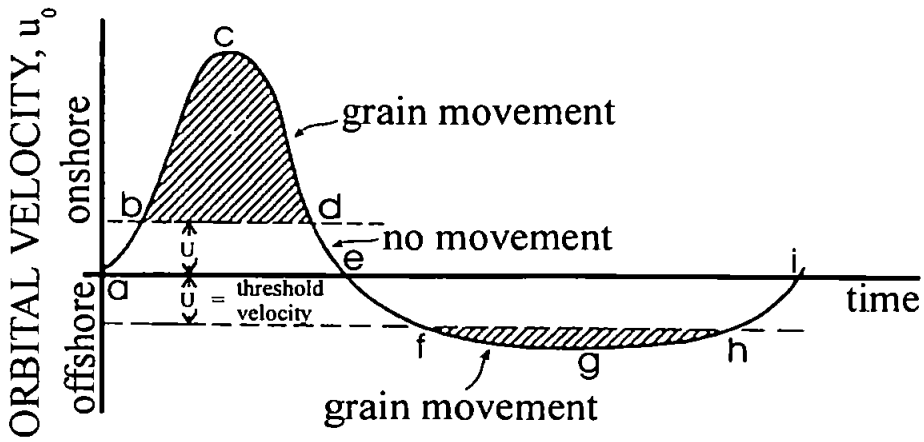

Figure 2.3.6 Sediment transport in relation to wave asymmetry, from Komar (1976).

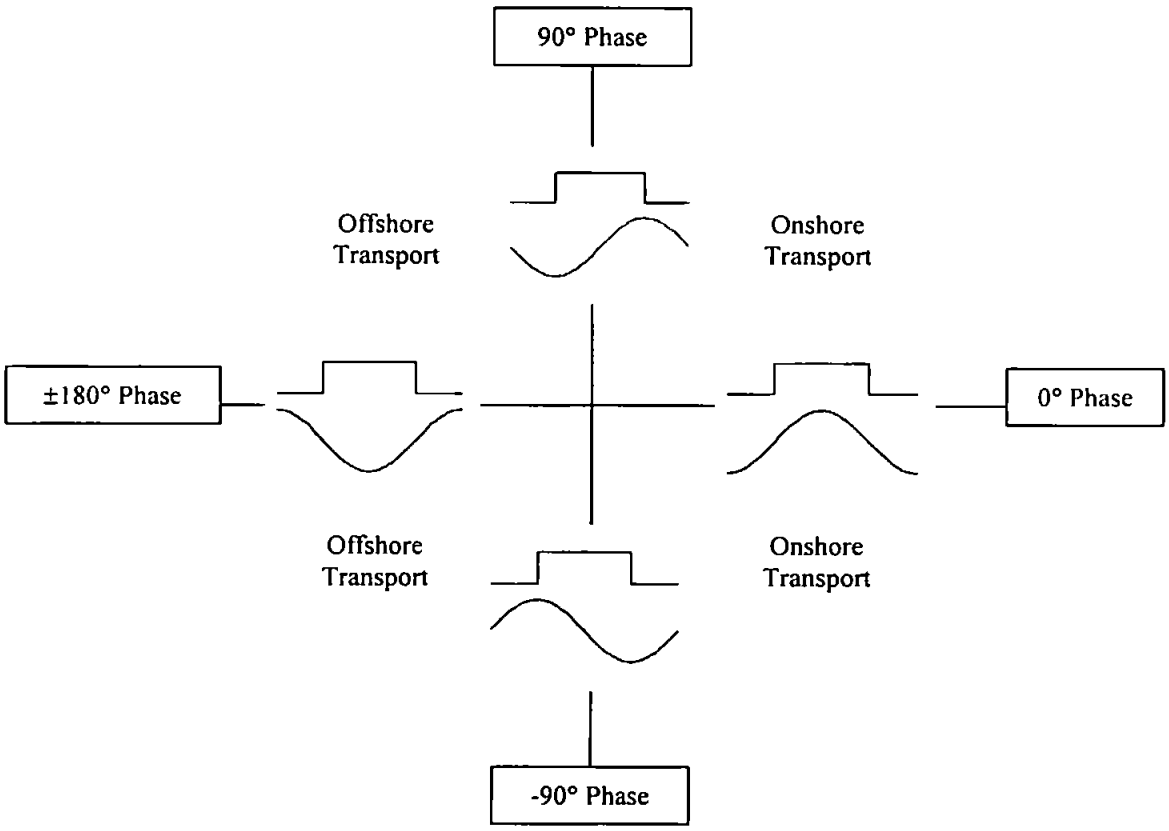

Figure 2.3.7 Transport directions inferred from suspended sediment concentration versus cross-shore velocity (*c*-*u*) phase. Here the onshore direction is taken to be positive, and the *c* and *u* signals are represented by a box and sinusoidal function respectively.

2.3.6 Summary: Sediment dynamics

For a plane bed, sediment motion is induced as a result of velocity at the bed exceeding a critical threshold. The distribution of suspended sediment in the vertical is related to the turbulence induced by the passage of waves, which will vary in the cross-shore with changes in wave height and breaking patterns (e.g. Falques *et al.*, 1999). However, where groups of high waves are observed, 'pumping' effects may also affect the levels of suspended sediment higher in the water column (as for Hanes and Huntley, 1986). Nonetheless, close to the bed measurements of suspended sediment concentration are likely to be representative of the instantaneous response of sediment to the hydrodynamic regime.

As a result of coupling between mean flow and skewed oscillatory components, sediment suspension and subsequent transport is likely to be biased toward a particular phase of velocity. For example, in the shoaling zone, where the mean current is onshore directed and the incident frequency waves are skewed toward the onshore directed phase of velocity associated with the wave crest, onshore transport has been observed (Hanes and Huntley, 1986). Conversely studies (e.g. Russell, 1990) cite offshore transport in the surf zone where, although the incident frequency component is onshore skewed, both the mean current and shoaled infragravity waves are offshore biased.

The infragravity frequency component of oscillatory transport increases in importance in the shoreward direction. This has been observed as both a result of the increased importance of infragravity energy near to shore (Beach and Sternberg, 1988, Russell, 1990), but also as a result of the largest incident frequency waves suspending sediment in phase with a strong infragravity wave velocity (Beach and Sternberg, 1991). Several studies note a reversal in the transport direction for frequencies within the infragravity band (e.g. Beach and Sternberg, 1991 and Aagaard and Greenwood, 1994).

It seems likely that ripples are associated with conditions where infragravity waves are rather less energetic compared to events where a plane bed will be observed. Ripple presence will affect both the grain motion threshold, and also the mechanisms for sediment transport, since when ripples are present, a secondary mechanism for suspension exists whereby sediment is entrained at oscillatory flow reversal. The concentrations of sediment suspended may also be increased by the destruction of a ripple field due to the passage of a group of large waves.

2.4 Discussion

Previously in this chapter it was noted that several types of model could reproduce qualitatively similar patterns of beach erosion and deposition. These included approaches which assumed that sediment was mobilised by incident frequency wave stirring and subsequently transported by either or both of the mean and infragravity components (e.g. Dally and Dean, 1984, O'Hare and Huntley, 1993), and an energetics based model (Russell and Huntley, 1999). Each model makes certain simplifying assumptions, which may or may not be correct. For example, field observations would appear to suggest that instantaneous velocity is more readily associated with sediment suspension than is the passage of a incident frequency wave.

This thesis has been motivated by the use of such process based assumptions regarding the role of the infragravity frequency component in sediment transport. Referring to the example above, if instantaneous velocity does indeed drive the majority of suspension in the nearshore, then it will become extremely important to model the shoaled infragravity wave close to shore, where under high energy conditions it may dominate the oscillatory velocity field.

Another common modelling assumption is the use of full reflection of the infragravity component from a shoreline reflection point. Other theoretical studies (Madsen *et al.*, 1997) have however, noted a frequency dependence for reflection even in the infragravity band. Both this study and work done outside the surf zone (e.g. Ruessink, 1998) have suggested that a level of interaction occurs between the incident and infragravity component. It would be useful to examine this type of relationship further, as the phase between modulated incident frequency waves and the infragravity component is liable to have a distinct bearing on the resulting sediment transport.

Since a strong infragravity component will be associated with high energy conditions, then from one modelling perspective infragravity dominated conditions provide a relatively simple case, in that both morphology and bedforms tend to be suppressed. In such a planar bed system, the sediment dynamics ought to be almost directly related to a relatively simple model of the hydrodynamic forcing (since for example, waves, once broken are unlikely to reform). The presence of bedforms will complicate a lower energy case, since they may well effect the phase of sediment suspension. The transition of a bed from a rippled to a

planar state could well further complicate assumptions regarding sediment 'pick up', and may occur as a result of the passage of several high waves within a group.

In the previous sections examples of a number of these problems have been cited. The aim of this study is to bring together results from different sites and across a range of hydrodynamic conditions with the aim of (qualitatively) finding the mechanisms driving, and effects of, high concentration, low frequency suspension events on sediment transport (see introduction chapter 1). In relating these events to an accurate description of the hydrodynamic regime, it is hoped that some of the processes that are most important to nearshore modelling can be highlighted. The field programme, two sites of which are taken from the existing British Beach And Nearshore Dynamics (B-BAND) dataset, is documented in the next chapter.

Chapter 3: Experimental Work

3.1 Selection of experimental data

Following the work of previous authors (e.g. Beach and Sternberg, 1991; Russell, 1993) the role of the infragravity component of sediment transport is likely to be most important during energetic storm events. Hence one aim of this work is to describe the role of infragravity frequency sediment transport through the nearshore zone, and over a range of moderate to high energy conditions. At the start of the project the intention was to conduct this analysis using a pre-existing dataset from the B-BAND programme (Russell *et al.*, 1991; Davidson *et al.*, 1993).

The problems to be addressed require simultaneous high frequency (>1Hz) measurements of sea surface elevation (for water depth and wave information), current and suspended sediment concentration. However, the data was also selected under the criteria that a range of hydrodynamic conditions was observed. These included:

- Ranges in incident wave energy, which might relate to the amount of infragravity wave energy observed.
- Ranges of breaking and non-breaking conditions, to examine the effects of groupiness.
- Ranges in beach reflectivity, which might affect wave reflection.

Initially tides were selected from B-BAND experiments carried out at Llangennith (South Wales) and Spurn Head (Holderness Coast) which had respectively been described by authors as exhibiting high energy dissipative (Russell, 1990; Davidson, 1991) and moderate energy intermediate conditions. Further, the beach topography at Spurn Head, which consists of a steep high tide beach ($\tan\beta \cong 0.1$) and lower gradient low tide terrace ($\tan\beta \cong 0.0235$), meant that at high water, conditions would be reflective. By virtue of the fact that all the experiments used in this thesis were conducted on macrotidal beaches in the UK, a cross-shore range of wave conditions were observed by the instruments in each case.

The instrumentation, which consisted of a pressure transducer (sea surface elevation data), electromagnetic current meter (current data) and optical backscatter sensor (measurements of suspended sediment concentration), was deployed with the instrument heads protruding

from the bed. Cables which provided power for the instruments and data transfer were buried in the beach and connected to a beach station just above the high water line. The length of cable used in these experiments constrained the maximum distance from the high water line at which the instruments could be positioned. Consequently, in the case of the Llangennith data, results came only from the inner surf zone, whilst the Spurn Head data came from between shoreline and shoaling zone due to the steeper beach gradient and smaller wave conditions. More detailed descriptions of the deployments are given by Russell (1990) (Llangennith) and Foote (1994) (Spurn Head).

In order to create a continuum between what were two relatively disparate sets of results, a further set of data was required. This need for extra data was fulfilled during a test deployment of a new instrument rig, which had been purchased as part of the University of Plymouth's commitment to the EU MAST III funded COAST3D programme. In this experiment the instruments were sited on a dissipative beach at Perranporth (Cornwall). The selected tide of data observed incident wave conditions which in energetic terms fell between those observed at Llangennith and Spurn Head.

In the next section the B-BAND programme, which has previously been documented by Russell *et al.* (1991), and Davidson *et al.* (1993), is described briefly, with particular reference to the experiments at Llangennith and Spurn Head. A more detailed description of the instrumentation and deployment at Perranporth is given in section 3.3.

3.2 The B-BAND programme

3.2.1 Experiment overview

Over recent years beach experiments have tended to be organised as large scale multi-institutional programmes. Such field deployments have included NSTS (Seymour, 1987), C^2S^2 (Willis, 1987), NERC (Horikawa and Hattori, 1987), SUPERDUCK (Martens and Thornton, 1987), and more recently DUCK94, SANDYDUCK97, and the ongoing COAST3D programme (Soulsby, 1998). The British Beach And Nearshore Dynamics programme (B-BAND, Russell *et al.*, 1991) was conceived as a similar collaborative venture, and was focused on sediment dynamics in agreement with recommendations following the NSTS experiment, which had largely examined hydrodynamics. It involved a number of UK institutions (the Universities of Cardiff, Plymouth and Hull), and along with its experimental aims, also had the intention of establishing a database of nearshore observations relating to the meso-/macro-tidal environment that is a feature of the British Isles coastline. More specifically Russell *et al.* (1991) set out the experimental aims as:

> "i) to quantify net suspended-load sediment transport rates, both alongshore and cross-shore, using direct field observations; to relate these observed rates to existing sediment transport models and hence propose improvements to the models; and, if possible, to estimate the divergence of transport rates at particular nearshore locations and compare the results with measured beach accretion or erosion.
>
> ii) to investigate the relative importance of steady flows, long waves (surf beat) and incident waves to the overall transport rates, for different distances offshore and under different wave conditions and beach slopes.
>
> iii) to use the results of our investigations to improve models of shoreline profile evolution. In particular models already under development, for example the SLOPES model (Hardisty, 1990) will be tested against the field data.
>
> iv) to identify the specific processes producing the profile of macro-tidal beaches, in comparison to those operating on the more widely studied micro- and meso- tidal beaches."

To fulfil the observational requirements of this statement, the B-BAND experimenters made a number of field deployments using arrays of instruments spaced in the cross-shore, longshore and vertical planes. Instruments included pressure transducers, annular and spherical electromagnetic current meters, and optical backscatter sensors. Thus data was gathered describing sea-surface elevation, cross-shore and longshore velocity, and suspended sediment concentration. These measurements were made in tandem with beach profile and depth of disturbance surveys (Foote, 1994). Due to the macrotidal nature of the B-BAND environments each instrument recorded sets of conditions attributable to different parts of the nearshore during an ebb-flood cycle. The whole suite of observations attempted to cover not only a range of energetic conditions, but also to represent three classes of beach state.

1. *Dissipative*; deployments at Llangennith (Gower peninsula, South Wales).
2. *Intermediate*; deployments at Spurn Head (Holderness coast, NE England).
3. *Reflective*; deployments at Teignmouth (South Devon, England).

From this three beach dataset (sites are shown in figure 3.2.1) three specific tides have been selected as being particularly appropriate to this study. Since one of the prime requirements of the data to be used are that as strong a low frequency component as possible is likely to be present, the selection process put an emphasis on the overall wave energy observed during any given tide. On this basis data from Teignmouth, and a number of days at Spurn Head were eliminated, leaving two tides from the Llangennith experiment and one tide from a storm event at Spurn Head as the best candidates for analysis. Descriptions of the deployments from which this data is taken, along with a further description of the beach sites are given in the next two subsections.

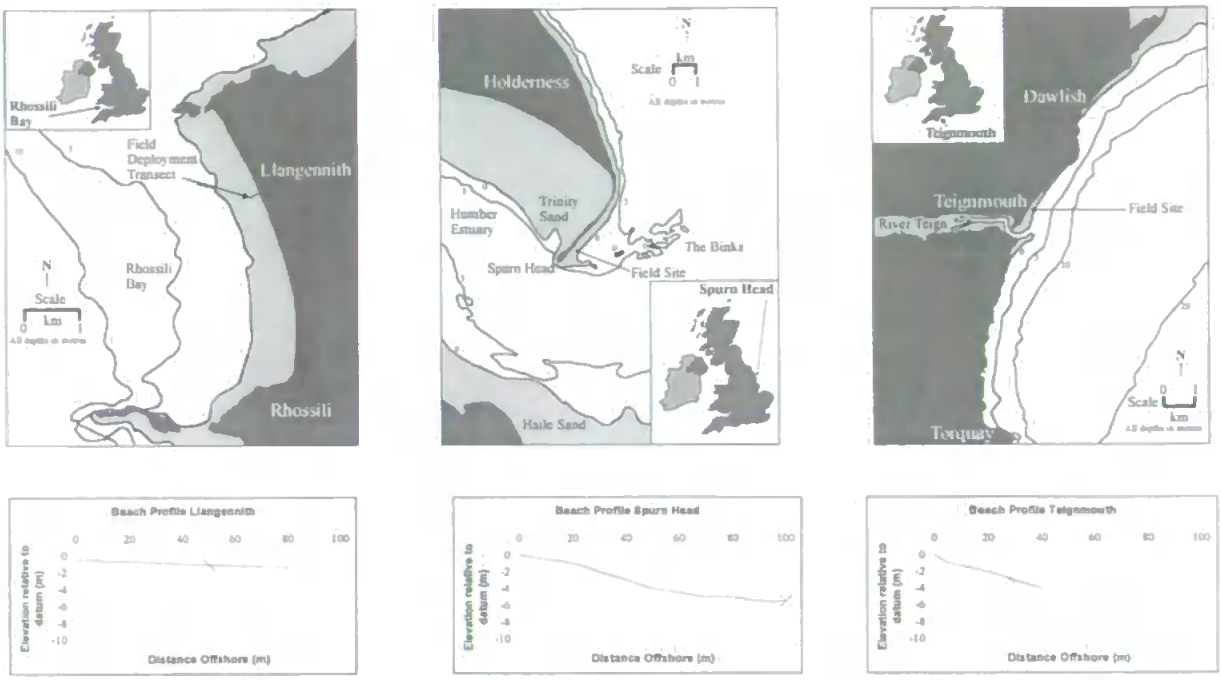

Figure 3.2.1 The B-BAND field sites, situation and profiles (from Russell and Huntley, 1999).

3.2.2 The Llangennith deployment

The Llangennith dataset comes from observations made on 22 July and 17/18 November 1988, which document calm and storm conditions respectively (Russell, 1990). The beach itself is sited at the centre of Rhossili Bay, on the west of the Gower Peninsula, South Wales, and some sixteen miles from the nearest major population centre, Swansea. The beach is made up of mainly non-cohesive fine quartz sand (D_{50}=0.23mm, Russell, 1993), and is west facing, such that it is open to an uninterrupted window of incident wave approach for Atlantic swell as well as local storm seas. Thus the beach can receive waves associated with fairly violent storm conditions. Davidson (1991) also notes that since the beach is relatively long (5km) with a tendency toward a plane profile, and likely to receive near normally incident swell, that observed surf zone processes are likely to be of a form which can be described in relatively simple two dimensional forms.

One eccentricity of this site is its proximity to the Bristol Channel, an area of particularly high tidal range. The tides are semidiurnal, and Davidson (1991) cites a neap range of 4.1m, and a spring range of 8.5m. In terms of the beach classification stated in section 2.1.3 by Masselink and Short (1993) the beach can be defined during moderate to stormy conditions (assuming an 2m high breaking waves with a peak period of 8 seconds) by Ω=6.25 and RTR>3. According to the Masselink and Short (1993) classification scheme this defines a dissipative environment, where generally the beach takes on a low slope planar profile and may tend toward a subdued two-dimensional bar trough morphology under persistent storm conditions. For the storm event observed by Russell (1990) and Davidson (1991), which occurred during neap tides, surveys show the relatively planar profile (figure 3.2.2) being maintained over the duration of the event. Following both these works, this thesis makes an assumption of a planar beach slope being maintained through the observation period, with gradient $\tan\beta$=0.0145.

The storm event featured in this analysis is represented by data from two consecutive high tides during the November 1988 deployment. A single rig of colocated instruments was positioned approximately 100m below the maximum high water line, and linked to a beach station (Land Rover) by a set of cables which had been buried into the sand at roughly 0.5m depth (figure 3.2.3, Davidson, 1991). Instrumentation consisted of a pressure transducer, electromagnetic current meter, and optical backscatter sensor (manufacturers and calibration details may be found in Russell, 1990 and Davidson, 1991). Details of

instrument heights are given in table 3.4.i. The system sampled at 3Hz over the course of the two high water periods for a duration of approximately 2 hours on each tide. Subsequently these tides will be referred to as 'Storm Day' and 'Storm Night'. The storm event comprised a sea consisting predominantly of a well-formed shore normal swell; significant breaker heights were estimated visually as approximately 3m during the Storm Day runs and 2.5m for the Storm Night runs, with the breaker type being spilling in both cases.

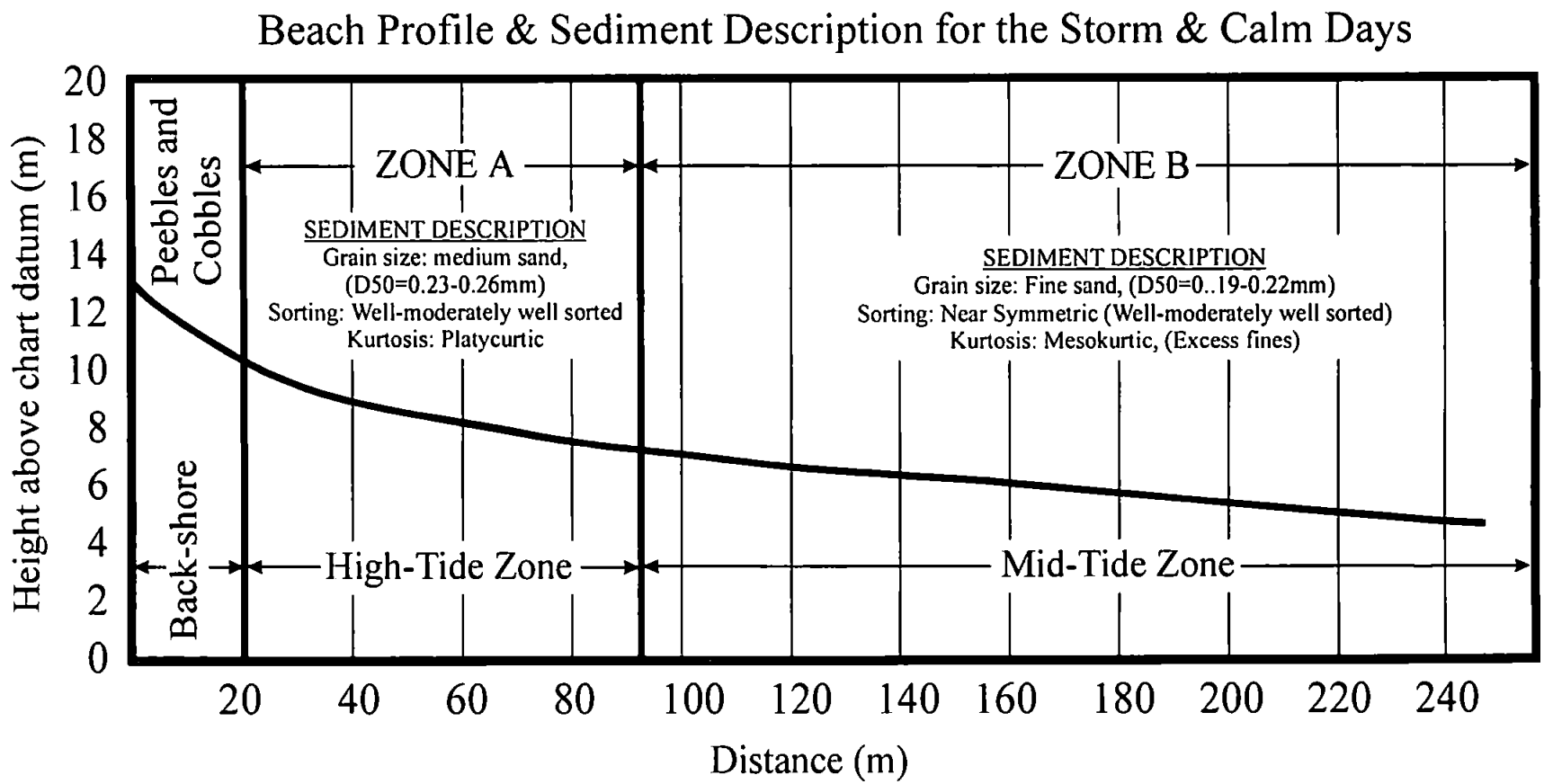

Figure 3.2.2 Llangennith beach profiles and description (from Davidson, 1991). The instruments were sited on the border of Zones A and B.

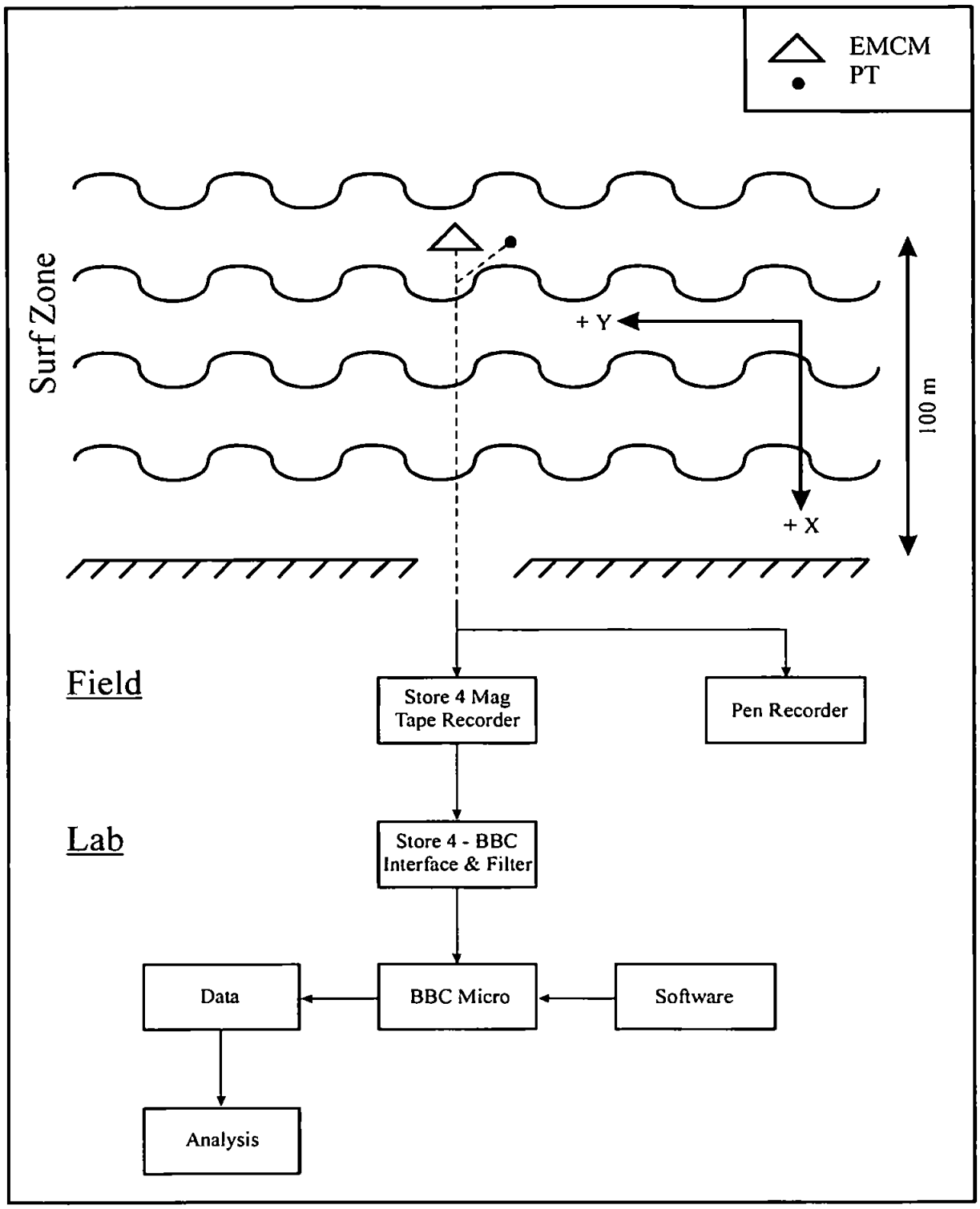

Figure 3.2.3 Schematic of the Llangennith field deployment (from Davidson, 1991).

3.2.3 The Spurn Head deployment

The Spurn Head data has been taken from observations made during a deployment of the B-BAND array over the period 16th-25th April 1991 (Davidson *et al.*, 1993; Foote, 1994). The study area is a 5km long sand and shingle spit extending into the mouth of the Humber Estuary, East Yorkshire. This region borders on the North Sea and is in close proximity to the Holderness coastline, an area which experiences high erosion and has been the source of much recent study as part of the large scale LOIS (Land-Ocean Interface Study) experiment (Prandle, 1994). Foote (1994) noted that most of the coarser sediments deposited around Spurn Head are likely to have their source as the Holderness cliffs.

In the region of the deployment, surveys found the beach to consist of a low tide terrace with a slope of $\tan\beta$=0.0235, and a more reflective high tide beach where $\tan\beta$=0.0975 (figure 3.2.4). Higher up the beach coarse sands and pebbles were observed, but at the instrument location sediment consisted mainly of a well-sorted medium-fine quartz sand (D_{50}=0.35mm). Using the same wave conditions as applied in the Llangennith case (H_b=2m, period 8 seconds) dimensionless fall velocity Ω would be approximately 4, putting the beach into the intermediate category of Masselink and Short (1993)'s beach classification. Neap and spring tide ranges vary between 3m and 6m respectively in this area, making the beach macrotidal, with the probable result of (generally) suppressed lower beach morphology. Data taken from this study were acquired during the neap part of the tidal cycle.

The tide causes strong rectilinear currents in the Spurn Head nearshore zone, which run parallel to the beach in a southwesterly direction on the flood and northeasterly on the ebb. A further effect of the tide was noted by Davidson *et al.* (1993), wherein a shingle ridge some 3km offshore of the spit (known as the Stony Binks) may dry out on large spring tides, causing offshore dissipation of wave energy around low water slacks. The wave field in this region generally comprises short fetch northerly incident waves, generated by storms in the North Sea.

The Spurn Head field experiment employed 7 pressure transducers, 10 electromagnetic current meters, and 9 optical backscatter sensors, which were deployed on the low tide terrace, sampling at 2Hz (manufacturers and calibration details in Foote, 1994). The instruments were arranged such that four arrays made up a square adjacent to a shore

normal array of four sensor stations (figure 3.2.5). Foote (1994) gives a full description of the wave climate and weather conditions during the observation period. For the purposes of this analysis the afternoon tide on the 23rd April 1991 was selected, the data being from observations made by instruments sited on a shore normal transect on instrument rigs A1 and A2 (instrument heights are detailed in table 3.4.i). This period of observation (32 17.04 minute runs, roughly 10 hours) saw the beach receiving a clean swell incident to the beach at a near to shore normal angle (see section 4.5.2), with offshore wave heights visually estimated at approximately 1.5m. The motivation behind this choice was again based on the likelihood of obtaining a relatively strong infragravity signal in the results. The combination of relatively energetic swell conditions with a light offshore breeze on this day also offered the best chance of conditions which were reasonably unaffected by local sea effects.

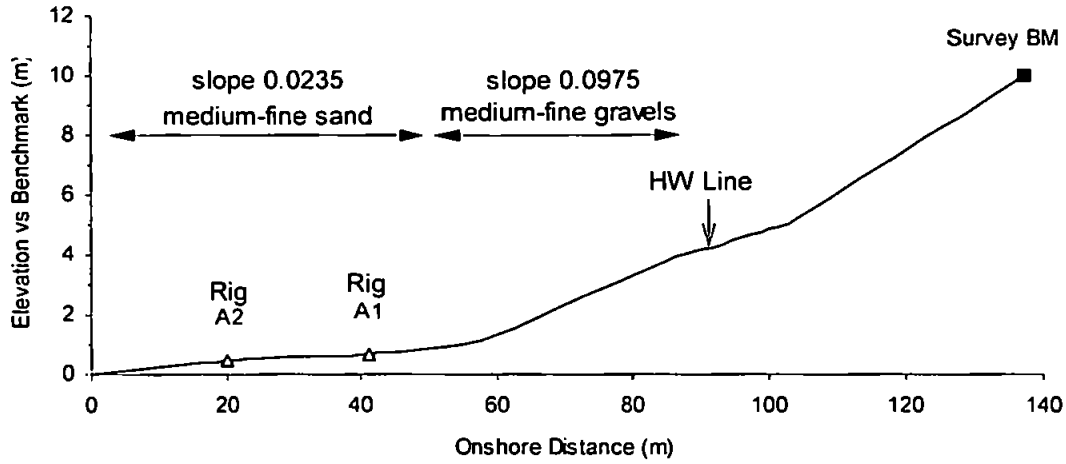

Figure 3.2.4 Spurn Head survey results, 23rd April 1991.

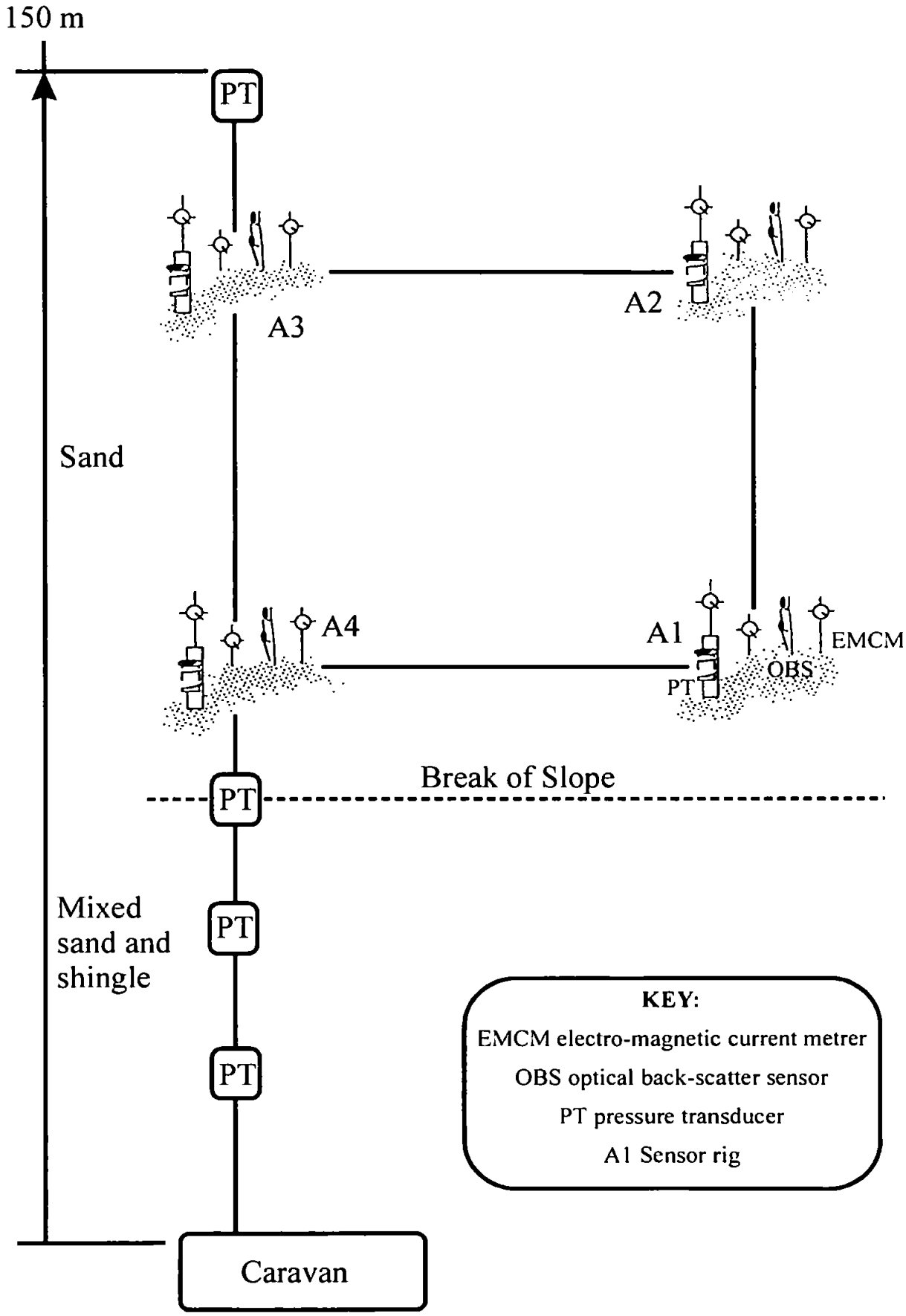

Figure 3.2.5 Schematic of the Spurn Head instrument array (from Foote, 1994).

3.3 The Perranporth field experiment

The Perranporth experiment was conducted in March 1998, when two University of Plymouth SLOT (Synchronous Logger for investigation Of sediment Transport) systems were deployed on the beach for one week. The experiment was conducted by Dr. J. Miles and Mr. P. Ganderton from the university, and had three aims:

1. To make a test deployment of the SLOT systems, prior to their use as part of the university's commitment to COAST3D.
2. To collect data which might supplement that taken from the B-BAND for this research.
3. To provide hydrodynamic measurements from a position offshore of a swash study also being conducted at Perranporth.

The deployment was successful in all three respects and yielded one tide of data appropriate to this project, when local storm sea waves with a breaking height of approximately 2m were incident on the beach. The next subsection describes the field site, whilst further details of the instrumentation and deployment are presented in subsections 3.3.2 and 3.3.3 respectively.

3.3.1 The field site

Perranporth is situated approximately 60 miles west of Plymouth on the Cornish north coast, and is a shallow sloped beach open to long range Atlantic swells (figure 3.3.1). The Cornish place name derives from its historical association with the landing of St. Piran, the patron saint of Cornish tinners, in the local bay or (in Cornish) 'porth'. The beach also has a historical association with the study of infragravity waves, as it was the site at which Tucker (1950) first observed 'surfbeat' (infragravity waves). More recently an ARGUS video system (Lippmann and Holman, 1990) has been installed at the beach as part of a long term video study involving collaboration between the University of Plymouth and Oregon State University.

The beach's west facing aspect makes it extremely susceptible to wave activity, be it from long range Atlantic swell, or from local seas generated by the prevailing local westerly and south-westerly winds. The resulting westerly/south-westerly prevailing direction of wave incidence means that generally energy will impinge on the beach at an angle of near to shore normal. High energy conditions, coupled with the relatively gentle bathymetry of the

beach (during the study the beach was near planar with $\tan\beta$=0.0165) leads to the development of wide surf zones during storm events. For the Cornish coastline the beach is also reasonably long (approximately 2 miles), with the only obstruction being a feature known as Chapel rock (a 50m diameter granite outcrop, approximately 5m high) positioned within one-quarter mile of the cliffs at the southern end of the beach. The beach consists mainly of medium-fine sands (D_{50}=0.25mm) and is macro-tidal, with mean tidal range approximately 5.5m, and a maximum range of over 7m. In terms of the beach Masselink and Short (1993) classification which was used in the previous section for the two B-BAND beaches, under moderate to stormy wave conditions (H_b=2m, with period 8 seconds) $\Omega \cong 6$, whilst $RTR \cong 3$, and thus Perranporth falls into the dissipative category. Similarly to Llangennith and Spurn Head, the Masselink and Short (1993) scheme predicts that at Perranporth morphology may be suppressed due to the high tidal range.

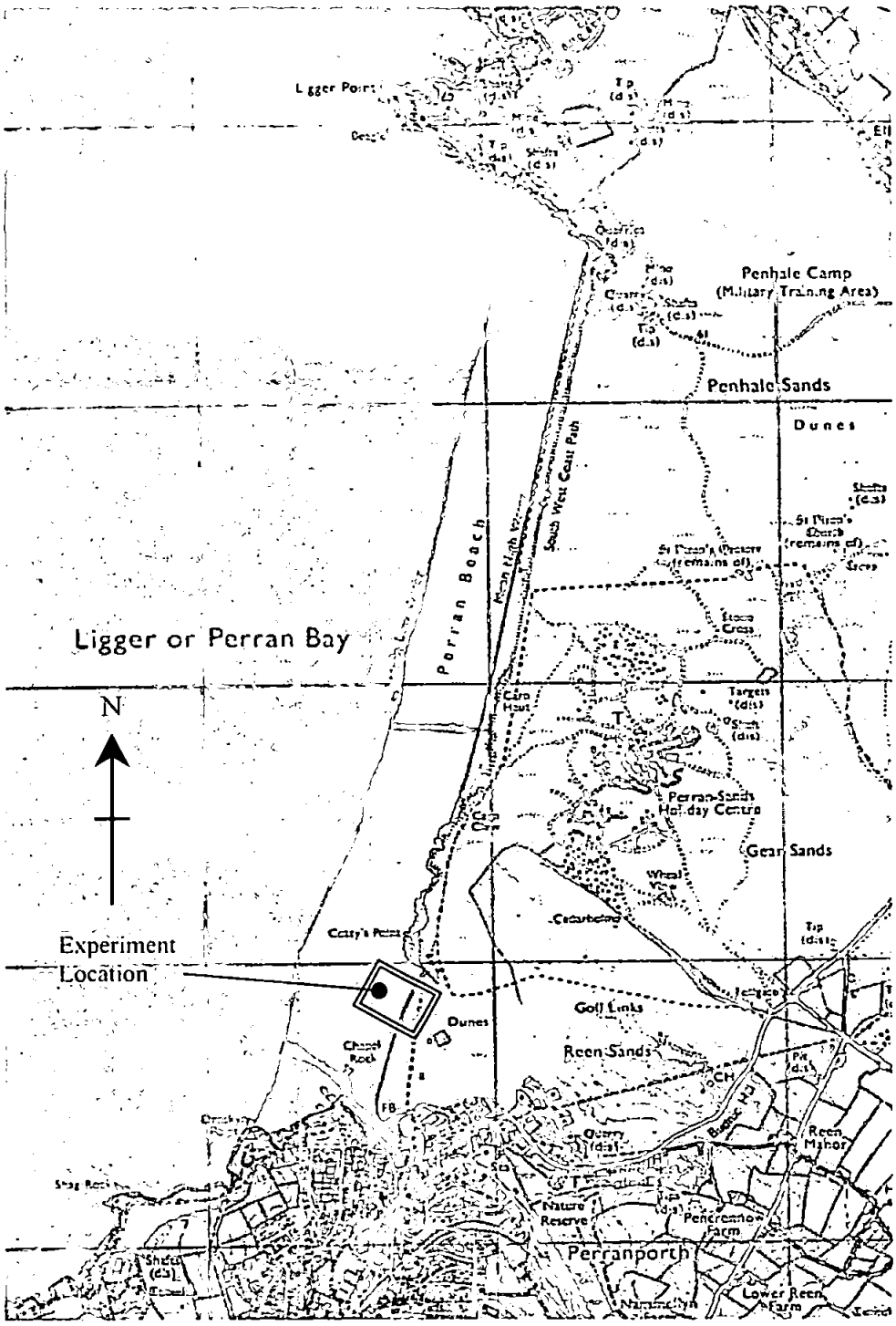

Figure 3.3.1 The Perranporth beach site.

3.3.2 The SLOT system

The SLOT (Synchronised Logger for investigation Of Transport of sediment) was designed by Valeport Ltd. (U.K.) to make in-situ measurements of wave, current and suspended sediment concentration data in the nearshore zone. The system satisfies several criteria for data gathering in the intertidal nearshore environment:

1. it is self contained, allowing for a flexible deployment without the constraints resulting from running power and data cables to a logging unit on the dry beach
2. the system can be relatively easily deployed in a short time by a small survey team (once again this is mainly due to the absence of long cables which would have to be dug into the beach)
3. the use of GPS (Global Positioning System) for a 'clock fix' allows multiple systems to be installed, which will all have the same time-stamp, and hence produce an integrated dataset.

Thus the SLOTs are essentially an evolution of the data gathering system used in the B-BAND, in which filtering and data storage are performed by a central unit which is deployed in-situ, a short distance from the instruments rather than at a shore station. With this type of system, the cross-shore placement of the instruments on a beach is constrained solely by tidal excursion, and hence more data may be gathered in terms of cross-shore coverage than with a cable to shore system.

The system is set up with power, data and communications channels all linked to a logging unit (schematic, figure 3.3.2). This central unit is housed in a 6" diameter, 18" deep stainless steel cylindrical casing, and contains a 1Mb memory CPU, plus analogue filters and electronics cards. Power comes from a separate rechargeable lead acid battery, which at 12V 14Ah is cited at giving enough system power for 17 hours continuous logging (Valeport manual, 1998). Four input data channels are used, of which logged data from instrumentation takes up two channels. Of these channels, one takes input from the two-axis current flow ElectroMagnetic Current Meter (EMCM), while the other receives analogue channel input from the Pressure Transducer (PT) and Optical Backscatter Sensor (OBS), which are linked via a junction box. The additional two inputs are used to initiate the logging procedures and take signals from the GPS and sea switch sensor. In the SLOT system the GPS receiver is used to establish a clock time; on power up the receiver searches for satellites and obtains a fix (from at least 3 satellites, a 2D fix) to establish time for the processor. This time is double checked and updated on the first activation of the sea

switch (logging commences). The sea switch works by obtaining a short between two electrodes when submerged in sea water; to assure submersion a delay time can be set whereby the short needs to be retained over the delay period in order for logging to start.

Communications are established between the logger and a PC using a DOS based software package via an RS232 link. This link is used both for data transfer and initialising the logger's sampling procedure. A screen capture from the interface program is shown in figure 3.3.3, in which the user commands are seen to be set using the function keys. Each function will not be detailed here, but particularly pertinent to the user are the commands relating to sample rate, data and memory, and sea switch delay. In the field the SLOT was set for continuous sampling mode, and the <SET SAMPLE RATE> command allowed for 1,2,4 or 8Hz sampling. The system was reset for the next tide by first using <ZERO MEMORY> to clear the logger, and then initialising the logging mode with the command <RUN SLOT>.

In order to conserve disc space on the logger data is saved in a binary format. This may be subsequently 'uploaded' and 'translated' by a PC via the SLOT software in order to obtain a text and numeric file. This file follows a spreadsheet format (figure 3.3.4) in which after a short header, data is listed in columns pertaining to date, time-stamp, pressure (dbar), optical backscatter voltage (mV), and current meter X and Y (ms^{-1}). Column length may be predetermined in the 'translate' routine.

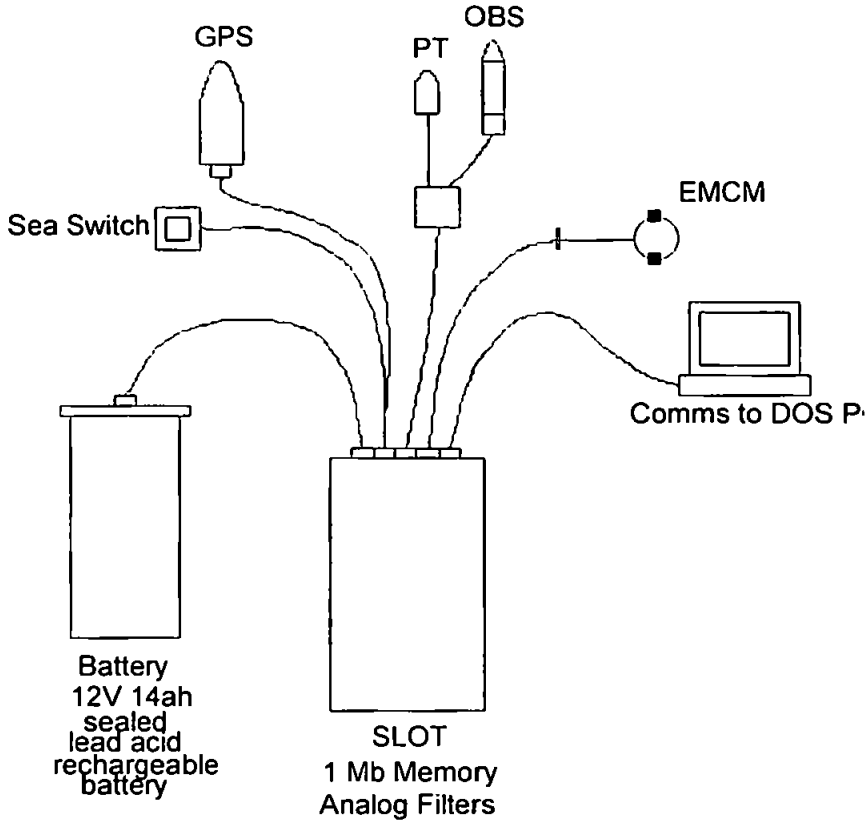

Figure 3.3.2 The SLOT system.

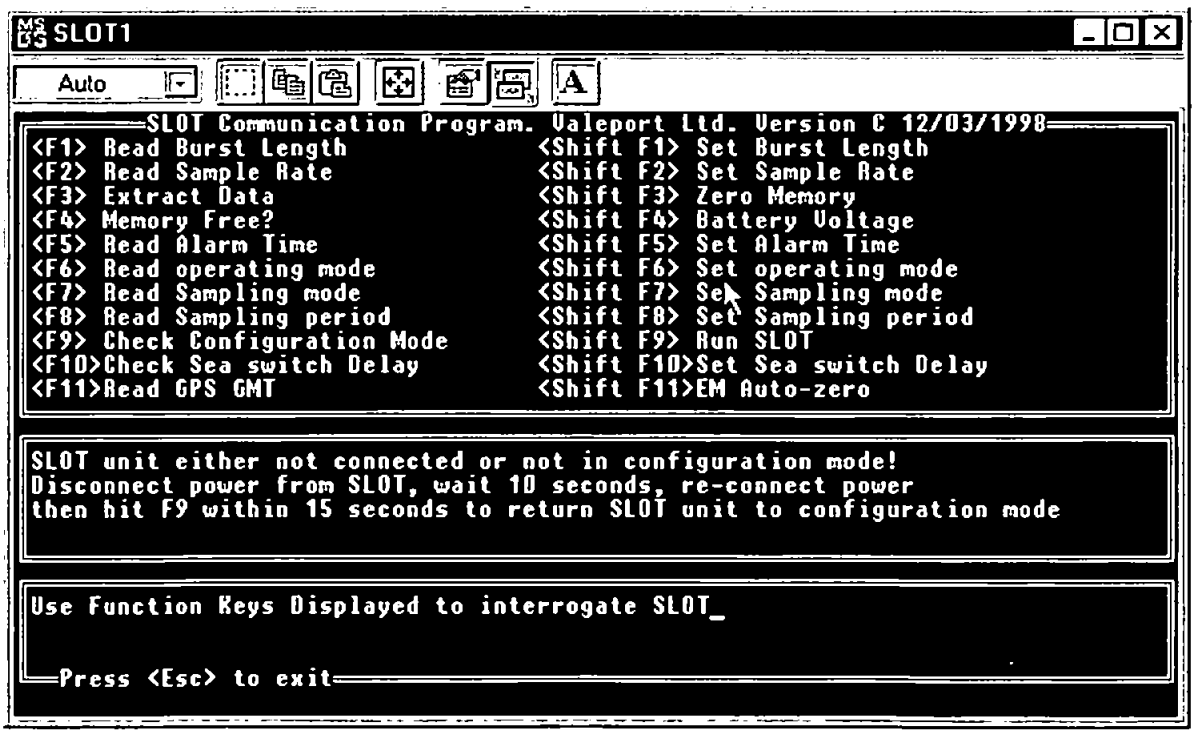

Figure 3.3.3 Screen capture of SLOT set-up programme.

	2a011100.000
File No.	0
Operating mode:	LOG
Sampling mode:	CONTINUOUS
Burst Length:	600
Sample Rate:	4
Sample Period:	15 Minutes
Latitude:	+52:36:06.9
Longitude:	+004:36:56.6
Height:	-15

Date	Time Stamp	Pressure (dBar)	OBS (Volts)	EMX (m/sec)	EMY (m/sec)
31/10/1998	46:32.0	9.041	-5.08	-0.354	-0.19
31/10/1998	46:32.3	9.041	4.481	-0.354	-0.19
31/10/1998	46:32.5	9.041	4.481	-0.354	-0.19
31/10/1998	46:32.8	9.041	-5.08	-0.354	-0.19
31/10/1998	46:33.0	9.041	3.841	-0.354	-0.19
31/10/1998	46:33.3	9.041	3.841	-0.354	-0.19
31/10/1998	46:33.5	9.041	4.481	-0.354	-0.19
31/10/1998	46:33.8	9.041	4.481	-0.354	-0.19
31/10/1998	46:34.0	9.041	3.841	-0.354	-0.19

Figure 3.3.4 Screen capture of spreadsheet format SLOT output file.

3.3.3 Instruments and calibration

Pressure Transducer

For the measurement of sea surface elevation the SLOT system employs a wave meter which operates by measuring variations of hydrostatic pressure under the sea surface. Such a method, whilst not providing a direct measurement, has proven reliable over past studies. It also has the advantages of producing a far less noisy signal than direct sea surface measuring devices such as wave staffs (e.g. Osborne 1990), whilst being a more rugged device which is easily adaptable to the surf zone.

At Perranporth a Druck 1830 series pressure transducer was used. The instrument uses a high stability micro-machined silicon sensing element which (along with the electronics) is isolated from the water by a titanium pressure module assembly (see figure 3.3.5). Pressure is exerted on the sensor via a set of radial inlet holes; the sensor head is further protected by a screw-on acetate nose cone. Overall instrument length is 96mm, and thus the instrument is compact and easily deployable colocated with an EMCM or OBS (e.g. plate 3.3.a). Druck cites an operating temperature range of -20°C to 60°C, and an ability to withstand burst pressures of 4 times the operating range. Accuracy, combining non-linearity and hysteresis, is quoted at ±0.1%, although temperature effects may also affect accuracy to ±0.5%.

For use with the SLOT system the Druck 1830 PT uses a range of 0-2 bar. Output from the sensor is a voltage, which is then logged (via conversion through the SLOT internal calibration file) in decibar with a resolution of 1mbar. Since 1dbar corresponds to 1m of sea water, fluctuations in sea surface elevation are easily derived from the logged time-series. Use of this type of instrument does mean that incident banded wave height values in the surf zone may be underestimated due to pressure variations caused by wave breaking. Foote (1994) demonstrated that the error from attenuation would be less than 6%. Actual sea surface elevations simply require the removal of an offset value. These were derived from runs prior to full immersion of the sensor, where the offset value is the value taken by the instrument when dry, which was added to a correction value for instrument height above the bed level.

Electromagnetic Current Meter

Cross-shore and longshore currents were measured using a Valeport spherical electromagnetic current meter (EMCM). This type of instrument employs Faraday's Law of electromagnetic induction. By setting up a magnetic field in the water, the instrument creates a potential gradient perpendicular to the direction of flow. Changes in potential on a horizontal plane are detected in the (perpendicular) X and Y directions by two sets of two electrodes housed in the EMCM head, such that when water flows past the instrument, the electromagnetic force generated across the electrode pairs is directly proportional to velocity. Thus with the instrument correctly aligned with respect to the beach, values can be obtained for both the longshore and cross-shore current.

As with all the instruments, the EMCM is designed to be a small and rugged tool for use in the energetic nearshore environment (plate 3.3.a). In an early laboratory study by Aubrey and Trowbridge (1985) the accuracy of this type of instrument within the surf zone was called into question because of effects on the magnetic field which may have been caused by turbulence. However subsequent studies by Doering and Bowen (1988), and Guza (1988), examining colocated EMCM and PT signals, plus numerous documented field deployments have shown this piece of kit to be a robust and reliable tool for nearshore studies. Valeport cite instrument accuracy at ±5%, and this type of instrument is generally accepted to be accurate in measurement of mean flows to $\pm 0.02\text{-}0.03 ms^{-1}$.

The Valeport spherical current meter employed with these SLOT systems has a 5.5cm diameter head. However, the electromagnetic field set up by the current meter extends to a spherical volume of diameter three times the head diameter, and thus to ensure correct operation of the instrument it is necessary to keep other instruments outside of this region (Valeport manual, 1998). The SLOTs convert output voltages via a calibration file to give current values in ms^{-1} over the range $\pm 3.5 ms^{-1}$, with a resolution of $1 mms^{-1}$. Prior to release to University of Plymouth, the EMCMs were calibrated in the Valeport tow tank, however a further 'offset calibration' was made in the field using a bucket of local sea water to yield a zero-current offset value.

Optical Backscatter Sensor

For measurement of suspended particulate matter the SLOTs use a D&A Optical Backscatter Sensor (OBS) to give a point measurement of suspended sediment concentration. This type of instrument was originally developed by Downing *et al.* (1981) and has since been used in numerous studies including, in addition to the B-BAND, work by Hanes and Huntley (1986) and Sternberg *et al.* (1990). The principal of operation of the OBS is based on the detection of the reflected return of infra-red radiation from the suspended particulates (figure 3.3.6), the same principle used by the nephelometer. However, the OBS differs from a standard nephelometer as it detects only radiation scattered at angles greater than 140°. This allows the OBS to be designed as a smaller more rugged instrument for use in highly energetic nearshore zones. One drawback with using this type of sensor is that only point measurements can be made by a single OBS.

The sensor itself consists of a high intensity infrared emitting diode, a detector made up of four photodiodes, and a linear, solid state temperature transducer. These components are housed in a glass-filled polycarbonate head using optical grade epoxy. The entire unit including the connector housing is 115mm long with a 31mm diameter. Backscatter strength will relate to the mixture of sediments at an individual site, although there is no suggestion of spurious measurements being made due the presence of bubbles in the water column (Downing, *pers comm.*, Miles, 1997). Similarly instrument accuracy also relates to the sediment type being measured, with D&A quoting a value of ±3.5% for sand.

The SLOT records OBS voltages, which are post calibrated to yield suspended sediment concentrations. Due to the differing nature of sediments at different sites, OBS response must be calibrated using a homogeneous suspension of sediment taken from the experiment site (Downing *et al.* 1981), and hence a sand sample was taken from Perranporth. In the laboratory, increasing quantities of this sand were added to a known volume of water, stirred into suspension and logged by the OBS. At the same time pipette samples of the water column were taken. These were then filtered, dried and subsequently weighed to yield concentration values against which the recorded OBS voltages could be compared. The results of the calibration, which was carried out by Dr. J. Miles and Mr. P. Ganderton are given in table 3.3.i, whilst the calibration curve is shown in figure 3.3.7.

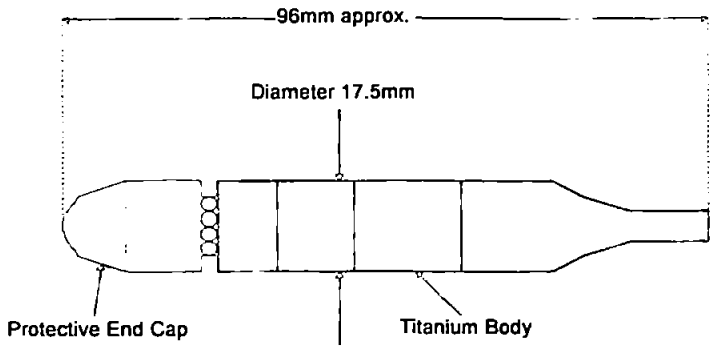

Figure 3.3.5 Druck 1830 pressure transducer head.

Plate 3.3.a Example deployment of colocated EMCM and PT.

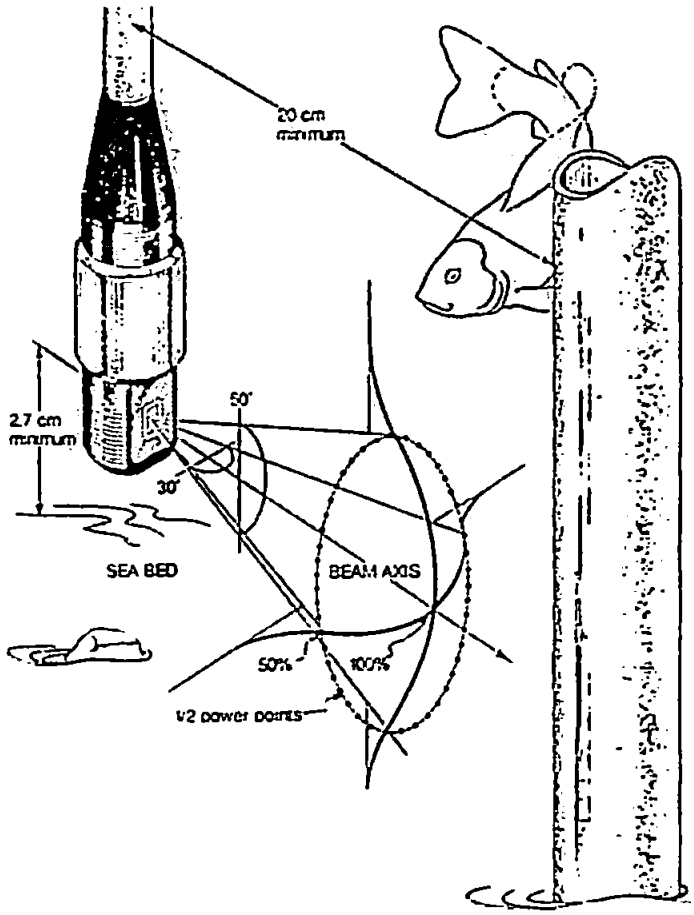

Figure 3.3.6 Optical Backscatter Sensor system (from D&A Instruments Manual, 1988).

Filter Paper	Concentration (kgm^{-3})	Slot 1 Voltage
1	0.80	-0.13
2	1.76	-0.23
3	3.32	-0.33
4	3.55	-0.45
5	5.36	-0.53
6	6.98	-0.67
7	9.04	-0.79
8	12.38	-1.04
9	16.76	-1.29
10	27.40	-1.78
11	22.90	-2.08

Table 3.3.i Calibration values for SLOT 1 OBS.

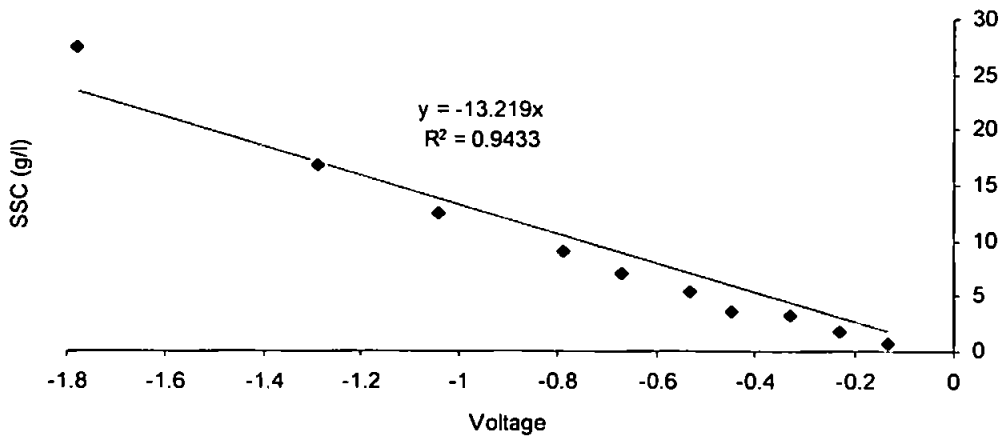

Figure 3.3.7 SLOT 1 OBS calibration curve.

3.3.4 The Perranporth field Deployment

The instruments were deployed in relation to a shore normal transect (schematic, figure 3.3.8). Along the transect, just below the high water mark, various electronics were sited for a contemporary swash study whilst one SLOT was positioned 85m further offshore. The second SLOT was positioned 8.8m further south. The instrumentation to be tested consisted of

SLOT 1: EMCM, PT, OBS

SLOT 2: EMCM, OBS

In the field the instruments, battery and logging units were secured on poles driven into the sand, and were partially buried (figure 3.3.9, and plate 3.3.b). The GPS and sea switch units were attached to the logger/battery pole. In order not to compromise EMCM performance, the OBS and PT were positioned approximately three EMCM head diameters away (0.165m) as suggested by the manufacturers instructions. Prior to field deployment the logger casing was fitted with a sacrificial zinc anode to reduce corrosion on the main casing.

In total three tides were logged by the SLOTs during a small storm event (wave height offshore approximately 2m). After each tide instrument heights (heights are given in table 3.4.i) were noted, EMCM offsets taken, and the logged data downloaded to a laptop PC before the system was re-initialised for the next series of runs. During the experiment a series of surveys along the transect were made using standard levelling techniques. Results of the survey for 26/3/98, with heights given relative to a temporary benchmark set up at the surf club building, are given in figure 3.3.10, which shows the beach having a relatively plane profile with slope gradient $\tan\beta=0.0165$.

The two SLOTs successfully logged data on a total of seven channels (2xEM-X, 2xEM-Y, 2xPT, 1xOBS) for three tides and totalling 50 17.04 minute runs (i.e. 14.15 hours logged data). For the purposes of this study the results sections (Chapters 5 and 6) have used the data from the 26/3/98pm tide (18 runs), gathered by SLOT 1 (and will hence have EMCM, PT and OBS data as gathered in the aforementioned B-BAND experiments). During this tide significant wave heights were visually observed as being approximately 2m, with breaker type generally being spilling.

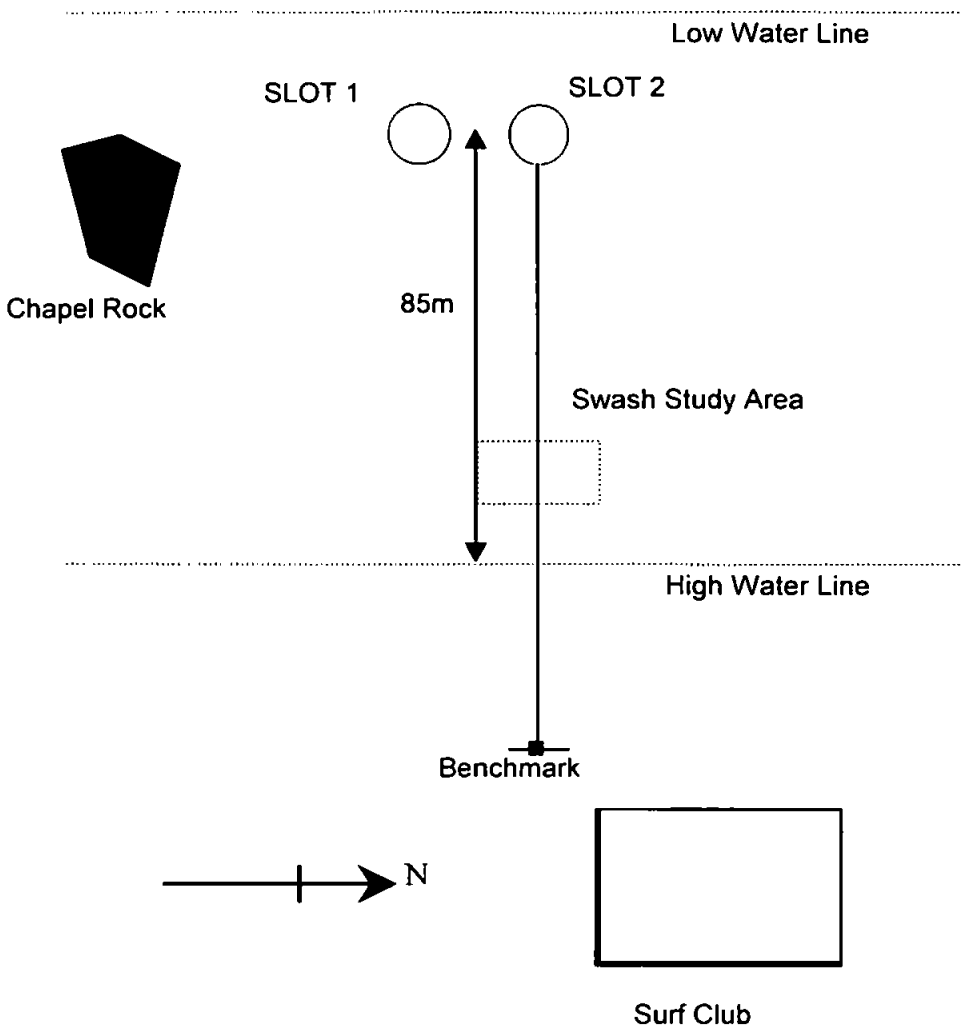

Figure 3.3.8 SLOT deployment schematic.

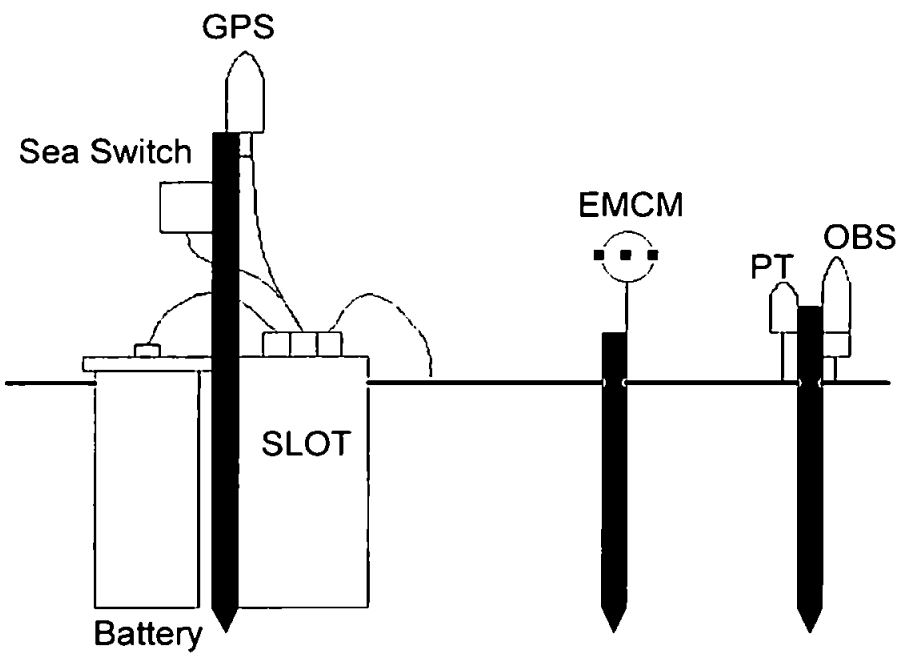

Figure 3.3.9 SLOT components deployment.

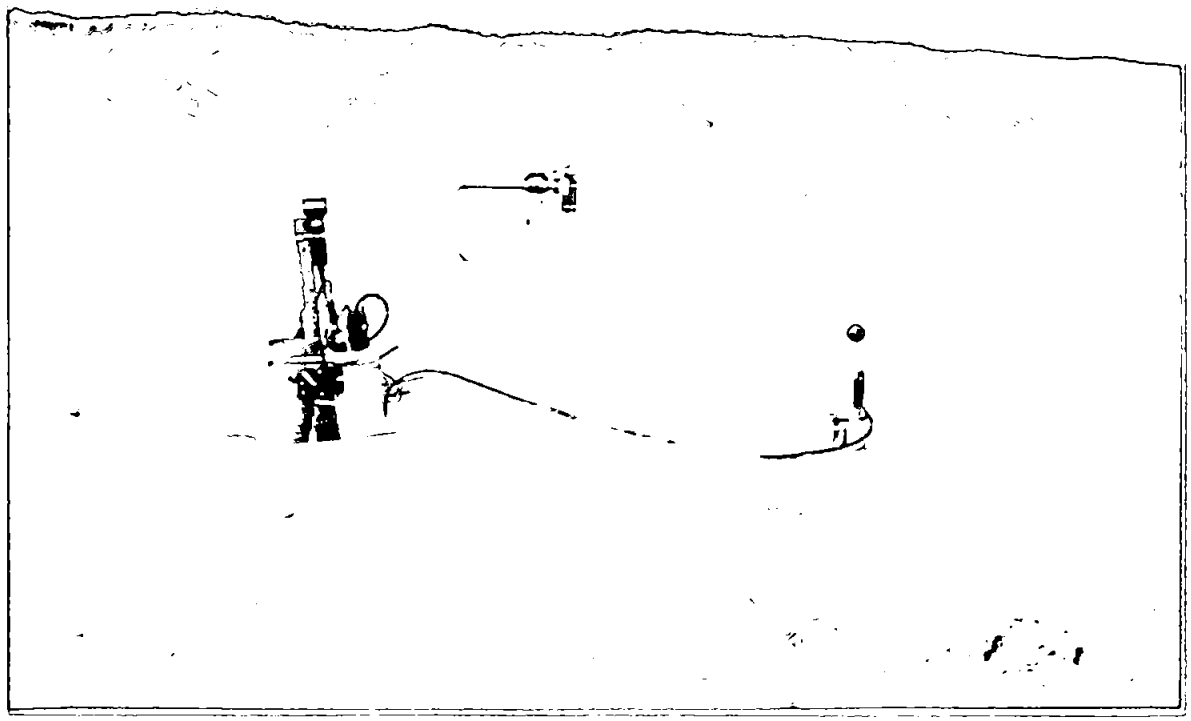

Plate 3.3.b Example deployment of SLOT system (from Egmond-aan-Zee experiment, October 1998).

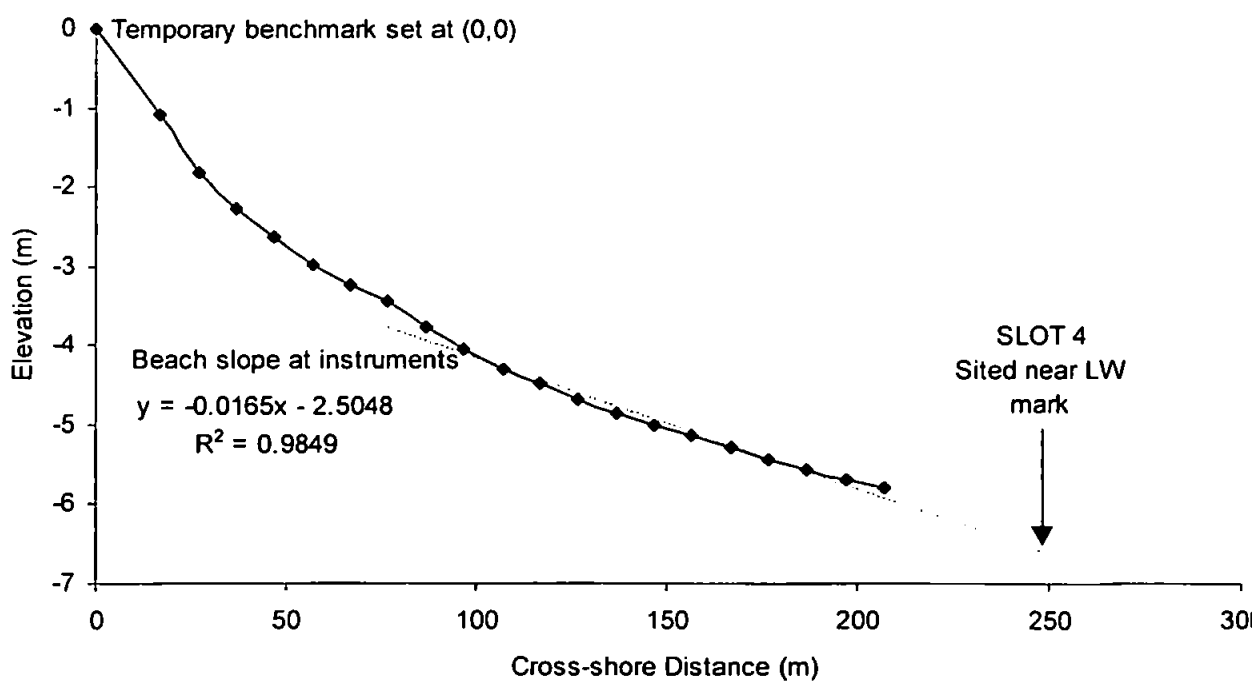

Figure 3.3.10 Perranporth level survey, 26/3/1998.

3.4 Summary: Experimental work

This chapter has briefly described three field experiments from which the data to be analysed were taken. The aim in selecting data was to compile a dataset which described a range of energetic and topographic conditions, whilst being likely to contain significant low frequency variations in hydrodynamic forcing. With this in mind four tides of data from the three experiments will be considered in the subsequent chapters:

- *Llangennith, Storm Day and Storm Night*; high energy swell dominated storm waves (wave height 3m) incident on a dissipative beach.
- *Perranporth*; wind sea wave (wave height 2m) dominated storm event on a dissipative beach.
- *Spurn Head*; medium energy (wave height 1.5m) swell dominated waves incident on an intermediate (reflective at high water) beach.

The Llangennith and Spurn Head tides used in this study form part of the B-BAND dataset. Although it was essentially a test of new equipment, the Perranporth experiment produced new data with this research in mind. The type of instrumentation used was common to all three experiments, and was deployed in a manner generally employed in beach experiments. A summary of the beach sites, offshore wave heights and instrument heights are given in figure 3.4.1 and table 3.4.i.

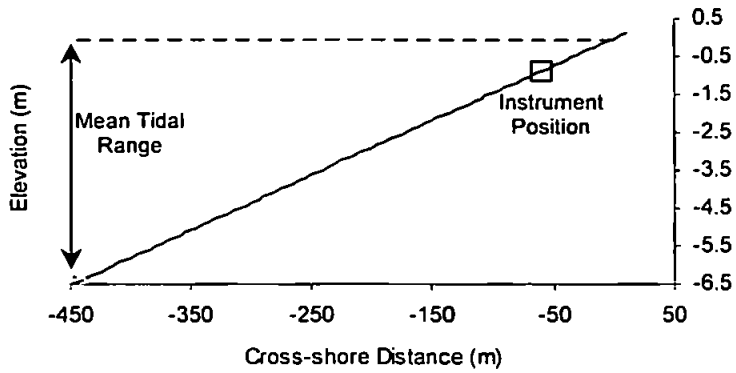

Llangennith:
Offshore H_{sig}=2-3m
tanβ=0.0145*
D_{50}=0.23mm*

*value at instruments

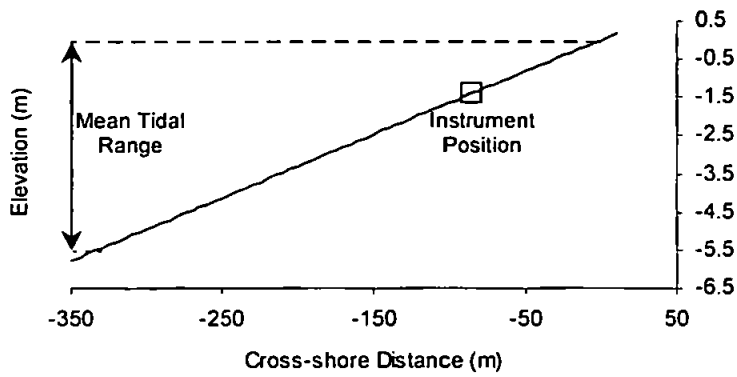

Perranporth:
Offshore H_{sig}=2m
tanβ=0.0165*
D_{50}=0.25mm*

*value at instruments

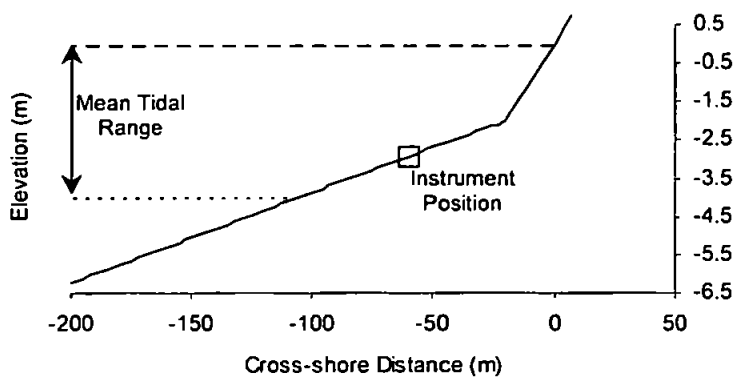

Spurn Head:
Offshore H_{sig}=1.5m
tanβ=0.0235*
D_{50}=0.35mm*

*value at instruments

Figure 3.4.1 Schematic summary of the beach sites at Llangennith, Perranporth and Spurn Head.

Site	Tide/Sensors*	Offshore H_{sig} (m)	Observation Period	Instrument Heights (m)		
				PT	EMCM	OBS
Llangennith	Storm Day	3	2 hours	0.08	0.12	0.04
	Storm Night	2.5	2.5 hours	0.08	0.12	0.04
Spurn Head	Bottom	1.5	9 hours	0.16	0.10	0.10
	Middle	1.5	9 hours	N/A	0.25	0.17
Perranporth		2	5 hours	0.08	0.12	0.04

* Unless otherwise stated the following work will use results from the bottom sensors on the Spurn Head Rig A2 array.

Table 3.4.i Summary of instrument deployments at Llangennith, Spurn Head and Perranporth.

Chapter 4: Data Processing

4.1 Data details

The data examined in chapters 5 and 6 has been taken from three beach sites, two (Llangennith and Spurn Head) from the B-BAND experiment, and the third from the Perranporth experiment as described in chapter 3. The Llangennith data is further split into observation periods over consecutive tides during a single storm event denoted as Storm Day and Storm Night. A summary of the data details is given in table 4.1.i.

Time-series length

The time-series length used for each of the datasets was determined for each case according to several criteria. For example, a nominal sampling period (run) of 17.04 minutes was employed previously with the Llangennith dataset (Russell, 1990, Davidson, 1991). Often a longer record is employed, for example when examining low frequency hydrodynamics, in order to obtain a sufficient resolution at the low frequencies in spectral analyses. However, for the type of macrotidal environment featured in this analysis, the use of a long record must be traded off against changes in conditions that might be induced by tidal variations in water depth at the sensors. This consideration determined the time-series length chosen by Russell (1990) and Davidson (1991). From these results, the dominant low frequency processes were seen to be sufficiently energetic to afford a further shortening of the time-series length in this work without losing the main features of the spectral estimates, allowing for an increase in the number of runs making up the dataset (and thus increasing the cross-shore resolution of run data-points, see section 4.5.3). In this analysis, both the Llangennith tides are made up of runs of 2048 sampling points, which with a sampling rate of 3Hz give a time-series length of 11.23 minutes. Overall the Llangennith dataset comprises 12 runs from Storm Day and 14 from Storm Night.

The Spurn Head time-series are retained in the form used by Foote (1994). For this dataset the sampling rate used was 2Hz and thus the minimum suitable time-series length (2048 points) was set at 17.04 minutes in order to obtain a sufficient number of degrees of freedom for spectral estimates. The period over which observations were taken at Spurn Head on a given tide was longer than at Llangennith, and the single tide used in this work is made up of a suite of 32 runs. The Perranporth time-series are also 17.04 minutes long,

but since for this experiment the sampling rate was set at 4Hz, consist of 4096 points. The tide of data used here consists of 18 runs.

Calibration and data integrity

Previous users of the B-BAND data had stored the files used in a fully calibrated form and for details of the calibrations and the data stored the reader is referred to the relevant literature (Russell, 1990, Davidson, 1991, Foote, 1994). Calibration details and methods for the Perranporth data are given in chapter 3.

Occasional spurious points existed in the raw data, and these were identified through visual inspection of the run time-series. For all the datasets, where possible, individual spurious points within the time-series have been adjusted by assigning a value generated from an interpolation between the surrounding values. Since the sample rate for all the data is much higher than the frequency of the processes being discussed in this work, these adjustments should have less effect on the results than leaving spurious values in the time-series. However, where some time-series have had sectors of corrupted data (as might occur for example, as a result of fouling of the instruments, or electrical noise affecting data logging), which could not be corrected for in the processing stage, the runs have been eliminated from the analysis. These 'bad runs', which were not used in the analysis outlined in this chapter are given in tables 4.1.i-iv.

Use of the Matlab® package

Virtually all of the data analysis and modelling described in this work was carried out using the PC based Matlab® software package. Matlab® is specifically designed to deal with mathematical functions and manipulation of matrices, and has the added facility of a Signal Processing Toolbox designed for time-series analysis. Thus much of the following analysis was dealt with simply by applying a Matlab® function to a multiple set of time-series which were stored in matrix form. Other more complex analyses (e.g. bispectral analysis, section 4.2.1c, PCA analysis, section 4.4.3, MLE analysis, section 4.5.2) employed established Matlab® routines written by researchers at Plymouth University.

Tide Name	Run length (minutes)	Sampling Frequency	No. of runs in tide	Data Channel*	'Bad Run' Numbers
Storm Day	11.23	3Hz	12	η	
				u, v	
				c	12
Storm Night	11.23	3Hz	14	η	
				u, v	
				c	6,14
Spurn Head (Bottom sensors)	17.04	2Hz	32	η	5
				u, v	5,30
				c	5,23
Perranporth	17.04	4Hz	18	η	14
				u, v	14
				c	14

* Data channels describe the following measurements:

η, sea surface elevation derived from pressure transducer (PT) measurements

u, cross-shore velocity derived from electromagnetic current meter (EMCM) measurements

v, longshore velocity derived from electromagnetic current meter (EMCM) measurements

c, suspended sediment concentration derived from optical backscatter sensor (OBS).

Table 4.1.i Thesis dataset run details, 'Bad Runs' are those which contain sectors of spurious data and have not been included in this analysis.

4.2 Time-series analysis

This and subsequent sections in this chapter deal with the analysis of the time-series extracted from the PT, EMCM and OBS data. The segments of data examined are assumed to follow a statistical definition of a stationary stochastic time-series. Each time-series analysed (i.e. η, u, v, c as defined in table 4.1.i) will therefore represent a process as a function of an independent variable (time, t). The time-series should exhibit no general trend (the process is 'stationary') and future values within the time-series should only be able to be partly determined from past values (the process is 'stochastic', Chatfield, 1989). Since the independent variable used is time, the analysis performed on the data was conducted in either the time or frequency domain.

The following sections will give a brief account of the theory behind each of the processing techniques involved before noting the practical details of the processing performed on the Llangennith, Spurn Head and Perranporth datasets.

4.2.1 Frequency domain analysis

Frequency domain spectral analysis techniques, applied to time-series such as wave data, are based on Fourier analysis. The method assumes that an oscillatory time-series $x(t)$ may be approximated by a finite sum of sinusoids of discrete frequency. Mathematically this is expressed as

$$x(t) = \frac{a_0}{2} + \sum_{r=1}^{k} (a_r \cos rt + b_r \sin rt), \tag{4.1}$$

where

$$a_0 = \frac{1}{\pi} \int_{-\pi}^{\pi} x(t) \mathrm{d}t \tag{4.2}$$

$$a_r = \frac{1}{\pi} \int_{-\pi}^{\pi} x(t) \cos rt \mathrm{d}t \qquad r = 1,2,\ldots \tag{4.3}$$

$$b_r = \frac{1}{\pi} \int_{-\pi}^{\pi} x(t) \sin rt \mathrm{d}t \qquad r = 1,2,\ldots \tag{4.4}$$

The contribution of each frequency to the overall range of the function is defined by the coefficients a_r and b_r. Hence a Fourier analysis of a time-series serves to partition the variability of the series into contributions from discrete frequencies (harmonics).

4.2.1a The autospectrum

The autospectrum is employed for analysis of the contribution of component frequencies to a single time-series. The type of averaged autospectrum used in this work is derived from the periodogram function $I(\omega_p)$, where ω_p represents the (discrete) set of component frequencies making up the periodogram. The periodogram is the Fourier transform of the autocovariance function (γ_k) of the time series $x(t)$, and defines the degree to which two observations from the series, sampled at a lag of k vary. Mathematically

$$I(\omega_p) = \sum_{k=(-N-1)}^{N-1} \gamma_k \, e^{-i\omega_p k / \pi} \tag{4.5}$$

where

$$\gamma_k = \sum_{t=1}^{N-k} (x_t - \bar{x})(x_{t+k} - \bar{x})/N \,, \tag{4.6}$$

and N is time-series length. The periodogram coefficients are of order $x^2(t)$, and considering the case of a time-series of wave driven sea surface elevation, would be analogous to a measure of energy distribution over the periodogram frequencies.

The periodogram does not provide a good estimate for a continuous energy spectrum of frequencies. However, it may provide the basis for a good spectral estimate if appropriately smoothed. Welch (1967) proposed a scheme whereby a spectral estimate was created by time-averaging short, modified periodograms taken from segments of the original time-series. The modification is made to the time-series segments by applying a weighting function, or 'window' (e.g. Parzen,Tukey-Hanning, c.f. Chatfield, 1989), to smooth the data. Welch (1967)'s spectral estimate may be expressed as

$$\hat{P}(f_n) = \frac{1}{K} \sum_{k=1}^{K} I_k(f_n) \,, \tag{4.7}$$

where K is the number of segments (of length l) of the original time-series (length N) used to generate the spectral length. The values for $\hat{P}(f_n)$ are defined over a range of $0 \leq f_n \leq 1/2\Delta t$, where Δt is the sampling interval for the time-series. The maximum value taken by $f_{N/2}=1/2\Delta t$ is known as the Nyquist frequency. The level of resolution of the frequency domain (bandwidth) is defined by the Nyquist frequency and segment length l, which sets the number of discrete frequency bins being used in the resulting spectrum.

The spectrum produced using the Welch method is a statistical estimate. Therefore it is necessary to apply a level of confidence to the peaks and troughs of spectra. Estimates of

confidence may be derived from percentage points of the χ^2 distribution (Jenkins and Watts, 1968). Jenkins and Watts (1968) pointed out that such confidence intervals will be constant over a logarithmic scale, and hence used such a scale for the spectral density axis. The multipliers for the confidence interval are calculated based on degrees of freedom derived from the number of segments making up the spectral estimate and the window function used. In this analysis, 50% overlapping segments and a Hanning window were used to generate time-series autospectra. Nuttall (1971) computed the degrees of freedom for such an estimate and found that

$$\text{EDF} = 3.82\frac{N}{l} - 3.24, \tag{4.8}$$

which when expressed in terms of K (for a 50% overlap $=2N/l-1$) is

$$\text{EDF} = 1.91K - 1.333. \tag{4.9}$$

From these equations it can be seen that for a time-series of fixed length any increase in the value of the EDF will arise from lowering the value of l, which will be to the detriment of bandwidth, i.e. bandwidth and degrees of freedom are inversely proportional.

A computationally efficient technique such as the Fast Fourier Transform (Press *et al.*, 1968) is required to perform the Fourier transforms necessary in these analyses. However this method does require that segment length l is an integer power of two in order to perform its computations. The MATLAB *spectrum* routine employs the FFT transform algorithm and Welch method of power spectrum estimation to generate both autospectra and cross-spectra (see next section). Table 4.2.i summarises the details regarding spectral resolution and confidence levels for each of the datasets processed.

4.2.1b The cross-spectrum

Levels of covariance over the frequency domain between two time-series, may also be analysed in a method analogous to that presented in the previous section. Jenkins and Watts (1968) define the smoothed cross-spectral estimator, based on the covariance function $\gamma_{12}(t)$ between the two series, as

$$\overline{C}_{12} = \int_{-T}^{T} \gamma_{12}(t) e^{-i2\pi f t} dt \tag{4.10}$$

$$= \overline{L}_{12} - i\overline{Q}_{12}. \tag{4.11}$$

Which yields the smoothed cross-spectrum

$$\hat{P}_{12}(f_n) = \mathrm{E}[\overline{C}_{12}(f_n)]. \tag{4.12}$$

$\overline{L}_{12}$ defines the co-spectral part of the cross-spectral estimate and $\overline{Q}_{12}$ the quadrature part. Hence,

$$\hat{\Lambda}_{12}(f_n) = \mathrm{E}[\overline{L}_{12}(f_n)] \tag{4.13}$$

is defined as the co-spectrum between the two time-series, i.e. the measure of variance between the parts of the two time-series that are operating at a lag equal to an integer multiple of π. Conversely,

$$\hat{\Pi}_{12}(f_n) = \mathrm{E}[\overline{Q}_{12}(f_n)] \tag{4.14}$$

defines the quadrature spectrum, and quantifies variance between the time-series at a phase lag of $n\pi/2$ (n an odd integer). The complex nature of $\hat{P}_{12}(f_n)$ means that it cannot be simply plotted against the frequency domain, and hence the cross-spectrum is illustrated by a number of differing plots derived from the co- and quadrature spectra.

For example the coherence function

$$\hat{K}_{12}(f_n) = \frac{\hat{\Lambda}_{12}^2(f_n) - \hat{\Pi}_{12}^2(f_n)}{\hat{P}_{11}(f_n)\hat{P}_{22}(f_n)} \tag{4.15}$$

gives a measure of linearity between the two time-series (over a scale of 0 to 1), i.e. how the two time-series vary together. The degree of lag between linearly related frequencies observed in the coherence spectrum may be derived from the phase spectrum defined as

$$\hat{F}_{12}(f_n) = \arctan\left(-\frac{\hat{\Pi}_{12}^2(f_n)}{\hat{\Lambda}_{12}^2(f_n)}\right). \tag{4.16}$$

In the following analysis, cross-spectral estimates will be used to examine the relationships between simultaneous measurements of wave elevation, current and suspended sediment

concentration. For example, in the case of a wave field consisting of purely progressive waves, a cross-spectral analysis of sea surface elevation and velocity would expect to show high levels of coherence at all frequencies in the spectrum, and a corresponding zero phase. The distribution of energy in the sea surface elevation and velocity autospectra would be expected to show the same peaks and troughs in both, and this would also be mirrored in the cross-spectrum.

Producing confidence limits for coherence and phase is a far more complicated task than for the autospectra examples given previously, since at present it is not possible to derive a probability distribution appropriate to these spectra. In general though, in interpreting these spectra we are only interested in significant deviations of coherence from zero. This allows a simple calculation to be made for a biased upper limit for zero coherence (Goodman, 1957)

$$c_{bias}^2 = 1 - \alpha^{2/EDF-2} \tag{4.17}$$

where α defines the confidence limit value (e.g. for 95% confidence α=0.05), and from which bias may be removed since

$$Bias = \frac{2}{EDF}(1 - \hat{K}_{12}^2(f_n)), \tag{4.18}$$

yields an unbiased estimator for the upper limit of zero coherence according to

$$c_{unbiased}^2 = c_{bias}^2 - \frac{2}{EDF}(1 - c_{bias}^2). \tag{4.19}$$

Thus, for example, where EDF=12 (e.g. the B-BAND data), then the biased 95% confidence limit for zero coherence will be 0.45, and the unbiased confidence limit 0.36.

Jenkins and Watts (1968) also derive confidence limits for the phase spectrum by finding a transformation whereby the new function is approximately Normal. In this case the function is $\tan \hat{F}_{12}$, which leads to a derivation of confidence limits derived from both phase and coherence values. An illustration of the confidence banding produced by this method is given in figure 4.2.1, for values of coherence ($\hat{K}_{12}^2$) between 0.1 and 0.9.

Data processed using the cross-spectrum used the same segment lengths as those for the autospectra and therefore confidence estimates were made using the degrees of freedom values given in table 4.2.i.

Dataset	Points per run	Sampling frequency	Segment length	Resolution	EDF	Confidence 95%	Multipliers 90%
Llangennith	2048	3Hz	512	0.00586Hz	12	2.71 0.51	2.29 0.57
Spurn Head	2048	2Hz	512	0.00391Hz	12	2.71 0.51	2.29 0.57
Perranporth	4096	4Hz	512	0.00782Hz	27	1.83 0.63	1.67 0.67

Table 4.2.i Autospectra processing details.

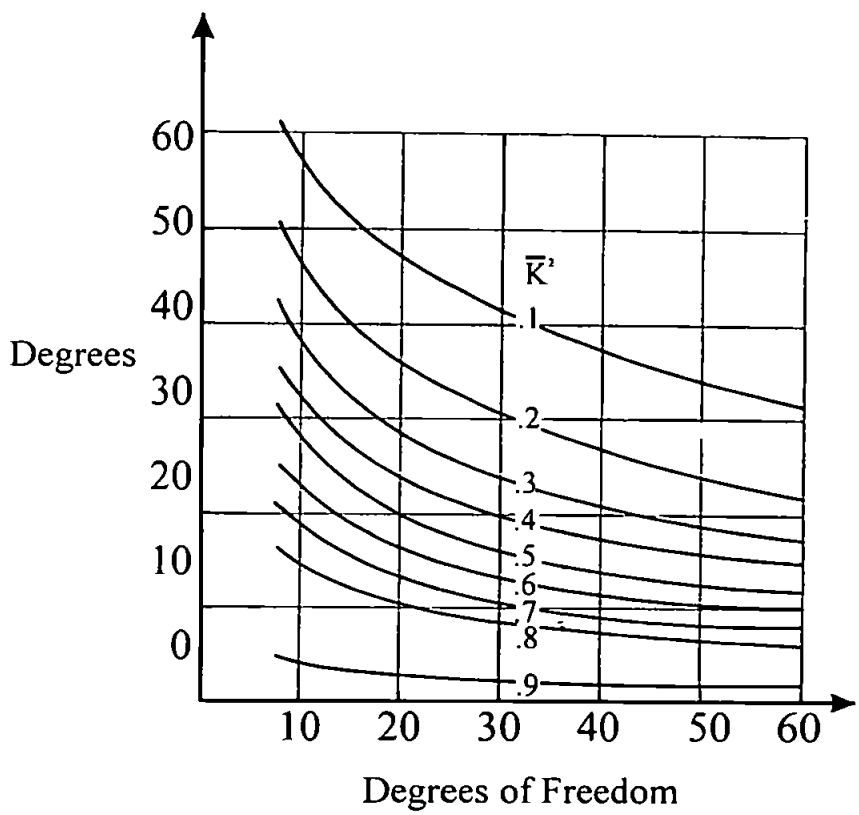

Figure 4.2.1 95% Confidence limits for cross-spectral phase estimates (from Jenkins and Watts 1968), for values of coherence ($\overline{K}^2_{12}$) between 0.1 and 0.9.

4.2.1c The bispectrum

Where the power spectra discussed previously are based upon the second moment of a time-series such as $x(t)$, the bispectrum is formally defined as the Fourier transform of the third order correlation function of a time-series (Hasselmann *et al.*, 1963). Mathematically the auto-bispectrum is defined by

$$B(f_j, f_k) = \frac{1}{(2\pi)^2} \int_{-\infty}^{\infty}\int_{-\infty}^{\infty} S(\tau_j, \tau_k) e^{-i(f_j\tau_j + f_k\tau_k)} d\tau_j d\tau_k \tag{4.20}$$

$$S(\tau_j \tau_k) = E\left[x(t)x(t+\tau_j)x(t+\tau_k)\right] \tag{4.21}$$

Where τ is a lag, f is the frequency and $E[]$ is the expected value, or average, operator. The complex bispectral estimate $B(f_j,f_k)$ may also be expressed in terms of Fourier coefficients (Kim and Powers, 1979) as

$$B(f_j, f_k) = \mathrm{E}\left[A(f_j)A(f_k)A^*(f_{j+k})\right], \tag{4.22}$$

where $A(f)$ denotes a complex Fourier coefficient and * a complex conjugate, for a 'triad' of frequencies where $f_j+f_k=f_{j+k}$.

Examining this last equation further, it is notable that the bispectrum takes on a zero value if the average triple product of the Fourier coefficients is zero. Elgar and Guza (1985) pointed out that this would be the case if the Fourier modes were independent of each other, i.e. for the random phase relationships between modes in a linear wave field. Conversely non-zero values in the wave field bispectrum will provide a measure of any nonlinear interaction occurring between frequencies in a given $f_j+f_k=f_{j+k}$ triad.

Since the bispectrum describes interaction between Fourier modes, it is defined by a triangle on the frequency-frequency plane with vertices at ($f_1=0, f_2=0$), ($f_1=f_{N/2}, f_2=f_{N/2}$) and ($f_1=f_{N/2}, f_2=0$), where $f_{N/2}$ is the Nyquist frequency. The convention adopted in discussing the bispectrum is that $B(f_j,f_k)$ indicates the nonlinear interactions for the triad $f_j+f_k \rightarrow f_{j+k}$. Within this convention however, no indication of the direction of flow of energy within a frequency triad is given. However, the bispectrum is also complex, and therefore can be expressed in terms of its biamplitude and phase. The normalised versions of these, respectively the bicoherence and biphase, were given by Kim and Powers (1979) as,

$$b^2(f_1, f_2) = \frac{|B(f_1, f_2)|^2}{E\left[|A_{f_1}A_{f_2}|^2\right]E\left[|A_{f_1+f_2}|^2\right]}, \text{ where } 0 \le b^2(f_1,f_2) \le 1, \tag{4.23}$$

$$\beta(f_1, f_2) = \arctan\left[\frac{\mathrm{Im}\{B(f_1, f_2)\}}{\mathrm{Re}\{B(f_1, f_2)\}}\right]. \tag{4.24}$$

Physically, the bicoherence will indicate phase coupling between frequencies (with a non-zero value) and the fraction of power resulting from such phase coupling. This indicates the degree to which a frequency in a triad is forced by the coupled frequencies (e.g. a bound wave) or exists in the wave field as free wave energy. Biphase, which measures the ratio of the real and imaginary components of the bispectrum, will indicate the nature of these interactions, i.e. whether the frequency interactions are summed or difference interactions. For incident frequency waves, summed interactions would lead to forcing of a higher harmonic, whilst difference interactions would cause forcing of an infragravity frequency wave.

Therefore the bispectrum can provide information on both the degree of nonlinear forcing occurring between the dominant components in a wave field and the resulting redistribution of wave energy. The evolution of the bispectrum through the nearshore can also be used to parameterise wave shape (Doering and Bowen, 1995) and this is discussed further in section 4.3.2.

Haubrich (1965) described a 95% confidence limit on (normalised) zero bicoherence where

$$b^2_{95\%} \geq 6 / EDF. \tag{4.25}$$

For the normalised estimate of bicoherence in equation 4.23, Elgar and Guza (1985) suggest a confidence level of approximately one-quarter of this value, but employed the value derived from equation 4.25 as a conservative estimate. The same approach has been adopted here, and it is also assumed that for all significantly bicoherent frequency pairs that biphase estimates will be stable (Elgar and Guza, 1985). In this work all bispectral estimates were made using a segment length of 256 points, and therefore estimates from Llangennith and Spurn Head data have 27 degrees of freedom, whilst the Perranporth estimates have 54 degrees of freedom. The trade off for these increased degrees of freedom is that the spectra will have a resolution that is half that of the values given in table 4.2.i.

4.2.2 Time domain cross-correlation

As an alternative to the cross-spectrum, which analyses the variation of two time-series over the frequency domain, within the time domain correlation between two time-series may be assessed by generating values for cross-correlation

$$\gamma_{xy}(m) = \mathrm{E}\left[x_n y_{n+m}\right] \tag{4.26}$$

where x_n, y_n represent stationary random processes, $-\infty<n<\infty$, and m describes the time-lag. For the discrete time-series of finite length examined in this work lagged cross-correlations were computed for the demeaned time-series following

$$c_{nxx}(m) = \sum_{n=0}^{N-|m|-1} x(n)y(n+m)\,, \tag{4.27}$$

to give raw correlations. These were subsequently normalised such that at zero lag, time-series autocorrelation is identically equal to one (Matlab Manual, 1992).

The result of this analysis is a sequence of cross-correlations of length 2N-1, where the zero lag value is found at element N. For these cross-correlations, 95% confidence intervals were established according to the method employed by Garrett and Toulany (1981). This technique used a reduced number of points N^* where

$$N^* = \frac{1}{N} + \frac{2}{N^2}\sum_{j=1}^{N_0}(N-j)r_{xy}(j), \tag{4.28}$$

N is the number of points in the time-series, r_{xy} is the autocorrelation coefficient of the product of the two time-series to be correlated and N_0 is the number of lags until a zero crossing is made by r_{xy}. The 95 % confidence level for N* is then

$$1.96/\sqrt{N^*}\,, \tag{4.29}$$

(Jenkins and Watts 1968). It is notable that the number of degrees of freedom in a correlation plot is liable to be far larger than that of a spectral estimate. Therefore some discrepancies may exist between 'significant' peaks observed in the time and frequency domain analysis plots presented in chapters 5 and 6.

4.3 Summary Statistics

4.3.1 Hydrodynamic parameterisations

For each of the runs, an assessment of mean water depth and current was further augmented by statistics describing wave height and oscillatory current range. Significant wave height (H_{sig}) is determined using

$$H_{sig} = 4\sqrt{\mathrm{Var}[\eta]}\,. \tag{4.30}$$

This is a standard wave statistic used by authors, following Guza and Thornton (1980). The significant wave height is defined as the height of the highest one third of the waves. Since Var[η] may be directly evaluated from the area under the η autospectrum, values of H_{sig} could be generated for both the infragravity and incident frequency oscillatory components by integrating between the upper and lower frequencies banding each component, i.e. 0.005-0.05Hz infragravity, 0.05-0.5Hz incident.

Foote (1994) noted that some attenuation of wave height, due to pressure variations caused by wave breaking, would be experienced in the surf zone. Subsequent calculations made by Foote (1994) showed however, that for the depths seen in the dataset (up to approximately 2.5m) the correction factor for the incident frequency waves (which diminishes at lower frequencies) would be less than 6%. Since this correction factor was relatively small, it was not applied in this work.

A further parameter, the breaker index (γ, Weggel, 1972) was computed using the relationship

$$\gamma_{sig} = \frac{H_{sig}}{h} \tag{4.31}$$

where h is the mean depth value for each run.

A parameterisation analogous to H_{sig} was also made for the oscillatory components of velocity. Following the above definition of significant wave height, this parameter attempts to describe the range over which velocity is seen to vary (from negative to positive) for the largest one-third of the waves. However 'significant velocity' values will give no indication of the extent to which oscillatory flow is biased in the onshore or offshore directions. Velocity skewness or asymmetry describes this instead.

4.3.2 Sediment suspension and flux

The degree to which sediment was resuspended by wave action during a run was assessed using suspended sediment concentration time-series variance. Mean concentration could also have been used to assess the change in resuspension between runs, but in this analysis was found to behave similarly to the variance. Again the advantage of using a variance based measure was that the contributions of infragravity and incident frequency components could be established from the area under the appropriate sections of the c autospectrum.

Time-averaged cross-shore sediment flux $\left(\overline{c.u}\right)$ averaged over wave cycles, was also evaluated for each of the runs. Following Jaffe (1984), flux was further decomposed into mean and oscillatory components using

$$\overline{c.u} = \overline{c}.\overline{u} + \overline{c'.u'} \tag{4.32}$$

where $\overline{c}.\overline{u}$ represents the mean and $\overline{c'.u'}$ the oscillatory component. The oscillatory part was further decomposed into infragravity and incident frequency fluxes using the area under the c-u co-spectrum (after Russell, 1990). It should be noted that a discrepancy will exist between $\overline{c'.u'}$ and the sum of the infragravity and incident components of flux due to the nature of the spectral estimate and the fact that frequencies above the incident band will also contribute to $\overline{c'.u'}$ calculated directly from the time-series (Russell, 1990). However in an examination of the data the observed error was generally seen to be less than 10%.

4.4 Time-series filtering and reflection analyses

In order to examine the relative contributions of the incident and infragravity frequency oscillatory components, and subsequently incoming and reflected infragravity waves, the original η and u time-series were further decomposed to yield these signals. Details of the processing involved are given in this section and are summarised in figure 4.4.1.

4.4.1 Separating the incident and infragravity components

In the autospectra generated from the wave time-series in each of the datasets a trough may be seen between the dominant infragravity and incident banded spectral peaks (figure 4.4.2). The locations of these troughs in the frequency domain can be observed occurring at approximately half the value of the dominant component in the incident frequency band, and Huntley *et al.* (1993) noted similar well defined troughs as a feature of numerous other field data. Using the frequency of the first trough in the infragravity band as a boundary, the demeaned η and u time-series were then divided into low and high frequency signals by using a low and high pass with a time domain elliptical filter. An example of the filter's shape over the frequency domain is illustrated in figure 4.4.3, based on a cut-off frequency of 0.04Hz. The filter cut-offs used for this work are given in table 4.4.i.

One aspect of operation of a standard time-domain filter is to apply not only a change in gain to frequencies banded by the high/low pass, but to also induce a change in phase between high and low passed frequencies. Since comparisons between high and low frequency waves form an essential part of this analysis, such phase shifting would present a problem. The Matlab® *filtfilt* routine however, processes the input data in both forward and reverse directions, resulting in a zero phase filter, and hence it was deemed fit to apply this type of time domain filter to the data in this analysis. To double check that no unwanted shifts in frequency occurred using the *filtfilt* routine, a frequency domain filter (which has no phase effects) generated by the author was also applied to a sample of the data for comparative purposes. Figure 4.4.4 shows a raw time series and the results of a low pass filter using both the time and frequency domain techniques. Whilst the time domain filter was seen to produce a slightly weaker signal, little unwanted phase shift between either of the filtered signals shown in figure 4.4.4 exists.

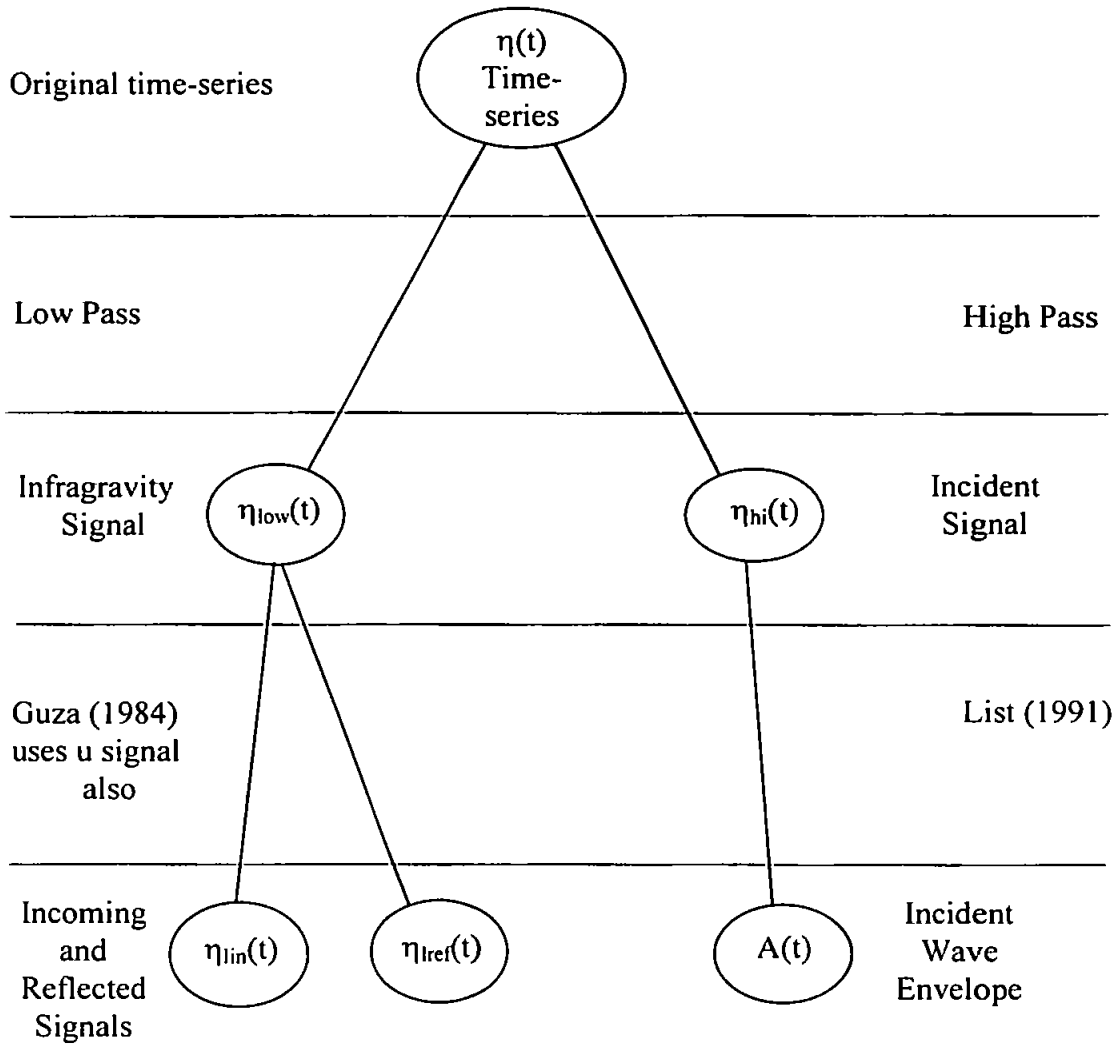

Figure 4.4.1 Reprocessing of the wave signals.

Dataset	Filter Cut-off
Llangennith	0.040 Hz
Spurn Head	0.045 Hz
Perranporth	0.040 Hz

Table 4.4.i Filter cut-offs used in processing.

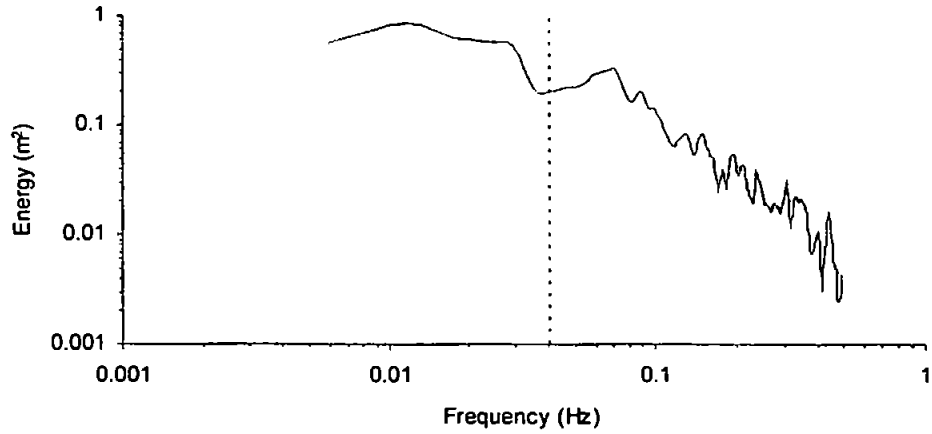

Figure 4.4.2a Sample sea surface elevation spectrum from Llangennith (Storm Day), plus the cut-off frequency used in the elliptical filter (indicated by the dashed vertical line).

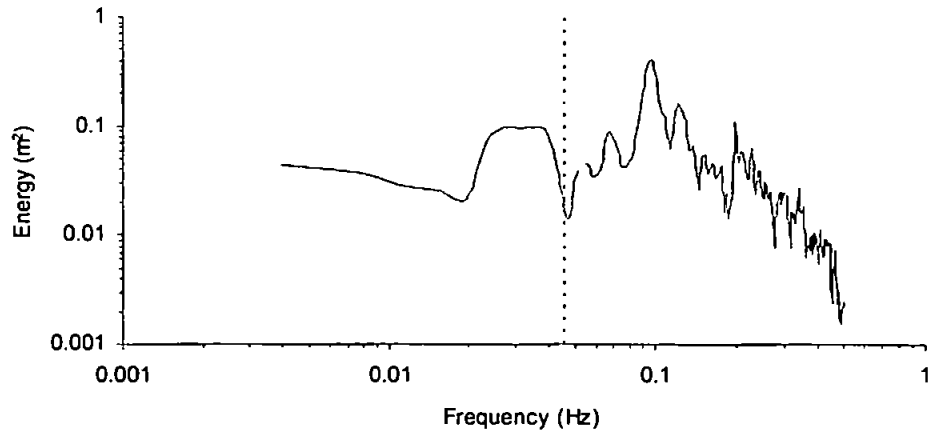

Figure 4.4.2b Sample sea surface elevation spectrum from Spurn Head, plus the cut-off frequency used in the elliptical filter (indicated by the dashed vertical line).

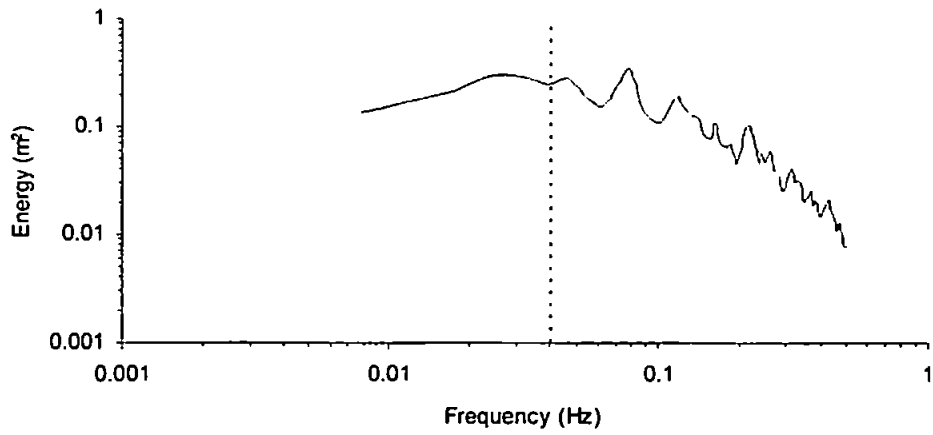

Figure 4.4.2c Sample sea surface elevation spectrum from Perranporth, plus the cut-off frequency used in the elliptical filter (indicated by the dashed vertical line).

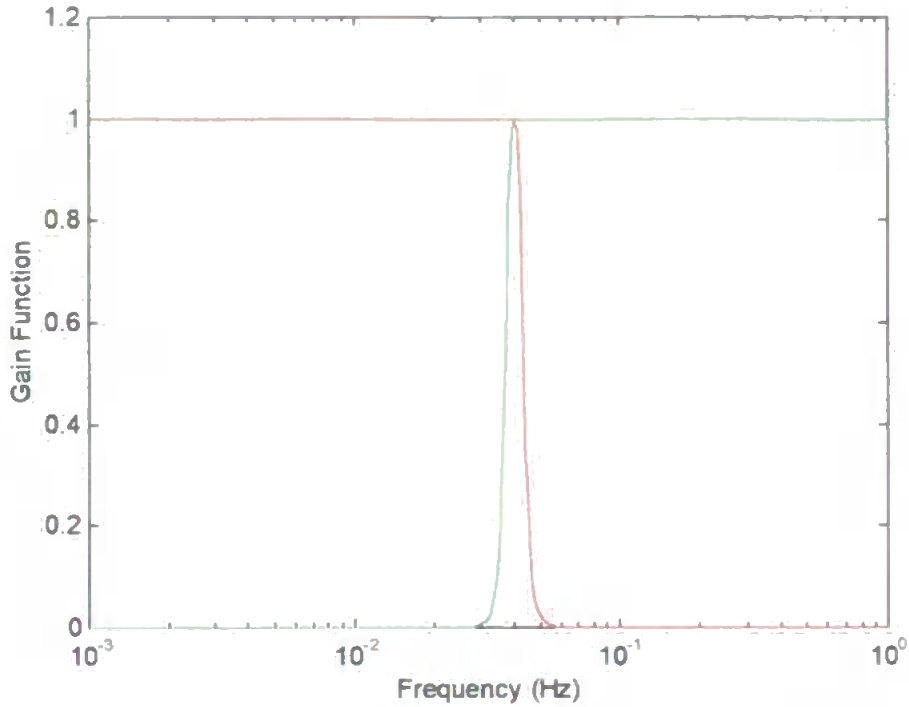

Figure 4.4.3 Time domain filter used for Llangennith data, red dotted line indicates low pass filter, green line high pass.

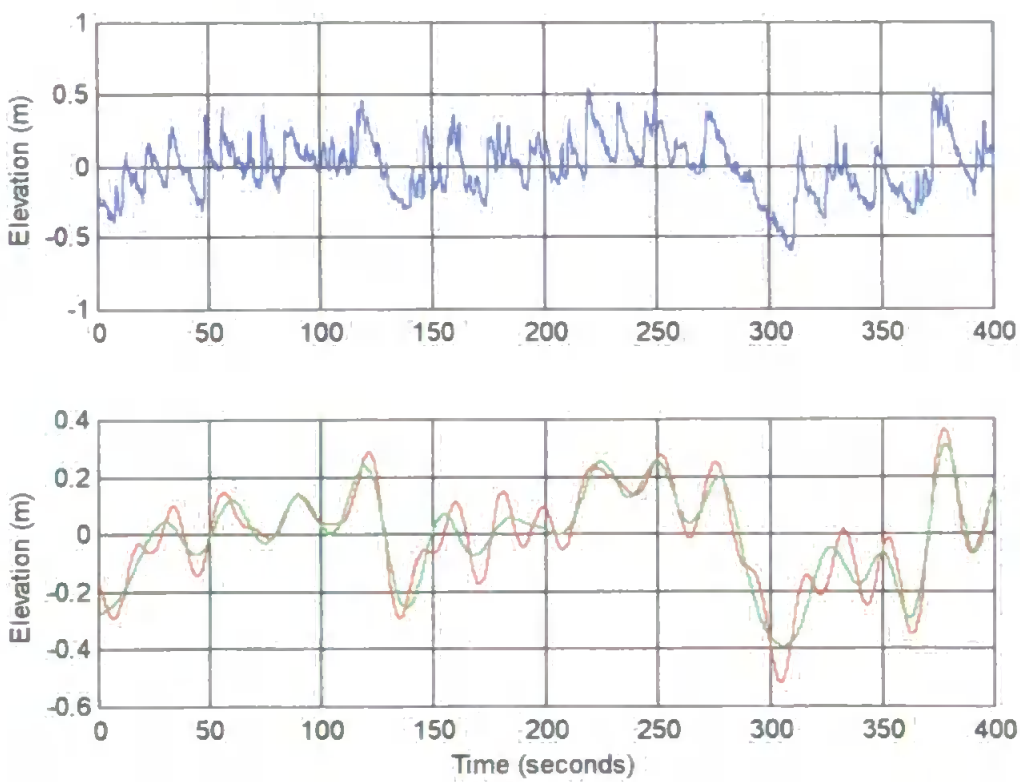

Figure 4.4.4 Sample time-series and comparison between a frequency domain low pass filter (red), and the results of a zero-phase time domain elliptical filter (green) using the Matlab® *filtfilt* routine.

4.4.2 Derivation of the incident wave envelope and groupiness factor

Modulations of incident wave heights were assessed through generation of a time-series for 'wave envelope', and the derivation of a groupiness factor (*GF*). The envelope time-series was generated following the method employed by List (1991). In this method a high pass filtered time-series is put into modular form (to simulate wave heights whilst avoiding non-linear effects which could be created by squaring the time series), low pass filtered and subsequently multiplied by $\pi/2$. The multiplication factor of $\pi/2$ is used in calculating the envelope as, if it is assumed that over a half wave period the wave time series $\eta(t)$ will have a sinusoidal form with amplitude a, then over the same interval the low pass filtered $|\eta(t)|$ will have a value of

$$\frac{1}{\pi}\int_0^{\pi} a\sin(\theta)\mathrm{d}\theta = 2a/\pi\,, \tag{4.33}$$

List (1991). Using this method, the resultant time-series shows modulation with time of the incident frequency wave amplitudes (figure 4.4.5) and is denoted

$$A(t) = \frac{\pi}{2}\left|\eta_{hi}(t)\right|_{low}. \tag{4.34}$$

Following List (1991) a normalised *GF* was estimated using

$$GF = \frac{\sqrt{2\,\mathrm{Var}[A(t)]}}{\overline{A}(t)}. \tag{4.35}$$

Foote (1994) also describes a groupiness factor using the relationship

$$GF = \left\{\overline{\left[\left(\eta_{hi}^2(t)\right)_{low}\right]^2}\right\}^{\frac{1}{4}}. \tag{4.36}$$

Since the latter is not normalised its value will show a strong relationship to incident wave height as well as modulation of these waves. Both groupiness factors will be used and compared in Chapter 5.

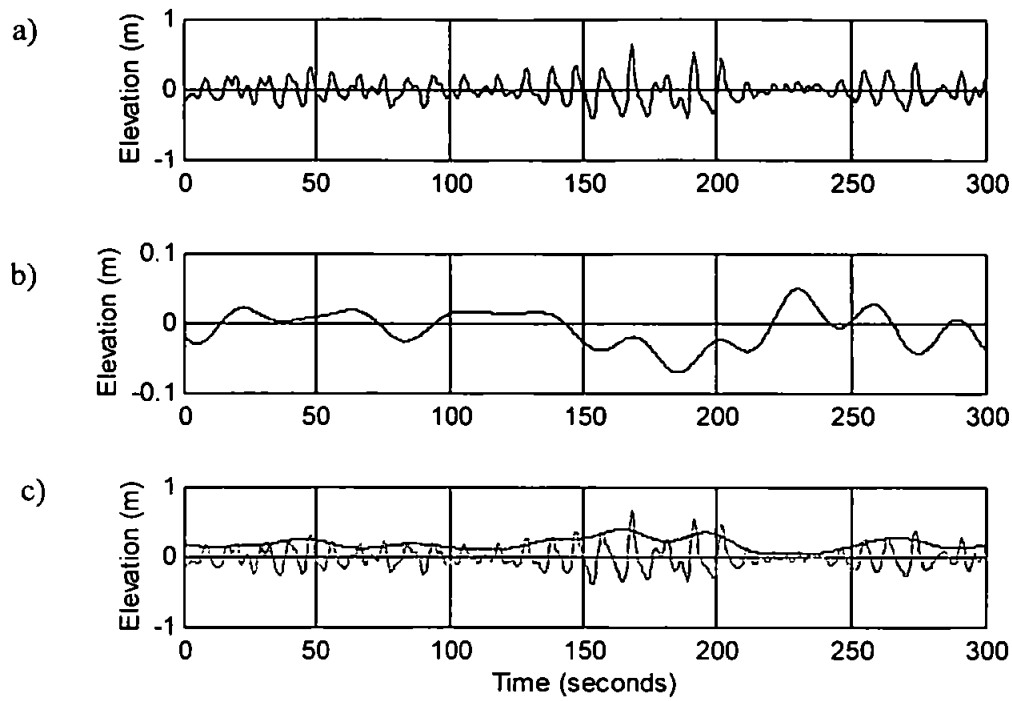

Figure 4.4.5 Separation of a) a demeaned η time-series into b) a low frequency (infragravity wave) signal and c) the high frequency (incident wave) plus wave envelope signals.

4.4.3 Reflection coefficient analysis

In the course of this thesis, reflection will be assessed with respect to frequency using simultaneous time-series of sea surface elevation and cross-shore velocity. Methods based upon 'time domain' (Bowen and Guza, 1976) and 'frequency domain' (Tatavarti, 1989) techniques are available for such analysis, but Huntley *et al.* (1995) found difficulties in using both of these techniques with real data. For example, in the case of the time domain technique uncorrelated signal noise would bias reflection coefficients toward unity. Similarly, the frequency domain technique suggested by Tatavarti (1989) showed frequency dependent biases, which would be difficult to account for in real data.

In this work, frequency dependent reflection coefficients were calculated using the Principal Component Analysis (PCA) technique described by Tatavarti *et al.* (1988). This method employs the sea-surface elevation versus velocity cross-spectra to produce values of gain and phase between the incoming and reflected wave signals as for the frequency domain technique. However, PCA modifies the cross-spectrum used by employing only the first eigenvector of the spectral estimate, under the assumption that this extracts the correlated part of the cross-spectrum whilst leaving unwanted noise in the higher frequencies. Huntley and Simmonds (1994) found that this method did provide essentially unbiased estimates of reflection for simulated data (see also Huntley *et al.*, 1995).

The first eigenvector of the η-u cross-spectrum is used to calculate frequency dependent gain $\left(\hat{G}(f_n)\right)$and phase $\left(\hat{\theta}_{\eta u}(f_n)\right)$ functions. These can then be used to generate frequency based reflection coefficients, and incoming versus reflected wave phase following the relationships

$$R^2(f_n) = \left[\frac{1+\hat{G}^2(f_n) - 2\hat{G}(f_n)\cos\hat{\theta}_{\eta u}(f_n)}{1+\hat{G}^2(f_n) + 2\hat{G}(f_n)\cos\hat{\theta}_{\eta u}(f_n)}\right] \tag{4.37}$$

and

$$\tan\phi(f_n) = \frac{2\hat{G}(f_n)}{1-\hat{G}^2(f_n)}\sin\hat{\theta}_{\eta u}(f_n). \tag{4.38}$$

In calculating the cross-spectrum from which reflection coefficient and phase are derived, the routine devised for this analysis uses the same spectral techniques, segment lengths etc. stated in section 4.2. A limit on this method was noted by Huntley *et al.* (1995), whereby an assumption of wave propagation normal to the reflector (the beach) is necessary. This has been made in this analysis, and is examined further in section 4.5.2.

4.4.4 Derivation of incoming and reflected wave time-series

As will be seen in chapter 5, the chief interest in wave reflection analysis for these datasets is in the infragravity frequency component. In this work both demeaned sea surface elevation and low frequency filtered signals were further separated into an incoming and reflected wave signal in the time domain following a method proposed by Guza *et al.* (1984). In this situation a time domain technique was employed rather than using a technique based on spectral estimates. This was deemed appropriate because the time-series used in the analysis were relatively short and therefore only allowed for a limited level of resolution at the low frequency end of the spectrum. It was felt that an output time-series generated by reverse transforming such spectral estimates might be more distorted from reality, as a result of this lack of spectral resolution, than the time-series generated by the time domain method.

The Guza *et al.* (1984) method employs shallow water theory (applicable where $L/h>20$), where

$$\eta = \sqrt{\frac{h}{g}}u \tag{4.39}$$

and η is sea surface elevation, u cross-shore velocity, h depth and g is acceleration due to incident. Therefore an onshore/offshore propagating characteristic for η could be generated according to

$$\eta_{in} = \frac{1}{2}\left(\eta + \sqrt{\frac{h}{g}}u\right) \text{ and } \eta_{ref} = \frac{1}{2}\left(\eta - \sqrt{\frac{h}{g}}u\right). \tag{4.40}$$

An analogous approach was applied to produce incoming and reflected cross-shore velocity time-series. Similarly to the PCA analysis, this technique requires an assumption of a shore normal wave approach to the beach if the results are to be interpreted with confidence.

4.5 Application of data for a description of processes through the cross-shore

Observations from macrotidal beaches such as those in the B-BAND programme and Perranporth will be temporally variable, in that water depth at the sensors will change during the tidal cycle. This will have the effect of altering the position (versus the mean shoreline) from which the observations are made, i.e. as depth increases the instruments become further displaced from the shoreline and vice versa. Whilst this effect has the drawback of constraining the length of time-series which may be used to examine processes, the apparent 'movement' of the sensors does lead to the possibility of deriving a cross-shore distribution of processes from a number of time-series taken by one set of instruments.

For such an interpretation is to be applied, certain checks on the data used in this analysis needed to be made such that a distribution of cross-shore processes could be determined from the 'run' time-series. This section shows checks made on

- 'stationarity' of conditions, i.e. whether the wave climate changes during any given observation period
- direction of wave approach, which might particularly affect reflection analyses

4.5.1 'Stationarity' of conditions

When examining the analysis results, for ease of interpretation it was deemed useful to be able to assume that the incident wave conditions remained constant throughout the observation period. An ideal check on the incident wave climate might come from a wave gauge located in deep water near the experimental site, where tidal effects would be minimised. However, such data was not available in the studies featured in this work. Instead wave data from the instruments came from locations between the inner surf zone and wave shoaling zone.

With this in mind the check employed here involved comparison of η autospectra (from each dataset) for runs on the flood and ebb phases of a tide where the mean water depth was similar. Spectral confidence limits could then be employed to check if wave conditions were changing. This was done by using a null hypothesis that the distributions of energy observed come from the same wave fields. In spectral terms, it would be expected that if

the wave conditions changed to a great extent between runs, then the resulting spectra would fall outside of a spectral confidence band.

This hypothesis was applied across the incident frequency band only, as the possibility existed that infragravity wave energy in the nearshore might indeed be time variant. It might be acceptable to assume that infragravity bound long wave energy is directly related to the incident frequency waves outside of the surf zone (Longuet-Higgins and Stewart, 1964). However closer to shore, overall infragravity wave energy could vary between the flood and ebb phases of the tide should standing wave structures have been set up during the high water slack period.

Figures 4.5.1a-d show example intercomparisons between appropriate run pairs taken from the thesis dataset. Using the incident banded part of the spectrum only will have a drawback when examining data from the inner surf zone such as that from Storm Day, Storm Night and Perranporth (see section 5.1), because breaker heights in this region are expected to be saturated and therefore increasing storm conditions would not change the incident banded part of the spectrum. However, decreasing energy conditions, where breaker heights become non-saturated would cause a drop in incident frequency spectral energy. This might have been observed during the Storm Night tide (figure 4.5.1b), where a drop in energy is seen between the flood and ebb runs. Nevertheless energy remains within the 95% confidence limit, and it is assumed for this work that wave energy did not change significantly during the Storm Night observations. For all the other data, flood and ebb spectra are virtually identical, and therefore the incident wave conditions are assumed to remain consistent throughout the majority of the Storm Day, Spurn Head and Perranporth tides.

Figure 4.5.1 Example comparisons of sea surface elevation spectra for stationarity test.

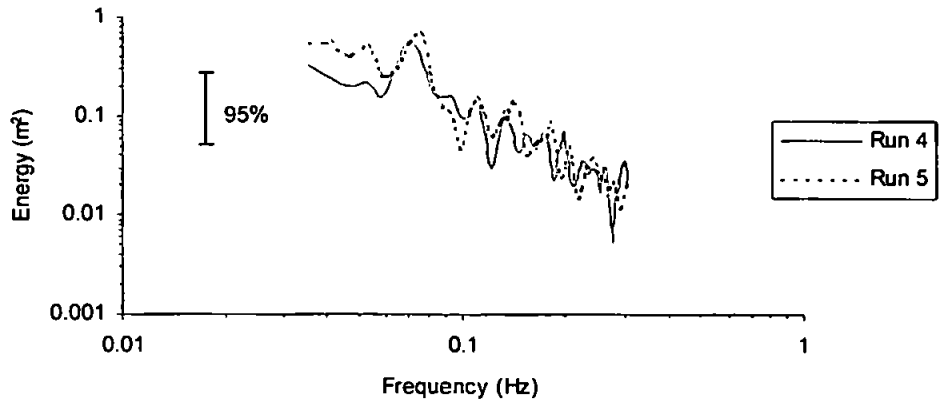

a) Storm Day run 4 versus run 5.

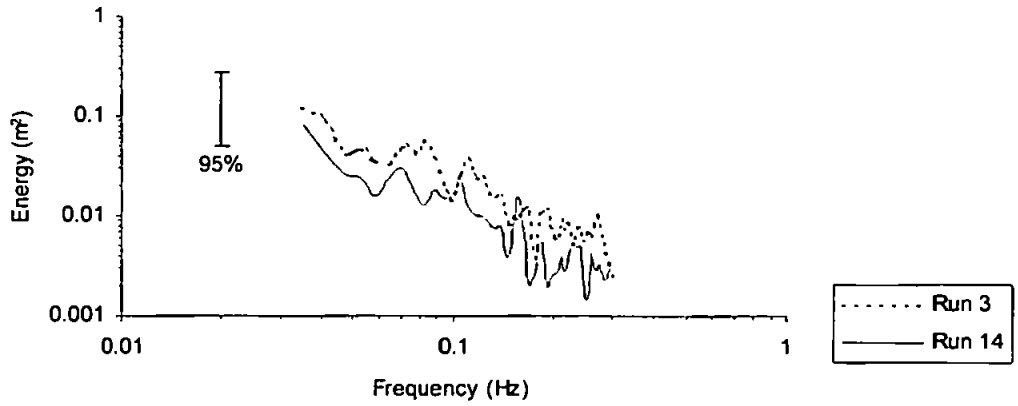

b) Storm Night run 3 versus run 14.

Figure 4.5.1 Example comparisons of sea surface elevation spectra for stationarity test.

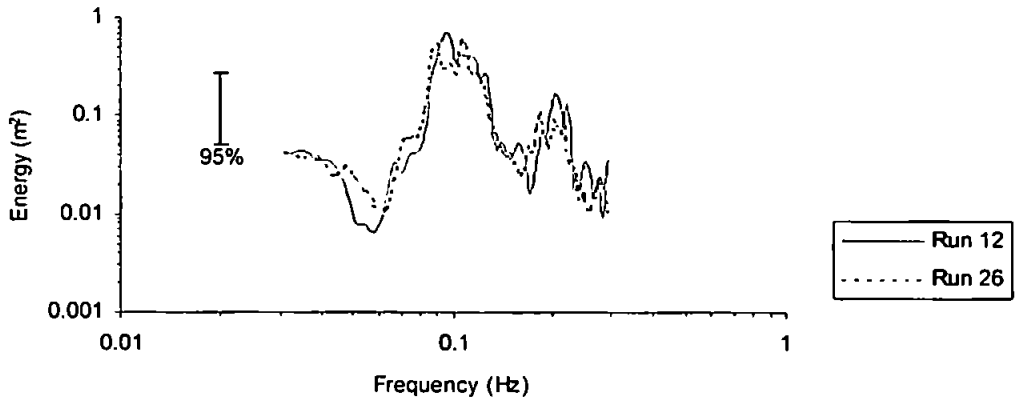

c) Spurn Head run 12 versus run 26.

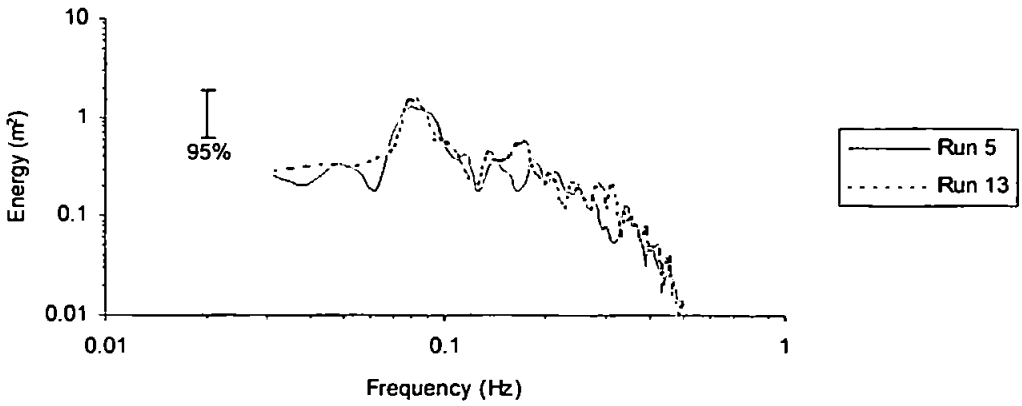

d) Perranporth run 5 versus run 13.

4.5.2 Wave direction

Since the processes examined in this work are being approached in a purely cross-shore sense, a check on the direction of wave incidence was necessary. In particular, such an assumption is integral to the reflection analysis methods being employed in this work. Both Russell (1990) and Davidson (1991) noted that for the Llangennith data longshore variance was almost negligible and surmised wave approach to be almost shore normal. The angle of this beach to the prevailing swell direction also suggests this was a likely scenario.

However, the Spurn Head site is found on an area of coastline where wave approach is generally oblique. In this case a Maximum Likelihood Estimator (MLE) method (Huntley *et al.*, 1995) was used to derive a directional wave spectrum. MLE requires that a minimal reflected component is present in the time-series used. Since for Spurn Head the dominant incident frequency waves' energy is mostly dissipated through breaking (see section 5.1.2), assessment of wave direction was based on the peak at the dominant incident wave frequency. This assessment was made for runs outside of the surf zone, and it was further assumed that in this region the incoming infragravity waves would still be bound to the incoming swell. Thus both the observed swell waves and their corresponding bound infragravity component would travel at the same angle with respect to the shoreline.

It is considered that application of the MLE technique to this field data can be justified by the results, which appeared consistent, both between individual runs within the data and with experimenters' visual observations of wave approach. Figure 4.5.2 shows a typical result from Spurn Head based on a segment length of 256 and with a directional resolution of 5°. Angle of wave attack is seen to be approximately 5° from shore normal at the dominant peak at 0.1Hz. This suggests that a sensible analysis of oscillatory processes could be made using the cross-shore component only. In the course of processing a further check was applied to this assumption by making a comparison between 2D and 3D PCA analyses of wave reflection (e.g. figure 4.5.3). These were found to be similar enough to suggest a direction of wave approach near to shore normal.

Similarly a check was made on the Perranporth data, where much of the incident wave energy came from a local sea in addition to a swell. The directional spectrum results from a typical run (run 13) are shown in figure 4.5.4. In the figure the main peak at 0.1Hz, and its first and second harmonic are all seen to have an angle of incidence near to zero. The extra

harmonic peaks observed in figure 4.5.4 in comparison to figure 4.5.2 can be put down to the onset of wave breaking, since the Perranporth runs were taken from inside the surf zone.

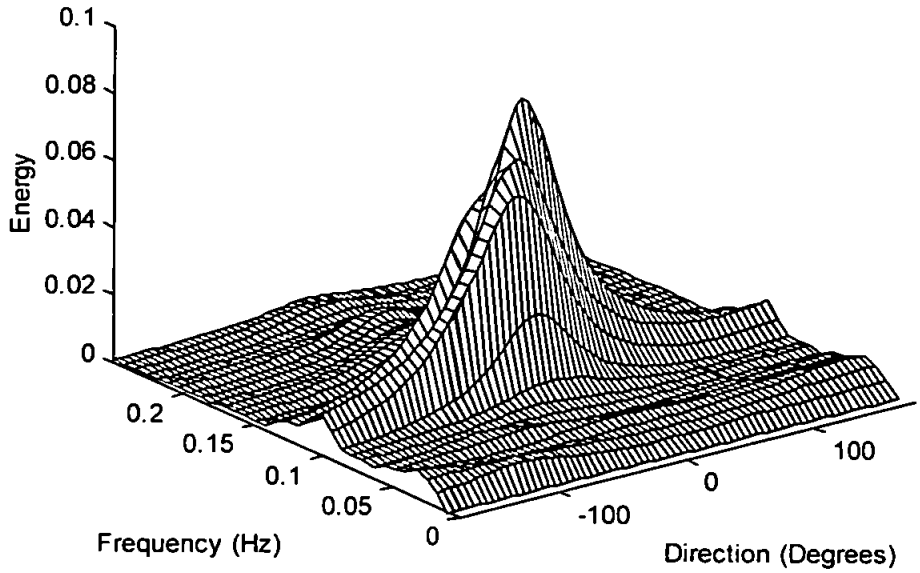

Figure 4.5.2 Example of a directional wave spectrum, Spurn Head run 20, rig A2.

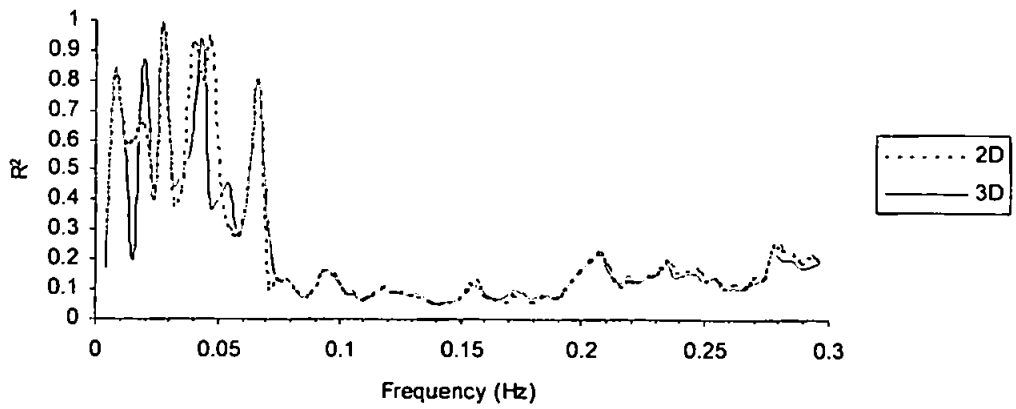

Figure 4.5.3 Corresponding results of run 20 2D and 3D PCA analysis.

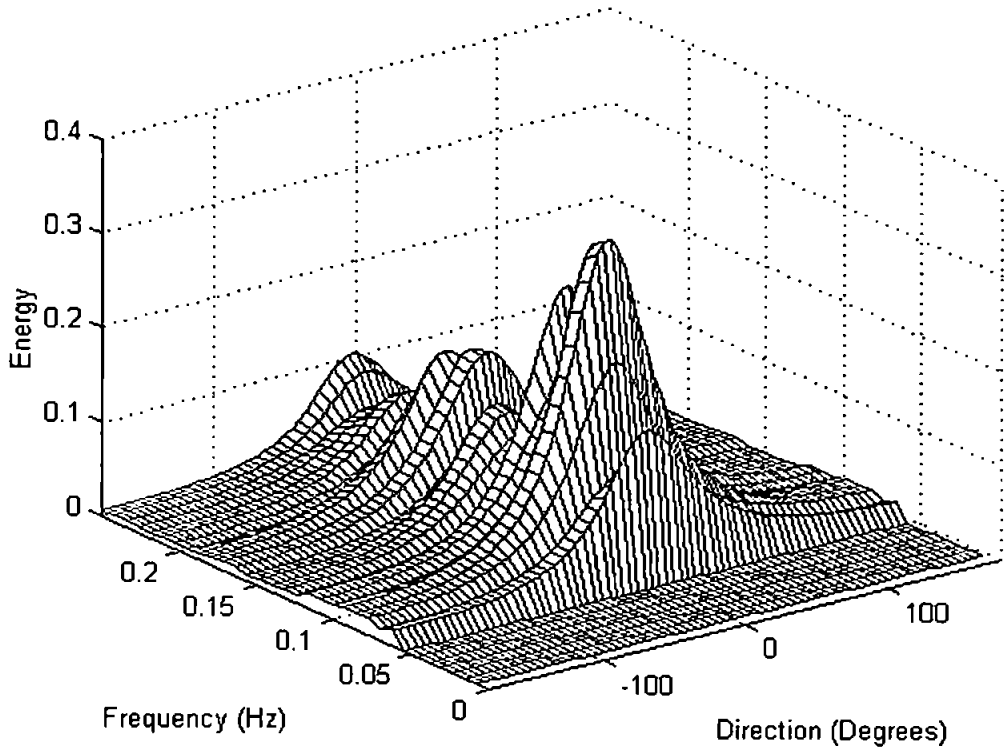

Figure 4.5.4 Example of a directional wave spectrum, Perranporth run 13.

4.6 Summary: Data processing

In this chapter the main analysis techniques used with the data have been discussed. In addition to visual inspection, time-series measurements of water depth, current and suspended sediment concentration will be represented in subsequent chapters by statistics representing each run, and the results of spectral analyses. Comparisons between time-series were made using both frequency (cross-spectral) and time-domain (cross-correlation) methods.

Infragravity wave signals and signals representing modulations of incident frequency wave heights were derived via filtering techniques. In this work a time-domain filter was used, but by employing a forward and reverse filter technique, no phase shift was observed between raw and processed signals. Further investigations of wave reflection (using a Principal Component Analysis technique) and non-linear interactions in the wave field (using bispectral analysis) were also conducted.

Chapter 5: Results I, Hydrodynamics

In this investigation of infragravity variations in sediment suspension and transport, the analysis first provides a description of the hydrodynamic regimes observed at each of the three beach sites featured in this study, and will focus on low frequency variations that may be observed in the oscillatory components. Whilst it is acknowledged that sediment dynamics may well be forced by the instantaneous velocity, which will comprise of a mean current as well as gravity and infragravity wave related velocities, it is these latter two components which will provide the time variations of interest to this thesis. Indeed, in the case of low frequency sediment suspension, it was noted in chapter 1 that large events were related to a combination of the mean component, and a strong infragravity velocity coupled with a larger than usual incident frequency wave. In examining these events, it is therefore necessary to understand the nature of the waves in both the infragravity and incident bands of the spectrum. Outside of the surf zone, particular attention may also need to be paid to low frequency variations in incident frequency wave height modulation, because, for example, low frequency variations in sediment suspension observed by Hanes and Huntley (1986) were attributed to wave groupiness. In this case, subsequent waves of increasing height increasingly stirred up sediment.

Sections 5.2 and 5.3 respectively examine the behaviour of the infragravity waves and modulation of incident frequency waves. The example in chapter 1 suggests that the phase between the two components will also be important, and this is also addressed in section 5.3. Section 5.4 investigates the level of interaction between incident and infragravity components in what is an extremely non-linear system. Firstly however, section 5.1 gives a description of the basic hydrodynamics of the three beaches in this study.

5.1 Overview of the hydrodynamics at Llangennith, Spurn Head and Perranporth

5.1.1 Basic hydrodynamics

All three field experiments employed an instrument rig which remained at a fixed position, but experienced changes in the hydrodynamic regime as water depth over the instruments increased and decreased during the flood and ebb phases of the tide. At Llangennith the instruments went from being dry to a maximum submergence in approximately 1m of water, at Spurn Head 3m and at Perranporth 2.2m. Correspondingly the data from each site describes the hydrodynamics at varying points within the nearshore.

To illustrate this, figures 5.1.1a-c show the value of breaker index $\gamma=H_{sig}/h$ (where H_{sig} is incident frequency wave significant wave height and h depth) plotted versus depth for each of the beach sites. At both Llangennith and Perranporth (figures 5.1.1a and 5.1.1b) the breaker index takes a near constant value independent of the depth at which the measurement was made for most of the observations. This is indicative of saturated wave breaking, i.e. all the waves are broken and have their heights depth limited. Following the hydrodynamic division of the nearshore given in section 2.1, this defines this data as coming from the saturated inner surf zone (although breaking appears non-saturated for very shallow water, h<0.5m, at Perranporth). The values of breaker index for the Llangennith and Perranporth data are respectively γ=0.45 and γ=0.55. These may be compared with Weggel (1972)'s value of γ at the onset of breaking derived for monochromatic waves in a flume of 0.78, and the value observed by Guza and Thornton (1983) in a fully saturated surf zone of γ=0.42. Unsurprisingly the breaker index values from Llangennith and Perranporth are rather nearer to the value of Guza and Thornton (1983) since this was derived from field observations of broken waves. However, the work of Horikawa and Kuo (1966) suggests that the value of γ at the onset of breaking may well be nearer to that found by Weggel (1972), and that the breaker index will undergo a decrease from this value to the one observed in the inner surf zone during wave transition through the outer part of the surf zone.

In figure 5.1.1c, the Spurn Head breaker index increases with decreasing depth. Whilst this might indicate that shoaling of unbroken waves will continue right up to the shoreline, a more likely explanation of this behaviour is the existence of an (constant) offset error in the pressure transducer depth measurements. Examining the breaker index for the observed values,

$$\gamma_{Obs} = \frac{H}{h_{Obs}}, \tag{5.1}$$

wave height H in a saturated surf zone may be substituted, using the correct value for breaker index and the offset value,

$$H = \gamma(h_{Obs} + offset). \tag{5.2}$$

This yields,

$$\gamma_{Obs} = \gamma + \frac{offset}{h_{Obs}}. \tag{5.3}$$

The effect of the second term on the right hand side of equation 5.3 is to cause a large increase in γ_{Obs} near to shore as $h_{Obs} \rightarrow 0$. This agrees with the behaviour of the breaker index value in figure 5.1.1c. Furthermore, figure 5.1.3a shows a good linear fit (r^2=0.99) between depth and wave height in shallow water at Spurn Head, indicative of the saturated surf zone assumed in equation 5.2 (this was also observed visually by the experimenters, Davidson, 1999, *pers. comm.*). The intercept for the regression in this case is greater than zero, and indicates a constant offset value for the observed depths of 0.425m.

Breaker index values processed to include this depth offset are also plotted on figure 5.1.1c (as the unfilled triangles) and show saturated breaking behaviour when the instruments are near to shore, whilst in deeper water breaker index gradually increases toward the saturation value. Such an evolution of breaker index through the cross-shore suggests that in this case the onset of wave breaking will take place for a critical index value which is very similar to the saturated value. This contradicts the observations of Horikawa and Kuo (1966). It should also be noted that in figure 5.1.1c the offset values have only been corrected for on the y-axis. This has been done for ease of comparison between data points, but the depth-offset effect will also be to shift data points to the right along the x-axis. It should also be noted that having discussed the possibility of an offset existing in the Spurn Head data, for the remainder of this work depth values shall be used without making such a correction. This is because, with data of this age, confirming the offset by checking the instrument is not possible, and also in later sections in the thesis, results will be compared using normalising schemes derived from this data by previous authors who had not made such a correction (e.g. Russell and Huntley, 1999, see section 5.1.3).

Also plotted in figure 5.1.1c are observations of cross-shore velocity versus depth (grey squares). In the figure these values make a zero crossing at a depth of approximately 1.5m. This reversal of the mean current direction is suggestive of a transition between the shoaling zone and surf zone (Davidson *et al.*, 1993), and therefore defines runs with

observed depths of less than 1.5m (runs 1-9, 29-32) as being inside the surf zone, whilst the remainder of the data describes the incident frequency wave shoaling region. For the offset corrected γ values, the breaker index at this point takes a value near to that for saturated wave breaking, which suggests that at this point most waves will have commenced breaking. Thus a number of runs in depths greater than 1.5m may have observed non-saturated outer surf zone conditions, where the incident frequency waves will have been a mixture of shoaling and broken waves. This is discussed further in section 5.1.3.

The mean current at Spurn Head has an offshore directed maximum of $0.2ms^{-1}$ in the surf zone and rather smaller onshore maximum of $0.05ms^{-1}$ in the shoaling zone. Data from the inner surf zones at Llangennith and Perranporth also show an offshore directed mean flow, but whilst for Llangennith the current is strong (up to $0.5ms^{-1}$), at Perranporth only a weak offshore flow is measured (current maximum is $0.15ms^{-1}$). Tables summarising the cross-shore velocity field for each tide of data are given in Appendix I.

Figures 5.1.2-5.1.4 compare the evolution of the incident and infragravity banded parts of the oscillatory component of the hydrodynamics through the nearshore at each beach site. Each figure consists of a plot of frequency banded significant wave height (infragravity 0.005-0.05Hz, incident 0.05-0.5Hz) versus depth and examples of the sea surface elevation (η) and cross-shore velocity (u) autospectra from runs at different depths. Autospectra from the whole dataset are also summarised by tables in Appendix I.

At Llangennith infragravity wave heights increase toward shore as an effect of wave shoaling, whilst incident wave heights are diminished through breaking (figure 5.1.2a). This behaviour is observed for both the Storm Day and Storm Night tides, but during Storm Day infragravity energy levels are much higher. This coincides with visual observations by the experimenters, who noted a general decrease in the energy of the storm event between the two tides (Russell, *pers. comm.*). The spectra (figures 5.1.2b and c) are taken from a set of Storm Day runs, and are dominated by energy at low frequencies. For the runs in these figures water depths are run 4; 1.06m, run 6; 1m and run 9; 0.73m. The u autospectrum shows the lowest frequencies (<0.02Hz) increasingly dominating the spectrum with decreasing depth (figure 5.1.2c). Elsewhere in the spectra, a peak is observed corresponding to the dominant incident wave frequency (0.07-0.08Hz, 12-15 seconds). Higher infragravity frequencies are also energetic, but both this and the incident part of the spectrum diminish in energy in shallower water between run 6 and run 9.

At Spurn Head, the behaviour of the infragravity waves, as shown in figures 5.1.3a indicates that energy at infragravity frequencies remains relatively constant throughout the observations. Infragravity energy is secondary to that at gravity frequencies for all runs but those when the instruments are nearest to shore (runs 1-4, figure 5.1.3a). In both the sea surface elevation and cross-shore velocity autospectra, with the exception of those runs nearest to shore, incident frequency wave energy, with a significant peak at approximately 0.1Hz, dominates the spectra (figures 5.1.3b and c). The figures show spectra derived from a time-series observed when the instruments were in the shoaling zone (run 23), and a run from the surf zone (run 6). In the plots, energy at 0.1Hz diminishes between the shoaling zone (run 23) and the surf zone (run 6), whilst an increase in established energy at lower infragravity frequencies is observed. A further feature, particularly in a number of the sea surface elevation spectra (figure 5.1.3b), is that two peaks may be seen in the infragravity range, toward the lower end of the band at approximately 0.01Hz, but also at approximately 0.03Hz. However, at this stage it should be noted that peaks and troughs in the infragravity band as a whole might well be an effect of the presence of standing or partially standing waves. This will be discussed further in section 5.3.

At Perranporth, infragravity significant wave heights remain constant through the region observed (figure 5.1.4a), but are secondary to the incident frequency waves except when the instruments are in the shallowest water depths. Again this suggests that less shoaling of the infragravity waves occurred at Perranporth than was observed at Llangennith. The main peaks in the sea surface elevation autospectra (figure 5.1.4b) at the infragravity frequencies are at a rather higher frequency than in the Llangennith and Spurn Head cases. At Perranporth the dominant infragravity waves have periods in the range 30- 50 seconds. The dominant incident wave peak frequency corresponds to a periods of 9-12 seconds. Similarly to the spectra from the other sites, the fact that rather less dissipation of energy occurs at infragravity frequencies through the nearshore is best illustrated by the cross-shore velocity autospectra (figure 5.1.4c). In figure 5.1.4c the series of autospectra show the decrease in incident frequency wave energy (due to wave breaking) with decreasing depth from run 8 (h=2.14m) through to run 13 (h=1.78m) and to run 17 (h=0.61m). Conversely, at infragravity frequencies an increase in the amount of energy occurs between the runs in the cross-shore velocity spectra.

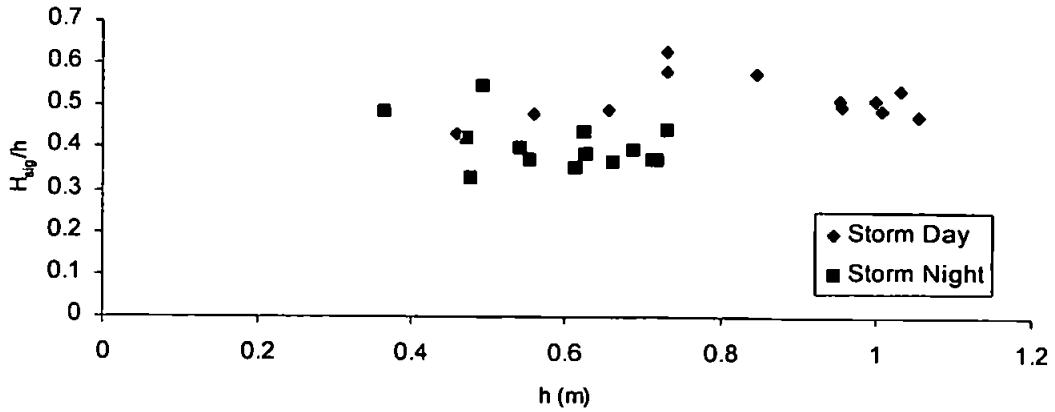

Figure 5.1.1a Distribution of incident wave breaker index versus depth for Llangennith Storm Day and Storm Night tides.

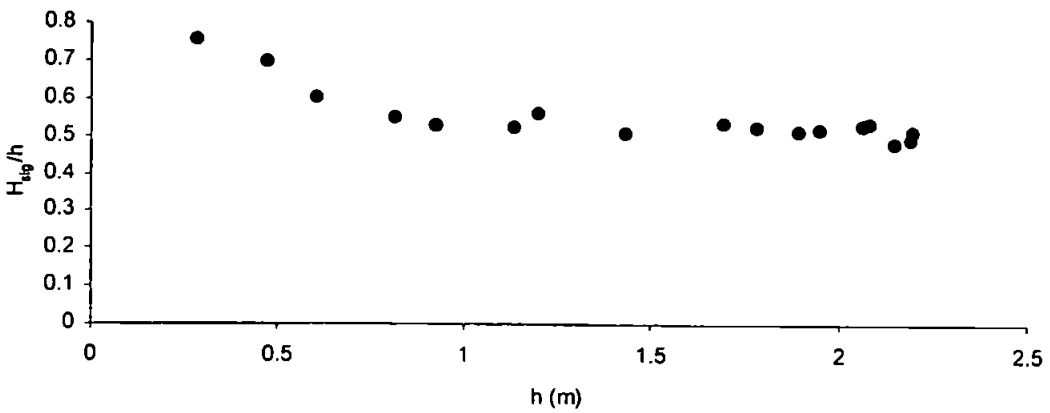

Figure 5.1.1b Distribution of incident wave breaker index versus depth for Perranporth.

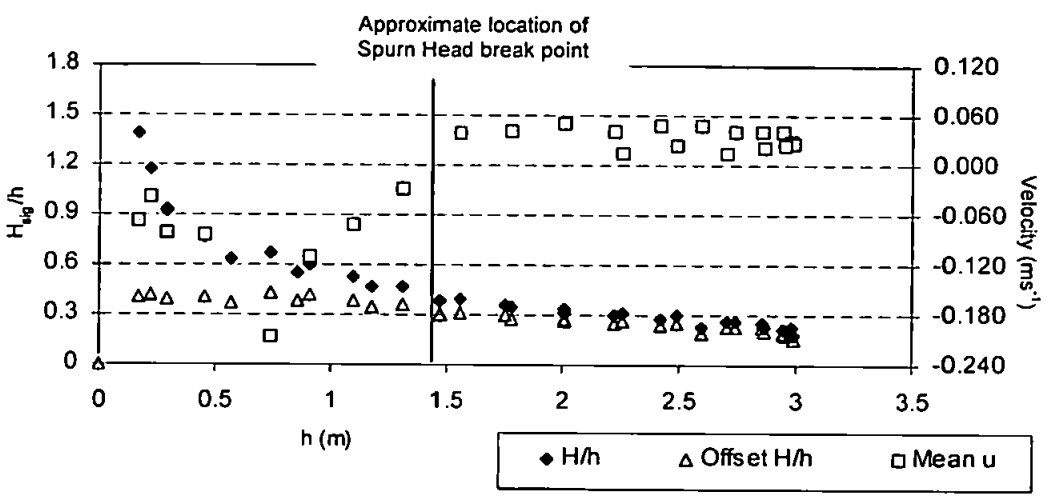

Figure 5.1.1c Distribution of incident wave breaker index and mean current versus depth for Spurn Head.

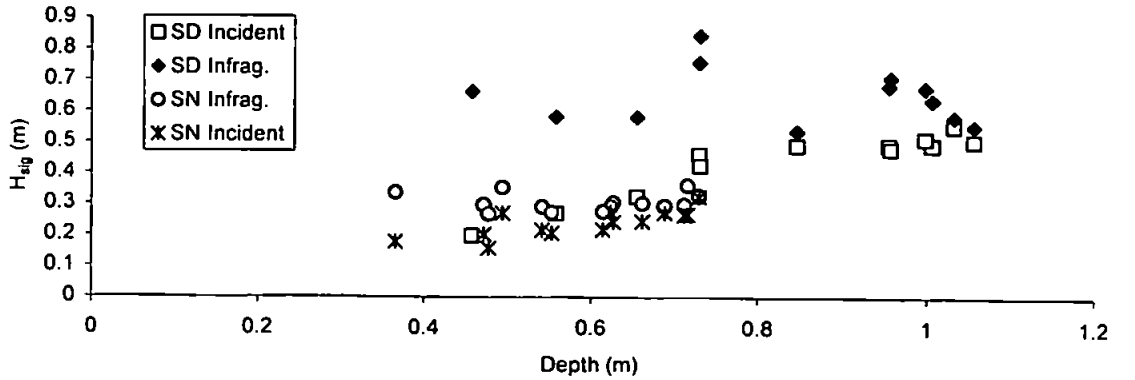

Figure 5.1.2a Distribution of incident and infragravity banded significant wave height versus depth for Llangennith Storm Day and Storm Night tides.

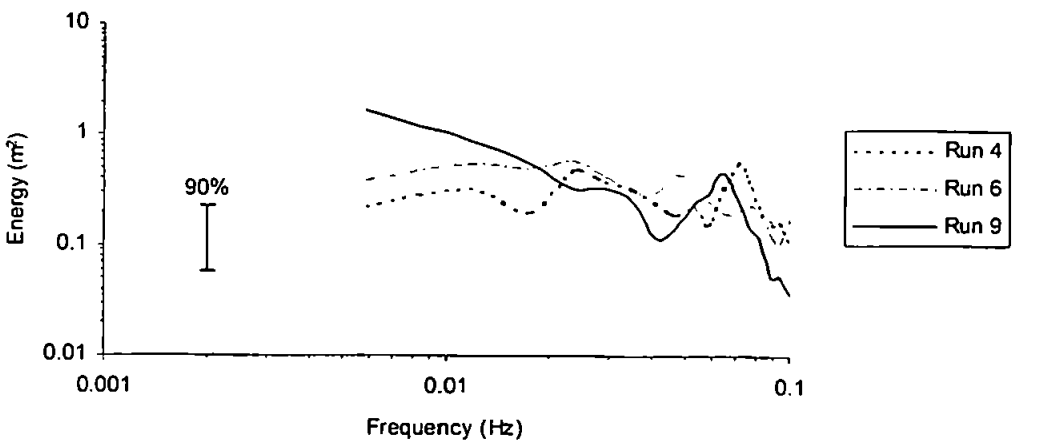

Figure 5.1.2b Evolution of η autospectra on ebb tide, Storm Day runs 4 (h=1.06m), 6 (h=1m) and 9 (h=0.73m).

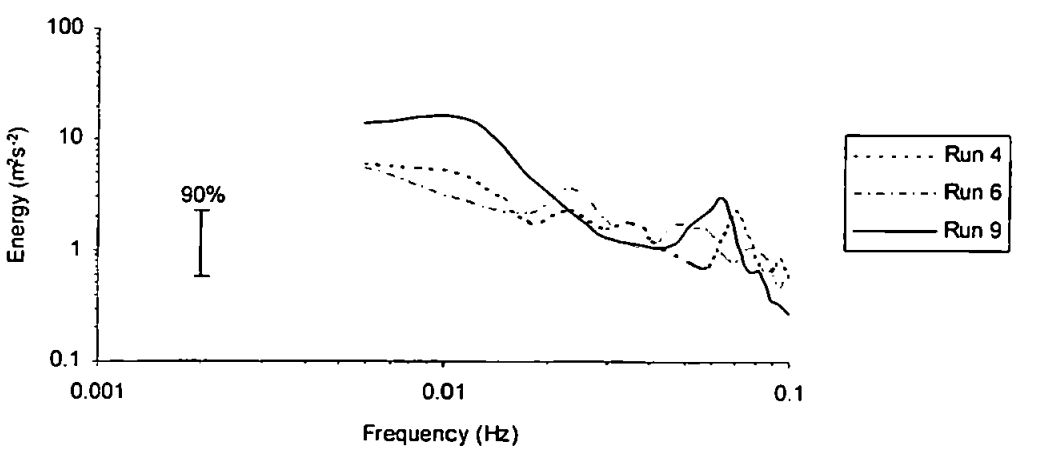

Figure 5.1.2c Evolution of u autospectra on ebb tide, Storm Day runs 4 (h=1.06m), 6 (h=1m) and 9 (h=0.73m).

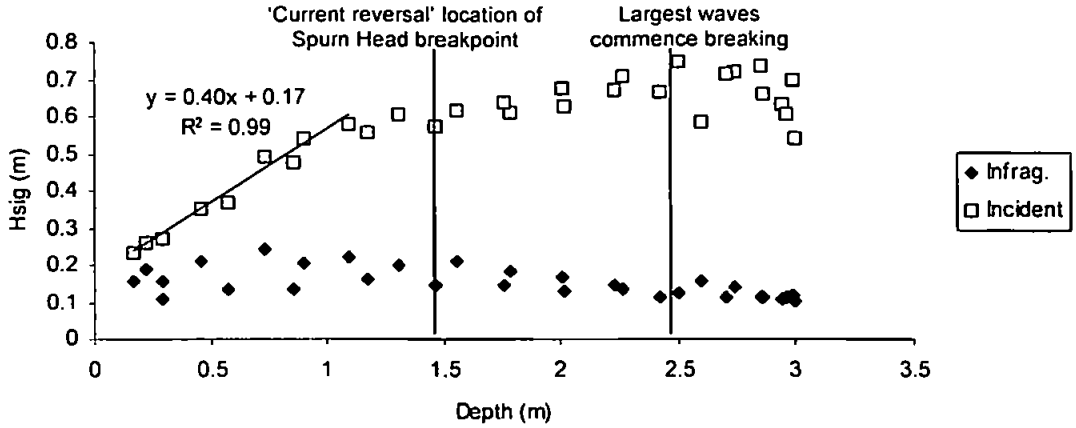

Figure 5.1.3a Distribution of incident and infragravity banded significant wave height versus depth for Spurn Head. Regression line shows saturated wave breaking in shallow water.

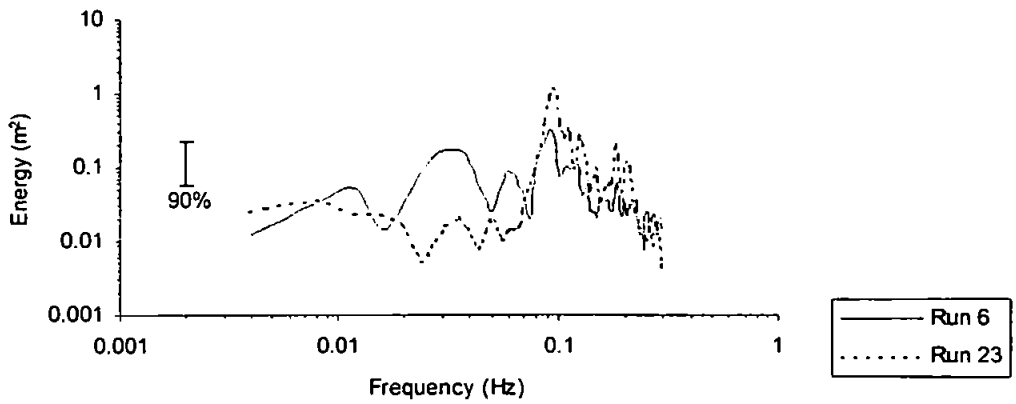

Figure 5.1.3b Evolution of η autospectra on flood tide, Spurn Head rig A2 runs 6 (h=0.74m) and 23 (h=2.71m).

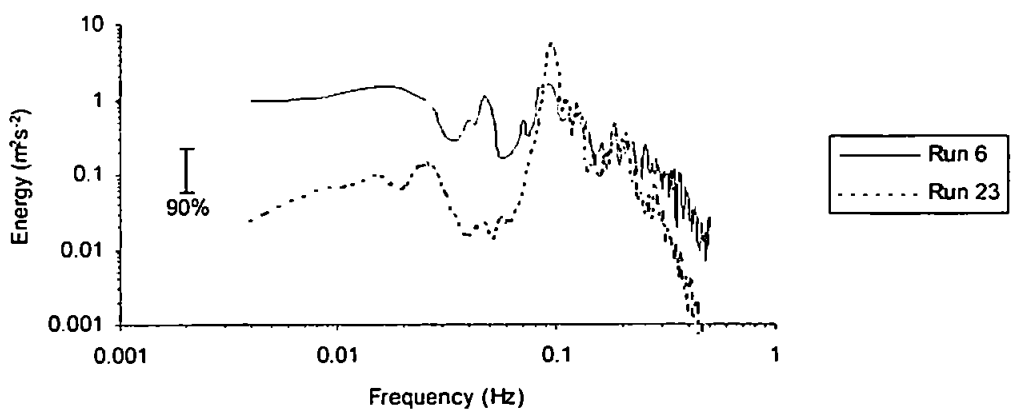

Figure 5.1.3c Evolution of u autospectra on flood tide, Spurn Head rig A2 bottom EMCM runs 6 (h=0.74m) and 23 (h=2.71m).

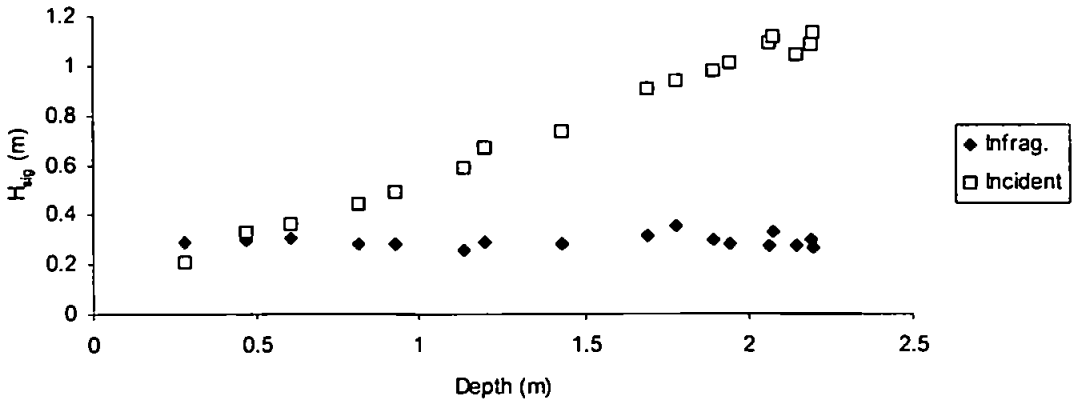

Figure 5.1.4a Distribution of incident and infragravity banded significant wave height versus depth for Perranporth.

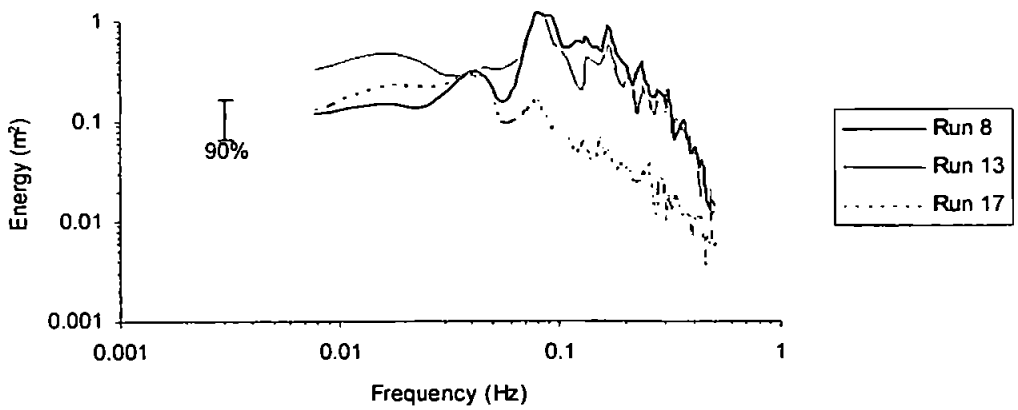

Figure 5.1.4b Evolution of η autospectra with decreasing depth, Perranporth runs 8 (h=2.14m), 13 (h=1.78m), 17 (h=0.61m).

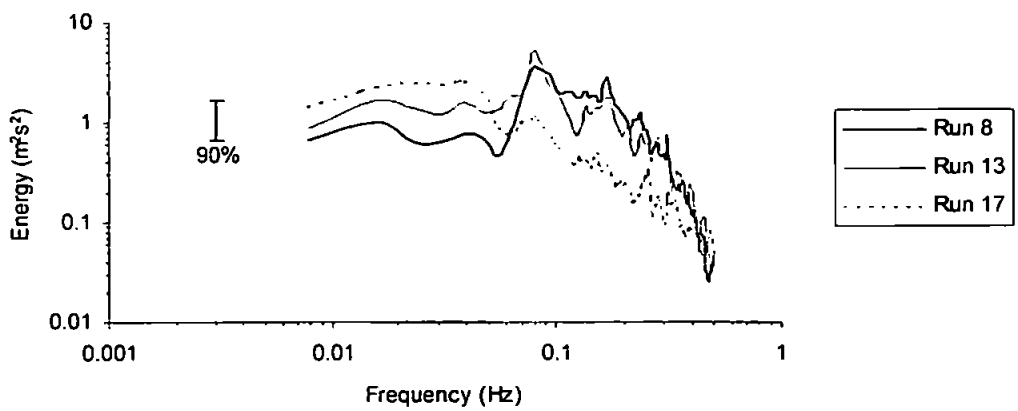

Figure 5.1.4c Evolution of u autospectra with decreasing depth, Perranporth runs 8 (h=2.14m), 13 (h=1.78m), 17 (h=0.61m).

5.1.2 Comparison of the three field sites

In following the conventions set out in chapter 2, the complete dataset may be described by changes in incident frequency wave behaviour and beach type. In the terms of the B-BAND programme, Spurn Head was defined as an intermediate beach, whilst Llangennith defined a dissipative example. From observations of wave height, the Perranporth data fits between the two other datasets, but the beach is more like Llangennith in that it has a low gradient topography. Thus at Perranporth the surf zone is considerably wider than at Spurn Head. Therefore the Perranporth site is considered in this work as dissipative.

The beaches are also rather different in terms of the incident wave field and their coverage of the hydrodynamically defined zones of the nearshore. As was shown in figures 5.1.1a-c, the Spurn Head data covers the shoaling zone and outer and inner surf zones, whilst only the inner surf zone is described by the Llangennith and Perranporth datasets. The observations from both of these latter sites were made through relatively wide inner surf zones right up to the edge of the swash zone. In energetic terms, the Llangennith data observed the largest wave heights (H_{sig} between 2.5 and 3m at breaking), and hence the largest surf zone width, and the longest incident frequency peak wave period (approximately 12-15 seconds). From a combination of the data and visual observations it is suggested that the Llangennith wave field possesses the strongest swell component in comparison to the local sea. At Llangennith a strong undertow was observed.

Spurn Head also experiences a significant cross-shore mean current, which changes in orientation from being offshore directed in the surf zone to onshore directed in the shoaling zone. Whilst the breakers at Spurn Head have the smallest heights in the whole dataset (H_{sig}<1m), visual observations made by the experimenters still points to these waves having had a more well formed 'groupy' offshore structure than was observed at Perranporth. In the Perranporth data, although conditions were reasonably energetic (breaker H_{sig} approximately 2m), the waves were a result of a wind driven local sea. The mean current observed at Perranporth was almost negligible.

The distribution of wave energy through the frequency domain at the three sites is examined in figure 5.1.5 which shows sea surface elevation autospectra from the three datasets, taken from runs when the instruments were in approximately 1m of water. The three spectra are compared directly by normalising the y-axis with respect to the Nyquist frequency to give a spectral density value. A significant increase in infragravity frequency

energy is observed from the Spurn Head run to the Perranporth run, with a further increase to the Storm Day run. Whilst the Storm Day run has most of this energy at the lowest frequencies, at Perranporth the peak energy is observed at a higher infragravity frequency. Peaks at the primary incident wave frequency can be seen in the spectra of all three runs, but this peak dominates in the Spurn Head case. At higher frequencies (>0.3Hz) the spectral 'roll-off' follows an identical relationship for all three spectra, which linear regression showed to be based on f^{-2} (with r^2=0.9). This suggests a uniform behaviour for frequencies above the dominant incident wave frequency for all the sites in the dataset.

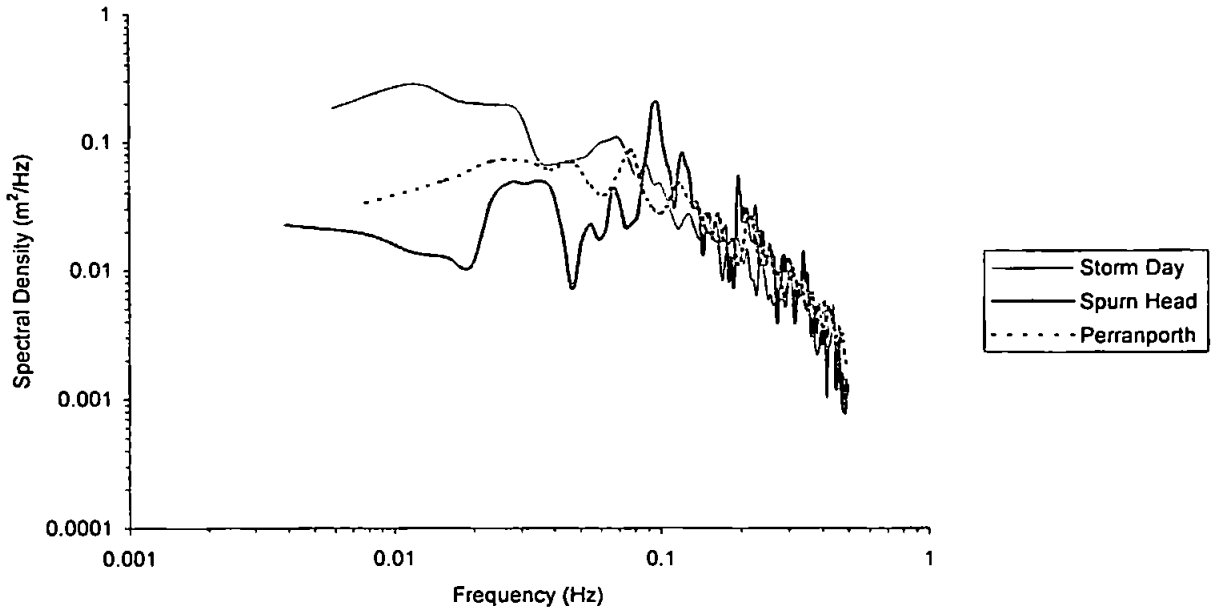

Figure 5.1.5 Comparison of the (normalised) η spectrum observed during the Storm Day, Spurn Head and Perranporth tides, when depth of water at the instruments was approximately 1m. Runs are Storm Day run 7 (h=0.9m), Spurn Head run 7 (h=0.9m), Perranporth run 16 (h=0.93m).

5.1.3 Normalised parameters for a comparison of the data

As an aside to the main results, this subsection sets out two parameters which will be used in comparison of data from the three beach sites during this chapter and chapter 6. Both parameters aim to provide a description of instrument position in the nearshore. The first is a 'normalised cross-shore distance' derived from the division of instrument depth by an assumed depth for the onset of breaking (h/h_b), following Russell and Huntley (1999). This scheme sets the shoreline at h/h_b=0 and the breaker line at h/h_b=1. Thus for values of less than 1, data is observed from the surf zone, whilst for values greater than 1 observations are taken from the incident wave shoaling zone.

This scheme may be subject to some error in its use of a fixed value for the break point, whereas in fact wave breaking will commence over a wider breaking zone. However, the method at least defines a clear point at which the surf zone can be said to start. At Spurn Head the breakpoint is defined by the depth at which the mean cross-shore current reversed, as indicated in figure 5.1.1c (h_b=1.5m). For the Llangennith and Perranporth data the break point depth is derived following Russell and Huntley (1999), by coupling an observed significant wave height at the onset of breaking with Weggel's (1972) onset of breaking value for γ of 0.78. For example, for the Llangennith Storm Day data, observed H_{sig} at breaking was 3m, which leads to a normalising h_b=3.85m. For Storm Night h_b=3.21m and for Perranporth h_b=2.56m. It is notable that the chosen breaker index is rather larger than that observed in the inner surf zone for either of these datasets (γ=0.42 at Llangennith and 0.55 at Perranporth). However, if as is predicted by the literature (e.g. Horikawa and Kuo, 1966), breaker index undergoes a sharp decrease between onset of breaking and the inner surf zone, using such (smaller) values could well serve to overpredict surf zone width.

In figure 5.1.6 this cross-shore normalisation is used to illustrate the entire dataset in terms of wave height, which has also been normalised by dividing by the observed breaker height. Thus in figure 5.1.6 the normalised wave heights at the breaker line should take a value of 1. In the Spurn Head data outside of the surf zone (h/h_b>1), normalised wave heights do increase beyond 1, indicating wave heights in deeper water which are larger than at the prescribed breaker line. Intuitively this would appear incorrect, but is a result of using the reversal of cross-shore mean current to define the breakpoint. In section 5.1 it was noted that this reversal occurred when breaking was near saturated and that offshore of this position outer surf zone conditions might be observed. Regarding this breakpoint

position in figure 5.1.3a, larger wave heights are observed offshore of the breakpoint than at the breakpoint, with the H_{sig} maxima occurring at a depth of approximately 2.5m. Thus runs in the depths between 1.5m and 2.5m experience outer surf zone conditions where only a few waves may have commenced breaking, whilst all waves are likely to be shoaling in depths greater than 2.5m. In terms of the normalisation scheme employed then, normalised wave heights can take values of greater than 1.

A clear difference in gradient of wave decay can be observed between the saturated and non-saturated surf zones in figure 5.1.6, with decay under saturated conditions being much steeper. However, a separation can also be seen between the Spurn Head data and those runs from Llangennith and Perranporth. This is partially a result of the suggested depth offset present in the Spurn Head data, and it is worth noting that if such an offset were applied, its effect would be to compress the distribution of the Spurn Head data points along the x-axis about the value 1. However, the data separation is also an effect of the way the saturated surf zone data from Llangennith and Perranporth has been normalised. By employing Weggel's (1972) onset of breaking criterion for normalising the surf zone rather than the observed saturated breaker index values, this scheme assumes that near the breaker line (where normalised wave heights will be equal to 1) wave heights will undergo a very sharp change in height just after the onset of breaking (Horikawa and Kuo, 1966). Such a change was not observed in the Spurn Head data.

Autospectra from the surf zone, as for example in figure 5.1.5, also show that the surf zones examined in this work show marked differences in infragravity wave energy. These characteristic differences in the surf zones at the three beaches are overlooked in the normalisation scheme proposed by Russell and Huntley (1999) but are likely to be particularly relevant to the processes examined in this study. Figure 5.1.7 shows the ratio of incident (gravity frequency) energy (E_g) to infragravity frequency wave energy (E_{ig}) plotted against normalised cross-shore position. The data shows a good degree of continuity between the shoaling zone (Spurn Head data) where E_g/E_{ig} is high, through to the saturated inner surf zone observed in the Perranporth, Storm Day and Storm Night data very close to shore. In this region, incident wave energy has diminished due to wave breaking whilst infragravity wave energy has increased due to wave shoaling. Therefore infragravity energy is dominant and E_g/E_{ig} is low. The ratio of gravity to infragravity energy does change quite dramatically through the nearshore, and this is reflected in the use of a logarithmic form for the y-axis.

For the data in this thesis, the facts that values of E_g/E_{ig} fit together well, and that E_g/E_{ig} decreases monotonically through the nearshore, mean that this factor may be coupled with the cross-shore normalisation described above to provide a second representation of the dataset. The parameter

$$\frac{h}{h_b}\frac{E_g}{E_{ig}}, \tag{5.4}$$

will define the nearshore in terms of energy-distance space, and will tend toward zero for infragravity dominated inner surf zones such as those in the Storm Day and Storm Night tides, and toward high values in the shoaling zone, where incident frequency waves will dominate. In the thesis this parameter will not be used to derive relationships for the data, nor is it intended for use outside of the thesis dataset. Instead it will be used solely for the purpose of describing categories of the nearshore zone which are represented by the individual tides of data from Llangennith, Spurn Head and Perranporth. For example, figure 5.1.8 illustrates the hydrodynamic characteristics of the data by plotting breaker index versus the above parameterisation.

Figure 5.1.8 shows that the majority of data from each of the three beach sites exhibits a different type of behaviour. Because of the large changes in the ratio of gravity to infragravity energy the x-axis is plotted in logarithmic form, but this also gives a more detailed picture of the surf zone. Also included in figure 5.1.8 are some intuitively defined boundaries and labels for the behaviour of the data with respect to its spatial position and relative energy contribution. Saturated wave breaking is defined for regions in the diagram where H/h values are reasonably constant, and take observed values of between 0.35 and 0.55.

The Llangennith (Storm Day and Storm Night) data comes almost exclusively from an infragravity frequency dominated saturated inner surf zone, whilst the Perranporth surf zone is also saturated, but is generally dominated by incident frequency wave energy. Interestingly, some high breaker index values can be observed in the data for runs close to shore when the surf zone is infragravity energy dominated. The Spurn Head data falls into the incident dominated wave shoaling zone, and non-saturated (outer) and saturated (inner) surf zones. This classification of the Spurn Head dataset has been made using the offset breaker index values (discussed in section 5.1.1), which are shown in figure 5.1.8 as the unfilled triangles. The Spurn Head breakpoint region is denoted in the diagram by x-axis values between 10 and 30 (between the solid lines). Some unwanted cross-over is observed in the data, for example data from the inner surf zone at Perranporth takes similar values to

data from the breaker line at Spurn Head. This cross-over was reduced by using the observed breaker index values from Llangennith and Perranporth in calculating h/h_b rather than the 0.78 employed in the normalisation scheme of Russell and Huntley (1999).

As a summary of the data therefore, figure 5.1.8 shows measurements being taken from;

- The incident wave shoaling zone, represented by Spurn Head data
- Incident wave dominated outer surf zone, Spurn Head data
- Incident wave dominated saturated inner surf zone, Perranporth and Spurn Head data
- Infragravity wave dominated saturated inner surf zone, Llangennith data.

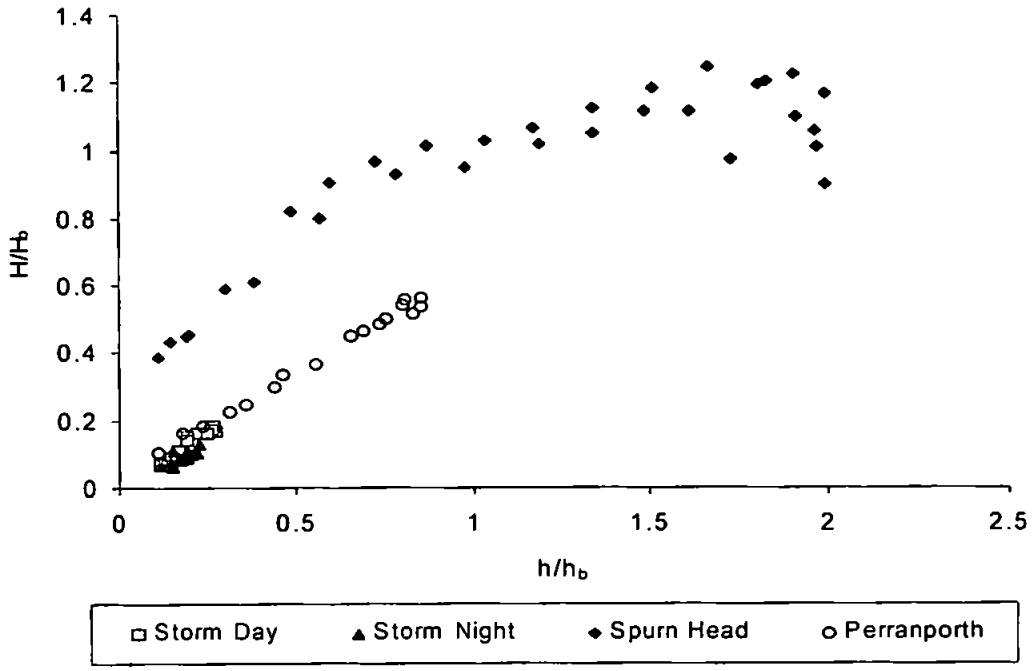

Figure 5.1.6 Normalised significant (gravity frequency) wave heights versus normalised surf zone position for the Llangennith (Storm Day and Storm Night), Spurn Head and Perranporth datasets. In the normalisation scheme the value 1 represents the breaker line.

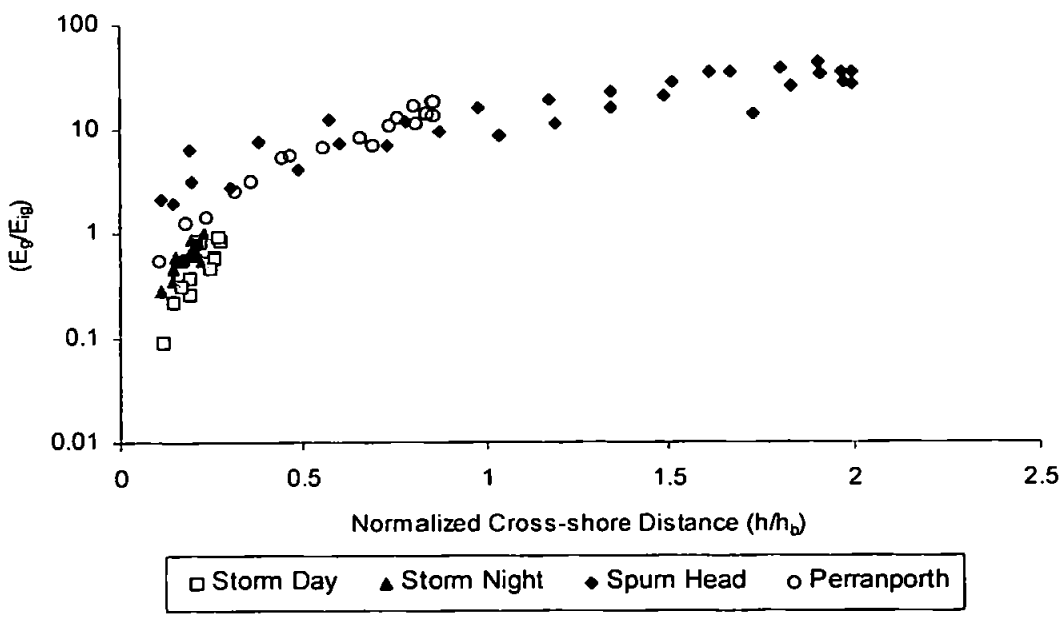

Figure 5.1.7 Ratio of gravity to infragravity frequency wave energy plotted versus normalised surf zone position for the Llangennith (Storm Day and Storm Night), Spurn Head and Perranporth datasets. In the normalisation scheme the value 1 represents the breaker line.

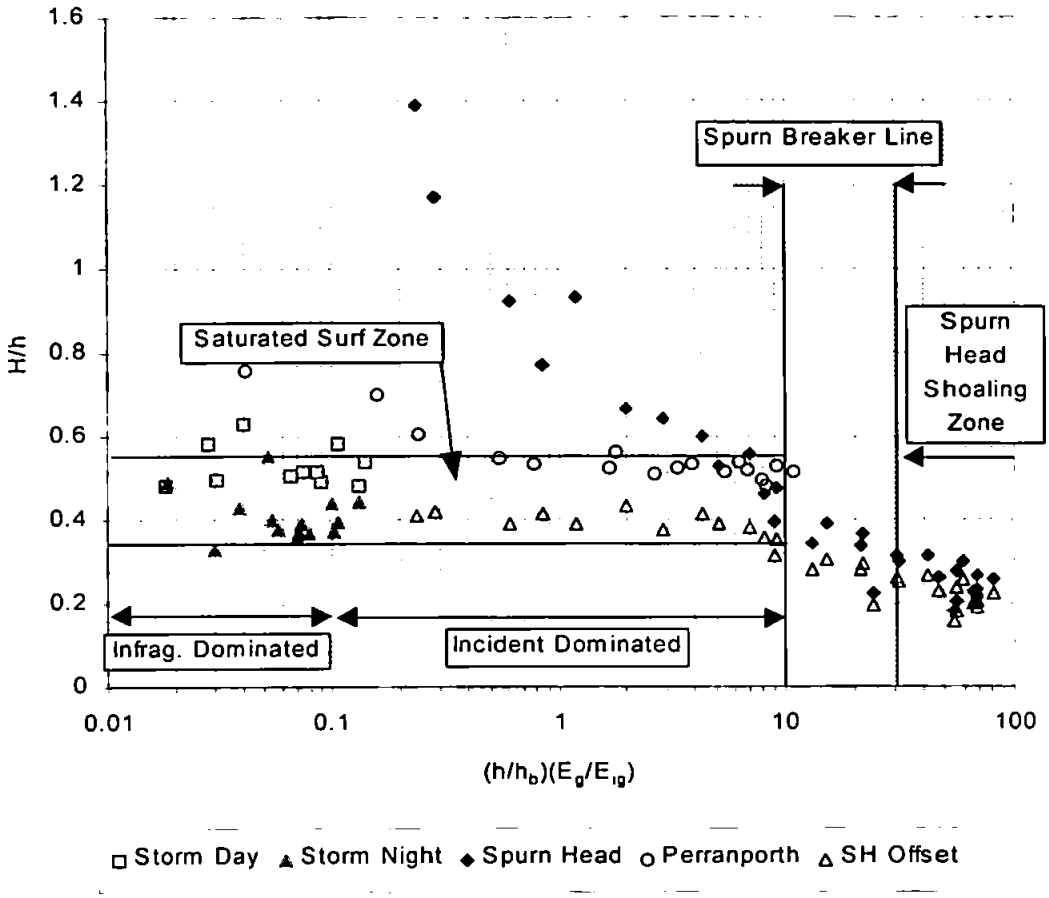

Figure 5.1.8 Distribution of breaker index values versus energy-distance space for the entire dataset. The *x*-axis parameter is a product of the ratio of gravity to infragravity frequency wave energy and the normalised surf zone position.

5.2 Nature of the infragravity wave field in the nearshore

The summary of beach sites in the previous section showed that the surf zone will vary in character according to the behaviour of the infragravity wave component. For example, the dataset shows incident wave energy dominating the Perranporth and Spurn Head runs for all but a few Perranporth runs, when the instruments were in very shallow water near to shore. Conversely, for the Llangennith data, and the Storm Day tide in particular, the surf zone is infragravity dominated. Storm conditions in this latter case described a well formed energetic swell incident on the beach, as opposed to Perranporth which was slightly less energetic and dominated by local sea waves, or Spurn Head where wave energy was substantially lower.

In investigating the way the infragravity component behaves in the nearshore, and in the surf zone in particular, it is necessary to describe the degree to which the incoming infragravity waves are free or forced by the gravity component, along with the extent to which the shoreward directed waves may be dissipated and reflected. Establishing the degree of infragravity wave reflection has ramifications for the formation of standing wave structures in the surf zone, which in turn affect the phase between the gravity and infragravity components making up the oscillatory part of the instantaneous velocity field.

5.2.1 The infragravity wave field at Llangennith

In terms of the thesis dataset, the Llangennith data contains the largest amounts of energy in the infragravity band. Following theoretical assumptions, this energy should be a result of incoming infragravity waves, which in the surf zone propagate shoreward as free waves, and are then reflected. The interaction between incoming and reflected waves may well form a standing wave field. With this in mind, and as a first step in examining the distribution of infragravity frequency wave energy, a comparison is made between the low frequency part of the sea surface elevation autospectrum from some of the Llangennith runs, and predicted standing wave spectra. The predicted spectra are based on the assumption of a fully developed standing wave field with a solution applicable to the case of a leaky wave or high mode edge wave. In generating the predicted spectra, the square of the amplitude of a zero order Bessel function solution for standing leaky waves was used, and it was assumed that 100% reflection occurred at the shoreline for all frequencies in the infragravity band.

The Bessel function solution for standing waves on a slope are expressed (following Hotta *et al.*, 1981) as,

$$\eta = aJ_0\left(2\sigma\sqrt{\frac{x}{g\tan\beta}}\right) + bY_0\left(2\sigma\sqrt{\frac{x}{g\tan\beta}}\right), \tag{5.5}$$

where J_0 and Y_0 are zero order Bessel functions, and a and b coefficients. σ is frequency, x is the distance from the reflection point, g acceleration due to gravity and $\tan\beta$ beach slope, and therefore elevation values will show a sensitivity to both beach slope at the position at which measurements are taken in the cross-shore. For reflection at the shoreline $Y_0 \rightarrow 0$, and thus b must also be set to zero (Davidson *et al.*, 1993). Therefore for a simple planar beach such as Llangennith,

$$\eta = aJ_0\left(2\sigma\sqrt{\frac{x}{g\tan\beta}}\right). \tag{5.6}$$

Figure 5.2.1 shows such a function plotted against frequency-distance space,

$$\frac{\sigma^2 x}{g\tan\beta}. \tag{5.7}$$

The diagram indicates that for a given position in the cross-shore, different frequencies will show a response with differing levels of energy if standing waves are formed. Maximum amplitude is found at an antinode, and zero amplitude at a node.

The predicted spectrum is made up of points taken at discrete frequencies, corresponding to the spectral bin frequencies used in the analysis, although a white spectrum is assumed (i.e. input energy for the model will be the same at all frequencies). The predicted spectrum will not necessarily show a zero in energy corresponding to nodal behaviour, but should give a good indication of the peaks and troughs that might be expected to be seen in a spectrum derived from standing waves. Conversely, a broad banded progressive wave field would see a spectrum almost devoid of peaks and troughs. This comparison assumes a strictly two dimensional case for wave energy distribution and ignores the possible coexistence of low mode edge waves on this beach. However, in comparing infragravity frequency cross-shore and longshore velocities during the Llangennith tides longshore variance was found to be an order of magnitude less than that in the cross-shore. This suggests that the two dimensional assumption should be applicable in this case.

In figures 5.2.2 and 5.2.3, and similar plots in the next two subsections, the predicted spectral energy levels have been rescaled to allow a qualitative comparison between the theoretical and observed results. Figures 5.2.2 and 5.2.3 show respectively this comparison for water depths of approximately 0.75m and 1m. The change in the predicted spectrum

between these depths is quite substantial, with a smoothing of the lower end of the infragravity range of the spectrum as the depth increases, whilst higher in the infragravity band (0.04-0.05Hz) peak to trough amplitude increases. For all the runs, rather smoother spectra are produced by the observed sea surface elevation time-series. For run 9 (figure 5.2.2) and runs 4 and 6 (figure 5.2.3) variation in energy levels qualitatively similar to those predicted by a standing wave type can be seen in the infragravity band for frequencies less than 0.03Hz. Similar good agreement with a partially standing wave form for the infragravity frequencies was observed by Davidson (1991). However, for infragravity frequencies in the range 0.03-0.05Hz, particularly for run 9 (figure 5.2.2), where the instruments are in shallower water, the comparison between the spectrum predicted by the standing wave model and the spectrum derived from the observations is poor.

A reason for this lack of agreement between the standing wave model and observations at higher infragravity frequencies could well lie in the amount of infragravity energy being reflected from the beach. Values of reflection coefficient (R^2) through the frequency domain for the Storm Day and Storm Night runs are shown in figure 5.2.4, which shows strong, but not complete, reflection of waves at the lowest frequencies (R^2 is approximately 0.5). Thus a significant proportion of the energy in the infragravity part of the spectrum is lost during reflection, and therefore the autospectra should show a degree of progressive wave type behaviour. Higher in the infragravity band, reflection coefficients are lower again. However, a further feature of these diagrams is an increase in the reflection coefficient at higher frequencies (>0.02Hz) corresponding to a decrease in the distance of the sensors from the shoreline (the highest and lowest run numbers, note that in general the Storm Night observations are taken from nearer to the shoreline than those from Storm Day).

This effect may be seen rather more clearly in figure 5.2.5, which compares the spatial distribution of reflection coefficient at a lower (0.01172Hz) and higher (0.02344Hz) infragravity frequency bin. In the figure, the largest depth values see the instruments furthest offshore. At the lower frequency, the values of reflection coefficient, although scattered, generally show only a slight drop off with increasing depth. A more distinct curve is seen for the higher frequency however, and this effect can be attributed to dissipation of wave energy at the higher frequency (Baquerizo *et al.*, 1997). To explain this it is necessary to consider the relationship between the incoming and outgoing waves.

Initially an assumption is made that an incoming wave is breaking, such that incoming wave height is described as

$$H_{in} = \gamma h, \tag{5.8}$$

where γ is the breaker index and h depth. A reflected wave will follow the free wave deshoaling relationship, where

$$H_{ref} \propto h^{-1/4} \text{ (c.f. List, 1987).} \tag{5.9}$$

As a result, and assuming a constant value for γ, the reflection coefficient (R^2) should be related to depth as $h^{-5/2}$. Hence for a situation where the waves are being dissipated, as depth decreases the value of reflection coefficient should increase.

In figure 5.2.5 the above relationship has been plotted for comparison with the behaviour of the higher infragravity frequency. Both the predicted and observed values show the same trend for decrease in R^2 with increasing depth, although the predicted decrease is rather sharper than that of the observations. This is not surprising since for infragravity frequencies the sort of saturated wave breaking associated with a constant breaker index will not provide the mechanism for dissipation of infragravity wave energy, and thus a rather more energetic reflected signal would be expected than in the case described above. Nonetheless the behaviour of the higher infragravity frequencies do suggest that dissipation is taking place for incoming waves at these frequencies, whilst this is not apparent in the case of the lowest frequency infragravity waves.

Over the infragravity band as a whole, an examination may also be made of the shoaling/deshoaling properties of the incoming/reflected waves. Figure 5.2.6 shows, for Storm Day and Storm Night runs, significant wave heights for the incoming and reflected infragravity components. The values were derived from the incoming and outgoing sea surface elevation signal spectra. In the figures, whilst the reflected wave heights are smaller, both components see an evolution of wave height with depth consistent with the shoaling relationship for a constant energy flux,

$$H \propto \left(\frac{1}{h}\right)^{1/4}, \tag{5.10}$$

where H denotes wave height and h depth (c.f. List, 1987). In figure 5.2.6 this relationship (for the incoming waves) is represented by the dotted line. The relationship follows linear theory and suggests that both incoming and reflected components act as free waves in the surf zone with insignificant dissipation.

Relating this last result to the previous statements, it would appear that for Storm Day and Storm Night the infragravity wave energy is dominated by the lowest frequencies. These lowest frequency incoming waves are free in the region of the surf zone observed and only slightly dissipated at the reflection point. Higher in the infragravity band however, the distribution of the reflection coefficient implies that some dissipation of energy occurs as the waves propagate shoreward, but the loss of energy at these frequencies does not significantly affect the evolution of infragravity energy when computed over the whole band.

Also of interest in an analysis of wave reflection is establishing a reflection point for the incoming waves. Here an examination was made using the (time-domain) correlation between the derived incoming and reflected low frequency signals obtained from the Storm Night runs. The distribution of lag times is shown in figure 5.2.7, plotted against values for the predicted cross-shore position of the sensor array. Figure 5.2.7 also shows the results of a regression analysis between the observed lags and the lag times predicted using linear theory. This derivation follows the method employed by Masselink (1993) for a plane beach, but allows for a reflection point at any specified point in the cross-shore. Thus lag time is given by

$$Lag = \frac{4}{\sqrt{g \tan\beta}}\left[x^{1/2} - x_R^{1/2}\right], \tag{5.11}$$

where g is acceleration due to gravity, $\tan\beta$ is beach slope, x is the cross-shore position of the instrument, and x_R is position of the reflection point.

One source of error in assessing lag time might arise from using a value of x (derived from depth of water at the sensors) which ignores wave induced set up at the shoreline. To allow for this a correction factor was applied to the cross-shore position using

$$\frac{\partial\overline{\eta}}{\partial x} = \left(\frac{1}{1+8/3\gamma^2}\right)\tan\beta, \tag{5.12}$$

(Komar, 1998), where $\partial\overline{\eta}$ is the set-up value, $\tan\beta$ is beach slope and γ is the breaker index (for Storm Night γ=0.45). When this is applied to a derivation of the distance from sensor to shoreline (x') the solution is given by

$$x' = \frac{\overline{\eta}_o}{\tan\beta}\left(1 + a + a^2 + \ldots\right), \tag{5.13}$$

where $a = \left(\frac{1}{1+8/3\gamma^2}\right)$, and $\overline{\eta}_o$ is the observed mean depth at the sensor. Therefore,

$$x' = \frac{\overline{\eta}_o}{\tan\beta}\left(\frac{1}{1-a}\right), \tag{5.14}$$

and thus for the Llangennith datasets yields values of

$$x' = 1.075\frac{\overline{\eta}_o}{\tan\beta}. \tag{5.15}$$

The value of x_R used was derived by finding the best fit for the predicted lag equation to the observed data (r^2=0.80). Thus figure 5.2.7 suggests a reflection point for the lowest frequency infragravity waves of 2.4m from the mean shoreline position. This corresponds to an extremely shallow water depth of 3cm. If it is borne in mind that the shoreline position will in actuality have a dynamic variation in the cross-shore and that the waves being reflected have heights significantly larger than 3cm, then this calculated reflection point can be reasonably considered as being at the shoreline.

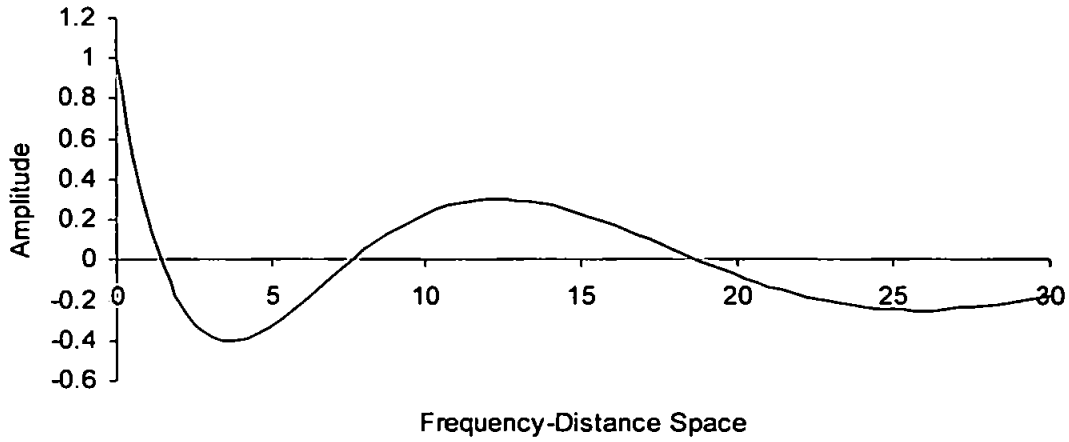

Figure 5.2.1 Schematic of a Bessel function plotted in frequency-distance space.

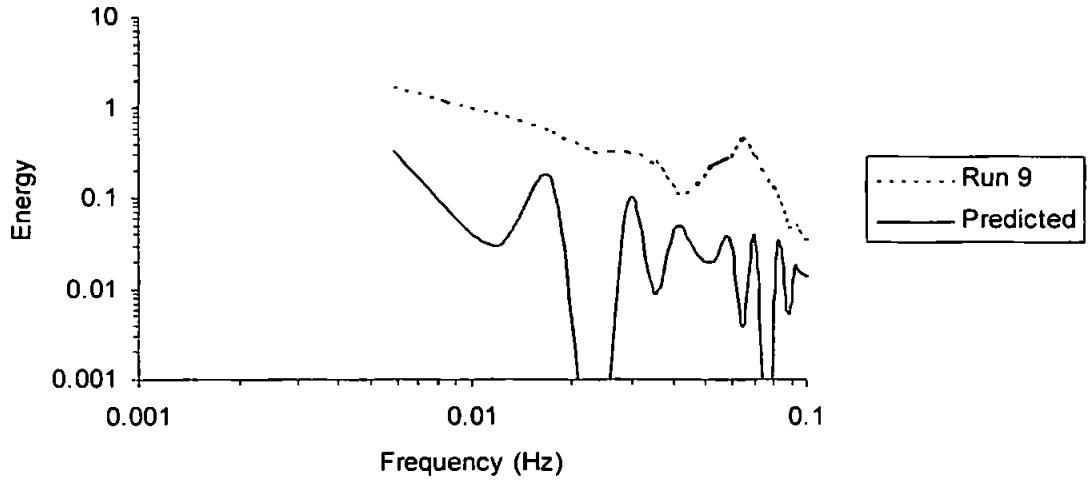

Figure 5.2.2 Comparison between predicted and observed sea surface elevation (η) spectra, Storm Day run 9. Water depth h=0.75m.

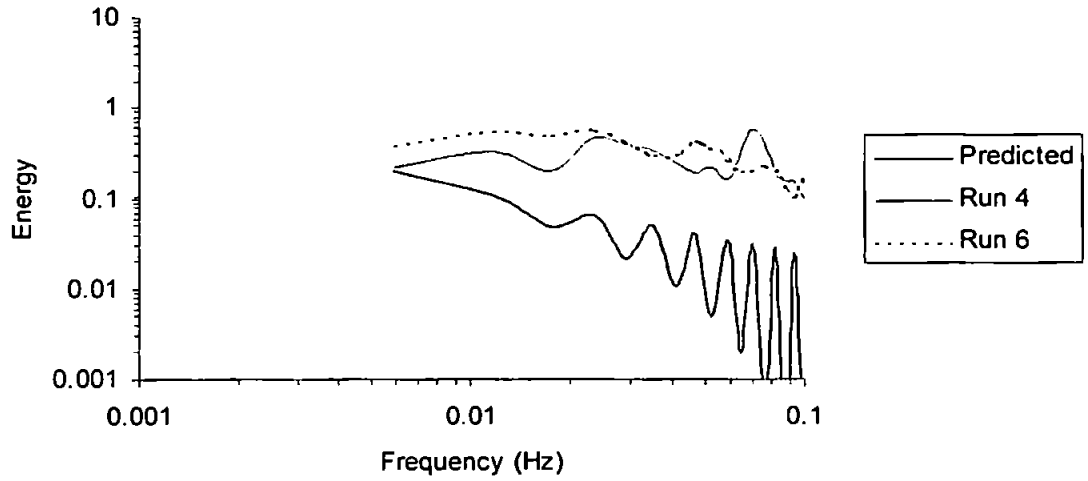

Figure 5.2.3 Comparison between predicted and observed sea surface elevation (η) spectra, Storm Day runs 4 and 6. Water depth h=1m.

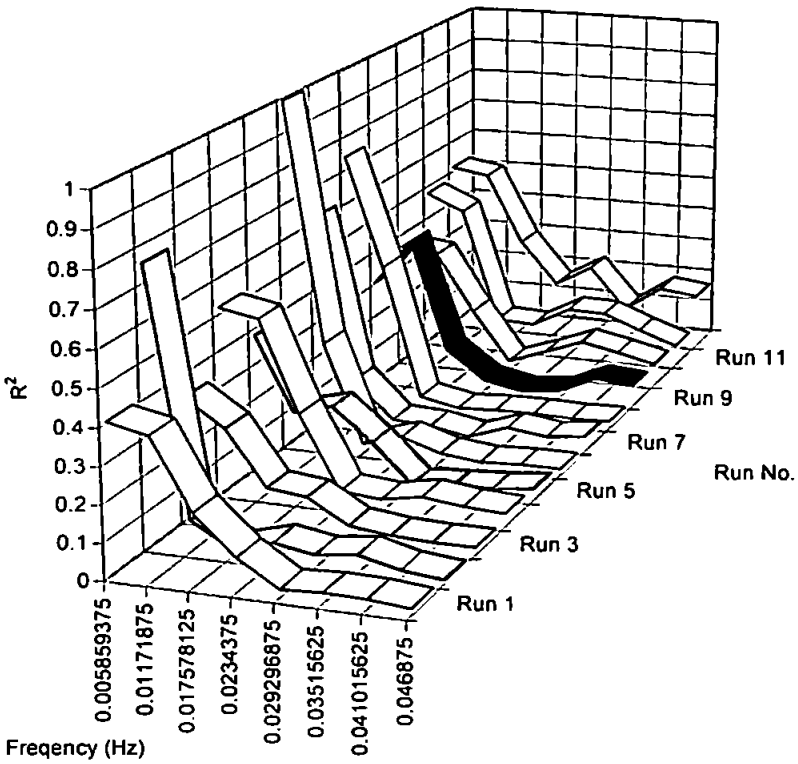

Figure 5.2.4a Values of R^2 for infragravity frequencies from Storm Day runs.

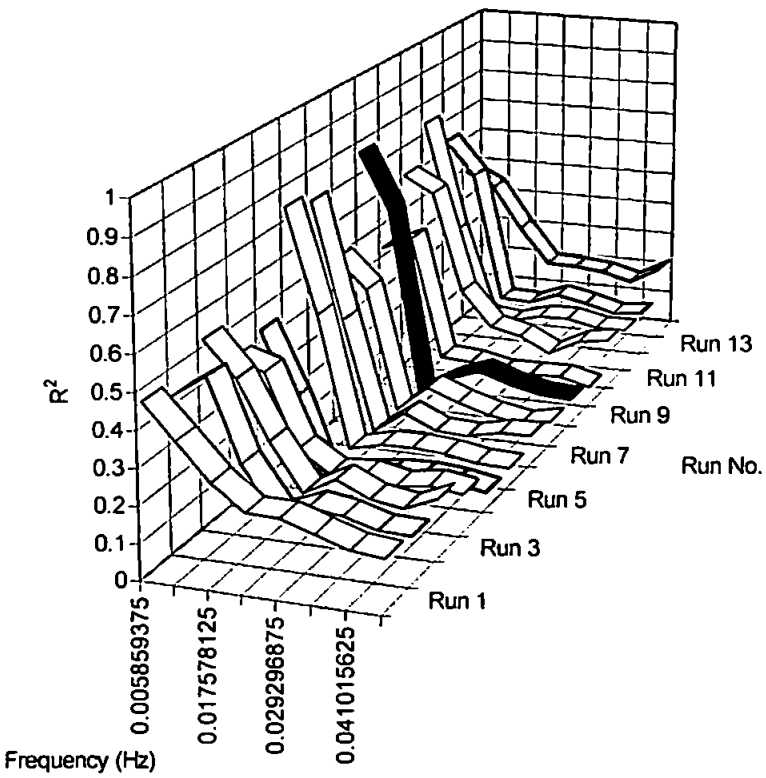

Figure 5.2.4b Values of R^2 for infragravity frequencies from Storm Night runs.

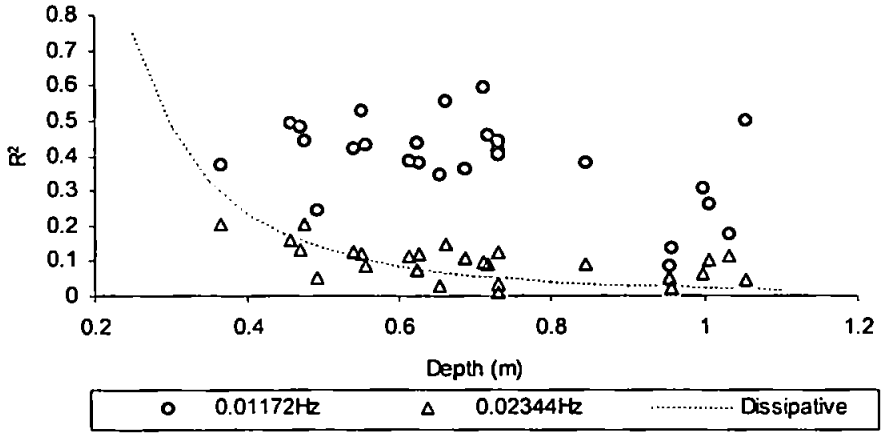

Figure 5.2.5 Comparison of Llangennith R^2 values versus depth for frequency bins at 0.01172Hz and 0.02344Hz. The dotted line indicates results of a dissipative type model.

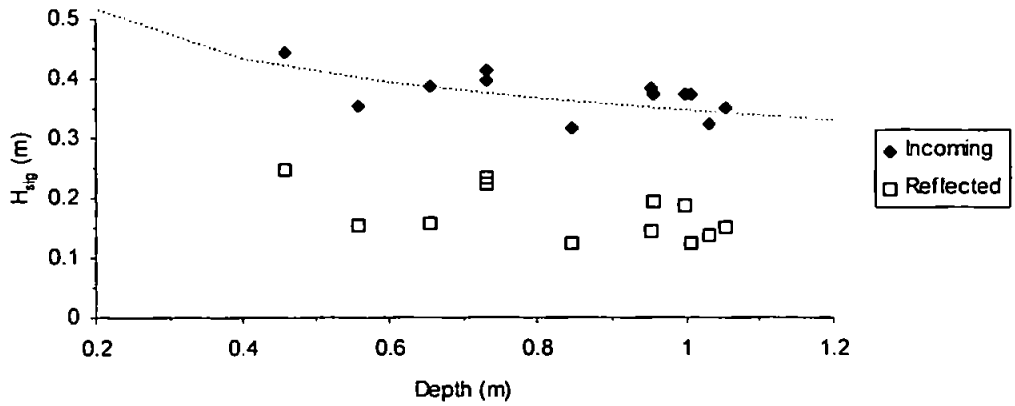

Figure 5.2.6a Incoming and reflected (total) infragravity frequency significant wave heights for Storm Day runs, the dotted line shows predicted shoaling of an incoming free wave using linear theory.

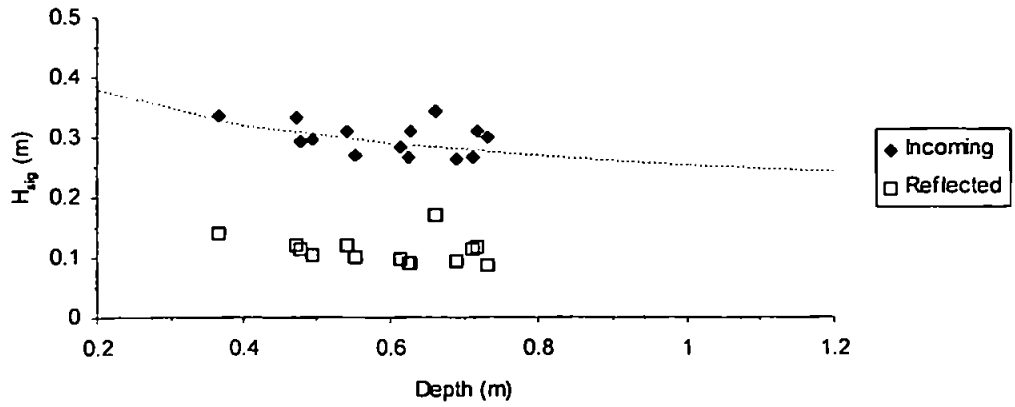

Figure 5.2.6b Incoming and reflected (total) infragravity frequency significant wave heights for Storm Night runs, the dotted line shows predicted shoaling of an incoming free wave using linear theory.

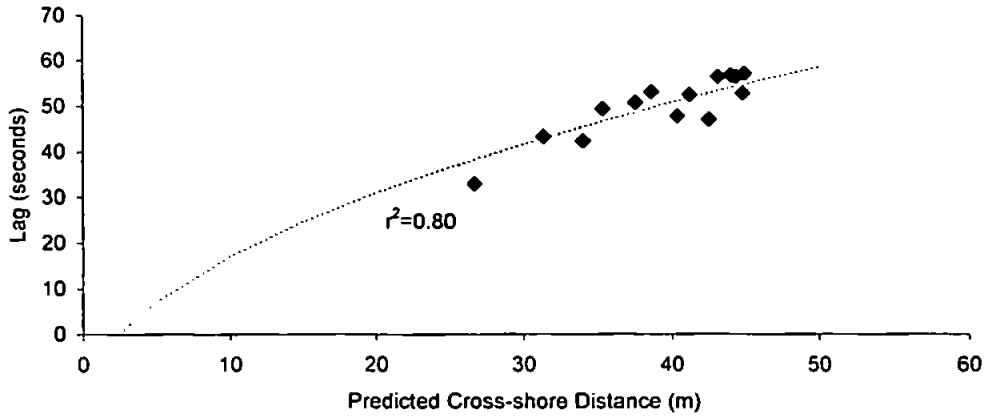

Figure 5.2.7 Spatial distribution of observed lag times for infragravity wave return from Storm Night runs. Dotted line shows regression for a linear theory prediction of lags.

5.2.2 The infragravity wave field at Perranporth

Figures 5.2.8 and 5.2.9 show a predicted standing wave spectrum and observed spectra for a number of runs taken from the Perranporth dataset. Again this two dimensional comparison is deemed valid by virtue of the fact that longshore low frequency velocity variance was found to be less than 20% of that in the cross-shore. For the Perranporth runs the comparisons between the predicted and observed spectra are poor This is particularly true for frequencies greater than approximately 0.02Hz, where observed peaks in energy are seen for frequencies that in the predicted spectra yield troughs. Unlike Llangennith, higher frequencies appear to provide an equally significant contribution to energy in the infragravity part of the spectrum when compared to the lower infragravity frequencies. If this is the case, the inference is that a strong progressive component may exist in the infragravity signal.

As evidence of this, figure 5.2.10 shows high reflection coefficients (R^2>0.5) only in the lowest infragravity frequency bins, which would suggest that only lower infragravity frequencies will have their energy reflected sufficiently to form partially standing wave structures. This may be seen further in figures 5.2.11 and 5.2.12 which show the incoming and reflected wave spectra for run 2 (h=0.81m) and run 12 (h=1.95m) respectively. A comparison of the figures shows incident frequency wave energy not only dissipated in the inner surf zone, but further diminished after reflection. The infragravity band observes a small increase in incoming higher frequency infragravity energy between deep and shallow water (at 0.02Hz). In both figures however, the majority of energy at the lowest frequencies is returned, whereas higher infragravity frequency energy is reduced in the reflected signal.

Infragravity wave heights remained at roughly the same value throughout the Perranporth surf zone in figure 5.1.4. Similarly the derived incoming wave heights (figure 5.2.13) show no major increase across the surf zone, and thus it appears that incoming infragravity waves both shoal and are dissipated in this region. Furthermore, the reflected wave energy, which is dominated by the lower infragravity frequencies, is much reduced in comparison to the incoming energy (figure 5.2.13). This again suggests that at Perranporth the infragravity part of the incoming wave spectrum is dominated by energy at the higher frequencies. This is different from the case observed at Llangennith, where lower infragravity frequencies dominated the spectrum and wave shoaling was observed in the surf zone (figures 5.2.6a and b).

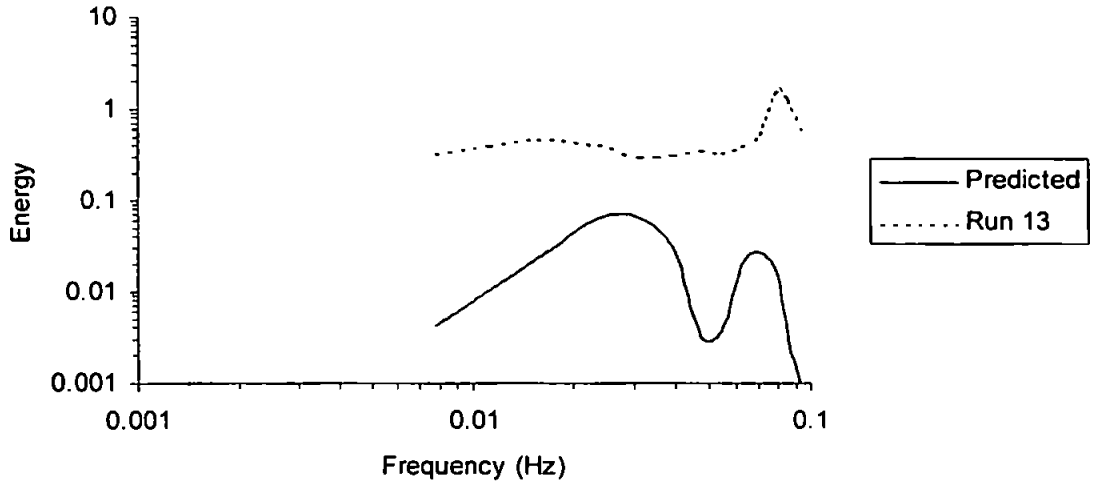

Figure 5.2.8 Comparison between predicted and observed sea surface elevation (η) spectra, Perranporth run 13 (h=1.78m).

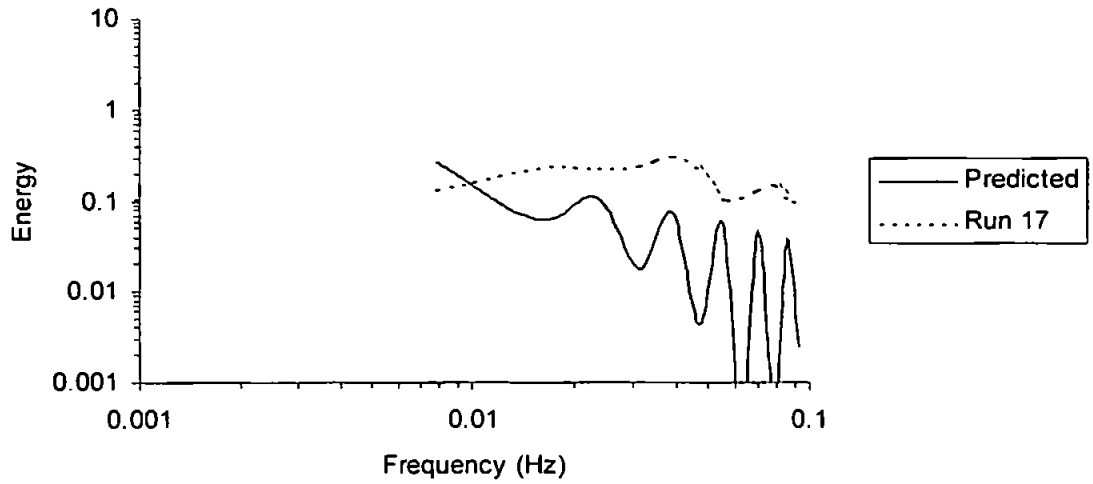

Figure 5.2.9 Comparison between predicted and observed sea surface elevation (η) spectra, Perranporth run 17 (h=0.61).

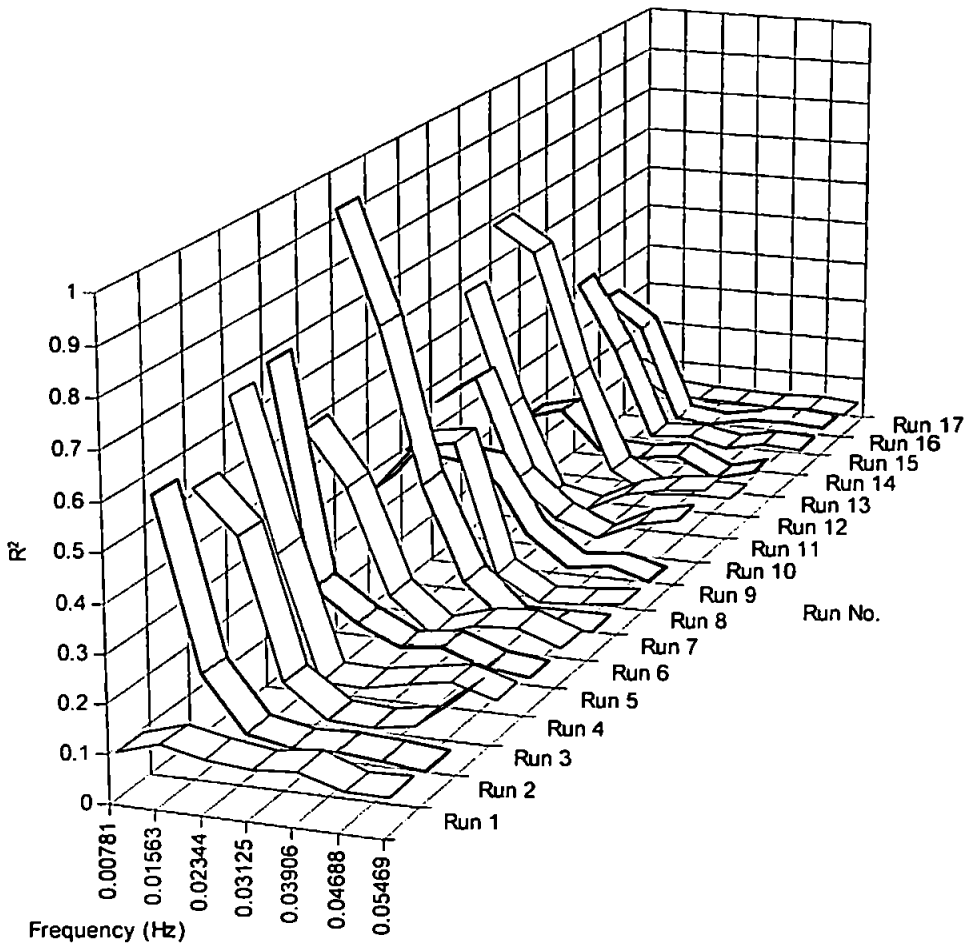

Figure 5.2.10 Values of R^2 for infragravity frequencies from Perranporth runs.

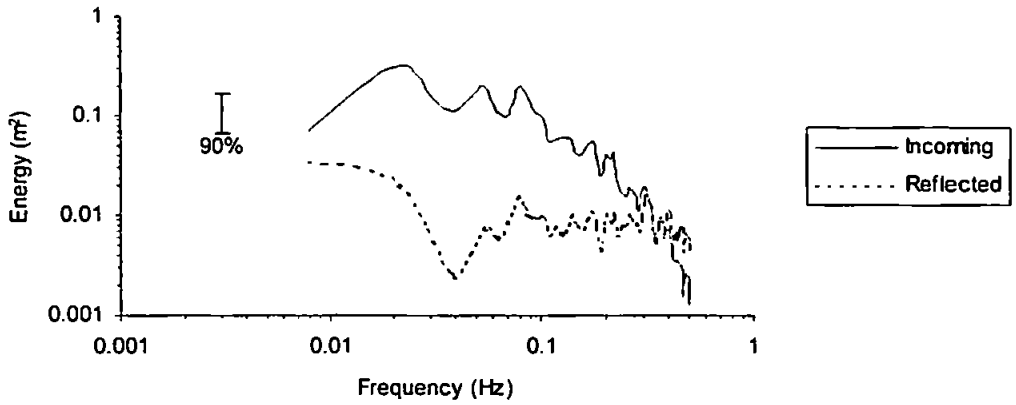

Figure 5.2.11 Incoming and reflected η spectra for Perranporth run 2 (h=0.81m).

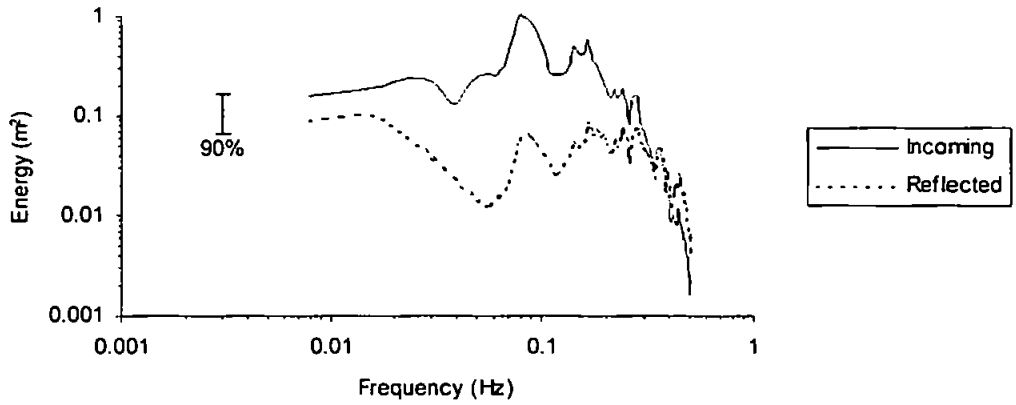

Figure 5.2.12 Incoming and reflected η spectra for Perranporth run 12 (h=1.95m).

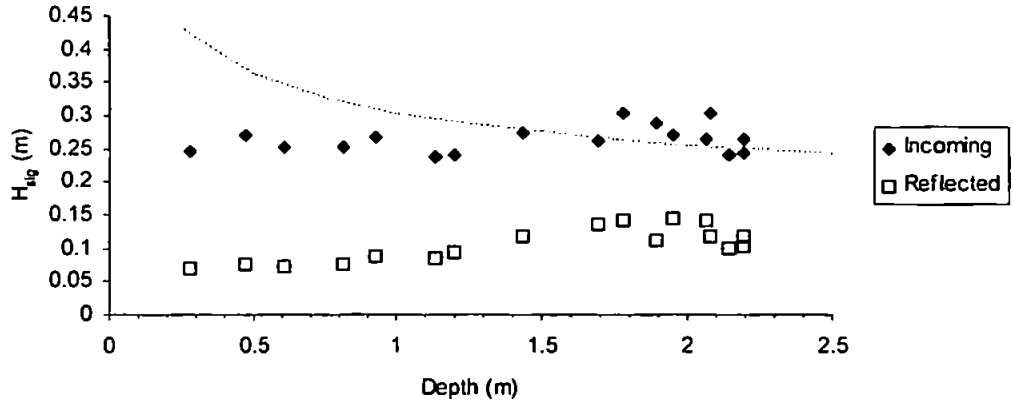

Figure 5.2.13 Incoming and reflected (total) infragravity frequency significant wave heights for Perranporth runs, the dotted line shows predicted shoaling of an incoming free wave using linear theory.

5.2.3 The infragravity wave field at Spurn Head

The Spurn Head profile consists of a steep high tide beach ($\tan\beta$=0.1) and lower gradient low tide terrace ($\tan\beta$=0.0235). To obtain predicted sea-surface elevation spectra in this case the Bessel function solution for a convolution of slopes presented by Davidson *et al.* (1993) was employed. Figures 5.2.14-16 suggest that at Spurn Head the observed spectrum is far better resembled by a standing wave type solution than at Llangennith or Perranporth. In one way this result is surprising in that for Spurn Head a significant amount of low frequency variability was observed in longshore velocity measurements (approximately 50% of that in the cross-shore), and therefore edge waves of low mode might have been expected to bias the observations. The good agreement in this case possibly suggests that for this data edge wave energy takes a high mode form, which has a similar cross-shore structure to the leaky mode solution used in the predicted spectrum.

The suggestion of standing wave activity occurring in the Spurn Head data is reinforced by a cross-spectral analysis of the sea surface elevation signals taken simultaneously from the PTs at rigs Al and A2. These instrument rigs were placed approximately 20m apart on a shore normal transect, with rig A1 nearest to the high water line. Theoretically, if standing waves formed then the two sea surface elevation signals should be coherent and have zero phase, or otherwise show near zero coherence if one of the instruments is coincident with a node. Here this analysis is illustrated for run 16, when the instruments were located outside of the surf zone (figure 5.2.17). In the figure incident wave frequencies are included as an example of the behaviour expected in the spectra for a progressive wave type. Figure 5.2.17 shows that the most energetic and coherent part of the spectrum is found in the infragravity band. At these frequencies the signals have a phase of zero, as opposed to the phase of 120° observed at the incident wave frequencies. Whilst the incident wave phase yields a lag time similar to that between the two points derived from linear wave theory, the zero phase at lower infragravity frequencies is indicative of a standing wave form.

For analysis purposes, one consequence of standing wave behaviour at these frequencies is that, within the infragravity band for any given spectrum, spectral troughs cannot necessarily be used to interpret that wave energy is not present for a given frequency through the nearshore as a whole. Nonetheless, a comparison between the three runs in figures 5.2.14-16, which correspond in order to a decreasing depth of water at the instruments, does hint at a relatively strong contribution to overall infragravity band energy being made by the higher infragravity frequencies.

With respect to the reflection analysis at the other two field sites, the fact that the Spurn Head observed sea surface elevation spectra resemble a standing wave solution would suggest that frequency dependent reflection coefficients at Spurn Head should be generally high compared to those at Llangennith and Perranporth. In figure 5.2.18, which shows values for R^2 at (bin) frequencies representing the lower (0.01172Hz) and higher (0.0273Hz) parts of the infragravity band plotted versus depth, this is seen to be true for the majority of runs, since reflection coefficients at both frequencies are near to 1 in many cases. However, at the higher infragravity frequency, the runs in the shallowest water depths correspond to a rather lower reflection coefficient. Also plotted on figure 5.2.18 is the beach slope at the shoreline versus depth at the instruments (dotted line), and an almost direct correspondence between this and the R^2 value at the higher infragravity frequency may be seen. These low reflection coefficients, associated with low beach gradient are more like the values seen at higher infragravity frequencies at Llangennith and Perranporth; sites which also have low beach gradients. This frequency-gradient dependence is examined further in the next section.

The change in the reflection coefficient at higher infragravity frequencies may well be responsible for the distribution of incoming and outgoing infragravity wave heights at the shallowest depths, as shown in figure 5.2.19. The figure shows wave height increasing with decreasing depth for the majority of runs. However, for those values where depth is less than approximately 0.75m, wave heights are diminished. Examining the distribution of wave height for depths greater than 0.75m first, inside and just outside of the breakpoint incoming and outgoing wave heights (which are derived from energy over the entire infragravity band) follow the free wave shoaling relationship and are of similar value. This suggests that for measurements made in this region the infragravity wave energy is free and almost fully reflected. Further outside of the surf zone the increase in wave height with decreasing depth is rather sharper, but is not as steep as is predicted by the bound wave shoaling relationship

$$H \propto \left(\frac{1}{h}\right)^{5/2}, \tag{5.16}$$

calculated by Ottesen-Hansen *et al.* (1981). This is not necessarily surprising since it is thought that in this region of the nearshore the infragravity component may be beginning to separate from the wave groups that force it.

For depths less than 0.75m an explanation for the decrease in wave heights may be found by considering the effect of the slope break at Spurn Head on wave shoaling and reflection. Marked on figure 5.2.19 is the depth at which the shoreline is coincident with a change in beach gradient, such that for depths greater than 0.75m waves will be incident on a shoreline with gradient of approximately 0.1. For depths less than 0.75m however, the shoreline is on the part of the beach with slope of less than 0.0235. This coincides with the change in wave behaviour seen in the figure. One explanation is that when the water depth at the instruments is small, the higher infragravity component is dissipated to some extent, due to the fact that the gradient at the instrument position is relatively low. This has been observed elsewhere in the results, and will mean that if the higher infragravity frequencies dominate the infragravity part of the spectrum, incoming wave heights may be less for these runs than when the water depth at the instruments is larger. However, reflection coefficients for these runs do not show any increase toward the shoreline as was observed at Llangennith, whilst shoreline gradient shows a decrease with decreasing depth (figure 5.2.18). This might suggest that in this instance more energy may be being lost in the reflection process than through dissipation of the incoming waves.

With this in mind, a comparison can be made between spectra of the incoming and reflected waves for one of the shallowest runs (run 2, h=0.22m, figure 5.2.20) and a run where the instruments are sited outside of the surf zone (run 16, h=2.74m, figure 5.2.21). A significant amount of energy at a higher infragravity frequency (>0.02Hz) is found in the incoming signal in the surf zone (run 2, figure 5.2.20), but is not fully reflected. However, outside of the surf zone the energy that is being reflected is seen to be of a similar value to that in the incoming signal. Therefore it would appear that inside the surf zone an increase in energy at approximately 0.03Hz occurs, but that some of this incoming energy is dissipated through the reflection process in run 2. This corresponds to when the waves are incident on the shallower shoreline beach slope. When the tide is sufficiently high for the shoreline to be positioned where the slope is steeper however (run 16), little energy in the infragravity band as a whole is dissipated. Thus when the shoreline slope is steep, the returning wave signal will retain much of the infragravity frequency energy, and therefore may well be of the same strength as that observed in the incoming waves near to or outside the breaker line.

This has a further consequence for the idea of standing wave structures being present in the Spurn Head data. In figure 5.2.17 the run 16 cross-spectrum between the sea surface elevation signals at two points through the cross-shore suggested standing wave behaviour

at infragravity frequencies. Figure 5.2.22 shows a similar analysis for run 2 and shows that whilst at the lowest frequencies a similar high coherence and zero phase is seen in run 2, two significant coherent peaks (at 0.02Hz and 0.04Hz) are found higher in the infragravity band. Both peaks show a phase lag of approximately 150°. At these frequencies the lag is significantly larger than that observed at the dominant incident frequency and suggests that these waves are not progressive. However, the fact that phase takes neither the 0° or 180° value expected for a pure standing wave, coupled with the lower reflection coefficients observed for run 2 suggests a partially standing wave form at the higher infragravity frequencies when shoreline slope is 0.0235.

The assumption of a reflection point at the shoreline (which was used for the predicted sea surface elevation spectra shown in figures 5.2.14-16) is checked in figure 5.2.23. The figure shows the phase relationship between the incoming and reflected component at the 0.0195Hz frequency bin for runs where the waves reflected from the high tide beach. The figure also shows a prediction of phase based on linear theory (equation 5.11) and a reflection point occurring at the shoreline. This comparison between the predicted and observed phase generally works well when reflection occurs at the steep gradient shoreline. In the early runs, where this prediction is not good, water depth at the slope break is low, and it may be that for these runs reflection occurs at this point rather than on the shoreline as was assumed in the model. Agreement between prediction and observations are also poor for run 20, but this could be an exception where the processing technique does not work well, possibly as a result of the relatively short time-series used in the analysis.

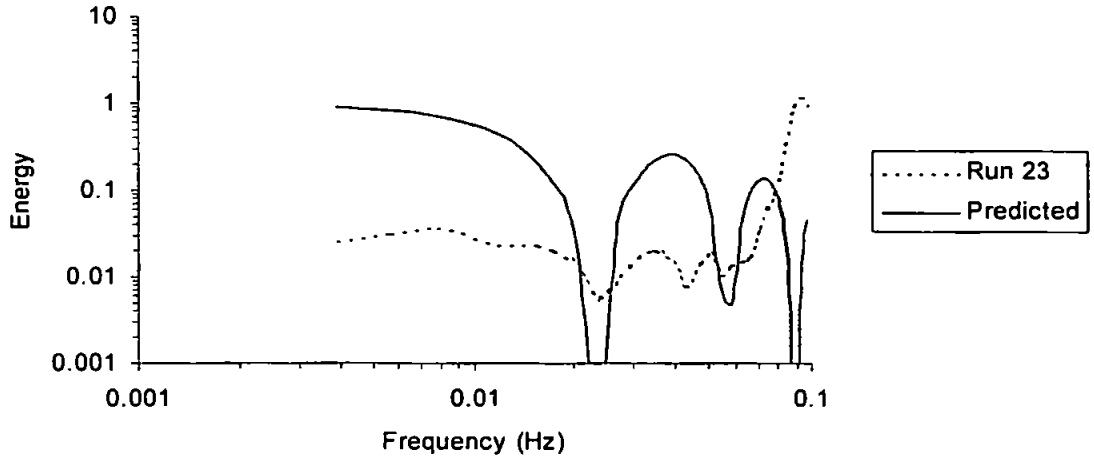

Figure 5.2.14 Comparison between predicted and observed sea surface elevation (η) spectra, Spurn Head run 23, incident wave shoaling zone (h=2.71m).

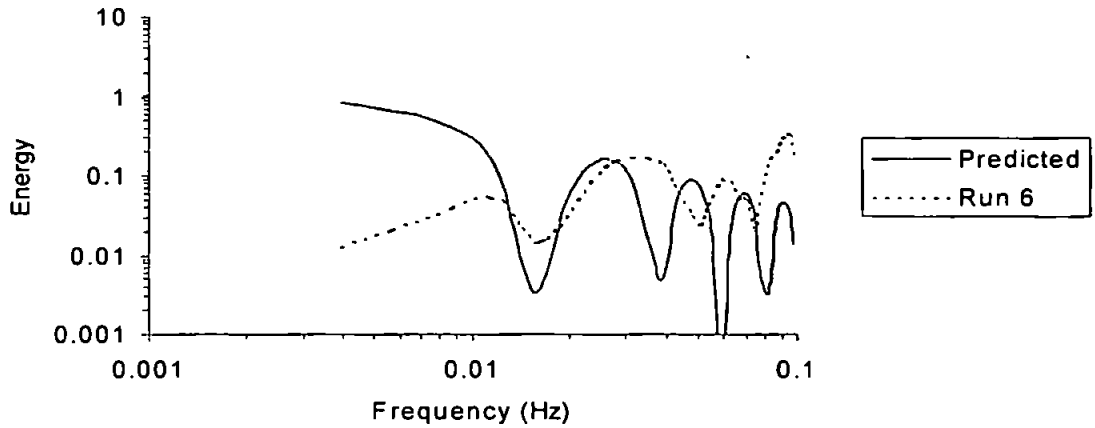

Figure 5.2.15 Comparison between predicted and observed sea surface elevation (η) spectra, Spurn Head run 6, outer surf zone (h=0.74m).

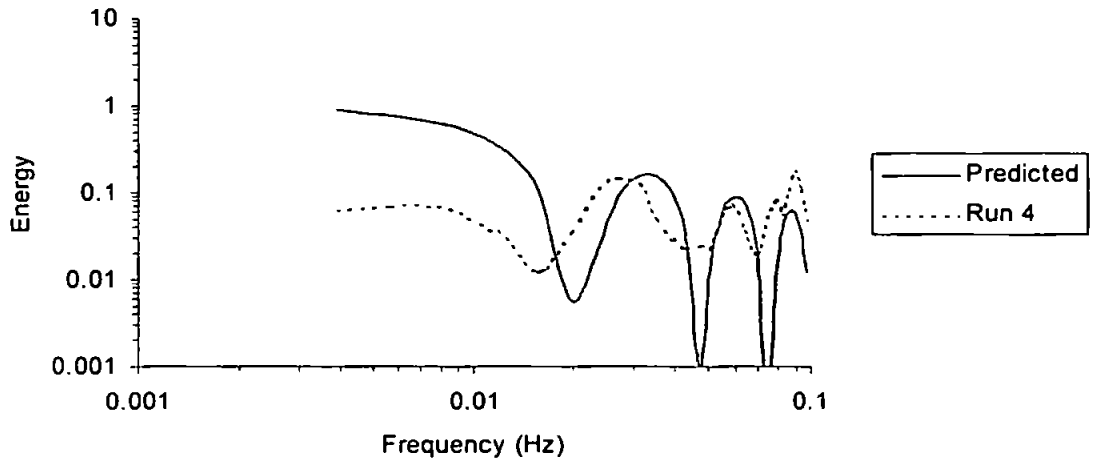

Figure 5.2.16 Comparison between predicted and observed sea surface elevation (η) spectra, Spurn Head run 4, close to shore (h=0.46m).

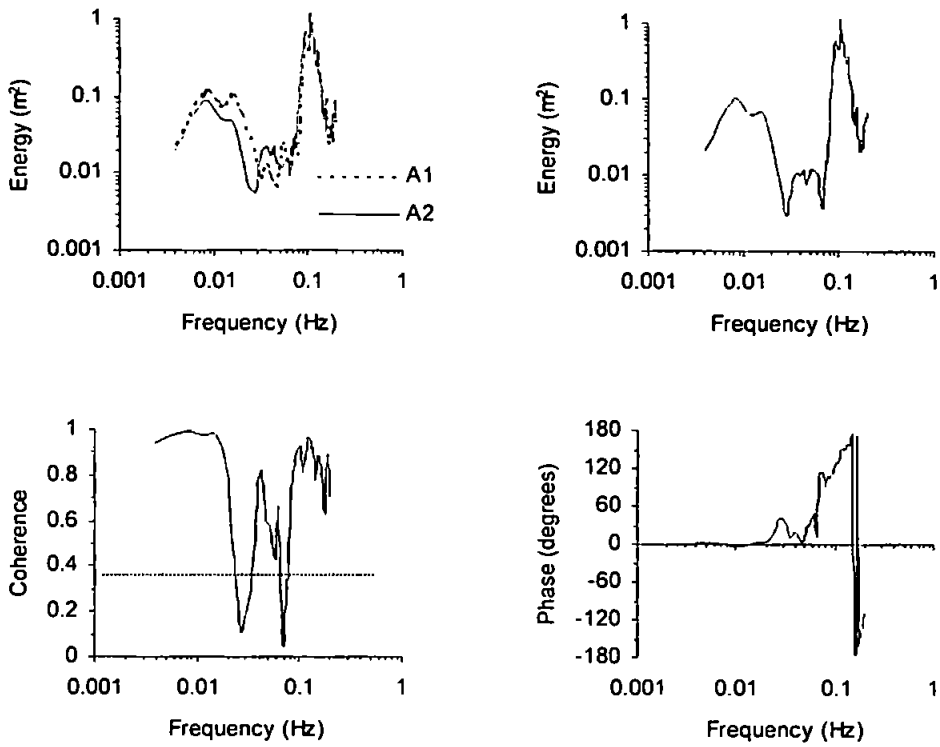

Figure 5.2.17 Spurn Head run 16 (h=2.74m) cross-spectra for η for A2 versus A1, clockwise from top left; autospectra, cross-spectrum, phase spectrum, coherence.

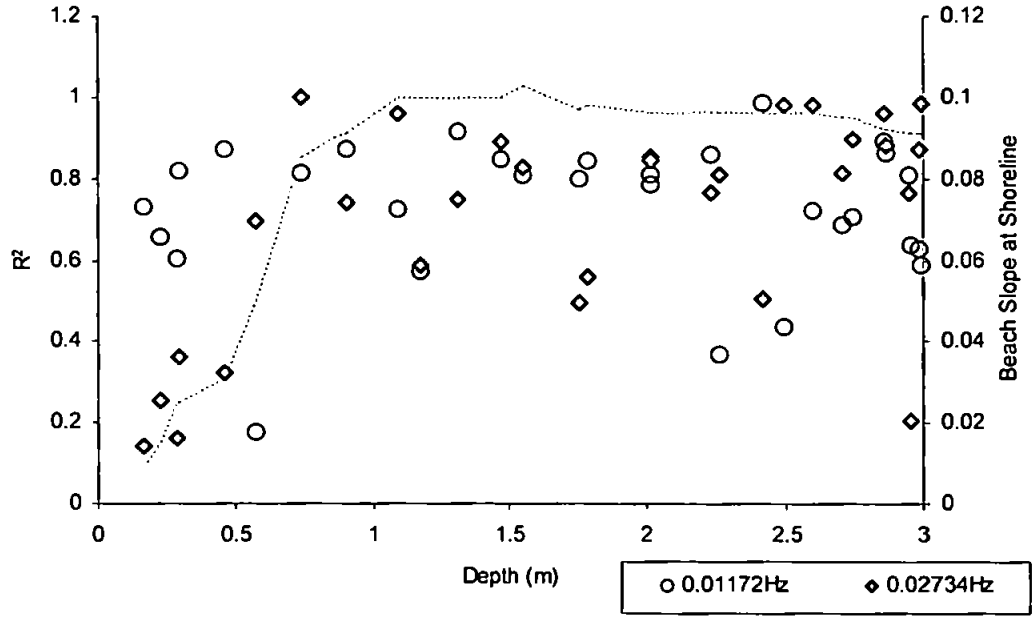

Figure 5.2.18 Spurn Head R^2 values versus depth for the frequency bins at 0.01172Hz and 0.02372Hz. The dotted line follows the beach slope at the shoreline for a given depth at the instruments.

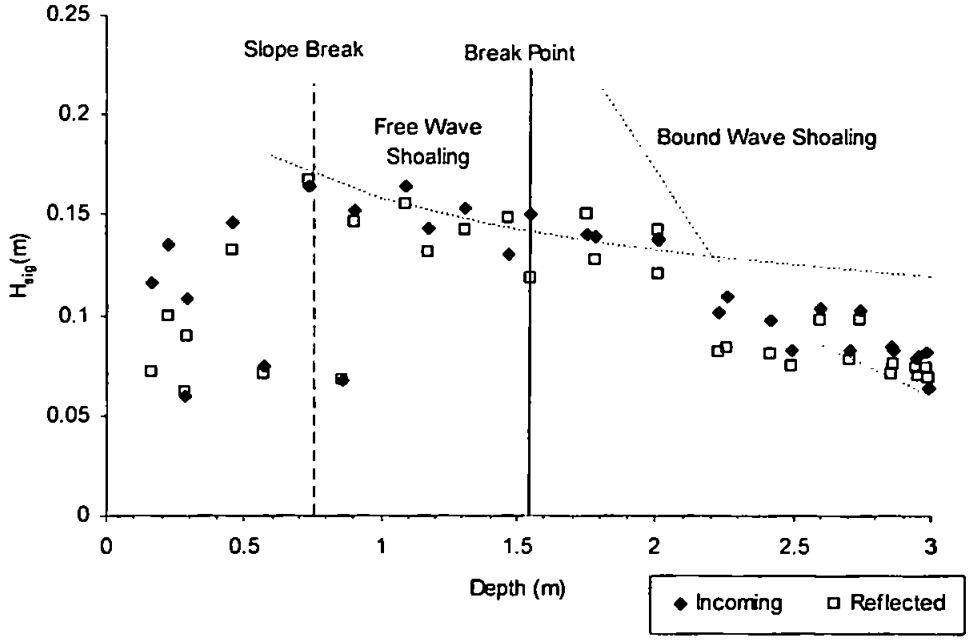

Figure 5.2.19 Incoming and reflected (total) infragravity frequency significant wave heights for Spurn Head runs. Dotted lines show theoretical bound and free wave shoaling relationships.

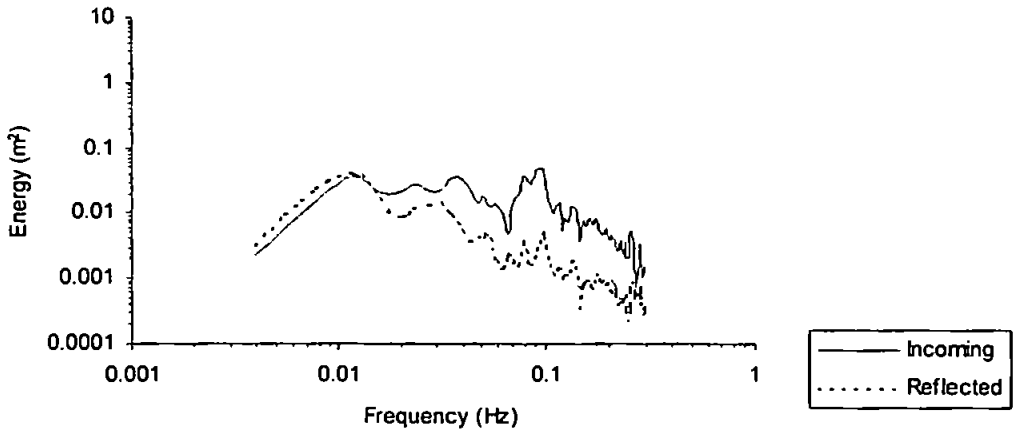

Figure 5.2.20 Incoming and reflected η spectra for Spurn Head run 2, surf zone (h=0.22m).

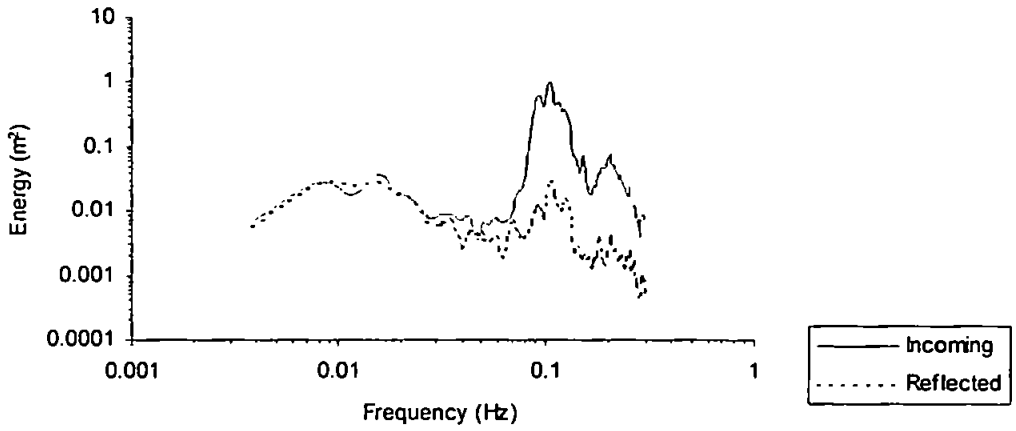

Figure 5.2.21 Incoming and reflected η spectra for Spurn Head run 16, shoaling zone (h=2.74m).

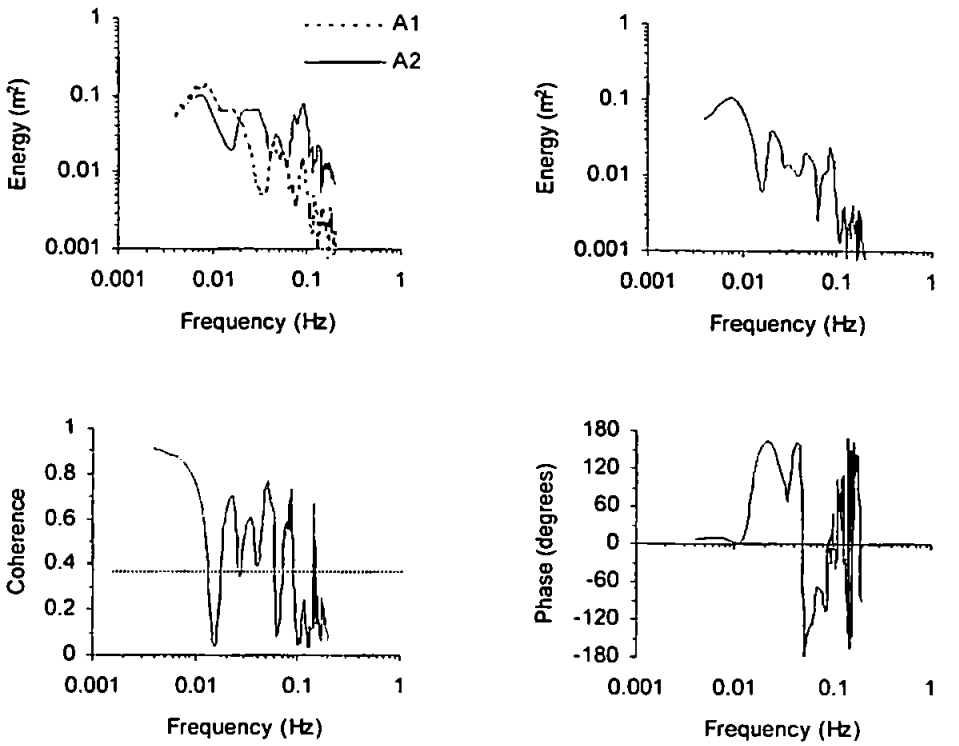

Figure 5.2.22 Spurn Head run 2 (h=0.22m) cross-spectra for η for A2 versus A1 clockwise from top left; autospectra, cross-spectrum, phase spectrum, coherence.

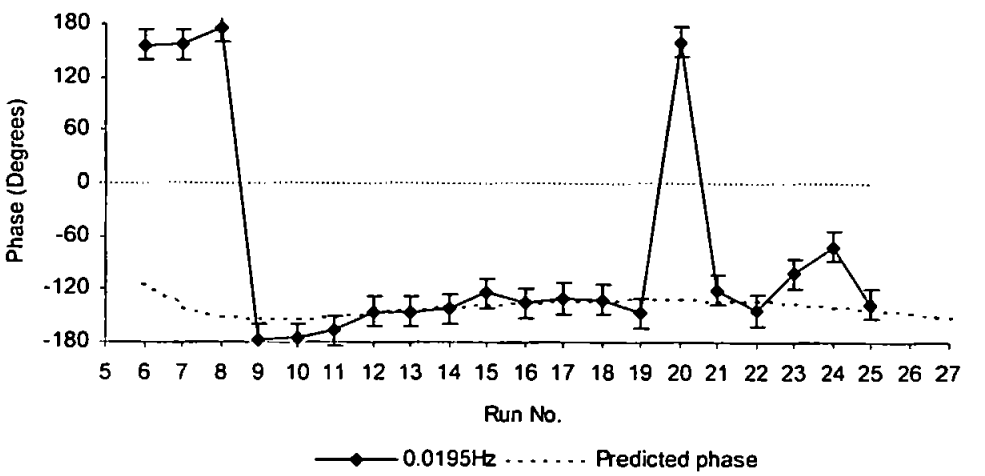

Figure 5.2.23 Temporal distribution of incoming-reflected wave phase at 0.0195Hz and predicted phase relationship using a reflection point at the shoreline. Bars on points indicate 95% phase error.

5.2.4 Frequency and shoreline gradient dependence for infragravity wave reflection

The infragravity wave field at all three beaches has been shown to possess a slightly different character at each. Furthermore, variations in behaviour were seen between the lower and higher parts of the infragravity frequency band. The two Llangennith datasets were found to be dominated by the lowest infragravity frequencies, which propagated as free waves in the surf zone without dissipation and were partially reflected (R^2=0.5) near to the shoreline. Whilst incoming energy was present in the higher infragravity frequencies, this was secondary and was dissipated in the surf zone prior to reflection. A similar set of circumstances were noted at Perranporth, but since a more significant contribution to energy came from the higher part of the infragravity band, led to slightly more dissipative behaviour in terms of the way energy across the infragravity frequencies as a whole varied with depth.

At Spurn Head, contributions to overall incoming and outgoing infragravity energy were seen at both higher and lower frequencies, and for most of the runs within the surf zone this energy behaved as for a free wave. With generally high values of reflection coefficient (R^2=1), the sea surface elevation spectra in section 5.2.3 closely resembled a standing wave solution. This was the case for all the runs where the waves were incident on a shoreline of steep gradient, but when the shoreline fell on to the low tide terrace (depth of water at instruments less than approximately 0.75m), reflection coefficients at the higher infragravity frequencies diminished. This coincided with a drop in the overall incoming infragravity energy and again it was suggested that this was due to a level of dissipation in the higher infragravity frequencies.

The type of frequency-gradient dependence for reflection cited here has previously been parameterised using the Iribarren number,

$$\xi = \frac{\tan\beta}{\sqrt{H_t/L_\infty}}. \tag{5.17}$$

Here H_t is wave height at the toe of the slope and L_∞ is deep water wavelength ($=2\pi g/\sigma^2$, σ is the radian wave frequency), and therefore this parameter is defined based on wave steepness and beach slope. At Spurn Head these values were calculated, for each run and for each of the PCA reflection analysis frequency bins. For each (bin) frequency the wave height at the toe of the slope H_{tf}, was determined from the proportion of incoming infragravity wave energy attributed to each frequency bin, and the overall infragravity wave height at the toe of the slope (H_t), such that

$$H_{tf} = \frac{E_f}{E_{ig}} H_t, \tag{5.18}$$

where E_f is the spectral energy at the bin frequency and E_{ig} total infragravity frequency band spectral energy. For cases of waves incident on the low tide terrace H_t was assumed to be 0.10m, the significant wave height on the deepest run. For runs when the shoreline was expected to be on the high tide beach, H_t was generated by taking the infragravity significant wave height at the instruments for that run, and applying the free wave shoaling relationship to obtain a wave height at the slope break. $L_{\infty f}$ values were also generated for each bin frequency. This approach assumes a perfectly linear system in which each of the frequency bins compared is assumed to behave independently.

Figure 5.2.24 shows the plot of reflection coefficient (R) versus Iribarren number for the Spurn Head data. In the figure the circles represent frequencies from the higher part of the infragravity band (f>0.02Hz) and the triangles frequencies from the lower part of the band (f<0.02Hz). The symbols are filled when the waves are incident upon the high tide beach ($\tan\beta$=0.1) and unfilled when incident upon a lower gradient part of the beach. Although the plot shows a lot of scatter, a general trend is observed whereby reflection coefficient increases with increasing Iribarren number. Iribarren number in this instance will become large with either an increase in beach gradient, or decrease in wave frequency, or both. Therefore the lowest infragravity frequencies incident upon steep beaches generally have the highest reflection coefficients.

The majority of previous comparisons between reflection coefficients and Iribarren number have focused on the incident frequency component reflected at a steep slope or wall (e.g. Giminez-Curto, 1979; Seelig and Ahrens, 1981; Hughes and Fowler, 1991; Mason *et al.*, 1997; Miles 1997). For most of these experiments Iribarren number values were smaller than those generated from the thesis data (e.g. for Seelig and Ahrens, 1981, Iribarren number took values less than 8) due to the steep slope and high frequency of the waves. It should also be noted that the Irribarren numbers generated in the aforementioned studies were based on the whole of the incident frequency band, rather than dealing with component frequencies, and therefore cannot be directly compared with these results.

In figure 5.2.24 the behaviour of the data is best described by a relationship similar to that described by Giminez-Curto (1979), where

$$R = a(1 - \exp(-b\xi)). \tag{5.19}$$

a and b are arbitrary factors in this relationship, and where Giminez-Curto (1979) found that for rubble mound breakwaters a=0.503 and b=0.125, for this data the fit line uses a=0.85 and b=0.125. The requirement that a is changed in this relationship likely relates to the difference in permeability between the breakwater studied by Giminez-Curto (1979) and the beach face from which waves are reflected in the thesis data. Again however, it is restated that a direct comparison between the Giminez-Curto (1979) results and those in figure 5.2.24 may not be made due to the different way in which the two sets of Irribarren numbers were calculated.

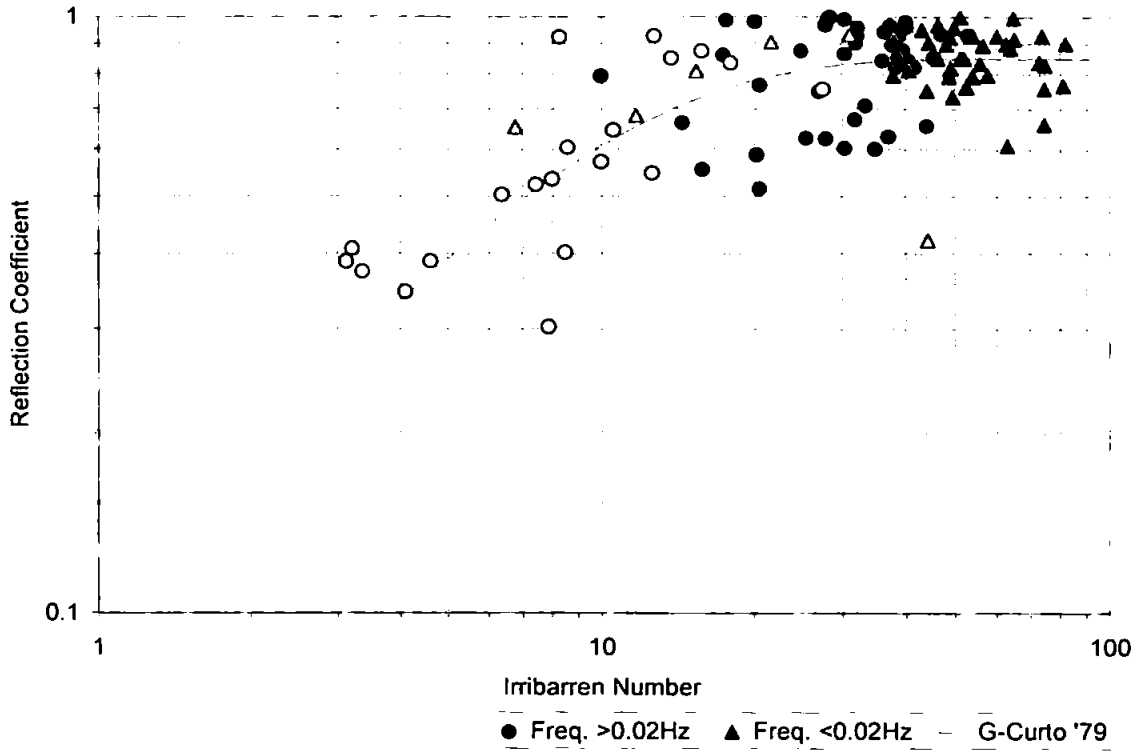

Figure 5.2.24 Spurn Head runs distribution of reflection coefficient (R) versus Iribarren number. In the figure filled symbols represent runs where the waves were incident upon the high tide beach ($\tan\beta$=0.1) and unfilled symbols when waves were incident upon a lower gradient part of the beach.

5.2.5 Summary: nature of the infragravity wave field in the nearshore

Even in the relatively energetic conditions described in this data, infragravity wave energy gives the largest contribution to overall oscillatory energy only very close to shore. Furthermore, the nature of the infragravity wave energy at each of the sites in the study was found to be variable, dependent upon the distribution of incoming wave energy between the lower and higher infragravity frequencies and beach slope.

Analysis of frequency dependent reflection coefficient, using a Principal Component Analysis technique, suggests that on a low slope beach incoming infragravity wave energy will not be fully reflected. Reflection coefficients were also found to be lower for higher infragravity frequencies (>0.02Hz) than lower infragravity frequencies (<0.02Hz). Further analysis has suggested that at least for intermediate/reflective beach slopes infragravity wave reflection may follow a trend which can be based on the Iribarren number. This result is analogous to research done for incident frequency waves on breakwaters and steep beach slopes. The Iribarren numbers covered in those studies and the lowest Iribarren numbers in this one are similar by virtue of the fact that in this work the waves are of an infragravity frequency but are incident upon a beach of lower gradient.

Two explanations might be offered for the low reflection coefficients observed at higher infragravity frequencies. First, that incoming energy is dissipated between the observation point and shoreline. Secondly, energy incident on the reflection point (in this work found to be very near to the shoreline for both low and high gradient beach slopes) may not be fully reflected. Results in this section suggest that both mechanisms may be in operation. Dissipation of wave energy at the higher infragravity frequencies meant that for those sites where these frequencies dominated energy in the infragravity band, less incoming wave shoaling was observed than might have been expected. Conversely, where the lowest infragravity frequencies dominated, incoming infragravity energy was observed to follow a free wave shoaling relationship through the nearshore.

Without 100% reflection, the dissipative beaches were characterised by infragravity wave behaviour which suggested a partially standing or progressive type of wave, whereas in more reflective conditions infragravity frequency energy distribution through the nearshore conformed to a leaky or high mode edge wave type solution. In some runs in the data a combination of standing and progressive type behaviours were observed corresponding to the lower and higher parts of the infragravity band respectively.

5.3 Modulation of the incident wave field

So far, in discussing low frequency hydrodynamics, this chapter has focused on infragravity waves. However, since finding the causes of both low frequency suspension and transport of sediment motivates the work in this thesis, low frequency variations of the incident frequency waves must also be considered. This section attempts to describe changes in incident wave 'groupiness' (i.e. low frequency variations in wave height) in relation to the behaviour of the waves through the cross-shore, i.e. changes that might be observed between the wave shoaling zone and outer and inner surf zones.

This section also investigates incident frequency wave modulations in terms of their phase with respect to the underlying infragravity waves. The analysis assesses how relevant the type of deep water phase relation between wave groups and bound long waves described by Longuet-Higgins and Stewart (1964) is to waves in the nearshore, and, as 'groupiness' is altered or possibly destroyed completely in the surf zone, how this will affect incident-infragravity wave phase.

5.3.1 Groupiness in the shoaling and outer surf zones

The spatial variations of the groupiness factors (*GF*) derived using the Foote (1994) and List (1991) methods (section 4.4.2) are plotted in figure 5.3.1 for the Spurn Head runs, which in this work are associated with the shoaling and surf zones. Both show a decrease in groupiness in the shoreward direction as an effect of increasing incident frequency wave breaking. Included in the figures is a dotted line indicating the predicted cross-shore position of the breaker line. It appears that for the Foote (1994) groupiness factor (figure 5.3.1a) a change in the gradient of the decrease of the groupiness factor is seen between the shoaling and surf zones with increasingly saturated wave breaking. List's (1991) factor tends to a constant near to shore (figure 5.3.1b). Both groupiness factors show relatively smooth changes through the observed region of the nearshore, despite the fact that gravity wave height modulation is likely to be radically altered between the outside and inside of the surf zone due to the onset of wave breaking. For the Foote (1994) groupiness factor this is not necessarily surprising since the formulation used,

$$GF = \left\{ \overline{\left[\left(\eta_{hi}^2(t) \right)_{low} \right]^2} \right\}^{1/4}, \tag{5.17}$$

is dimensional and particularly dependent on wave height, which will diminish as the waves break. Hence the change in gradient of decrease, observed in the Foote (1994) *GF*

inside the surf zone corresponds to increased wave breaking. The normalised groupiness factor described by List (1991) shows a smooth transition between shoaling and surf zones, but is derived directly from the incident wave envelope. From this perspective the List (1987) *GF* is felt to provide a better description of wave modulation independent of wave height, and hence will be the *GF* used in the remainder of this work.

Since incident frequency wave breaking in the Spurn Head dataset is non-saturated for depths greater than 1m, modulations of the waves in the surf zone should initially change from those observed in the shoaling zone as a result of the largest wave's heights being diminished through breaking. Furthermore, waves that offshore were the smallest will retain a non-broken form and continue to shoal until closer to the shoreline. As a result substantial changes in the incident frequency wave envelope and its relationship to infragravity fluctuations of the sea surface are expected between the shoaling and surf zones. For the Spurn Head data this is illustrated in figure 5.3.2 which shows sample time-series of the incident frequency waves, their envelope and the infragravity waves. Figure 5.3.2a shows an example of a run outside the surf zone (run 22, h=2.87), figure 5.3.2b a run at the breaker line (run 7, h=0.90m) and figure 5.3.2c a run in the inner surf zone near to shore (run 1, h=0.17m).

Possibly the easiest way to judge these results is to bear in mind the predicted deep water relationship between fully developed swell waves and a bound infragravity component (Longuet-Higgins and Stewart, 1964). This theoretical form should see modulated groups of incident frequency waves associated with an infragravity wave which is exactly 180° out of phase with the highest waves in the group (i.e. has its trough in phase with the highest waves, see also figure 2.2.1). A visual comparison of the time-series in figure 5.3.2 sees a general decrease in the level of modulation of the incident frequency waves toward the shoreline. The type of 'structured' modulation observed in run 22 (figure 5.3.2a), where a number of small waves are followed by a number of larger waves in a 'groupy' form is also lost in the runs from further shoreward. In all the runs in figure 5.3.2, the infragravity frequency time-series can be seen to consist of both higher and lower frequency modulations. At the lowest frequencies, run 22 (figure 5.3.2a) appears to exhibit the type of phase behaviour between the incident and infragravity components in deep water predicted by Longuet-Higgins and Stewart (1964), in that generally, the sea surface is depressed under groups of large waves and elevated under the smaller ones.

In run 7 (figure 5.3.2b) however, no similar relationship can be seen for the lowest frequency modulations, although the largest incident frequency waves are possibly associated with peaks in the infragravity signal corresponding to higher infragravity frequency modulations with a period of around 30 seconds. In run 1 (figure 5.3.2c) virtually all the incident waves should be of a broken form. In correspondence with this, any 'groupy' structure has been completely destroyed. Incident frequency wave modulations that occur in this time-series can be observed to be due simply to individual large breakers.

Since little relationship can be seen between incident frequency wave height modulations and the infragravity waves in the surf zone, a significant correlation between the incident frequency wave envelope and infragravity wave time-series may be expected solely for the runs in deeper water outside the surf zone. Figure 5.3.3 shows a frequency domain analysis of the two signals, and shows a coherent peak in the lower infragravity range associated with a phase lag of approximately 150°. This lag corresponds to a significant peak in correlation between the envelope and the incoming infragravity wave time-series for run 22, as is illustrated in figure 5.3.4. The peak shows a period of modulation of 60 seconds and is of a 'positive-negative' form, i.e. the peak in correlation occurs at a lag value of less than zero, whilst the trough is found at a lag greater than zero. Both frequency and time domain analysis are in agreement in finding that the trough of the incoming infragravity signal lags the largest incident frequency waves by approximately 5 seconds outside of the surf zone. A similar form of correlation was found by List (1987) and physically suggests that just prior to breaking, bound infragravity waves might detach from the wave groups.

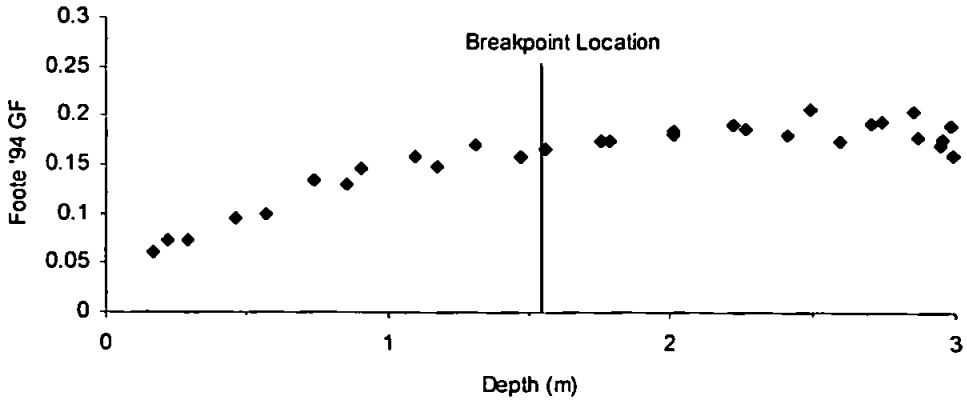

Figure 5.3.1a Foote (1994) 'groupiness factor' plotted versus depth for Spurn Head runs.

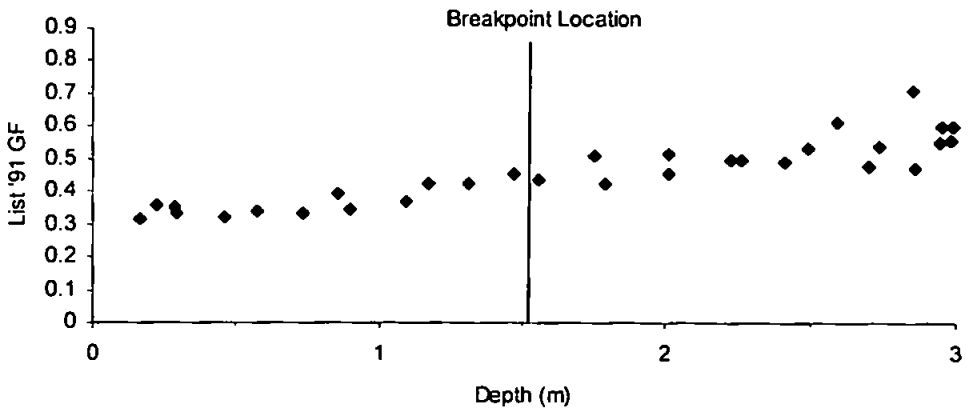

Figure 5.3.1b List (1991) 'groupiness factor' plotted versus depth for Spurn Head runs.

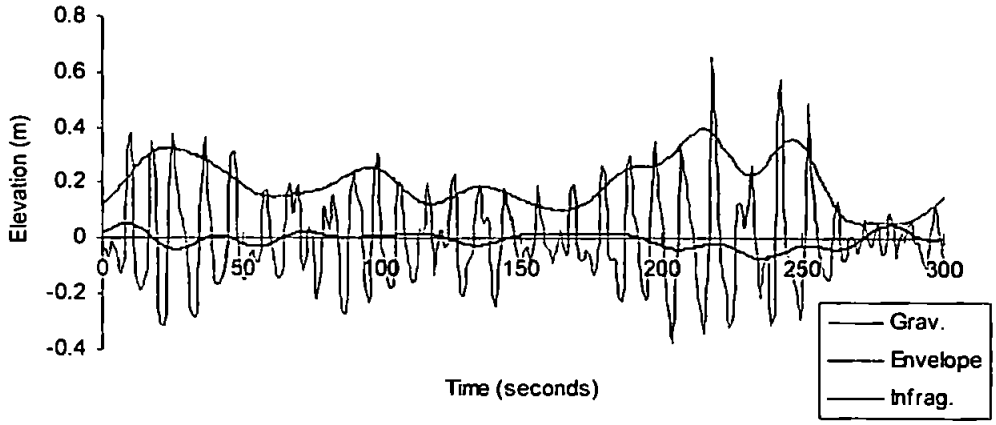

Figure 5.3.2a Spurn Head run 22 time-series for incident and infragravity frequency waves and the incident wave envelope, shoaling zone (h=2.87m).

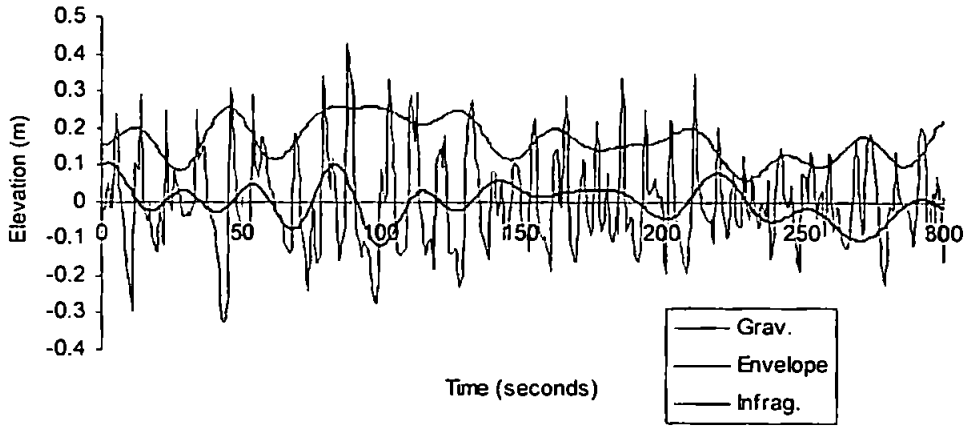

Figure 5.3.2b Spurn Head run 7 time-series for incident and infragravity frequency waves and the incident wave envelope, breaker line (h=0.90m).

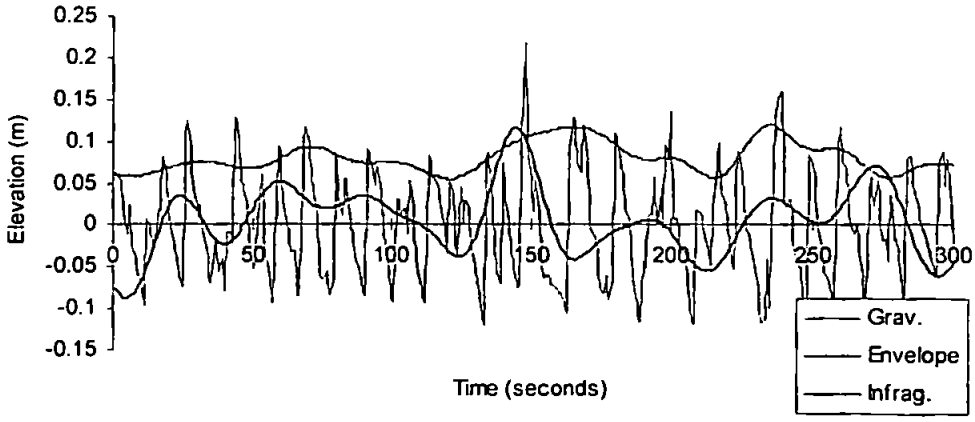

Figure 5.3.2c Spurn Head run 1 time-series for incident and infragravity frequency waves and the incident wave envelope, inner surf zone (h=0.17m).

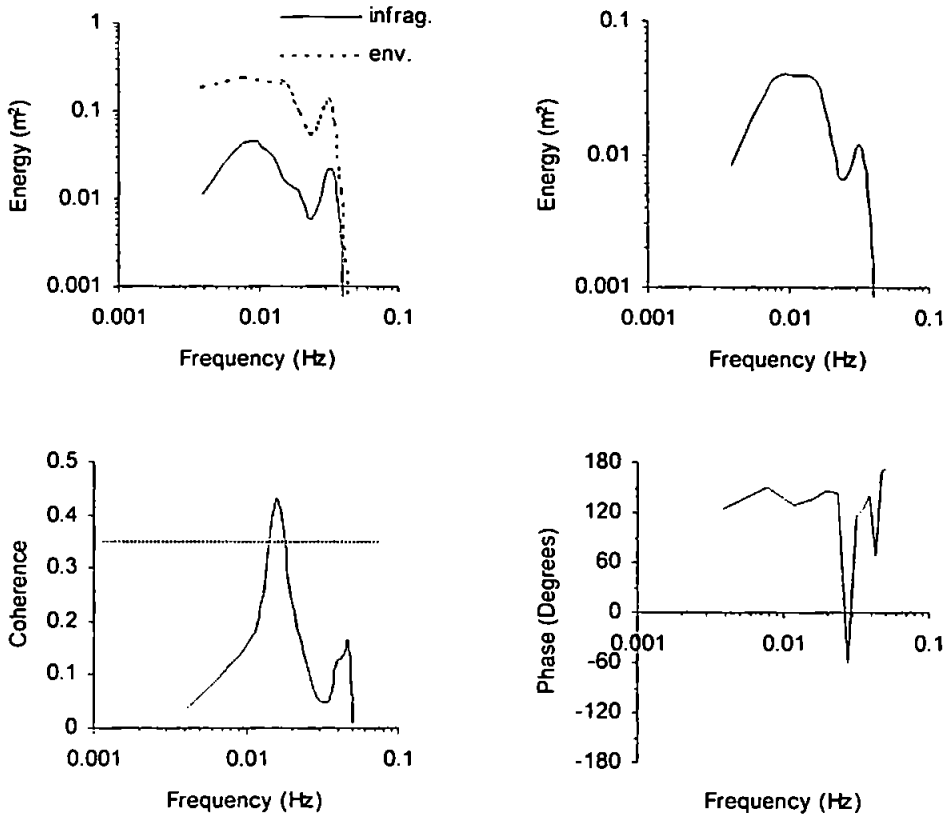

Figure 5.3.3 Spurn Head run 22 (h=2.87m) spectra for incident wave envelope versus infragravity η, clockwise from top left; autospectra, cross-spectrum, phase spectrum, coherence.

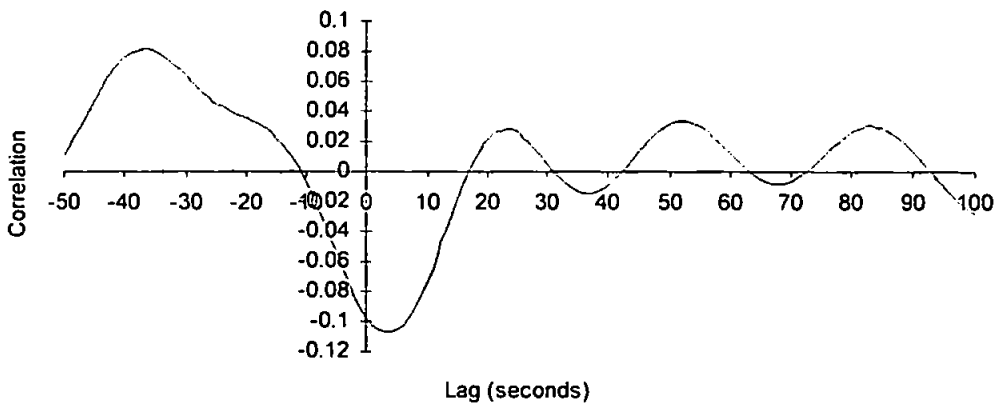

Figure 5.3.4 Correlation between incident wave envelope and incoming infragravity signal for Spurn Head run 22 (h=2.87m).

5.3.2 Incident wave modulation in the inner surf zone

In the previous section it was shown that the 'groupy' structure seen in deep water is dramatically altered by the onset of wave breaking. This occurs to such an extent that waves in the Spurn Head surf zone, although remaining modulated, cannot be considered strictly groupy. Whilst the Spurn Head case initially sees a mixture of broken and unbroken waves in the outer surf zone (non-saturated), near to shore breaking is saturated (e.g. run 1 figure 5.3.2c). At Llangennith and Perranporth the breaking incident frequency waves also exhibit behaviour suggesting that the surf zone observed is saturated (inner surf zone). This has been defined by observations of breaking wave heights being depth limited when an average is taken over a run time-series, which might suggest that modulation about the mean depth limited height will be small (i.e. breaking wave heights will tend to a single value). However, plots of the List (1991) groupiness factor versus depth in these inner surf zones (figures 5.3.5a and b) shows *GF* increasing with a decreasing depth of water. Physically this points to breaker height variation diminishing less rapidly than the mean wave height.

Time-series of the (breaking) incident frequency waves and their associated envelope are shown in figure 5.3.6 for two of the Llangennith Storm Day tide runs; run 5 when the instruments were sited in 1m of water, and run 10 where the water depth is 0.65m. In line with the decrease in depth, breaker heights and correspondingly the envelope are seen to decrease between the two figures. Common to both time-series is that the modulations are unstructured in comparison with the deep water descriptions of groupiness derived in theory and seen in figure 5.3.2a. For example, figure 5.3.6a shows long periods where waves are of a similar height and hence the envelope modulation is small, but also events where one or two larger breakers are found. These latter waves lead to larger modulations of the envelope with periods of approximately 30-40 seconds.

Thus breaker height modulations appear not to decrease as quickly as breaker height in the surf zone, but do not retain any discernible deep water group structure. These observations lead to the possibility that the breaking wave heights may be affected by depth changes due to the presence of infragravity waves. For example, if the assumption of a fully saturated surf zone is made, where breaking wave height is therefore proportional to depth, along with an assumption that the infragravity component is progressive in nature, then the largest breakers should be found on the crests of the infragravity waves, as these regions of the infragravity waves will give rise to the largest water depths. Alternatively if the

infragravity energy takes the form of standing waves, and the measurements are taken inshore of a wave antinode, those breakers which had been in phase with an antinode crest would likely be larger than those which had been in phase with the trough. The possibility of such a mechanism for forcing incident frequency wave heights is considered in more detail in the discussion in chapter 7.

Figures 5.3.7 and 5.3.8 show, for Storm Day run 5 and run 10 respectively, a time-series of the breaker envelope and corresponding infragravity frequency signal plus a frequency domain comparison between the two. Examining run 5 first, where depth at the instruments was 1m, figure 5.3.7a shows both signals to be dominated by oscillations of period 30-40 seconds, producing a significant peak in the cross-spectrum which is coherent and has a phase of -90° (figure 5.3.7b). This suggests that the lag between the largest breakers and a high infragravity frequency oscillation is such that the largest breakers are preceded by a depression in water level and followed by an elevation. In the coherence spectrum in figure 5.3.7b virtually no coherence is seen between the envelope and the lowest infragravity frequencies. In shallower water however (0.65m, run 10, figure 5.3.8), the infragravity signal is dominated by the lower infragravity frequencies and envelope-infragravity wave coherence is high in this part of the spectrum. The phase spectrum at these frequencies suggests that the largest envelope oscillations occur just before the crest of the lowest frequency infragravity waves. Additionally, the time-series in figure 5.3.8a hints at a lag similar to that seen in figure 5.3.7 still existing between the envelope and infragravity oscillations at periods of 30-40 seconds. This change in the spectrum at the lower infragravity frequency might suggest that in very shallow water, shoaled lower infragravity frequency waves at Llangennith could force breaker heights. In the Perranporth surf zone, little of a relationship was seen between the incident frequency wave height modulations and the infragravity signal save for the runs in the shallowest water depths.

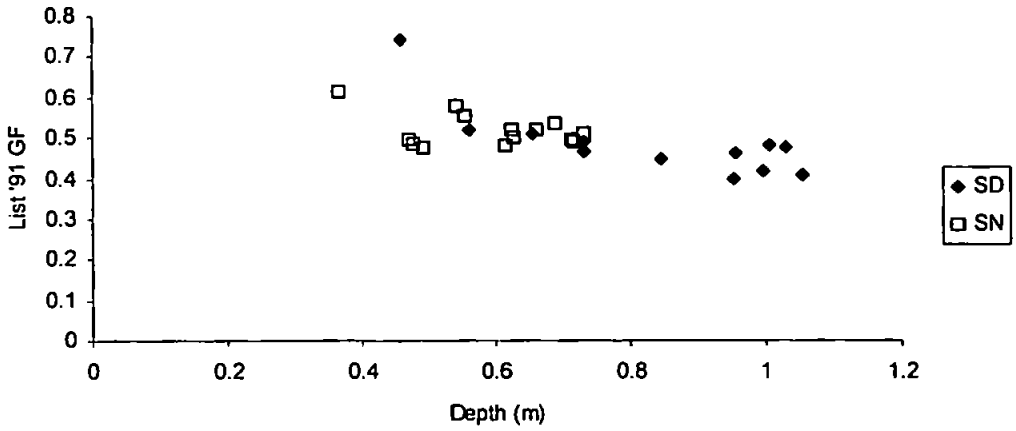

Figure 5.3.5a List (1991) groupiness factor versus depth for the Llangennith Storm Day and Storm Night tides.

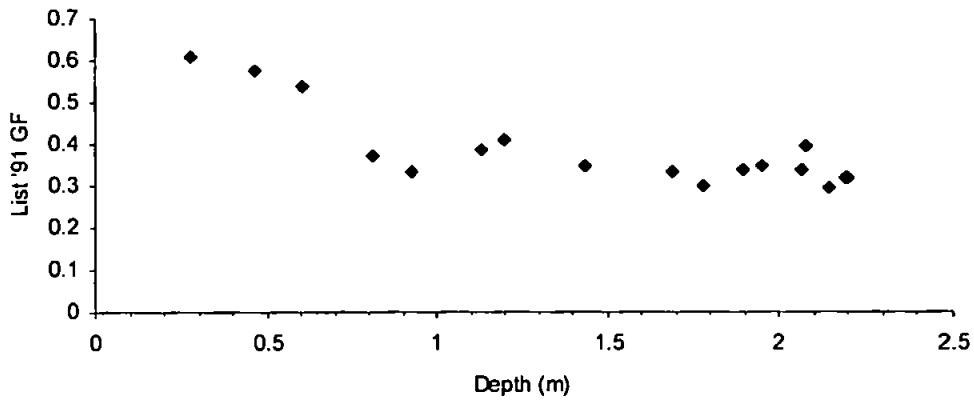

Figure 5.3.5b List (1991) groupiness factor versus depth for the Perranporth runs.

a)

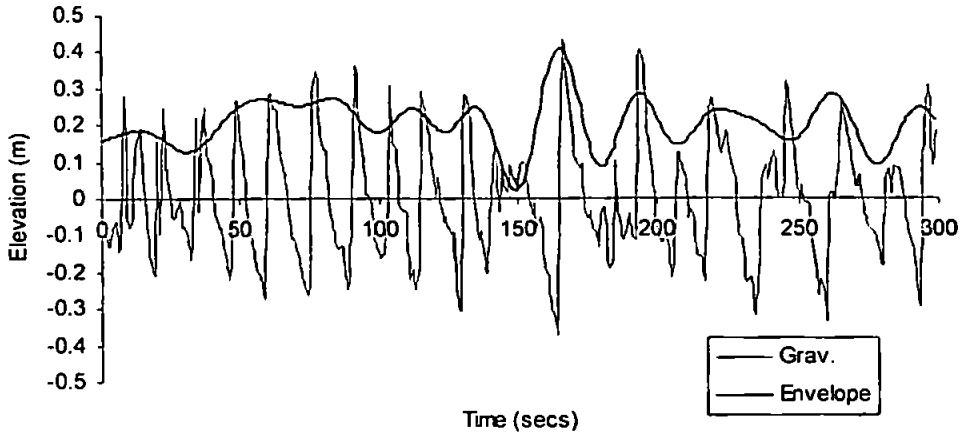

b)

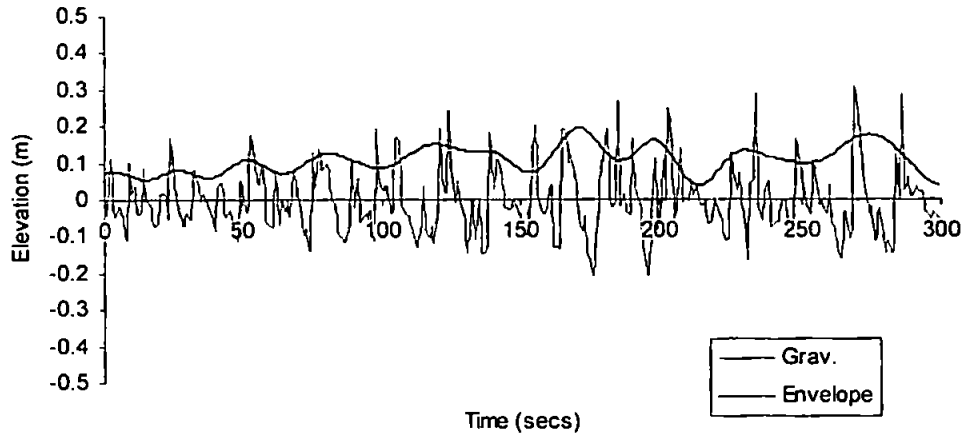

Figure 5.3.6 Time-series of incident wave signal and corresponding envelope for a) Storm Day run 5 (h=1.03m), b) Storm Day run 10 (h=0.66m).

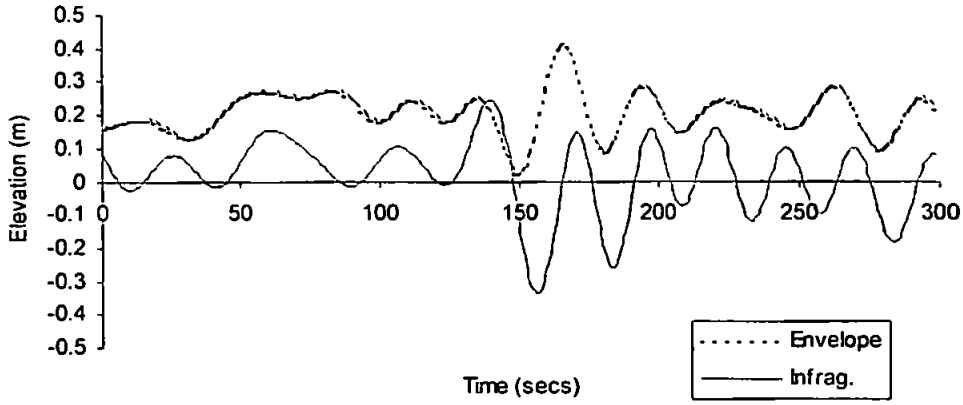

Figure 5.3.7a Time-series of wave envelope and infragravity η signal for Storm Day run 5 (h=1.03m).

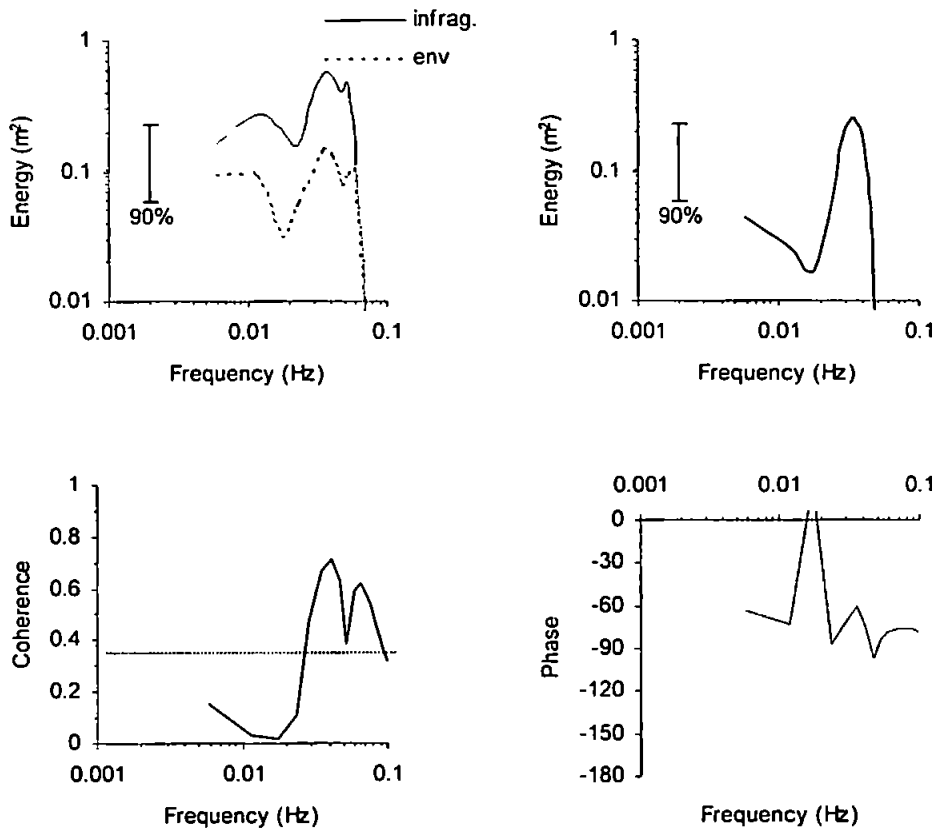

Figure 5.3.7b Storm Day run 5 (h=1.03m) cross-spectra for incident wave envelope versus infragravity η, clockwise from top left; autospectra, cross-spectrum, phase spectrum, coherence.

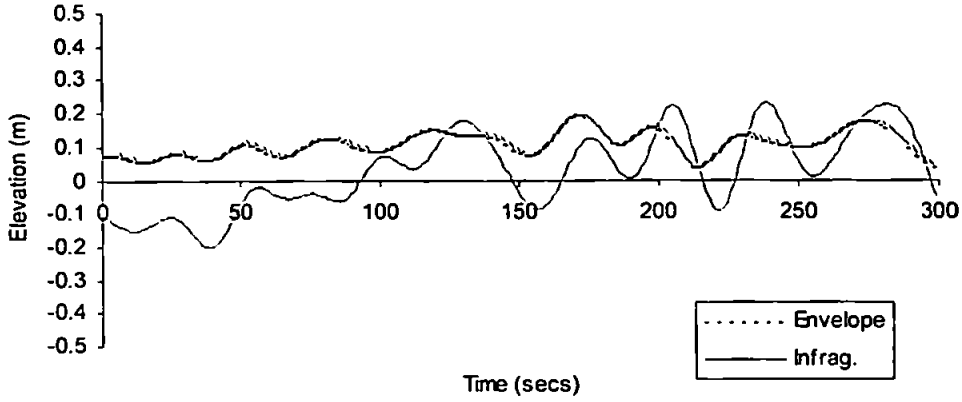

Figure 5.3.8a Time-series of wave envelope and infragravity η signal for Storm Day run 10 (h=0.66m).

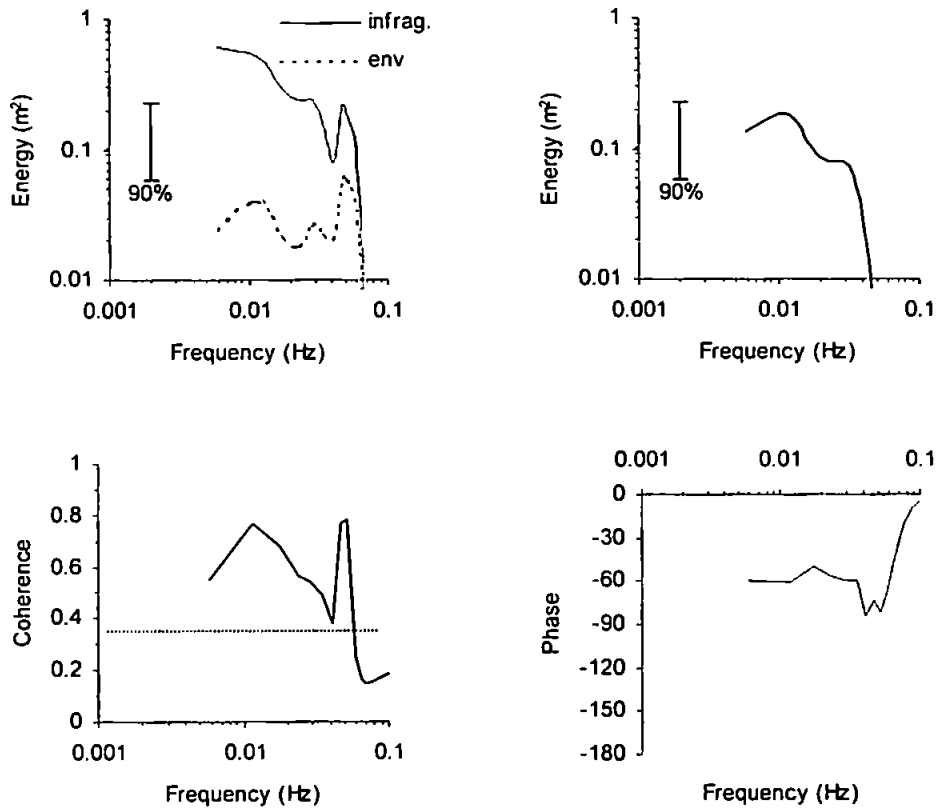

Figure 5.3.8b Storm Day run 10 (h=0.66m) cross-spectra for incident wave envelope versus infragravity η, clockwise from top left; autospectra, cross-spectrum, phase spectrum, coherence.

5.3.3 Summarising variations in *GF* and incident-infragravity wave phase through the nearshore

So far modulation of the incident wave field and incident-infragravity wave phase have been described for the data as separate sites. In this subsection the data is compiled to try and provide a better understanding of the evolution of these parameters through the nearshore.

Since the List (1991) groupiness factor is a normalised parameter, a direct comparison may be made between the *GF*s from all three beach sites. The *GF*s are presented in figure 5.3.9 plotted versus the normalised cross-shore distance. In the figure the Perranporth data is seen to match with that from Spurn Head in the mid-part of the surf zone. However an increase in normalised *GF* is observed in the inner half of the surf zone for both the Perranporth and Llangennith (Storm Day and Storm Night) runs. Although these *GF* values are similar to those outside the surf zone, they stem from individual large breakers occurring at low frequencies rather than any 'structured' long period changes in breaker height ('groupiness'). Hence the term 'groupy' cannot strictly be applied to modulations of wave height in the surf zone. The apparent increase in *GF* with decreasing depth indicates that this near to shore the degree of breaker height modulation does not decrease as quickly as the actual wave height.

In the previous two sections examples of the modulated incident wave envelope versus infragravity wave phase were given (figures 5.3.4 and 5.3.8). These suggested that the largest incident waves were lagged by the infragravity component such that the infragravity wave trough occurs just after the largest waves in the shoaling zone, but that in the inner surf zone the largest breakers preceded an infragravity wave peak. This change in phase can be represented through the nearshore by examining the correlation coefficient at zero phase, as has also been considered by Abdelrahman and Thornton (1987) and Foote (1994) (using the Spurn Head data). The data used in this thesis is compared in figure 5.3.10, plotted versus the normalised cross-shore distance. Figure 5.3.10 shows a clear trend in the data where correlation is negative in the shoaling zone and just inside the breaker line, but then crosses the zero line in the surf zone. Toward shore, positive correlation then increases. In the thesis dataset the Spurn Head data ties in well with observations from the Llangennith and Perranporth sites; Foote (1994) saw a similar good agreement between the Spurn Head data and that gathered by Abdelrahman and Thornton (1987). Physically, the negative correlations associate the largest incident waves with an

infragravity wave trough, whilst the positive correlations associate the largest breakers with an infragravity wave crest. Figure 5.3.10 therefore suggests that bound infragravity wave behaviour occurs outside of the surf zone, and does not discount the idea that near to shore infragravity waves may force breaker heights. However, the figure also shows confidence limits for zero correlation, derived following Garrett and Toulany (1981), which are denoted by the dotted lines. These indicate that although a clear trend may be seen in the data, for much of the surf zone (between a normalised cross-shore position of approximately 0.25 and 0.9) the largest incident frequency waves cannot be significantly correlated with either an infragravity wave crest or trough. In this region of the surf zone therefore a simple expression of incident-infragravity wave phase cannot be derived from this data with any mathematical confidence.

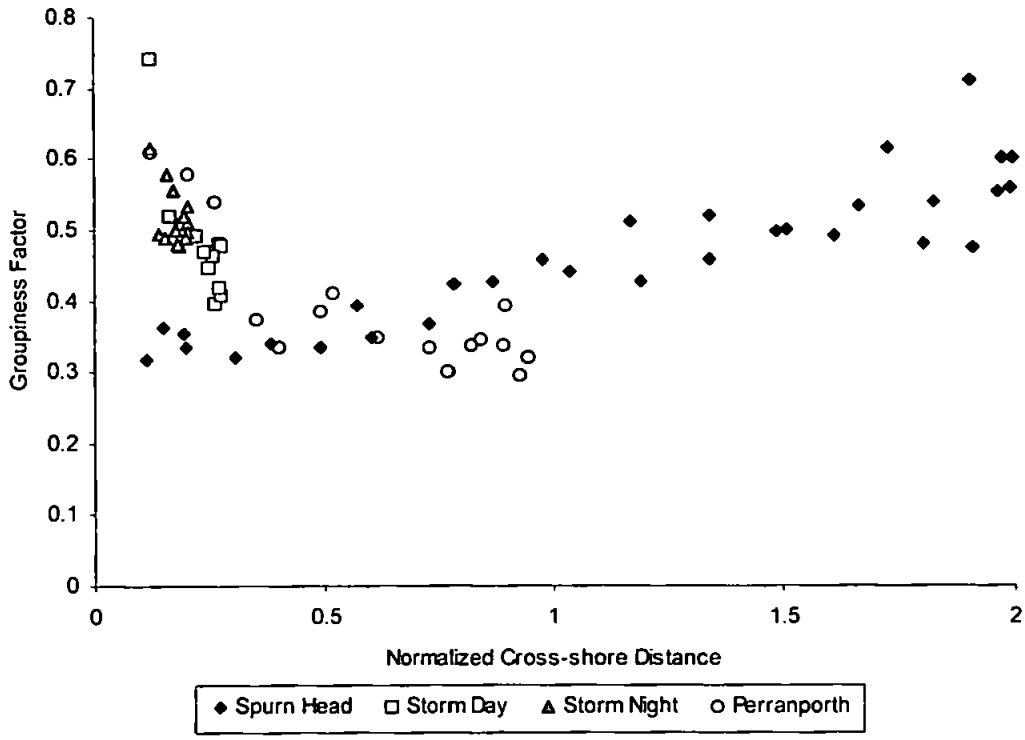

Figure 5.3.9 List (1991) groupiness factor plotted versus normalised cross-shore distance for the Llangennith, Spurn Head and Perranporth data.

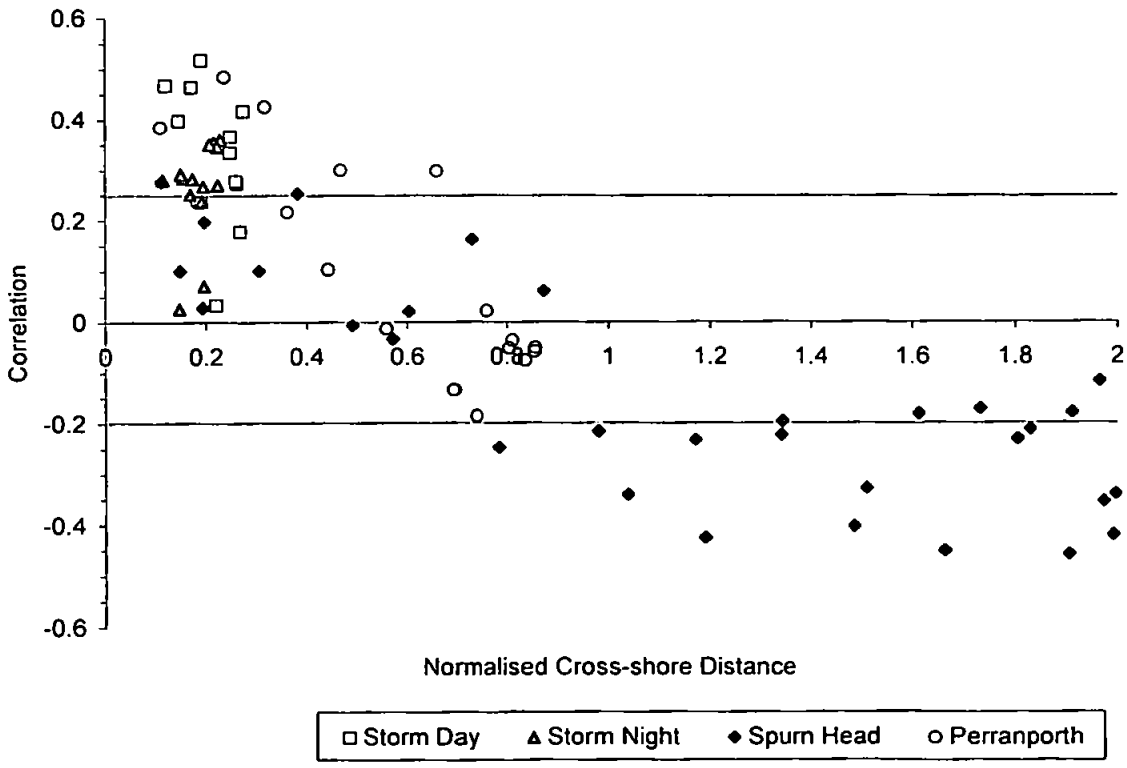

Figure 5.3.10 Zero phase cross-correlation values plotted versus normalised cross-shore distance for the Llangennith, Spurn Head and Perranporth data. The dotted lines indicate 95% significance levels for zero correlation.

5.4 Incident-infragravity wave phase and interaction through the nearshore

In the previous section, cross-spectral analysis of incident-infragravity wave phase suggested that outside the surf zone bound long waves begin to detach from wave groups. In the inner surf zone the analysis also noted a possible link between shoaled infragravity waves and modulated breakers. Cross-spectral analysis of the data regards the two processes as independent. However, it is acknowledged that the surf zone is a highly non-linear system in which inter-frequency interactions are likely to take place within the wave field. Thus further detail of incident-infragravity wave phase in the nearshore may be derived from an analysis of frequency interactions within naturally occurring wave fields. Such analyses can be made using bispectral techniques. For example, the bound long wave component in deep water was assessed by Herbers *et al.* (1994, 1995). Doering and Bowen (1995) studied nonlinearity in the incident wave velocity field in the shoaling zone and derived skewness and asymmetry values from the bispectrum for use as wave shape descriptors. Ruessink (1998) also made a bispectral study of breaking and non-breaking waves. The bispectral analysis of the data in this thesis gives results from further into the surf zone than either the Herbers *et al.* (1994, 1995), or Doering and Bowen (1995) studies.

5.4.1 Evolution of wave bispectra through the nearshore

This first subsection describes the cross-shore evolution of the sea surface elevation bispectrum over both the infragravity and incident frequency bands. Because of the range of the nearshore covered by the Spurn Head runs and the change in behaviour of the incident waves between the shoaling and surf zones, it was expected that at Spurn Head, more contrasting bispectra would be found than for the suites of runs from Llangennith and Perranporth. The results of the analysis results confirmed this. Here, results from Spurn Head are used to illustrate the evolution of the sea surface elevation bispectrum from the shoaling zone (figure 5.4.1) through the breaker line (figure 5.4.2) and into the surf zone (figure 5.4.3).

The bispectrum consists of both real and imaginary parts, but in the figures the real part only is shown for ease of interpretation. When discussing the bispectrum, a notation of $f_1+f_2 \rightarrow f_3$ is used, where $f_3=f_1 \pm f_2$. The absolute value of the bispectrum gives no indication of the direction of energy transfer between frequencies in a triad. Using the real part only will include this information however. Negative real values will indicate energy transferred

to a lower ('difference') frequency whilst positive values indicate energy transfer to a higher ('summed') frequency (Wells, 1967, c.f. Doering and Bowen, 1995).

Both types of interaction can be observed in figure 5.4.1, which shows an analysis of waves in the shoaling zone. Positive peaks in the bispectrum are seen at $B(0.1,0.11)$ and $B(0.1,0.21)$. These $B(f_g,f_g)$ (where f_g denotes the incident or 'gravity' band) interactions force summed frequencies (i.e. harmonics), and are a typical feature of wave shoaling. Thus the bispectral peak at $B(0.1,0.11)$ represents the 'peak-peak' sum interaction at the primary frequency (approximately 0.1Hz), which will force the first harmonic (at 0.21Hz). $B(0.1,0.21)$ indicates a further interaction occurring between the primary gravity frequency and first harmonic. A negative peak exists in the $B(f_g,f_i)$ (where f_i denotes the infragravity frequency) part of the real bispectrum at approximately $B(0.1,0.01)$. This represents the 'peak-peak' difference interaction, the physical interpretation of which is a bound long wave forced following 0.11Hz-0.1Hz=0.01Hz.

At the breaker line (figure 5.4.2) the summed interaction between the primary and first harmonic increases whilst the summed 'peak-peak' interaction diminishes. A physical interpretation of this behaviour is somewhat difficult in that this region sees further shoaling of the smallest waves whilst the largest waves have started breaking. However, closer to shore, the (figure 5.4.3) bispectral energy is much reduced and hence the overall level of $B(f_g,f_g)$ nonlinear interaction would seem to be reduced as a result of increased dissipation of wave energy through the breaking process. Similarly, the negative $B(f_g,f_i)$ peak indicating bound long wave forcing outside of the surf zone is not present in the bispectra from inside the surf zone, indicating that inside the surf zone the infragravity component is no longer forced by the incident waves.

The bispectra in figures 5.4.2 and 5.4.3 have been taken from a moderate energy non-saturated surf zone and show a general trend in the behaviour of the bispectrum through the nearshore. However, some further characteristics can be seen in bispectra from the saturated surf zones at Llangennith and Perranporth. For example, although overall bispectral energy reduces with increasing wave breaking, this process also sees nonlinear interactions occurring over an increased distribution of frequencies. This can best be seen in figure 5.4.4, which shows a run from the saturated surf zone at Perranporth where the bispectrum is relatively chaotic compared to the bispectra in figures 5.4.1 and 5.4.2. Because the surf zone at Perranporth becomes saturated relatively close to the breaker line, this type of observation may be seen in runs taken in rather deeper water than was the case

at Spurn Head, and hence where bispectral energy is much greater. For the run in figure 5.4.4 water depth was 2.2m. A similar depth of water during the Spurn Head observations would have seen the instruments in the shoaling zone, where the bispectra are of the type seen in figure 5.4.1.

Figures 5.4.5 and 5.4.6 show bispectra from the inner surf zone during the Storm Day tide, where water depths were respectively 1.01m and 0.73m. In these runs no strong $B(f_g,f_i)$ interactions are present indicating, as expected, that infragravity wave energy is free in the saturated surf zone. However, unlike the Spurn Head and Perranporth data, $B(f_g,f_g)$ interactions in figures 5.4.5 and 5.4.6 are also near zero in comparison to nonlinear $B(f_i,f_i)$ interactions, which dominate the bispectrum. Both figures 5.4.5 and 5.4.6 show a clear positive (summed) 'peak-peak' interaction at $B(0.03,0.03)$ and a negative peak at $B(0.02,0.01)$, indicating a difference interaction where the higher infragravity frequencies force a lower infragravity frequency. The strength of both of these peaks increases with the decrease in water depth, and figure 5.4.6 shows further development of a positive peak at $B(0.03,0.06)$, indicating a summed interaction between the peak and harmonic frequencies.

The behaviour at the infragravity frequencies in figures 5.4.5 and 5.4.6 therefore seems to fit with the model of shoaling waves, as the bispectra appear to describe a similar evolution of the bispectrum to figures 5.4.1 and 5.4.2. In both figures 5.4.1 and 5.4.5 a 'peak-peak' interaction at the primary frequency develops, which forces a higher harmonic, and a difference frequency interaction is observed forcing a lower infragravity frequency. With further shoaling (figures 5.4.2 and 5.4.6) the harmonic will then interact with the primary frequency. In the case of infragravity frequencies these interactions would suggest some redistribution of higher infragravity frequency energy toward frequencies in the lower parts of both the incident and infragravity wave bands. In the surf zone, energy distributed to incident frequencies will be dissipated, whilst energy distributed to the lower infragravity frequencies will lead to further shoaling of these waves.

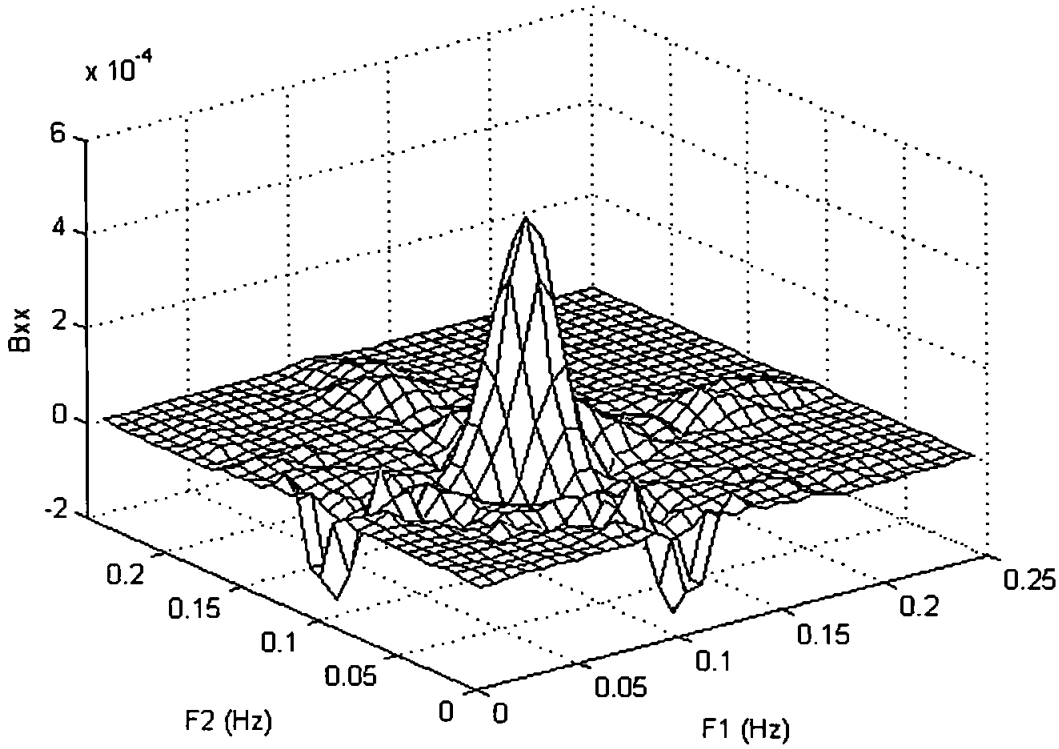

Figure 5.4.1 η bispectrum (real part) for Spurn Head run 20, shoaling zone (h=2.99m).

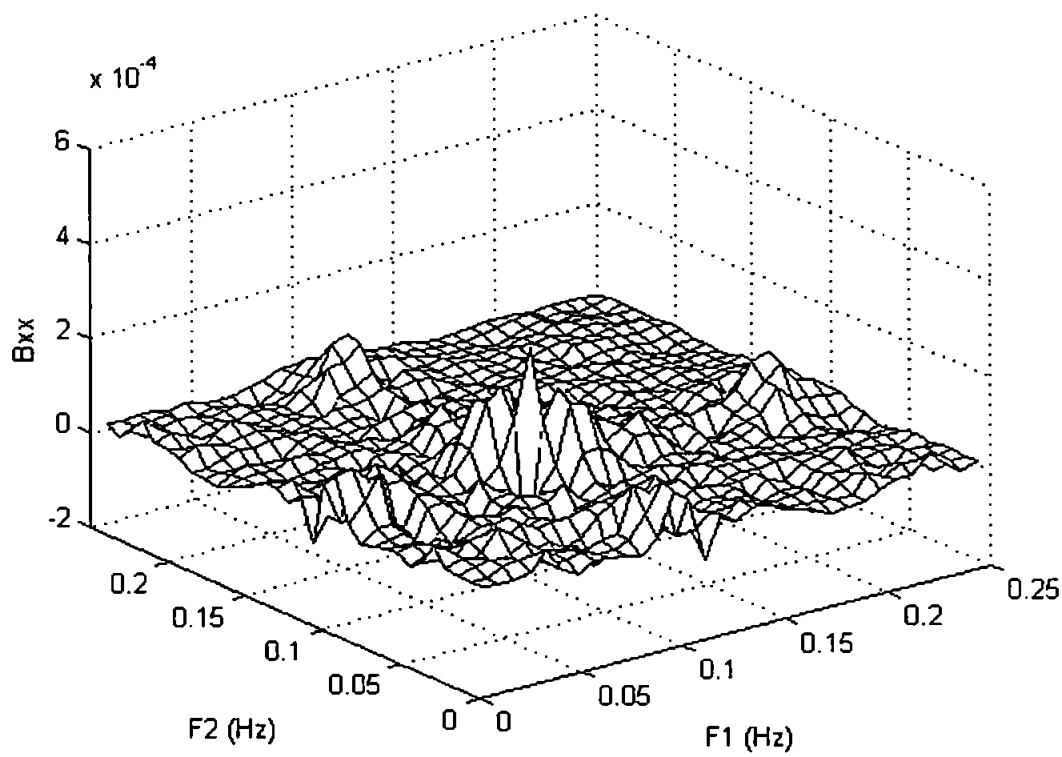

Figure 5.4.2 η bispectrum (real part) for Spurn Head run 8, breaker line (h=1.09m).

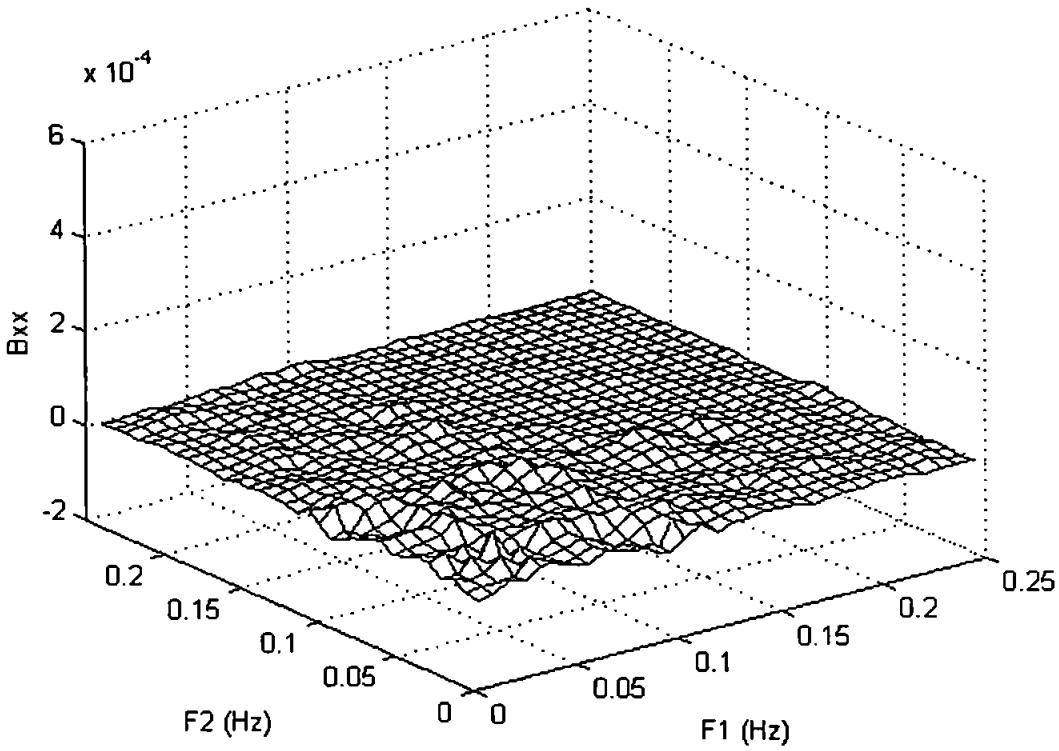

Figure 5.4.3 η bispectrum (real part) for Spurn Head run 4, surf zone (h=0.46m).

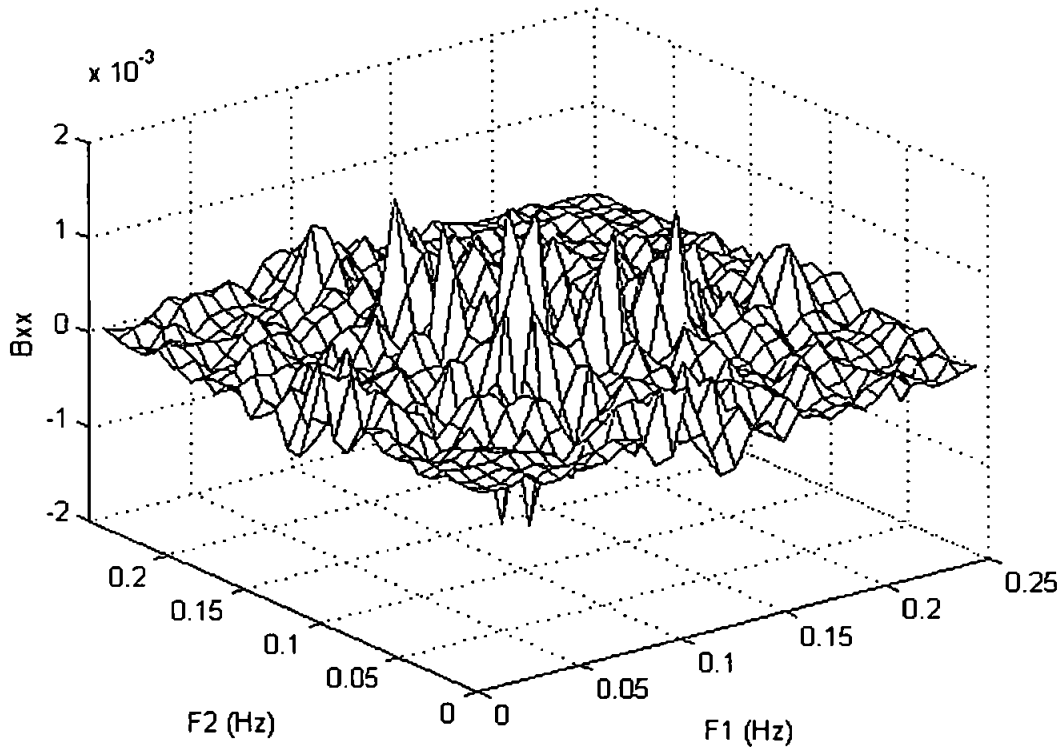

Figure 5.4.4 η bispectrum (real part) for Perranporth run 10, saturated inner surf zone (h=2.20m).

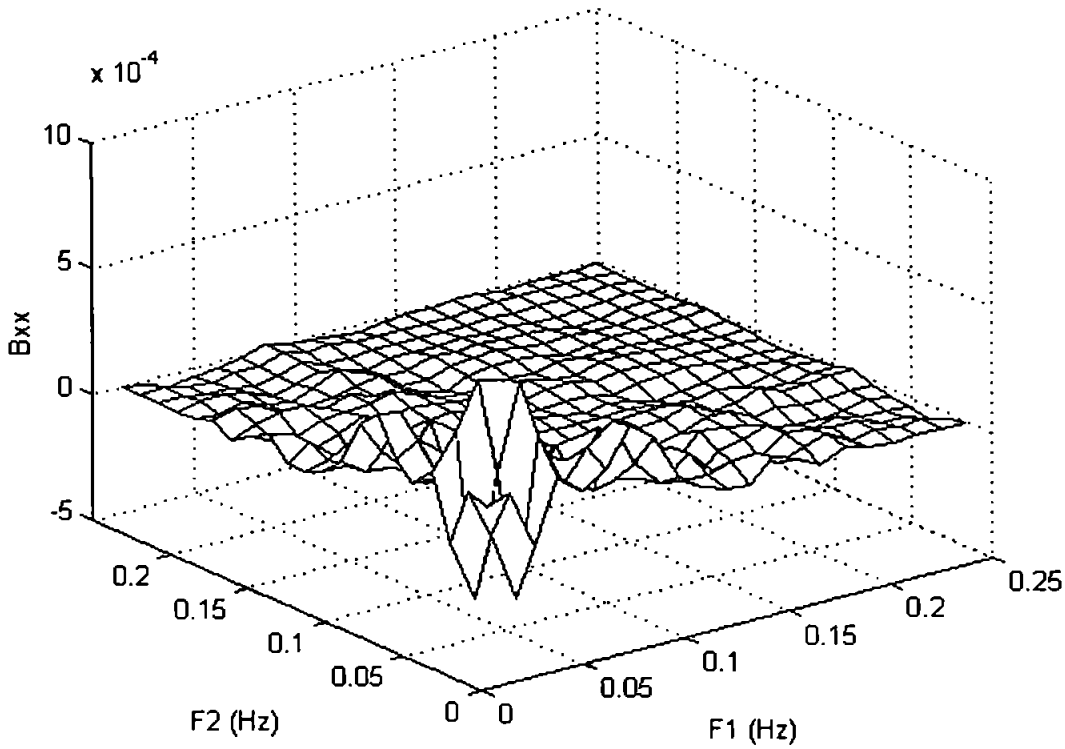

Figure 5.4.5 η bispectrum (real part) for Storm Day run 2, saturated inner surf zone (h=0.95m).

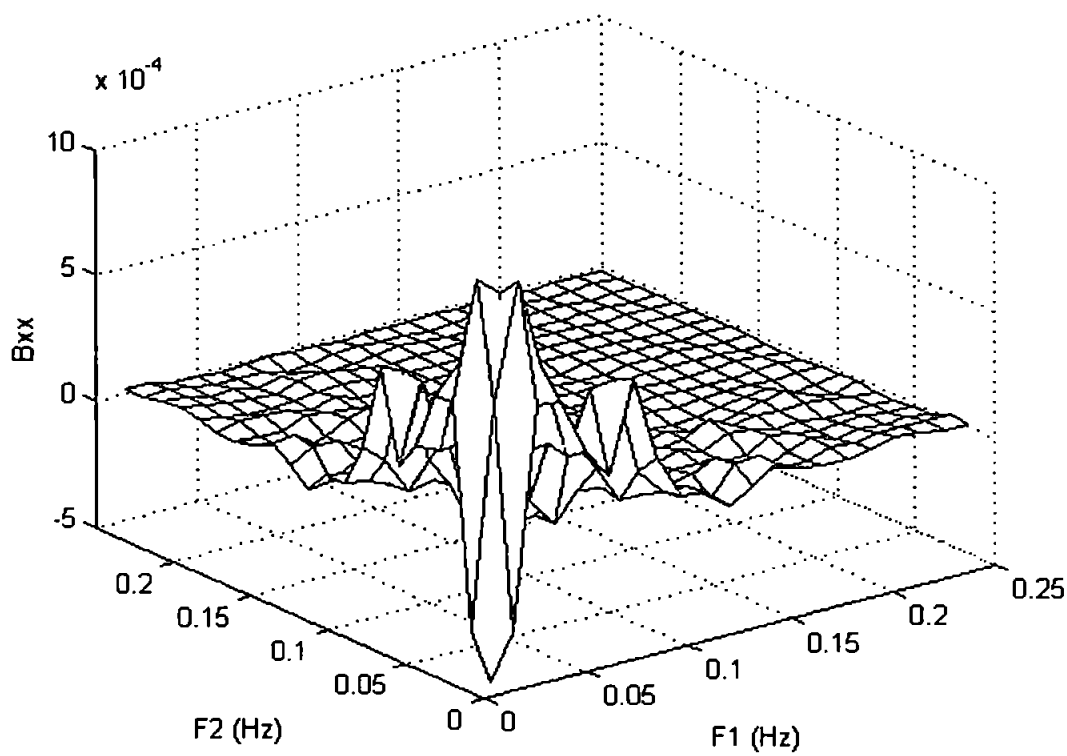

Figure 5.4.6 η bispectrum (real part) for Storm Day run 9, saturated inner surf zone (h=0.73m).

5.4.2 Incident-infragravity wave interactions

Analysis of the bispectrum described in the previous section suggested that in the incident wave shoaling zone wave groups forced a bound long wave as for the deep water case described by Longuet-Higgins and Stewart (1964). However, the lag between the wave group envelope and long waves noted in section 5.3.1 (figure 5.3.4) indicated that the waves did not adhere to the deep water phase relationship predicted by Longuet-Higgins and Stewart (1964). This subsection compares the observed incident-infragravity wave forcing with predicted deep water behaviour by examining the evolution of $B(f_g,f_i)$ bicoherence and biphase through the cross-shore. The bicoherence describes the level of nonlinear interaction occurring between frequencies and thus $B(f_g,f_i)$ bicoherence should be high for a bound long wave in correspondence with a biphase of ±180°. Conversely, free wave behaviour should be associated with zero bicoherence.

Figures 5.4.7 and 5.4.8 show the distribution of bicoherence and biphase with respect to the normalised cross-shore distance parameter. The bicoherence parameter was derived by calculating the volume under the normalised bicoherence spectra in the $B(f_g,f_i)$ region for the Storm Day, Spurn Head and Perranporth runs. Biphase values are given for points along the $B(fp_g,f_i)$ line of the spectrum (where fp_g denotes the primary 'gravity' wave frequency) where bicoherence was significantly greater than zero. The biphase values have been divided into points where f_i<0.02Hz and 0.02Hz<f_i<0.04Hz to indicate interactions between the primary and lower and higher infragravity frequencies respectively.

In the Spurn Head shoaling zone the incoming wave was found to be significantly correlated with the wave groups, although with a 'positive-negative' form where the (negative) peak in correlation associated with the infragravity wave trough lags the largest waves by approximately 5 seconds (figure 5.3.4). A possible inference from this and also from similar observations made by List (1987) and Masselink (1995) is that in the shoaling zone infragravity waves are already becoming detached from the gravity wave groups which force them. Biphase values in the shoaling zone and outer surf zones (normalised cross-shore distance greater than 1, figure 5.4.10) are in the range 90°-180°, indicating that a bound long wave may be forced by gravity frequency waves in this region, but does not adhere to the deep water phase relationship described by Longuet-Higgins and Stewart (1964).

Furthermore, shoaling zone bicoherence values in figure 5.4.7 are scattered. A number of these values could agree with a hypothesis that this 'detachment process' would lead to a decrease in the forcing of the bound long wave near to the breakpoint (figure 5.4.7 dotted line). Equally the data might suggest that the increasing differential in gravity wave heights with decreasing depth will mean that bound long wave forcing increases toward a maximum at the breakpoint despite the change in the lag between the bound waves and the overlying wave groups from that in deep water (figure 5.4.7 solid line). Rather more of the runs show bicoherence values which support this latter hypothesis and a similar result was observed by Ruessink (1998), who found that a maximum in bound long wave energy occurred at the breaker line of his field site.

Inside the surf zone $B(f_g,f_i)$ bicoherence levels initially diminish, indicating that infragravity waves become detached from the gravity frequency component with the onset of wave breaking. However, bicoherence does not decrease monotonically toward the shoreline. Instead figure 5.4.7 shows a minimum bicoherence value approximately one to two-fifths of the way through the surf zone, and shoreward of this bicoherence increases. Interestingly, this ties in well with the position at which correlation between incident wave modulation and the infragravity component in the surf zone becomes significant (figure 5.3.10).

The change in bicoherence is also illustrated in the bicoherence spectra shown in figures 5.4.9 and 5.4.10, which were taken from the outer and inner parts of the surf zone at Perranporth respectively. In both plots the z-axis values indicate exceedence of the 95% zero bicoherence estimate, and therefore all peaks are significant. An increase in interactions between all frequencies can be observed between these two plots, but is particularly marked in the $B(f_g,f_i)$ region of frequency-frequency space. This would suggest that whilst a linear type model may be appropriate for the majority of the surf zone since little inter-frequency forcing takes place, very near to shore this is not likely to be the case.

Corresponding to the increase in bicoherence near to shore, biphase is shifted to values less than 90° (figure 5.4.8). Such a biphase is indicative of a sum rather than difference interaction. This might suggest a physical process whereby some infragravity energy is redistributed to higher frequencies. If this is the case, then energy being redistributed to the incident frequency band is liable to be dissipated. Eldeberky and Battjes (1996) noted a similar behaviour with their Boussinesq model, which meant that infragravity waves did not shoal as expected under breaking wave conditions. Madsen *et al.* (1997) also described

results from their model where near to the swash zone the infragravity waves were seen to force the gravity component enough to affect breaker phase speeds.

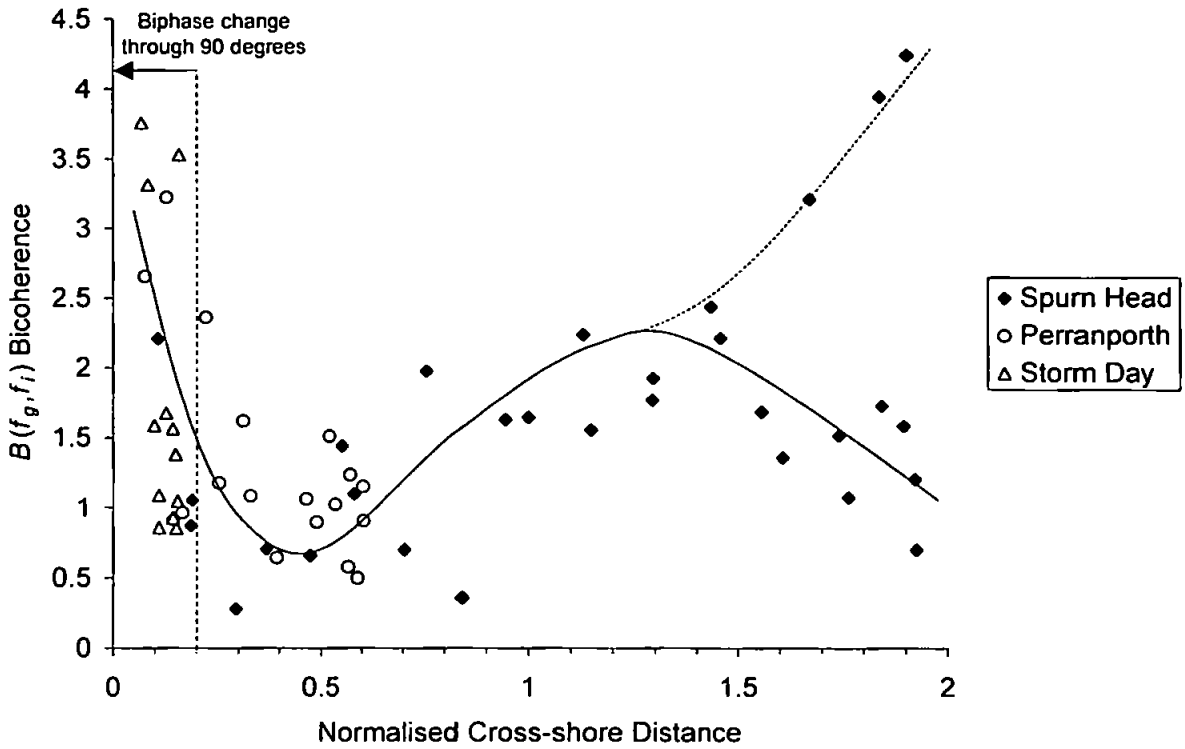

Figure 5.4.7 Cross-shore distribution of incident-infragravity frequency bicoherence values for Storm Day, Spurn Head and Perranporth runs.

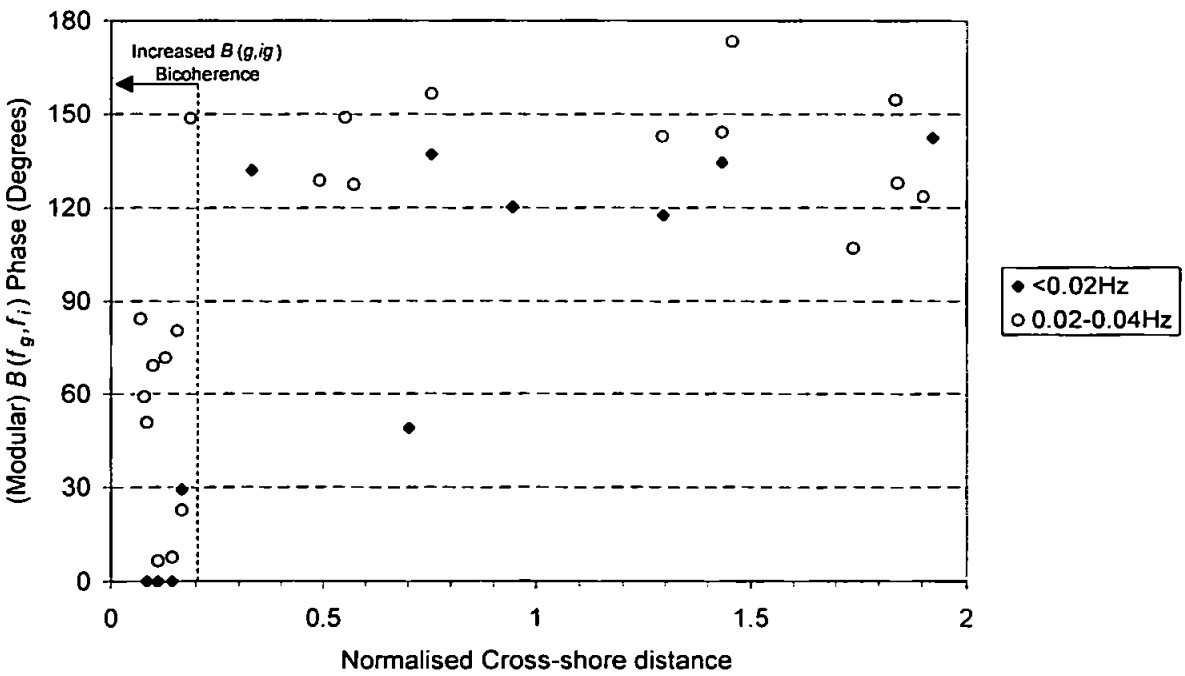

Figure 5.4.8 Cross-shore distribution of incident-infragravity frequency biphase, for bicoherent interactions between the primary incident frequency and the higher and lower infragravity frequencies.

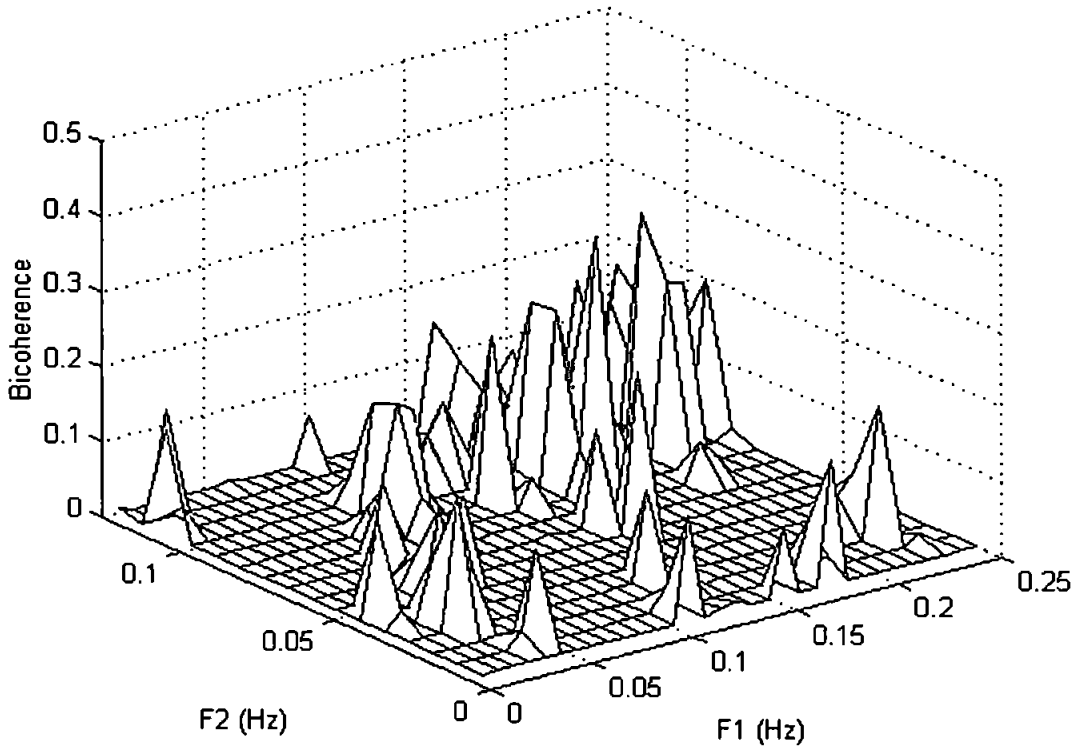

Figure 5.4.9 Bicoherence spectrum for Perranporth run 10, saturated surf zone, (h=2.2m). z-axis values indicate exceedence of the 95% zero bicoherence estimate

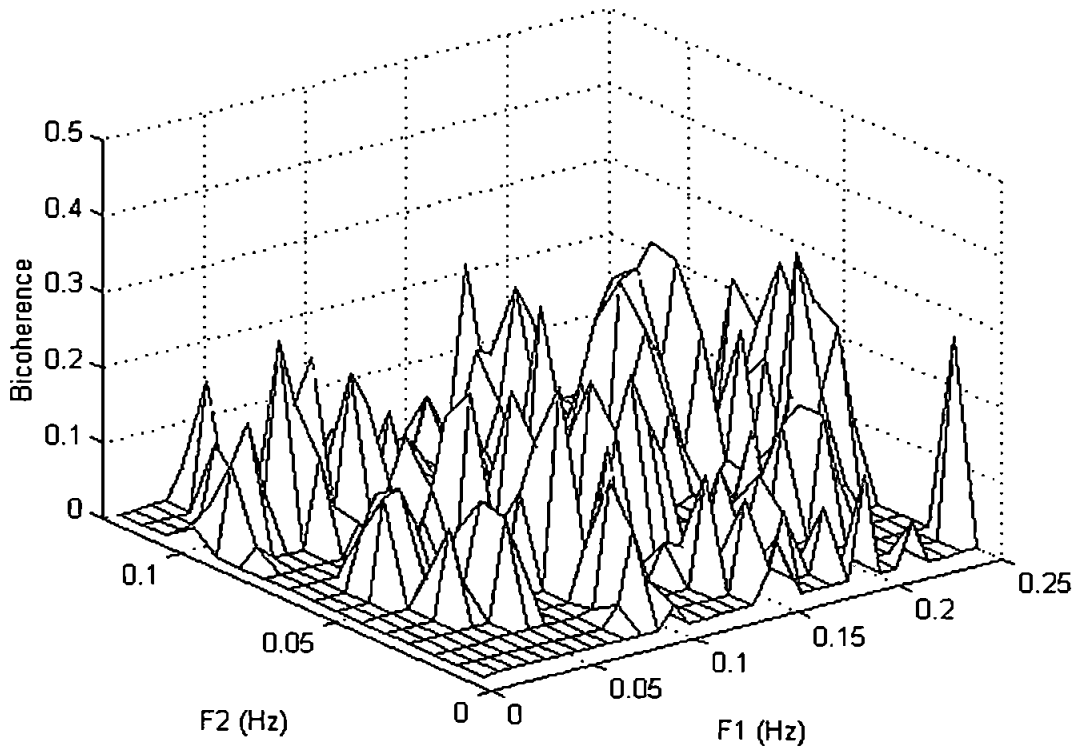

Figure 5.4.10 Bicoherence spectrum for Perranporth run 1, saturated surf zone, (h=0.47m). z-axis values indicate exceedence of the 95% zero bicoherence estimate

5.5 Summary of the low frequency hydrodynamics

The analysis in this chapter has focused on two types of variation in the oscillatory processes that occur on infragravity time scales. The natures of both the modulation of incident wave heights and distribution of infragravity energy varied between the intermediate (Spurn Head) and dissipative (Llangennith and Perranporth) sites, and with cross-shore position. A review of this chapter's results may be given by making a comparison of the conclusions drawn in this section with the distribution of the data as discussed in section 5.1.3. Figure 5.5.1 shows this representation of the dataset again. Each of the spatial-energetic categorisations of the diagrams are then associated with the results as follows.

Region A: Shoaling zone, incident frequency wave dominated (Spurn Head data).

The incident waves have a deep water 'groupy' form, and although the bound infragravity component begins to detach itself from the groups (phase increases past 180°), continues to be forced by the incident wave modulations up to the breaker line.

Region B: Outer surf zone, incident frequency wave dominated (Spurn Head data).

Incident frequency wave height modulations change dramatically, as the largest waves break, whilst the smaller waves continue to shoal. Infragravity wave shoaling conforms more to a free wave relationship, and at Spurn Head, since the beach slope is generally steep, wave energy throughout the infragravity band is reflected and leads to a standing wave type distribution of energy.

Region C: Inner surf zone, incident frequency wave dominated (Perranporth and Spurn Head data).

Incident wave height modulations are due to individual large breakers. At both Perranporth and Spurn Head the infragravity energy includes a significant contribution from higher frequencies, and when this energy is incident upon a shallow beach slope, it is dissipated in the surf zone. Consequently higher infragravity energy tends to a progressive (Perranporth) or partially standing (Spurn Head) form.

Region D: Inner surf zone, infragravity frequency wave dominated (Llangennith data).

Incident wave height modulations are due to individual large breakers, although for some of the Llangennith runs very close to shore the shoaled infragravity component may force breaker heights. At Llangennith the extremely energetic infragravity component is dominated by the lower frequencies which have the majority of their energy reflected, whilst the higher frequencies tend to be dissipated. This leads to a partially standing form for wave energy.

Generalising the results, incident frequency wave heights change from having a deep water 'groupy' structure outside of the surf zone towards a more random distribution in the inner surf zone. Onshore directed infragravity wave energy takes a bound long wave form in the shoaling zone, but these waves appear to be released just after the onset of breaking and propagate through the surf zone as free waves. Near to shore however, the behaviour of the infragravity waves suggests frequency dependence. Waves at the lowest infragravity frequencies were observed to follow a free wave shoaling relationship and have much of their energy reflected. At higher infragravity frequencies dissipation of wave energy occurs, possibly due to a dissipative interaction occurring between the breakers and the higher infragravity frequency waves. Furthermore, more higher infragravity frequency energy appears to be lost in the reflection process than at lower infragravity frequencies. The degree to which this occurs is also dependent upon the beach slope (i.e. less dissipation will occur on steeper beaches), therefore reflection coefficient shows a relationship to the Iribarren number. As a consequence of frequency dependent reflection coefficients taking values of less than 100%, the extent to which the infragravity energy takes on a standing or progressive form may depend upon beach slope and the dominant incoming wave frequency.

Analysis of phase between the incident and infragravity components showed that in the shoaling zone the bound long wave troughs are associated with the largest incident waves, whilst very close to shore the largest breakers tend to be in phase with the long wave crests. For much of the surf zone however, no significant correlation may be observed between the two components. Bispectral analysis suggests that in the main, non-linear interactions between the incident and infragravity components occur in the shoaling zone, where wave groups will force the bound waves, and very near to shore where the results hint at a dissipative interaction occurring between the breakers and the higher infragravity frequencies. Some forcing of breaker heights by a shoaled infragravity component may occur very near to shore.

Figure 5.5.1 Distribution of breaker index values versus energy-distance space for entire dataset. The x-axis parameter is a product of the ratio of gravity to infragravity frequency wave energy and the normalised surf zone position.

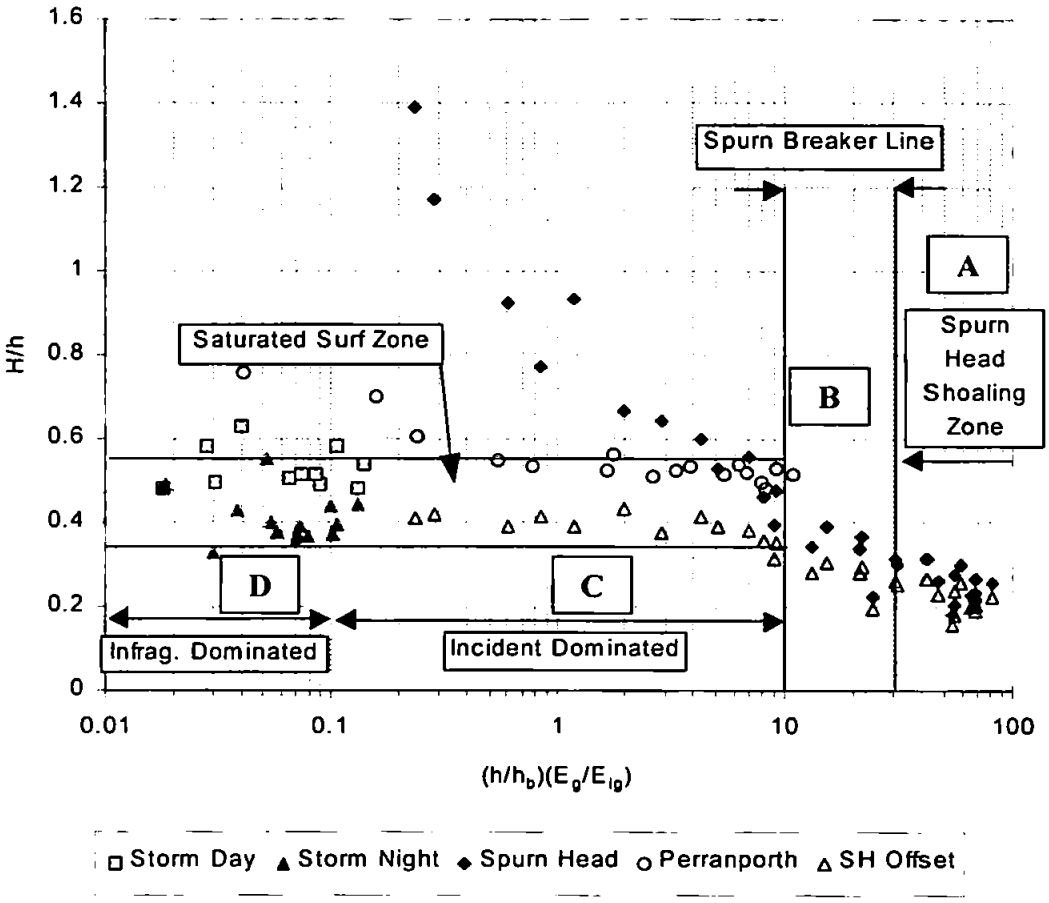

Chapter 6: Results II, Sediment Dynamics

The results in the previous chapter show that low frequency variations in the oscillatory velocity field occur at all of the three field sites featured in this dataset. In terms of the sediment dynamic problem described in the introduction however, further questions need to be addressed:

> Can these variations in velocity be directly related to larger than normal suspension events occurring at low frequencies?
>
> Will such events cause any qualitative deviation in sediment transport from the sort of results expected in a wave stirring-mean current transport or energetics type model?

This chapter attempts to address these questions. In section 6.1 low frequency variations in sediment suspension are examined by directly comparing time-series of instantaneous velocity with suspended sediment concentration. Sections 6.2 and 6.3 then examine the effect of low frequency suspension events on overall transport. A summary of the results is given in section 6.4.

It is worth pointing out that implicit in the sediment flux calculations presented in this chapter is the assumption that the type of point flux measurement made by a single OBS, as used in the results, is at least qualitatively representative of vertically integrated transport. This assumption has been made by previous authors (e.g. Foote, 1995). It is likely that in shallow water, measurements of velocity taken outside of the wave boundary layer will represent velocity throughout the water column. Furthermore, Foote *et al.* (1998) were able to demonstrate that the B-BAND point measurements of velocity were able to qualitatively predict depth-integrated flux using a velocity moments approach. Therefore in shallow water the argument that, in terms of behaviour, point measurements mimic total transport should hold provide it can be demonstrated that sediment concentrations respond to current instantaneously and are correlated with zero phase at different elevations above the bed.

Within this dataset the first proviso is satisfied throughout the results, and this may be seen in the examples given in section 6.1, where maximum suspension is always related either to a velocity or acceleration maxima. The correlation between the suspended sediment concentration signals at two points in the vertical was also checked for the Spurn Head data. For this experiment two OBS sensors had been deployed, one at 10cm above bed

level, and another at a height of 25cm. A comparison between the two signals found them to be well correlated, with correlation coefficients between 0.85 and 0.95 observed for virtually all the runs. Figure 6.0.1 shows the lag between the two OBS signals derived from this correlation analysis. In the diagram, for any given run the lag varies between 0 and 1 seconds, which when it is considered that sampling frequency for the Spurn Head experiment was 2Hz, corresponds to a lag between the two time-series of either one or two data points. The signals are thus in phase and hence similar changes in behaviour will be observed at both elevations above the bed. This result also undermines the hypothesis that in these cases, high concentrations of sediment are being observed at low frequencies as a result of the kind of 'pumping' effect seen under wave groups by Hanes and Huntley (1986). If this were the case a lag significantly greater than zero would be expected. Modelling work by Trouw *et al.* (1999) has also demonstrated that below elevations of approximately 20cm above the bed, this type of vertical diffusion of sediment will contribute the least to the type of variations observed in suspended sediment concentrations.

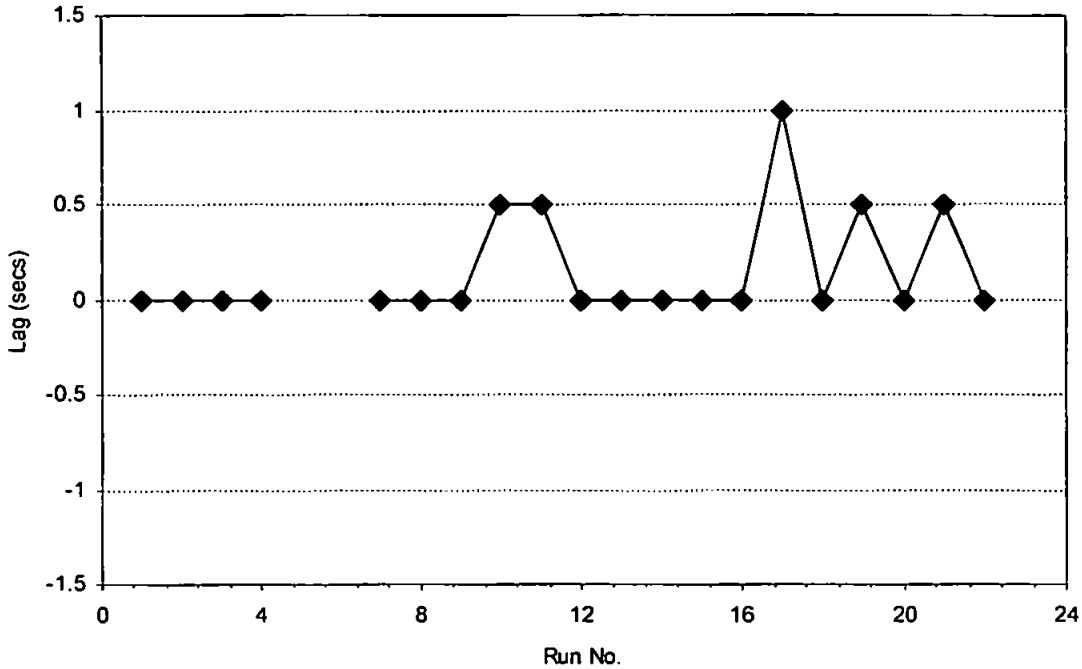

Figure 6.0.1 Spurn Head run 1-24 lags between bottom (10cm) and middle (25cm) OBS signals.

6.1 Infragravity frequency variations in suspended sediment concentrations

In this analysis of the sediment dynamics, the first step will be to identify low frequency variations in the observations of suspended sediment concentration and check if they are associated with the type of low frequency variations in hydrodynamics seen in the previous chapter. In the first two sections this is done simply by viewing time-series, with the aim of finding whether large suspension events occurring at low frequencies are linked to maxima in velocity or acceleration. Furthermore this examination should determine which of the hydrodynamic components are most important in causing such events.

6.1.1 Suspension at infragravity frequencies in the shoaling and outer surf zones - Spurn Head data

In figures 6.1.1 and 6.1.2 example time-series are shown from Spurn Head runs where the instruments were located in the shoaling and outer surf zones respectively. Diagrams of this type will be featured throughout this section and show a scatterplot of suspended sediment concentration versus cross-shore velocity, along with 'snapshots' from the run time-series which show suspended sediment concentration, cross-shore velocity, and the incident and infragravity components of cross-shore velocity.

Figure 6.1.1 illustrates the results from Spurn Head run 11, where the majority of incident frequency waves have shoaled to the point when they are just about to commence breaking. In the figure the velocity signal is clearly dominated by a groupy wave structure. This is reflected in the suspended sediment time-series in figure 6.1.1, which shows the largest suspension events to be of an incident frequency duration, and in phase with the largest waves. For example, events at 40, 150 and 280 seconds in the time-series see pairs of larger suspension events that have incident frequency timescale and can be directly attributed to the passage of large incident frequency waves past the instruments. In the scatterplot suspended sediment concentration appears to be driven by velocity but notably is also related to whether the flow is onshore or offshore directed. For both phases of flow, suspension increases with increasing velocity magnitude, but despite the fact that maximum onshore velocity values are larger than their offshore counterparts, the largest suspension maxima are found associated with the offshore directed flow. This leads to an asymmetric plot, with the gradient for suspension versus velocity rather more linear for positive cross-shore velocity values than for the negative velocities, which see a sharp increase in suspension for velocity magnitudes of greater than $0.4ms^{-1}$.

Figure 6.1.2 uses the time-series from run 8, when the instruments are inside the surf zone and wave breaking is nearing saturation (i.e. a majority of waves are likely to be broken). As a result, neither the suspended sediment concentration nor velocity time-series display the sort of 'organised' behaviour seen in figure 6.1.1. Instead, the largest suspension events in figure 6.1.2 tend to occur as single events, as opposed to as several events together. In the figure, events at 25, 110, 160, 220 and 230 seconds are driven by offshore directed velocity maxima resulting from a combination of a large incident frequency wave and a infragravity wave trough. In the scatterplot this is indicated by a bias in scatter where the largest suspension values are found for the strongest offshore directed currents. Suspension is therefore velocity driven, and since the mean current value is small, is directly a result of the combination of the oscillatory components in this case. Again however, the scatterplot shows that rather more sediment tends to be suspended in association with offshore directed velocity than with the onshore phase. Notably, when large incident waves are not observed in conjunction with an infragravity trough (e.g. at 90, 140 and 175 seconds) similarly large suspensions are not observed.

As for figure 6.1.1, the timescale of the suspension events in figure 6.1.2 remain in the incident band. Suspension maxima also remain similar between these two runs despite the onset of wave breaking that occurs between the shoaling and surf zones. The reason for the similarity in the scatterplots from the two runs is therefore likely to be due to the continued shoaling of the infragravity component, which in the surf zone supplements the incident frequency wave velocity field to a greater extent than it does in the shoaling zone. In the shoaling zone, low frequency variations in suspension can be attributed to incident frequency wave groupiness, and these suspension events will coincide with an infragravity wave trough due to the phase relationship between the incident waves and the bound long wave. However in the surf zone, whilst incident wave heights are shown to be variable in the outer surf zone, the largest sediment suspension events only occur when large waves are in phase with an infragravity wave trough.

Figure 6.1.1 Spurn Head run 11 (h=1.79m) c versus u scatterplot and time-series for c, u and incident and infragravity frequency u. In the scatterplot the dotted line denotes mean velocity.

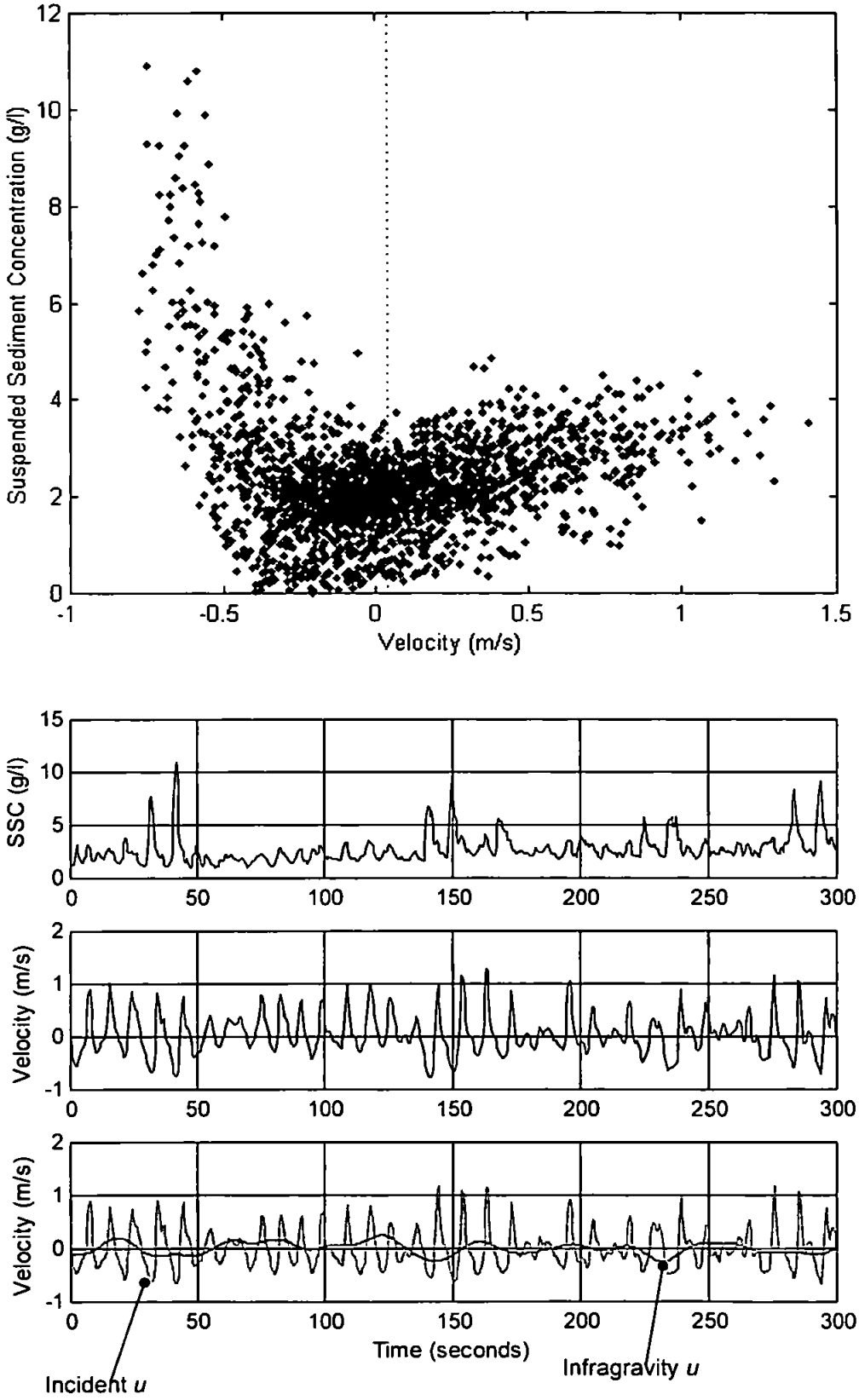

Figure 6.1.2 Spurn Head run 8 (h=1.09m) c versus u scatterplot and time-series for c, u and incident and infragravity frequency u. In the scatterplot the dotted line denotes mean velocity.

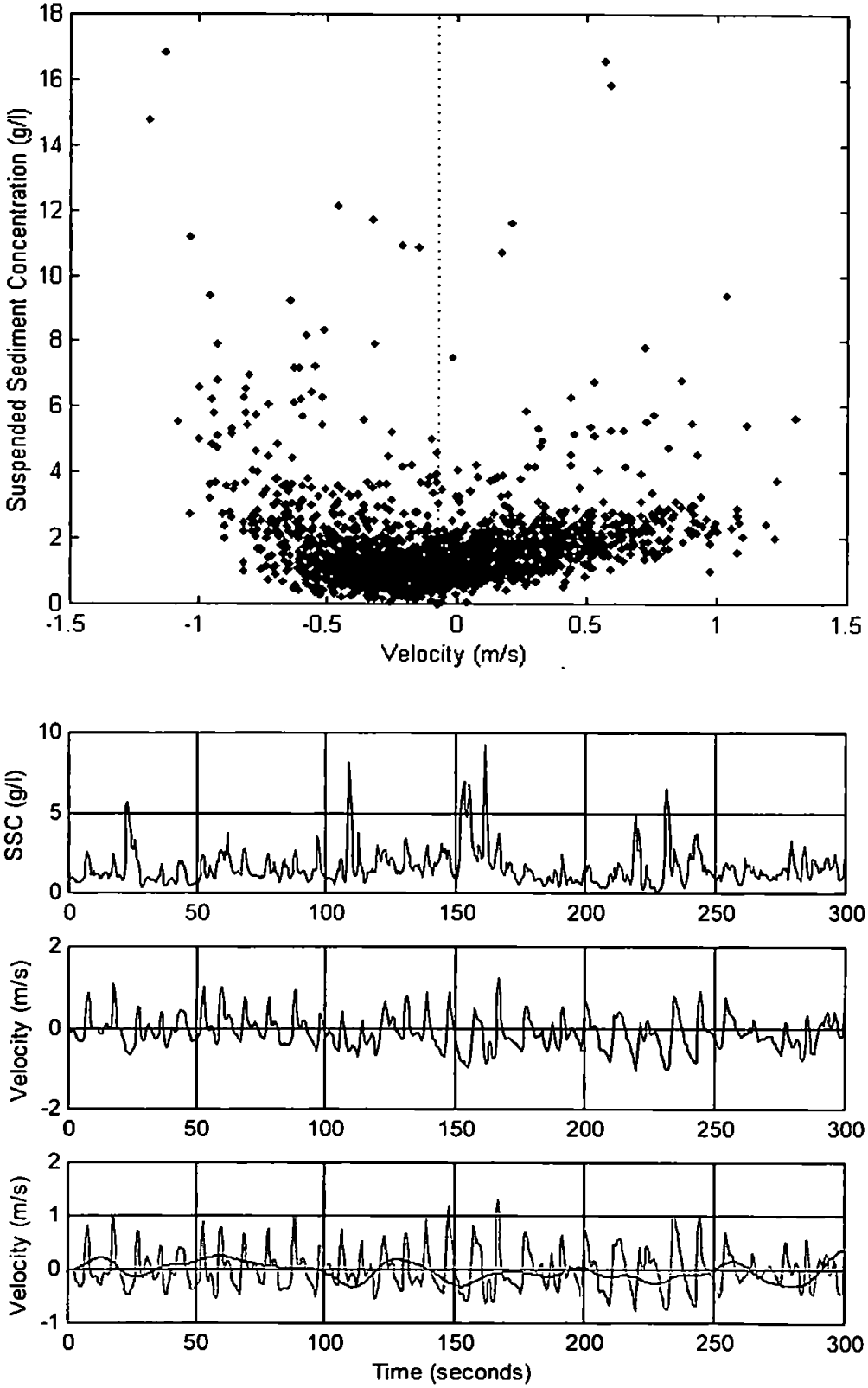

6.1.2 Suspension at infragravity frequencies in the inner surf zone

Whilst both the Llangennith and Perranporth runs are taken from the saturated inner surf zone, the spatial extent of the Perranporth dataset is rather larger, and includes runs where the incident frequency wave component provides the dominant source of wave energy. In this subsection the aim is to discuss changes in the suspended sediment time-series measured progressively closer to the shoreline.

Time-series representative of those runs observed furthest offshore whilst still in the inner surf zone are shown in figures 6.1.3 and 6.1.4. Here the runs selected are Perranporth runs 7 (figure 6.1.3) and 9 (figure 6.1.4). In both figures 6.1.3 and 6.1.4 the majority of small suspension events, which occur at incident frequencies, are observed associated with the offshore phase of velocity. In the scatterplots from figures 6.1.3 and 6.1.4 this is represented by an asymmetry where a majority of measurements between approximately $2gl^{-1}$ and $6gl^{-1}$ are observed in conjunction with negative (offshore directed) velocity values. On the onshore phase suspended sediment concentrations are not always observed to increase in response to an increase in velocity. The scatterplots in both figures show low suspension values even for high onshore velocities, although in figure 6.1.3 high levels of suspension are also seen in association with the onshore phase of velocity. The latter suspension events are observed in the time-series to result almost exclusively from the combination of the infragravity and incident components to yield a strong onshore velocity. This suggests that neither oscillatory component is strong enough to stimulate large events when the other component is near zero or offshore directed. These largest low frequency suspension events have an incident banded duration.

In run 9 (figure 6.1.4) the largest suspended sediment concentration measurements are found to correspond to velocities between $0ms^{-1}$ and $0.5ms^{-1}$. With these events in mind, an examination of the time-series, which compares acceleration to suspended sediment concentration (figure 6.1.5), shows the same events corresponding to a strong deceleration. Such an instance where deceleration is associated with flow reversal physically points to part of the wave just after the passage of a bore front. In a further examination of the time-series (figure 6.1.4) it can be seen that the larger suspension events in this run are associated with the passage of a bore occurring whilst the infragravity velocity field is onshore directed (for example, events in figure 6.1.4 at 25 and 60 seconds). Conversely, no events are observed when larger breakers are coincident with an offshore directed infragravity component. Thus it would seem that in order for the suspension events seen in

these runs to occur, one condition is for a strong flow to be set up near the bed onto which an opposite sharp flow is imposed. This is similar to a mechanism for the generation of turbulence proposed by Foster *et al.* (1997).

In shallower water, where the infragravity component is more energetic, the number of large suspension events increases, and again suspension appears to be primarily velocity driven. Figures 6.1.6 and 6.1.7 show that for both Perranporth run 1 (figure 6.1.6) and Spurn Head run 1 (figure 6.1.7) high suspensions are found at both the onshore and offshore directed velocity maxima. Again these maxima occur as a result of the combination of the infragravity and incident frequency velocities when a large incident wave is in phase with either an infragravity wave peak or trough. For example, in figure 6.1.6 the largest events are a result of the onshore velocity maxima that occur during the onshore phase of infragravity frequency velocity. Conversely, in the Spurn Head run the events at 90 seconds are associated with onshore directed velocity and an infragravity peak, whilst the larger event at 130 seconds is a product of the combination of an infragravity and incident wave offshore directed velocity. In both these figures the mean current is small, and hence the main contribution to velocity maxima comes from the oscillatory components.

Storm Day run 10 (figure 6.1.8) gives an extreme example of the results seen in the previous two figures. In the scatterplot from this run, extremely high suspended sediment concentrations are observed in association with both onshore and offshore directed velocity maxima. Suspension in this instance also occurs in association with flow reversal. Further examination of the Storm Day run 10 time-series shows that in association with the offshore directed velocity maxima, suspension events have a longer duration (around 30 seconds), than were observed in the previous examples. Corresponding to this, the figure also sees far larger values for infragravity frequency velocity than are noted in the Perranporth and Spurn Head datasets. For example the long lived suspension events found at 110 and 210 seconds are associated with maximum streaming of the infragravity frequency velocity offshore. Conversely the two suspension events at 140 and 160 seconds are associated with sharp changes in velocity at bore fronts and a large onshore directed infragravity velocity. These two events are of a incident banded duration.

Thus for Storm Day runs close to shore, the largest events which dominate the time-series are seen to coincide with the offshore phase of the infragravity oscillatory current, which is reinforced by the offshore directed mean flow. These events dominate the time-series to

such an extent that a correlation analysis between the suspended sediment concentration and sea surface elevation time-series (figure 6.1.9) from Storm Day run 10 shows a significant correlation between infragravity frequency troughs in sea-surface elevation (at approximately 0.01Hz) and the peak in concentration with a lag of -8 seconds. Physically this suggests that the largest suspension events are preceded by an infragravity wave trough. Furthermore, as was demonstrated in chapter 5, in the case of Storm Day run 10 the overall infragravity wave field is dominated by the incoming free waves. The correlation between both the incoming and reflected component velocities versus suspended sediment suspension is shown in figure 6.1.10. In terms of physically meaningful correlations it seems unlikely that correlations with a lag of larger than ±10 seconds will represent a process relevant to the suspension events seen in Storm Day run 10. Therefore the peak in significant correlation between the offshore directed velocity associated with the incoming waves and the suspended sediment concentration appears to indicate that the dominant contribution to the infragravity velocity field associated with the largest suspension events is from the incoming waves. Similarly a peak in correlation between suspended sediment concentration and the reflected velocity signal exists, but has a large positive lag (approximately 30 seconds). This suggests that in the processing the sediment suspended by the dominant incoming wave velocity simply remains well correlated to velocity in the reflected wave signal. However, the reflected wave does not show any evidence of driving suspension in the largest events.

The type of behaviour observed in this subsection would appear to be in conflict with the modelling hypothesis in which infragravity waves are seen to be standing in nature and basically are considered as a drift velocity component, only acting to transport sediment stirred into suspension by the incident frequency waves (e.g. Bowen, 1980). Instead the infragravity wave velocity field is found to supplement other components in generating a strong enough velocity to mobilise larger amounts of sediment, albeit at low frequencies. Furthermore several runs in the Storm Day dataset actually see sediment suspension directly associated with infragravity wave velocities, and with a strong correlation specifically to the incoming wave energy. In this case the infragravity energy involved in sediment suspension appears to be related to a progressive incoming component rather than standing wave energy.

Figure 6.1.3 Perranporth run 7 (h=2.06m) c versus u scatterplot and time-series for c, u and incident and infragravity frequency u. In the scatterplot the dotted line denotes mean velocity.

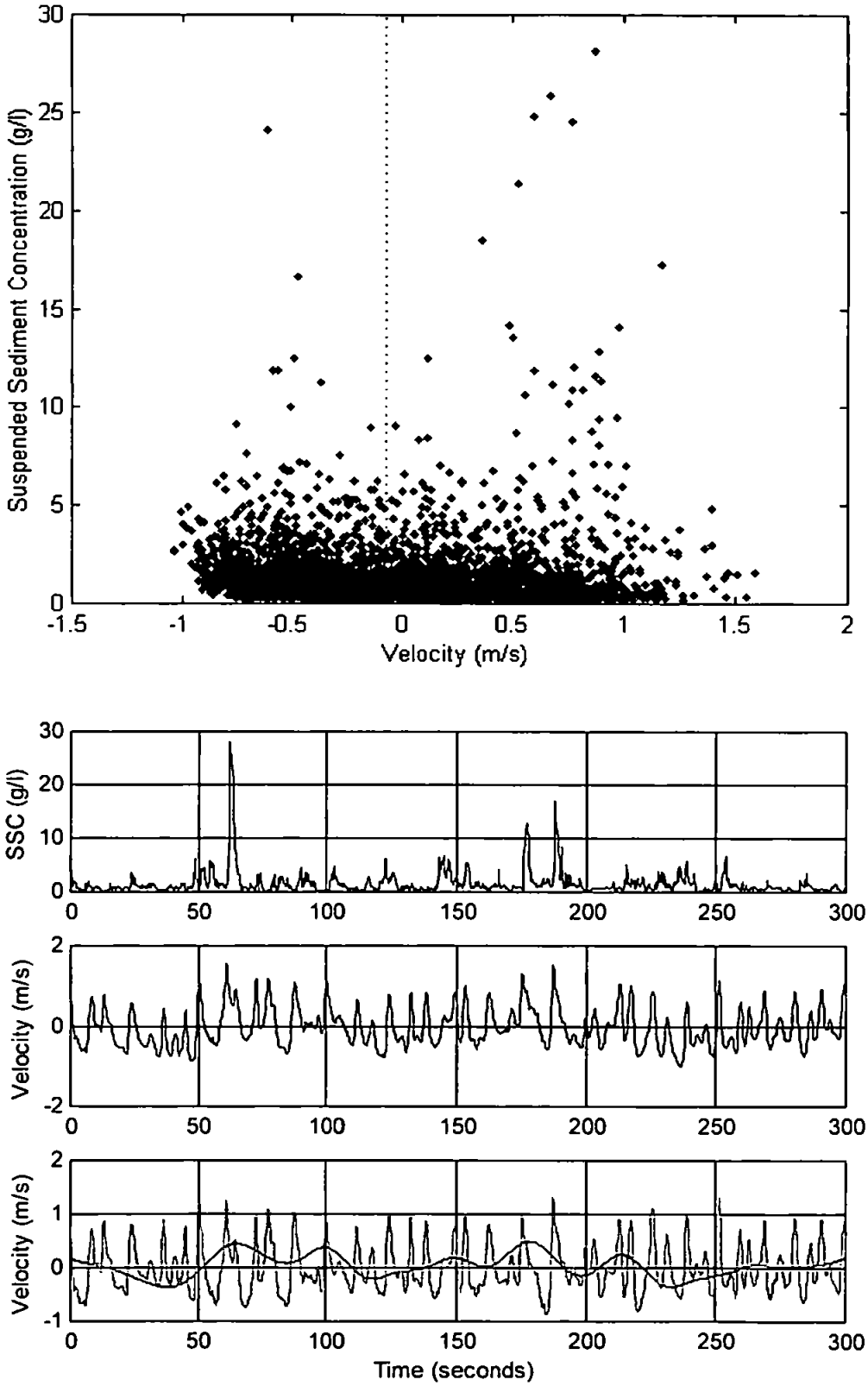

Figure 6.1.4 Perranporth run 9 (h=2.19m) c versus u scatterplot and time-series for c, u and incident and infragravity frequency u. In the scatterplot the dotted line denotes mean velocity.

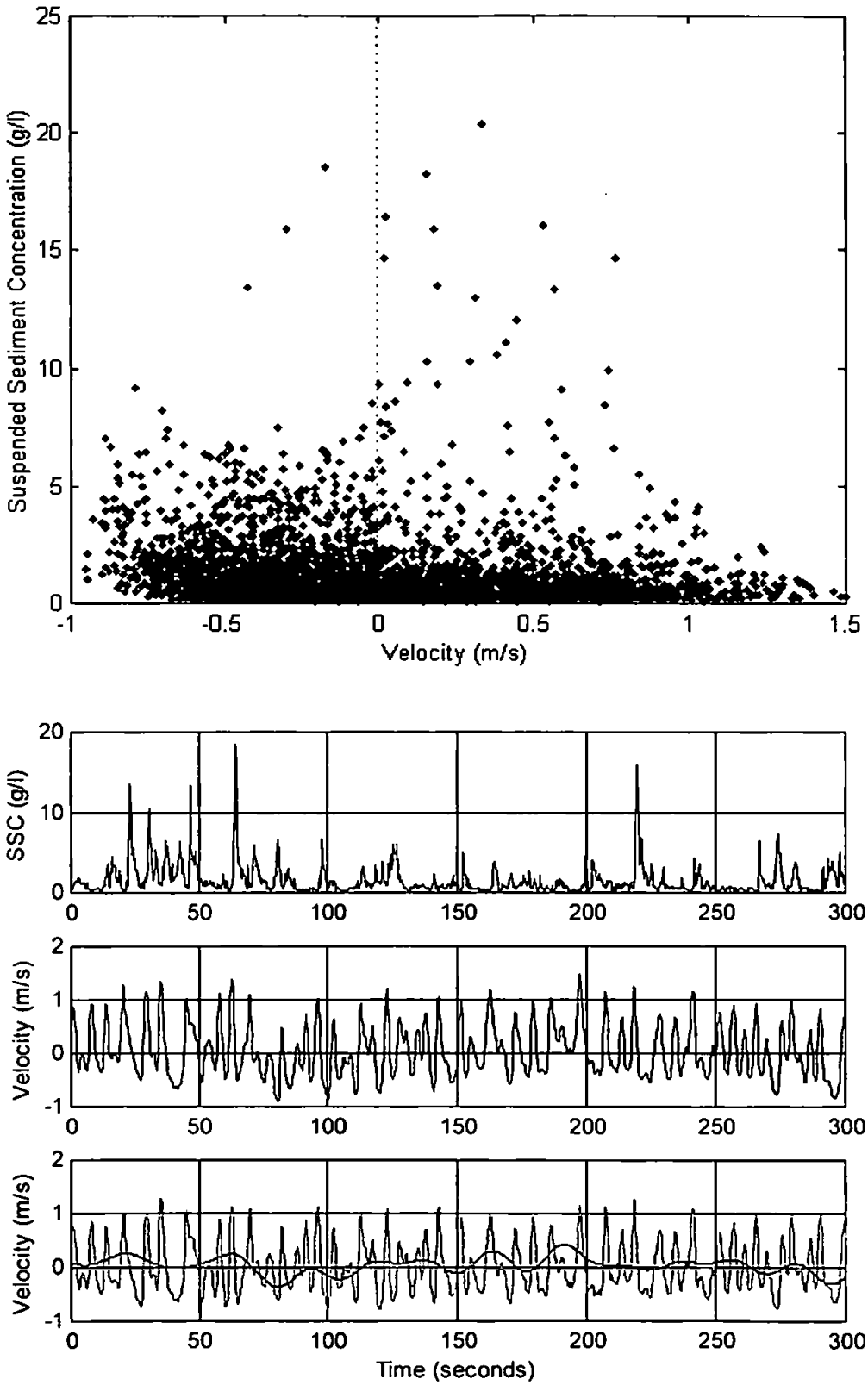

Figure 6.1.5 Scatterplot of c versus cross-shore acceleration for Perranporth run 9 (h=2.19m).

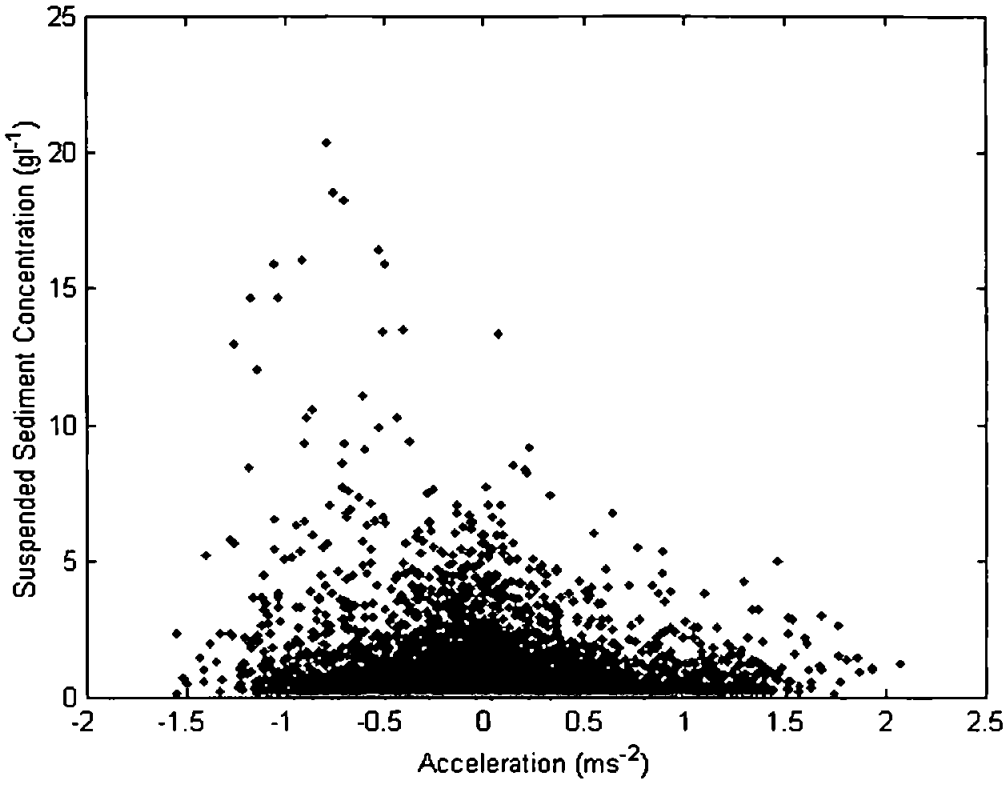

Figure 6.1.6 Perranporth run 1 (h=0.47m) c versus u scatterplot and time-series for c, u and incident and infragravity frequency u. In the scatterplot the dotted line denotes mean velocity.

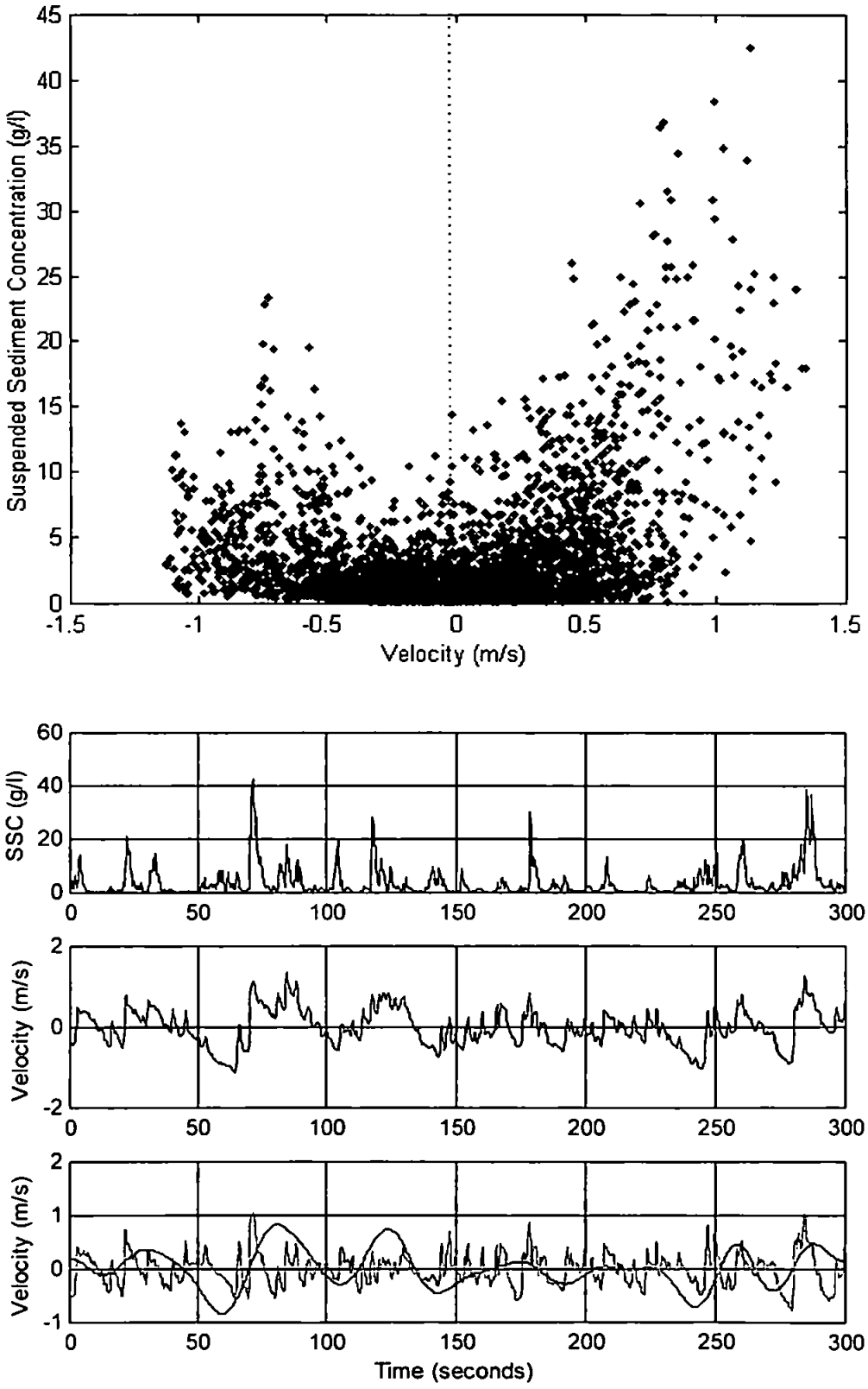

Figure 6.1.7 Spurn Head run 1 (h=0.17m) c versus u scatterplot and time-series for c, u and incident and infragravity frequency u. In the scatterplot the dotted line denotes mean velocity.

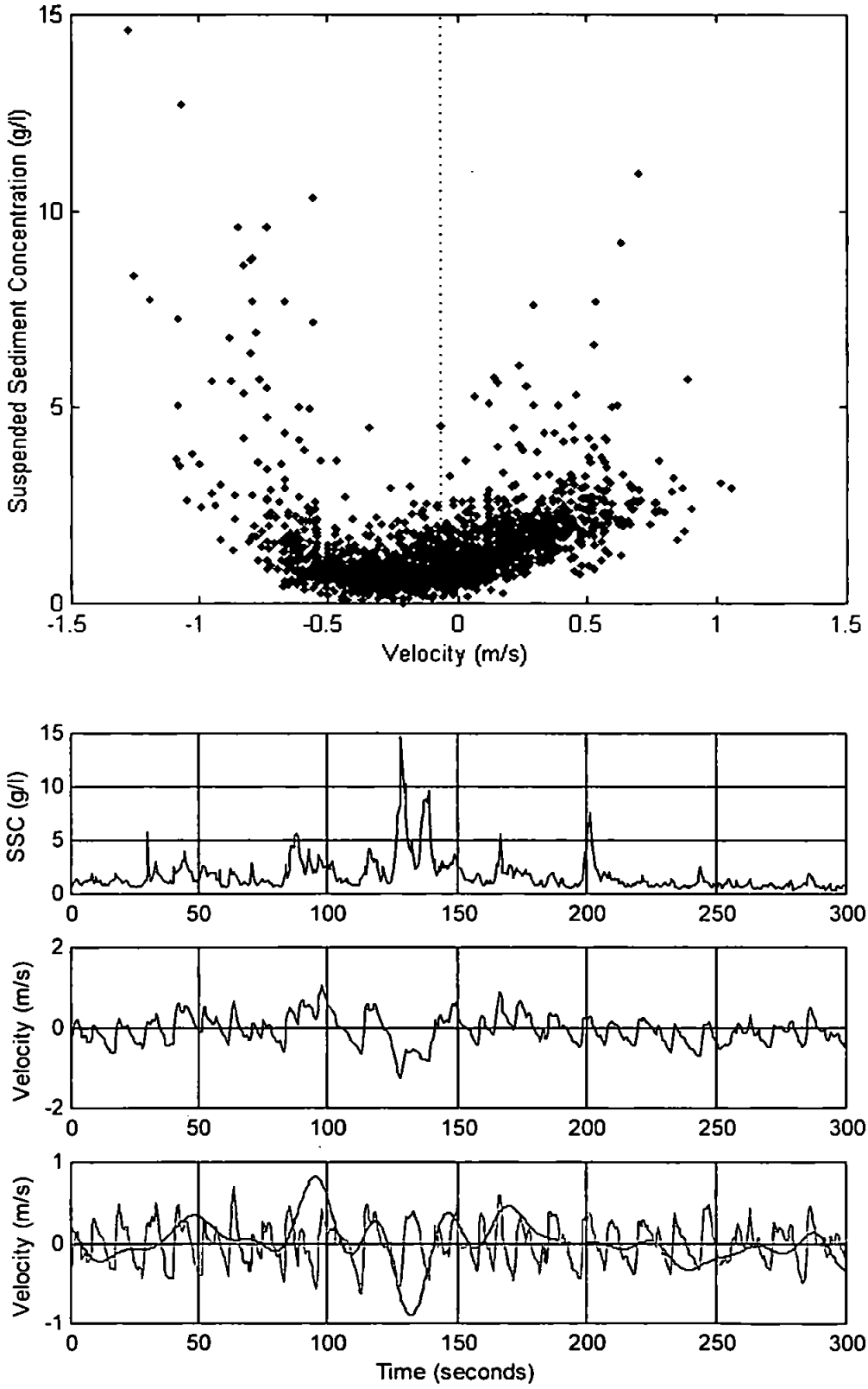

Figure 6.1.8 Storm Day run 10 (h=0.66m) c versus u scatterplot and time-series for c, u, and incident and infragravity frequency u. In the scatterplot the dotted line denotes mean velocity.

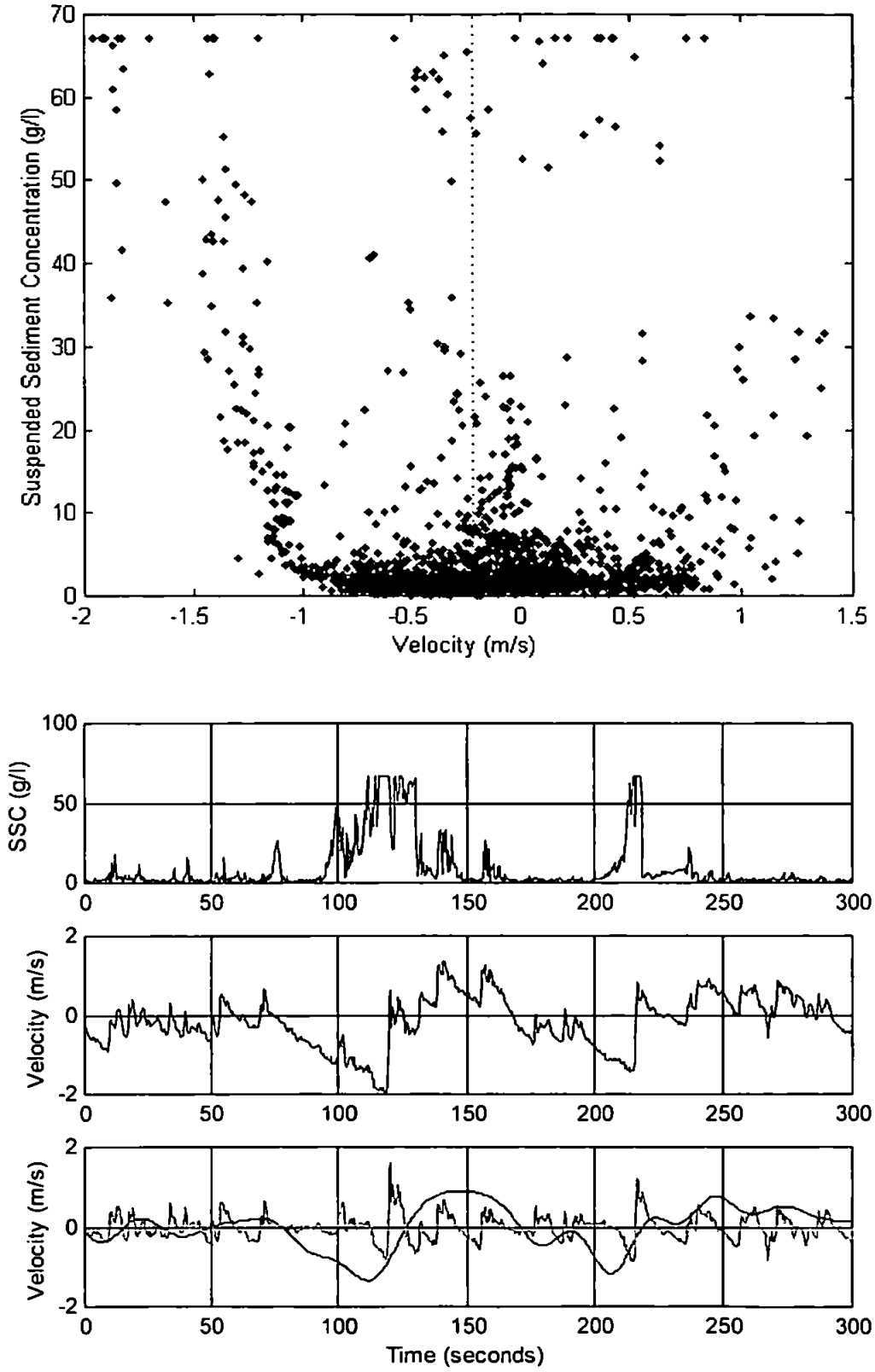

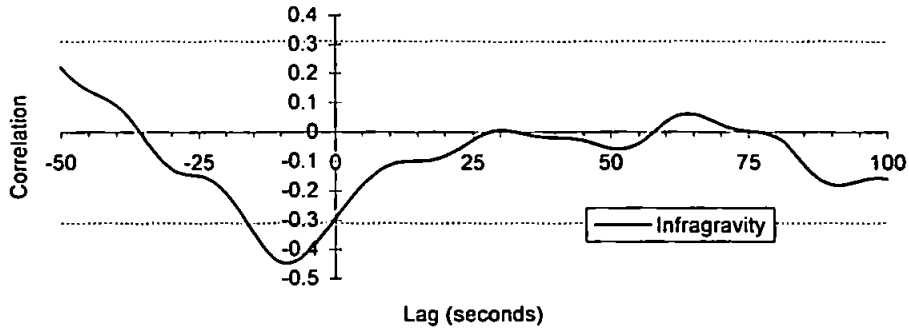

Figure 6.1.9 Correlation between c and time-series for the infragravity frequency variations of η, Storm Day run 10 (h=0.66m).

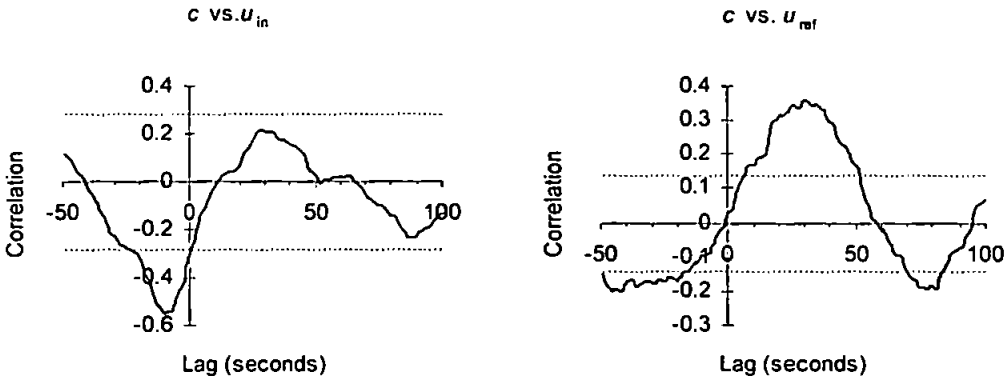

Figure 6.1.10 Correlations between c and the infragravity velocity signal for incoming and reflected waves, Storm Day run 10 (h=0.66m).

6.1.3 Contribution of the infragravity frequency component to suspension

In the previous two subsections it was demonstrated that, in the main, large sediment suspension events occurring at infragravity frequencies were frequently associated with maxima in velocity. In the shoaling zone these events were associated with incident frequency wave groupiness, whilst in the surf zone the velocity maxima inducing high sediment concentrations resulted from a combination of infragravity and incident wave related velocities, supplemented by mean flow. Unsurprisingly, as the infragravity component shoaled toward the shoreline it became more important in causing such suspension events. In an extreme example shown in section 6.1.2, infragravity provided the necessary stirring for suspension events to occur over an infragravity timescale.

The contribution of the infragravity frequencies to suspended sediment concentration variance can be represented by the parameter,

$$\frac{Esusp_{ig}}{Esusp_{tot}}, \tag{6.1}$$

where $Esusp_{ig}$ is the energy in the infragravity part of the suspended sediment concentration autospectrum and $Esusp_{tot}$ the total spectral energy. In figure 6.1.11a this (normalised) contribution to overall suspended sediment concentration variance made by the infragravity frequencies at each of the beach sites is shown plotted against normalised cross-shore distance. The figure shows a general increase in the infragravity contribution through the surf zone, but finds the values highly distributed in the first third of the surf zone from the shoreline.

The distribution of values near to shore may be explained by a comparison between the normalised infragravity contribution to suspension and the parameter

$$\frac{h}{h_b}\frac{E_g}{E_{ig}}, \tag{6.2}$$

which scales the x-axis as a function of position versus the breaker line and the ratio of incident to infragravity banded wave energy (figure 6.1.11b). This scaling attempts to provide a spatial and energetic definition of the dataset, and in particular gives more detail to inner surf zone data. In figure 6.1.11b the incident frequency wave shoaling region is seen for large values on the x-axis. For reference, the breakpoint in the Spurn Head data is marked on the diagram over values between 10 and 30. The infragravity wave dominated region near to the shoreline seen in the Llangennith data is found for small values of this parameter.

The scaling means that for data in the inner surf zone, where infragravity energy dominates (low x-axis values) the normalised infragravity contribution to suspension is highest. In the surf zone, as distance from the shoreline increases and the levels of infragravity wave energy decrease, the infragravity contribution to suspension decreases. In the diagram a fit to the data based on a

$$\left(\frac{h}{h_b}\frac{E_g}{E_{ig}}\right)^{-1}$$

relationship is indicated. However, the low frequency component contributes at least approximately 30% of total variance in all the suspended sediment time-series. Furthermore, whilst this fit looks acceptable in the surf zone, in the shoaling zone the trend in the data suggests that the contribution from the infragravity component to the overall variance increases slightly.

The reason for this may well lie in the relative contributions made by incident wave groupiness and the infragravity waves to variations in suspended sediment either side of the breaker line. In the shoaling zone the incident waves are seen almost solely as responsible for sediment suspension and lead to sets of two or three high concentration events occurring with every wave group (e.g. figure 6.1.1). However, just inside the surf zone this groupiness has diminished as the largest waves start to break and in this region the infragravity component is not particularly energetic. Hence less frequent and smaller low frequency events are observed just inside the surf zone, as for example in figure 6.1.3, than are observed in the shoaling zone. Near to shore the contribution made by the infragravity component to overall variance in suspension is seen to increase, but this is especially dramatic in the Llangennith data. This corresponds to shoaling of the particularly energetic infragravity wave component observed in the Storm Day and Storm Night data. These are associated with very large suspension events of infragravity duration.

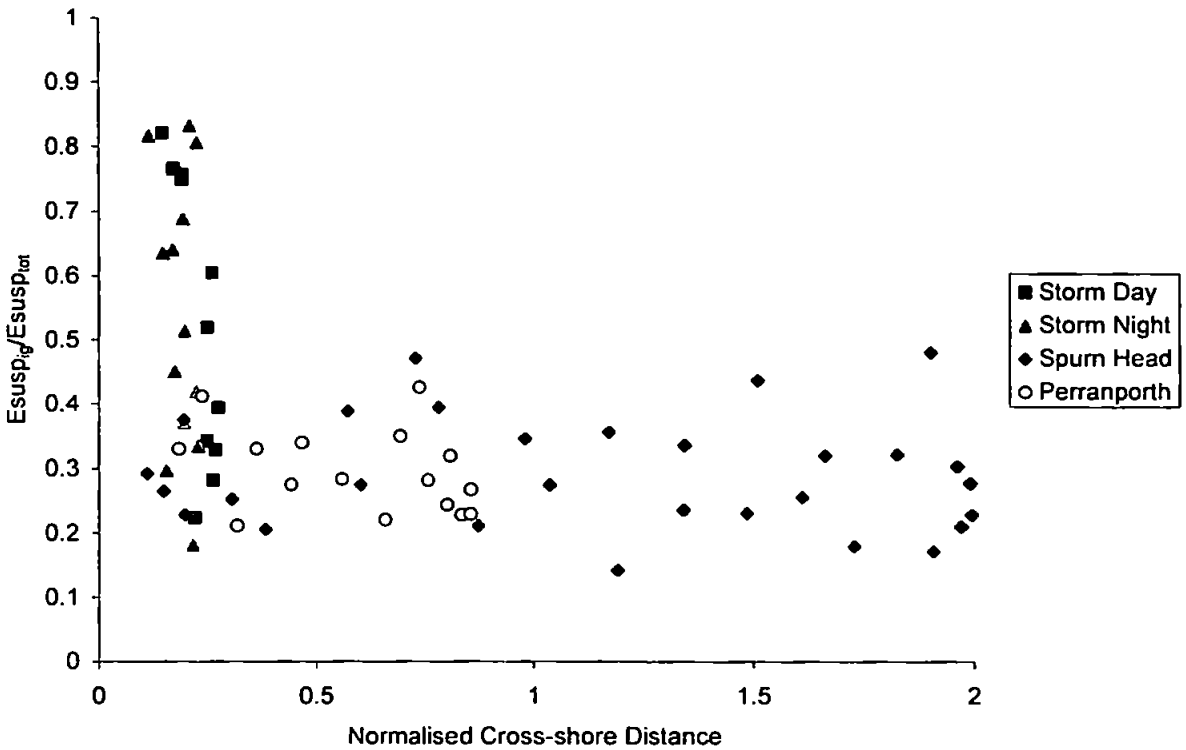

Figure 6.1.11a Normalised contributions to suspended sediment concentration variance plotted versus normalised cross-shore distance.

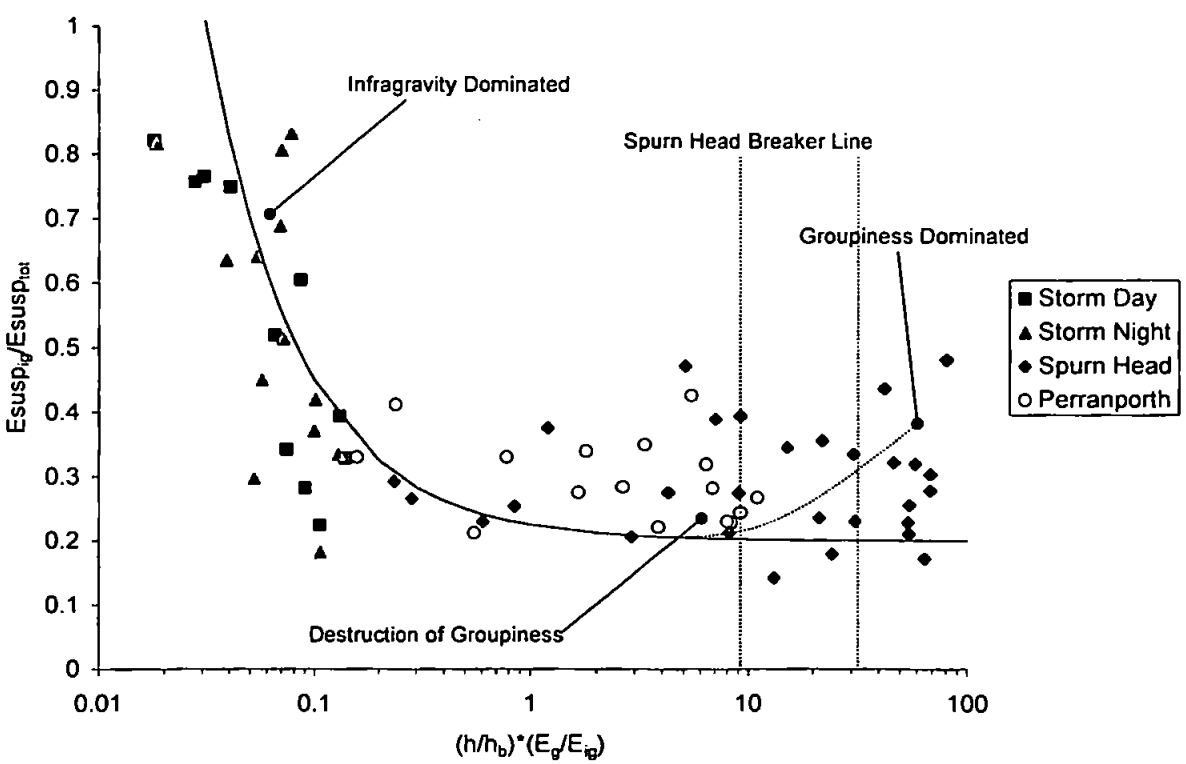

Figure 6.1.11b Normalised contributions to suspended sediment concentration variance distributed in distance-energy space.

6.1.4 Velocity phase 'asymmetries' in suspension of sediment

A further feature of the scatterplots in the previous subsections was an apparent asymmetry between the onshore and offshore directed currents in terms of how easily each mobilised sediment. For example, in figures 6.1.1 and 6.1.2 (Spurn Head runs 11 and 8) the highest concentrations of sediment were observed corresponding to the offshore velocity maxima, despite the strongest velocity maxima occurring during the onshore phase. Similarly for Perranporth run 7 (figure 6.1.3) although the maximum concentrations were associated with the strongest velocity maxima occurring on the onshore phase of velocity, the bulk of sediment was still suspended by offshore directed velocities. In section 6.2 it will be shown that this behaviour has ramifications for the resultant flux calculated from a given run.

In the Storm Day runs, the source of this asymmetry is obvious in the instantaneous velocity time-series, since the largest velocity maxima are found on the offshore phase (Appendix I). A further difference between the onshore and offshore phase of velocity in these runs is the duration for which a threshold velocity is likely to be exceeded. During the onshore phase such periods are associated with the incident wave band, whilst on the offshore phase sediment is mobilised over an infragravity duration. These latter suspension events are a result of a combination of infragravity and mean velocities, and the bias toward the offshore phase of velocity apparently results from a strong negative skewness in the lowest frequency infragravity waves (<0.02Hz).

On a rather smaller scale, a similar type of mechanism may be responsible for the asymmetry noted in Perranporth run 7. During this run the largest velocity maxima were observed during the onshore phase of velocity and correspondingly the largest suspension events were observed at the same times. However, sediment was more often mobilised, albeit at lower concentrations in association with offshore directed velocities. Figures 6.1.12 shows the results of an analysis in which the duration for which either an offshore or onshore directed velocity exceeded $0.5ms^{-1}$ was calculated from the time-series in Perranporth run 7. Despite the fact that the maximum onshore velocity was of a greater magnitude than its offshore counterpart, the majority of the longest exceedence times are found to occur for offshore directed velocities. It may well be that because of this, a rather more regular suspension of sediment occurred coincident with wave troughs, although the largest events occurred in conjunction with the crests.

At Spurn Head the high suspension concentrations observed on the offshore phase of velocity may well be due to a more complicated mechanism than has been assumed for the Llangennith and Perranporth cases. As will be discussed in the next subsection, an assumption may be made regarding the Spurn Head data that suggests ripples are present, whereas at Llangennith and Perranporth this is thought not to be the case. If this assumption is followed through, then at Spurn Head sediment will be suspended not only on the dominant onshore phase of velocity as for a flat bed, but will also be suspended (in high concentrations) by a vortex which forms at the flow reversal. Sediment suspended by this latter mechanism will be observed as it is advected past the instruments on the offshore phase of velocity. In such a case the largest suspensions will be observed 180° out of phase with the largest velocities (Trouw *et al.*, 1999). Thus in the scatterplots from the Spurn Head runs, sediment appears to be 'picked up' rather more efficiently by the offshore than the onshore phase of velocity. Despite this different type of mechanism for suspension, the offshore directed velocities will nevertheless provide the method of transport for sediment suspended in this fashion.

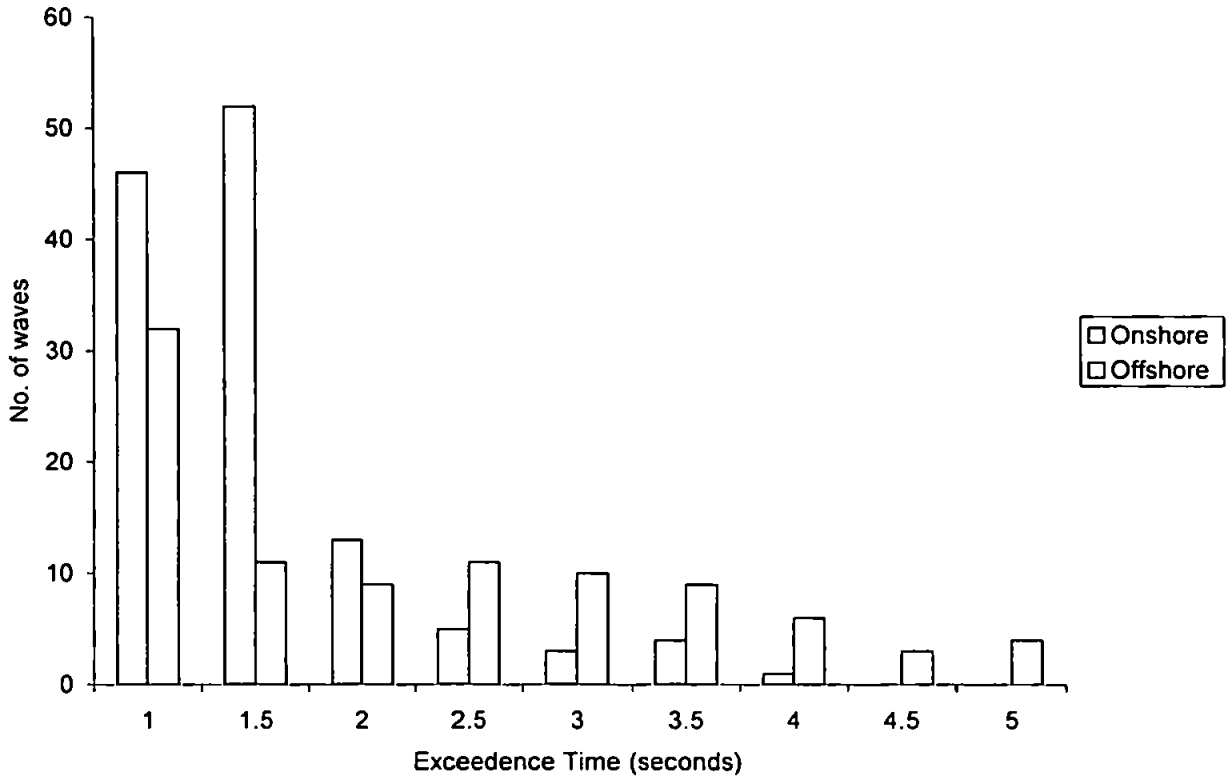

Figure 6.1.12 Perranporth run 7 (h=2.06m) velocity exceedence times, based on a velocity threshold of $0.5ms^{-1}$.

6.1.5 'Tidal asymmetries' in overall suspended sediment concentration

It is important to note that the contribution of the infragravity component to sediment suspension remains consistent despite large variations in the overall amounts of sediment suspended. Figures 6.1.13-15 show overall values (i.e. values computed over the whole of the frequency domain) for suspended sediment concentration from runs in (respectively) the Llangennith, Spurn Head and Perranporth datasets plotted versus depth. In each of the figures the flood tide runs are represented by filled symbols, whilst the ebb tide runs are marked by unfilled symbols. In this work the concentration value representing a run is derived in a manner similar to that of significant wave height, i.e. based on time-series variance. This parameter is used here rather than mean concentration since it can be related more directly to variance values for the incident and infragravity frequency components of suspended sediment concentration. In noting this however, the analysis did find that for all three datasets the run mean concentration values and 'significant' concentration values behaved in a qualitatively similar manner.

Figure 6.1.13 shows these values for the two tides at Llangennith. The flood tide runs show a pattern where overall suspension initially decreases in the shoreward direction but then increases in very shallow water in correspondence to the increasing shoaling of the infragravity wave component. However the ebb runs are more scattered and show such large values of suspension for a number of Storm Day runs that in the figure a logarithmic y-axis is necessary to show the data fully. All of these latter runs have time-series similar to that shown in figure 6.1.7 (Storm Day run 10) where infragravity timescale suspension events dominate the suspended sediment concentration signal.

For the Spurn Head runs (figure 6.1.14) the most notable feature of the figure is a set of runs (run 24-29) on the ebb tide where overall concentration is dramatically increased from that observed on the flood. These runs were described as a 'tidal asymmetry' in c variance when discussed by Davidson *et al.* (1993) (see section 2.3.3). Since no major change in the hydrodynamics was seen between ebb and flood, Davidson *et al.* (1993) suggested that this apparently anomalous increase in overall suspension was due to the destruction of the ripple field on the ebb tide. For the remainder of the thesis these anomalous ebb tide runs will be denoted as the SH24-29 runs. The formation of such a ripple field may tie in with the increase in suspension also seen on the flood tide runs during the high tide slack water period, when the instruments are in the largest depths of water. Otherwise, from the flood tide runs suspension is seen to increase to a maximum in the outer surf zone region, and the

decrease closer to the shoreline. Conversely, on the ebb tide suspension values decrease consistently through the surf zone.

At Perranporth (figure 6.1.15) the difference between values of 'significant' concentration observed on the flood tide and ebb tide runs is that an increase in suspension in the shoreward direction is seen through the cross-shore on the flood, whilst the ebb tide generally sees a decrease in suspension from the breakpoint through to the shoreline. Notably the asymmetry seen at Perranporth is the reverse of that at both Spurn Head and Llangennith, where the largest events were observed on the ebb phase.

Patterns of overall suspension documented by Beach and Sternberg (1996) and Hwang *et al.* (1996), where suspension maxima were observed at the breaker line whilst a decrease occurred in the shoreward direction, are not strictly adhered to in data from any of the thesis sites over a full tide. For example, for the Perranporth flood tide data, the values of 'significant concentration' increase toward shore rather than decrease shoreward of the breakpoint. This latter behaviour is seen for much of the ebb phase data of the tide (figure 6.1.15), but an increase in suspension is again observed when the instruments are nearest to shore. Meanwhile, at Spurn Head (figure 6.1.14), on the flood, concentrations inside the (non-saturated) surf zone are seen to be more variable than those at the breakpoint, and whilst on the ebb phase suspension diminishes through the surf zone, several runs in the shoaling zone (SH24-29) experience uncharacteristically large concentrations. In the Llangennith dataset, when the instruments are close to the swash zone, levels of suspension increase from those observed further offshore in the surf zone. Furthermore, on the ebb tide a dramatic increase is noted between several runs and the majority of others in the Storm Day data (figure 6.1.13).

One difference between this data and the two studies cited above can be found in the hydrodynamics. For example Beach and Sternberg (1996) saw plunging type breaking for relatively small waves (breaker height 0.5m), and found that their surf zone tended toward a saturated situation in terms of breaker index within 20m of the breaker line. Conversely the surf zones at Llangennith and Perranporth examined here are rather more energetic than that in Beach and Sternberg's (1996) study. This is particularly true at Llangennith where the infragravity component dominates the oscillatory velocity field toward shore. Spurn Head has a rather wider outer surf zone than was observed in Beach and Sternberg's (1996) study (approximately 40m). Thus the velocity fields and distributions of breaker induced turbulence are liable to be rather different in all these cases. The ebb tide at

Perranporth does behave similarly to Hwang *et al.*'s (1996) experiment, and indeed sees similar hydrodynamic conditions where moderately energetic waves (offshore wave height approximately 2m, period 5-7 seconds) are incident on a gently sloping beach. However the difference between the ebb and flood at Perranporth, and indeed the similar 'tidal asymmetry' at Spurn Head, does highlight further likely differences between different datasets. This may possibly lie in the behaviour of the bed, and needs to be explored further.

In the Storm Day and Storm Night datasets the increase in suspension very close to shore is probably an effect of the hydrodynamic components. Within this thesis Llangennith has been assumed to have a plane bed and sheet flow conditions as a consequence of the high values of both onshore and offshore instantaneous velocity maxima documented in Appendix I. These are seen to be well in excess of the value of $1ms^{-1}$ quoted for producing a plane bed by Reineck and Singh (1980). For those runs when the instruments are in very shallow water, and where suspended sediment concentration increases dramatically compared to observations from further offshore in the surf zone, the infragravity component dominates the velocity field to such an extent that suspension takes on an infragravity timescale. As was stated in section 6.1.3, it would seem likely that as a result of the longer lived stress applied over the bed rather more sediment is able to be mobilised.

At Spurn Head, the tidal asymmetry in suspension is also observed for runs when the instruments were in the shoaling zone. As has been stated earlier, in attempting to explain the reason for this type of behaviour, Davidson *et al.* (1993) suggested that bedforms could be responsible for such an asymmetry. It was proposed that ripples formed over the high water period and were then destroyed during the SH24-29 runs. Whilst this assumption cannot be proven fully without proper observations of the bed state, some further light may be shed on this hypothesis by examining the distribution of mobility number (ψ) values (as for Dingler and Inman, 1976; Hanes, 1997) from runs at each site. It may be recalled that within this classification, rapid ripple formation was suggested to occur for waves with mobility number of between 50 and 150. For values of mobility number in the range 150-250, a group of waves would destroy a ripple field, whilst waves with a mobility number of greater than 250 could destroy a ripple field on their own.

Following a wave-by-wave analysis of mobility number maxima, figure 6.1.16 compares the percentages of waves with mobility number in the above classes, for runs from the Storm Day, Perranporth and Spurn Head datasets. Whilst all the datasets see waves with

mobility numbers in the ripple forming range, for Storm Day 50% of the waves achieve mobility numbers in the ranges likely to lead to a plane bed, and at Perranporth this figure is approximately 35%. These statistics, where either one in two or one in three waves is large enough to wash out ripples, mean that for both datasets it is unlikely that a period of time will occur in which it is sufficiently calm for bedforms to be generated.

At Spurn Head, for nearly the whole of the time in any given run, the maximum current strength will still be likely to lead to ripple formation according to this classification. For example in the run in figure 6.1.16 ripple forming velocity maxima were observed for approximately 95% of the waves. However, in examining the mobility number time-series of run 24, which is the first of the SH24-29 runs, one peculiarity of this run is the occurrence of two consecutive high wave groups toward the end of the run, during which high mobility numbers are observed (figure 6.1.17). It may well be that these two groups plus another seen early in run 25 destroyed the ripple field built up over the preceding runs in the tide very quickly. This would have led to the higher suspension values seen in these two runs. As confirmation of this, figure 6.1.18 compares suspended sediment concentration versus cross-shore velocity scatter from Spurn Head run 15 on the flood tide with that from run 24 on the ebb. Water depth at the instruments was similar for both runs, but in the figure the spread of points in run 24 sees higher velocity magnitudes being obtained during this run. Correspondingly sediment suspension is increased, but this is particularly dramatic on the offshore phase, where the maximum concentration on run 24 is almost five times as large as that in run 15 (figure 6.1.18). Examining the distribution of mobility number between runs 15, 20 and 24 (figure 6.1.19) a difference is apparent in the percentages seen between the runs in the $150<\psi<250$ banding. The suggestion from these results is therefore that ripples did indeed form during the flood tide at Spurn Head, but were then destroyed simply by two or three slightly larger than usual wave groups.

In contrast to the other two datasets, at Perranporth, more suspension of sediment was observed on the flood tide than on the ebb. Also during the flood phase, observed concentrations decreased as the depth of water at the instruments increased. A similar flood tide distribution was observed on the tide preceding the one presented in this work and may also be observed in the Storm Night and Spurn Head data. Comparing the Perranporth data to the other two experiments in this study, bedforms are unlikely to have been present at Perranporth, and neither is the infragravity wave domination seen during the Storm Day tide observed at this site. Instead, it may be speculated that the behaviour of sediment

concentrations on the flood tide at Perranporth may lie in the deposition of more readily suspended material near to the instruments whilst the instrument rig is in the swash zone.

On the flood phase of the tide, the instruments are initially dry, then in the swash, and are then submerged sufficiently to start logging. It has been documented that large quantities of sediment are mobilised by swash (Beach and Sternberg, 1991). However, it could be that not all of the sediment mobilised when the instruments were in the swash was transported away from the instruments as the swash zone moved up the beach with the incoming tide. Thus, in the initial runs logged by the instruments, material that is easily suspended may well be present and resuspended by the observed currents. This material is then transported away from the instruments during the flood tide, and consequently on the ebb a higher velocity threshold will have to be exceeded in order for sediment to be suspended. Certainly this would seem to be the case in figure 6.1.20 which compares the flood tide run 1 with the ebb tide run 18, as despite run 18 having stronger offshore velocity maxima than run 1, less sediment is suspended even at the maximum values.

In comparing the three sites then, the tidal asymmetry in sediment suspension for Storm Day may be associated with asymmetry in the measured variations in the low frequency hydrodynamic component. At Spurn Head the tidal asymmetry in the shoaling zone can be attributed to a combination of hydrodynamic variations and the conditions at the bed. Storm Night, Spurn Head and Perranporth tidal asymmetry in the surf zone would seem to be solely a result of changing bed response to the hydrodynamic forcing.

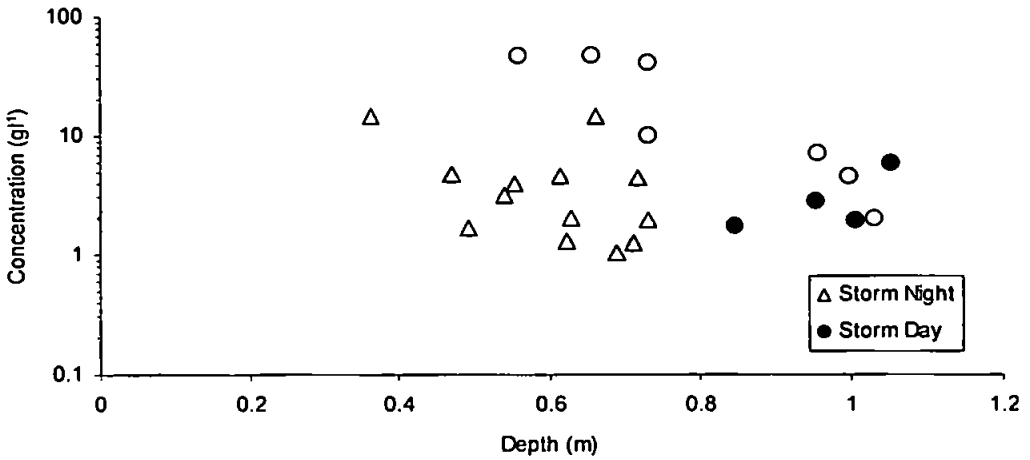

Figure 6.1.13 Distribution of 'significant concentration' values for Llangennith runs plotted versus depth. Unfilled symbols represent ebb tide runs.

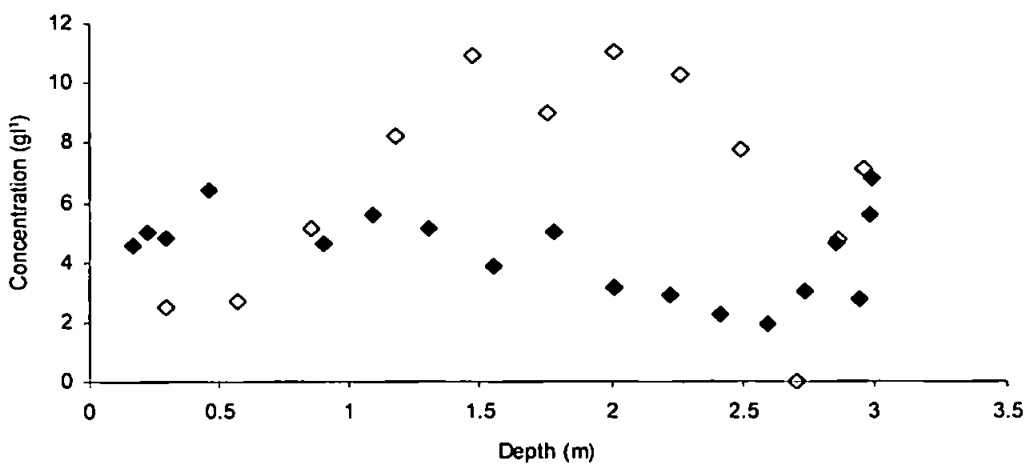

Figure 6.1.14 Distribution of 'significant concentration' values for Spurn Head runs plotted versus depth. Unfilled symbols represent ebb tide runs.

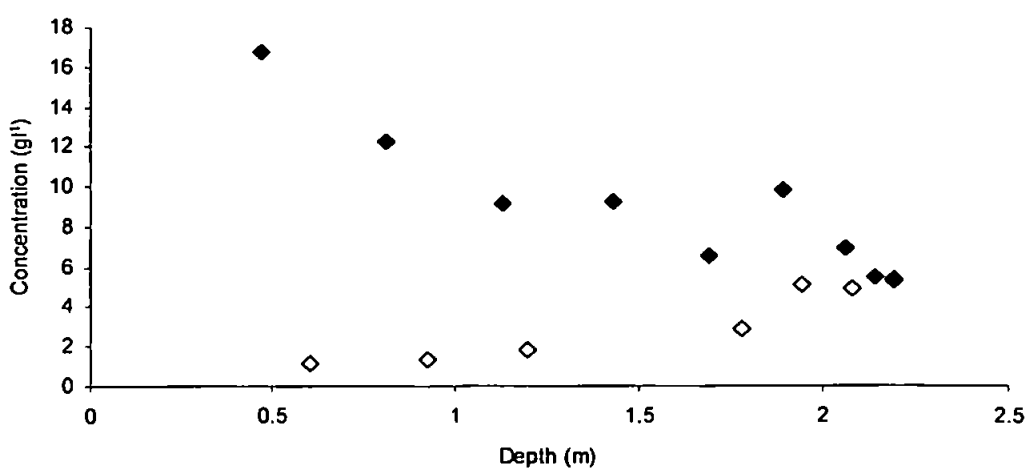

Figure 6.1.15 Distribution of 'significant concentration' values for Perranporth runs plotted versus depth. Unfilled symbols represent ebb tide runs.

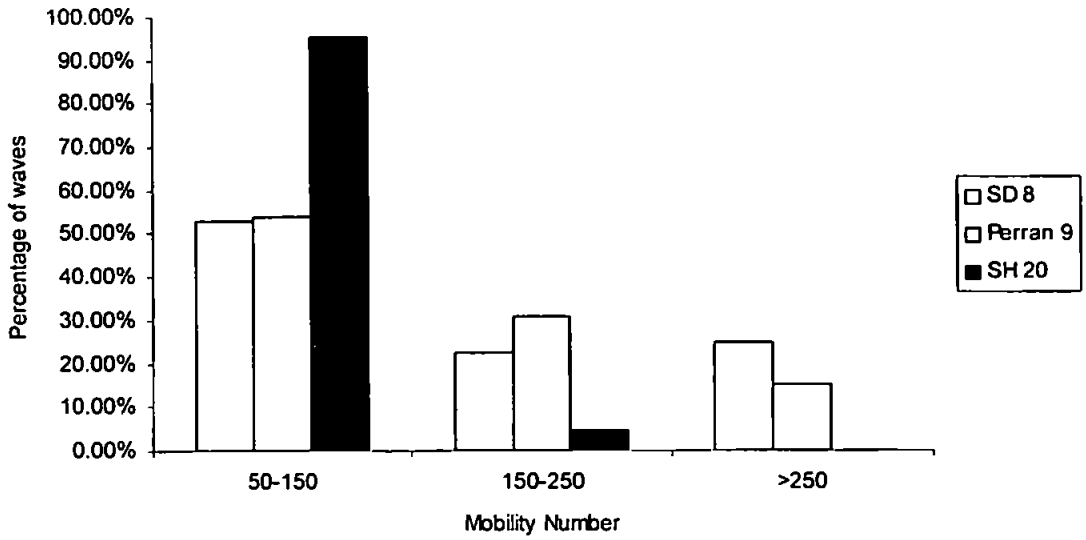

Figure 6.1.16 Distribution of waves with maximum mobility number greater than 50, for Storm Day run 8 (inner surf zone, h=0.73m), Spurn Head run 20 (shoaling zone, h=2.99m) and Perranporth run 9 (inner surf zone, h=2.19m).

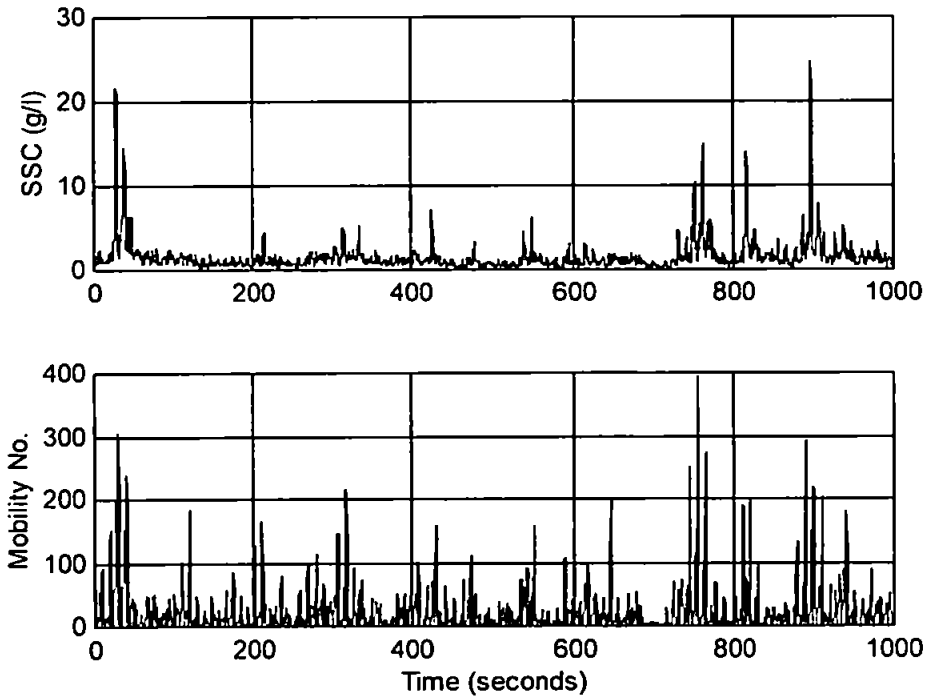

Figure 6.1.17 Time-series of suspended sediment concentration and mobility number from Spurn Head run 24 (shoaling zone, h=2.50m). The largest suspension events coincide with a set of high mobility number ($\psi(t)$ is consistently greater than 100) wave groups at the start and end of the run.

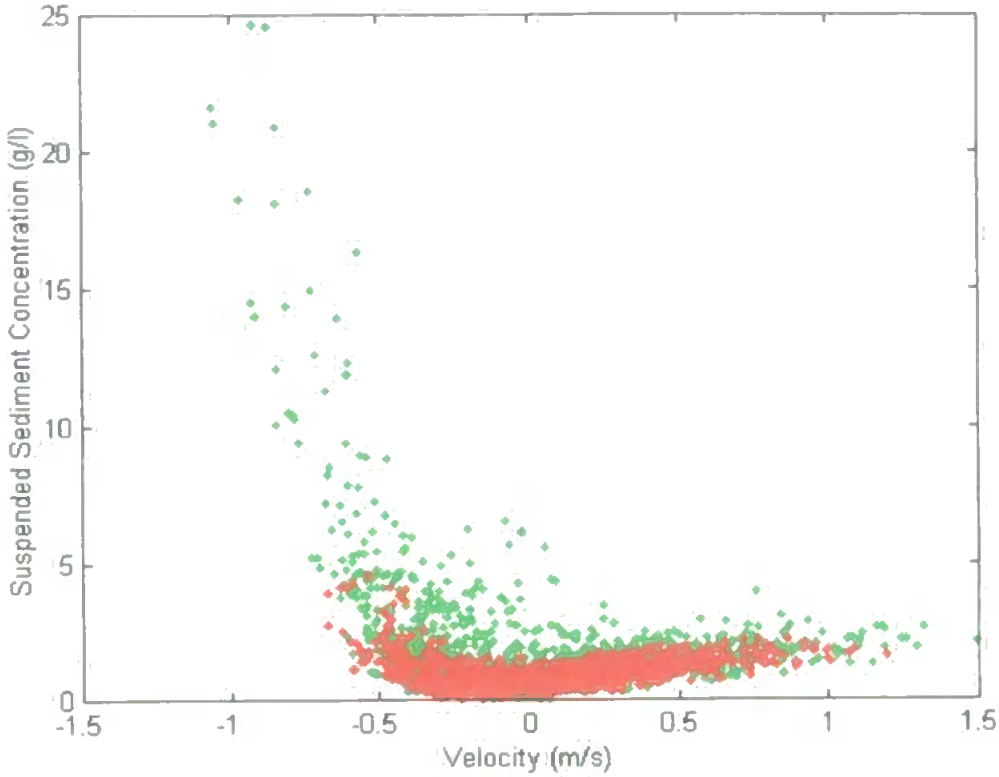

Figure 6.1.18 Scatterplot of c versus u for Spurn Head runs 15 (h=2.60m, red) and 24 (h=2.50m, green).

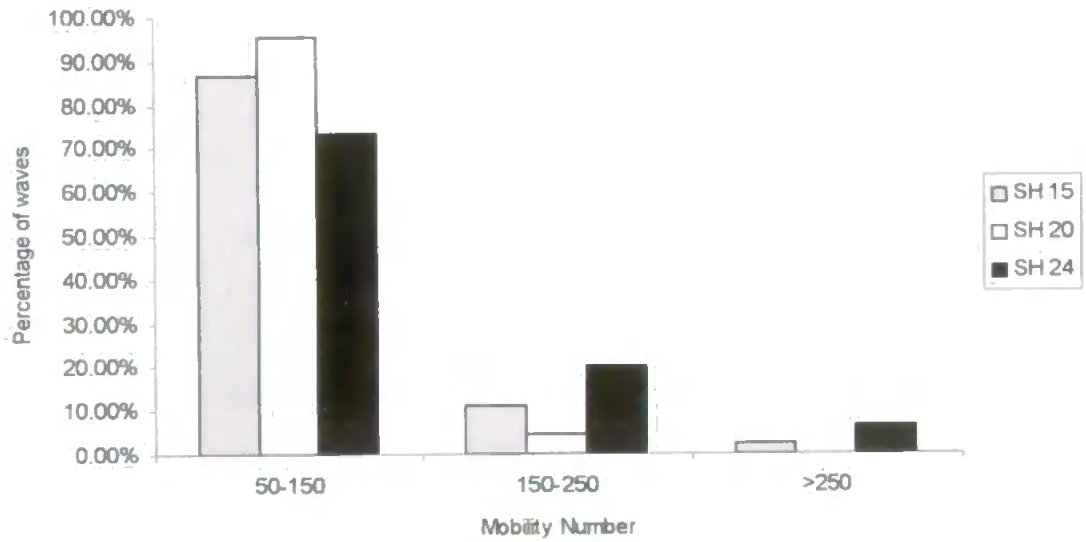

Figure 6.1.19 Distribution of waves with maximum mobility number greater than 50, for Spurn Head runs 15 (h=2.60m), 20 (h=2.99m) and 24 (h=2.50m).

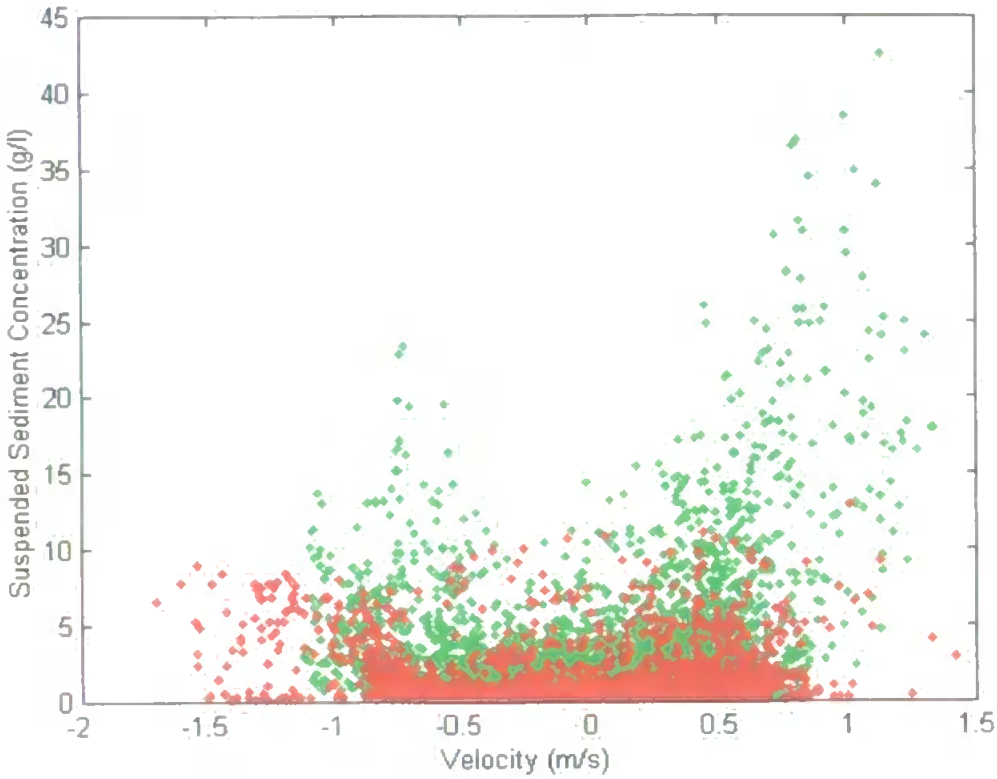

Figure 6.1.20 Scatterplot of c versus u for Perranporth runs 18 (h=0.28m, red) and 1 (h=0.47m, green).

6.1.6 Summary: Infragravity frequency variations in suspension of sediment

This section relates the hydrodynamic components described in chapter 5 to mechanisms involved in suspending sediment through the cross-shore region. Although some acceleration type events were documented in the inner surf zone, in virtually all the cases examined here suspension maxima were observed in conjunction with velocity maxima.

In the shoaling zone (Spurn Head data) the main component of the velocity field is due to the incident frequency waves. Despite the fact that wave velocities at these frequencies are biased toward the onshore phase due to the shoaling process, the largest suspension events were associated with the offshore phase of velocity, possibly due to the presence of bedforms. These events follow velocity magnitude, and thus the largest concentrations of suspended sediment are seen in conjunction with, and are of similar duration to, the largest incident frequency waves. Hence the suspended sediment concentration time-series matches both the individual waves and the wave groups seen in this region.

As wave breaking becomes increasingly saturated within the surf zone, the Spurn Head results continue to show large suspension events associated with offshore directed velocity maxima, but here driven by a combination of mean, infragravity and incident frequency components. The destruction of the groupy structure of the incident waves through breaking, means that in these instances the low frequency events, whilst still of a incident banded period, are discrete isolated events, occurring only when the largest incident frequency waves are coincident with an offshore directed infragravity wave velocity. Similar events are observed in the inner surf zone in the Perranporth dataset, but driven by onshore velocity maxima stemming from a coincidence between the largest breakers and with an onshore infragravity wave velocity.

The Llangennith data shows an inner surf zone dominated hydrodynamically by the infragravity components, and, when the instruments are just outside the swash zone, yields time-series which show suspension events with duration of infragravity period, as well as events with an incident banded period. The former suspension events appear to be associated with offshore directed velocity maxima arising from a combination of the undertow (mean) and infragravity and incident wave components. High concentration events of incident frequency wave duration were observed coincident with onshore velocity maxima, where breaker fronts occurred during a strong onshore directed phase in the infragravity velocity field (which thus overcomes the opposing undertow). However

because of the strength and duration of the offshore directed velocities in these instances, events associated with these periods of flow dominated the time-series.

These results point to the instantaneous velocity at the bed being the most important factor in the suspension of sediment in energetic situations such as the ones represented by Llangennith and Perranporth in this dataset. The upshot of this statement is that both infragravity and incident frequency oscillatory components, in conjunction with the mean flow, act to 'stir' sediment into suspension. This places an increasing importance on the infragravity component in suspension of sediment close to the shoreline, and when infragravity waves dominate the inner surf zone the infragravity frequency contribution to suspension becomes large. Also within this analysis asymmetries were noted not only in the 'pick up' of sediment associated with direction of flow, but also in the amount of sediment suspended on the ebb and flood phases of the tide. Whilst for Storm Day a hydrodynamically based reason was found for this behaviour, it is suggested that at Spurn Head and Perranporth the effect was more likely to have been due to variations in the response of the bed. Nonetheless, the contribution of the infragravity component of suspension, as shown in figures 6.1.11a and 6.1.11b, appears independent of the absolute value of the suspended sediment concentration.

6.2 Effects of infragravity frequency variations on sediment transport

Thus far this investigation has concentrated on examining the underlying processes causing low frequency irregularities in suspended sediment concentration. However, what effect such variations in hydrodynamics and suspended sediments have on overall flux of sediment needs to be assessed in order to justify whether the low frequency component requires closer scrutiny in a modelling context. Returning to the problem set out in the introduction to this thesis, the question can be asked;

> Do low frequency effects cause sediment flux to deviate qualitatively from the behaviour suggested by a) a model where the incident frequency waves stir sediment, which is subsequently transported by the mean flow, or b) an energetics type model?

Qualitatively, the two models cited above may yield a similar result for transport through the nearshore. Considering a 'wave stirring-mean transport' approach, flux direction at any point in the nearshore will be due to the mean component direction, whilst the magnitude will be related to wave energy and current strength. Considering the observations of mean current made both here, and by other authors, the resultant flux in such a model would see onshore directed transport outside of the surf zone, and offshore directed transport inside the surf zone. This is because the mean current is offshore directed inside the surf zone, and decreases from a maximum in the surf zone to near zero at the breaker line. Outside the surf zone the mean flow reverses direction to the onshore near the bed and increases toward a turning point somewhere in the shoaling zone. The position of the flux maxima with respect to these two current maxima will then be dependent upon the shoaling of the waves outside of the surf zone, and the dissipation of wave energy inside the surf zone.

The pattern of flux indicated by a velocity moments approach such as the one described by Russell and Huntley (1999), shows a similar form to the above model (figure 6.2.1). Russell and Huntley (1999) generated their 'shape function' using u^3 ('skewness') moments derived from data in the B-BAND experiment. In the surf zone offshore directed transport is predicted by a negative skewness, which is dominated by the mean component for much of this region. Near to the shoreline, infragravity waves were also observed by Russell and Huntley (1999) to be negatively skewed. In the shoaling zone the onshore directed transport predicted is due mainly to the fact that the incident wave velocities are onshore skewed in this region. The method discussed in this assessment has an advantage

over some other energetics models as it uses the results of real data rather than the results of a hydrodynamic model to produce the shape function. Therefore the time averaged model of hydrodynamic conditions obtained includes a genuine set of low frequency variations in the instantaneous current. The model is also appropriate to the discussion here, since the function generated by Russell and Huntley (1999) employed data taken from both Spurn Head and Llangennith.

In figure 6.2.1 the total normalised (u^3) moments generated from the Llangennith and Spurn Head data are plotted versus normalised cross-shore distance. The moment normalisation is made using $\langle u^2 \rangle^{3/2}$ and was applied to fit data from conditions of varying energy together. Russell and Huntley's (1999) shape function is also shown on the diagram and shows a fit to the data by using an order two polynomial, where

$$y = -0.52x^2 + 2.27x - 1.58. \tag{6.3}$$

Russell and Huntley (1999) also used data from a reflective site at Teignmouth in deriving this function and quoted a fit to the data of r^2=0.85. This predicts a convergence of transport directions just shoreward the breakpoint. By using a normalised value for velocity moment, the shape function can be constructed from a mixture of datasets, but when the normalising factor is removed a further variation in the moment predictors will be seen occurring in the surf zone toward the shoreline. For example, in the case where overall energy is diminished due to incident wave breaking, the non-normalised moment will also decrease, and suggests a decrease in transport.

As a comparison with the above flux predictors, the calculated fluxes from this dataset are shown in figure 6.2.2, plotted versus normalised surf zone position. In order to further compare the datasets, the values from the Spurn Head data have been rescaled (assuming a rippled bed) in order to ascertain fluxes at a similar point depth to those in the Llangennith and Perranporth data (0.04m). These computations were made using the approach adopted by Foote *et al.* (1998), and which followed Nielsen (1979) by assuming an exponential profile for sediment concentration above the bed. Therefore at a level z metres above the bed,

$$c(z) = C_0 \exp\left(-\frac{z}{L_s}\right), \tag{6.4}$$

where C_0 denotes a reference concentration at the ripple crest level and L_s is a vertical length scale.

Using this formula two elevations above the bed may be compared, since

$$\frac{c(z_1)}{\exp(-z_1/L_s)} = \frac{c(z_2)}{\exp(-z_2/L_s)}, \tag{6.5}$$

and thus

$$c(z_1) = c(z_2)\exp\left(\frac{z_1 - z_2}{L_s}\right). \tag{6.6}$$

For rippled beds, L_s follows the relationship (Nielsen, 1988, appendix)

$$L_s = \eta_r\left\{1.24\exp\left[-40(\omega_s/U_m)^2\right] + 0.2\right\}, \tag{6.7}$$

where $U_m = 2^{\frac{1}{2}}\langle\tilde{u}^2\rangle^{\frac{1}{2}}$ is the maximum orbital velocity of the waves, η_r is ripple wavelength and ω_s is sediment fall velocity. In the computations made, Spurn Head fall velocity was set at 0.047ms^{-1} and η_r estimated at 0.03m following Dyer (1986), as used by Foote *et al.* (1998).

In figure 6.2.2 the trend in the majority of the data is to follow the type of flux patterns described by the two models, and runs for which this occurs are represented by filled symbols. Outside of the surf zone the Spurn Head data generally shows onshore directed transport, which decreases to zero at the breaker line. Inside the surf zone the Spurn Head fluxes are offshore and tend to a maximum approximately one-quarter of the way through the surf zone. The values of flux from this region of the saturated surf zone at Perranporth are generally smaller than their Spurn Head counterparts but are nonetheless still offshore directed. The difference in flux magnitudes between the non-saturated (Spurn Head) and saturated (Perranporth) surf zones is most likely due to the difference in nature between the incident frequency waves in these cases, and the response of the rippled (Spurn Head) versus flat bed, in terms of the quantity of sediment suspended. Closer to shore flux values for all three beach sites tend toward zero for the filled symbol runs.

Within the data however, a number of exceptional runs may be observed, and these are denoted by the unfilled symbols. For Spurn Head and Perranporth, fluxes are computed within the data which show a change in direction from that predicted both by 'wave stirring-mean transport' and the 'shape function' approaches. For Spurn Head, four runs (SH24-27) show offshore transport occurring in the shoaling zone (figure 6.2.2, unfilled diamonds), whilst for Perranporth four runs (Perran1-4, figure 6.2.2, unfilled circles) yield an onshore flux in the inner surf zone. The direction of transport predicted by all the runs within the Storm Day data is the same as that predicted by the models, but three runs (SD9-11, figure 6.2.2, unfilled squares) deviate sufficiently from the remainder of the data, in terms of the observed flux magnitudes, that these are also marked by an unfilled symbol.

In the previous section, all of these exceptional runs were associated with 'tidal asymmetry' changes in the overall levels of suspension of sediment. Furthermore, it was suggested in section 6.1 that the changes in suspension in the SD9-11 and SH24-29 runs could be linked to low frequency variations in the hydrodynamics (although in the SH24-29 runs a change in the bed response was also suggested). Extending this theme to the case of sediment transport, in the next subsections the fluxes from each dataset are examined in more detail, to investigate whether the observed fluxes in these exceptional runs are also related to some change in behaviour associated with low frequency effects.

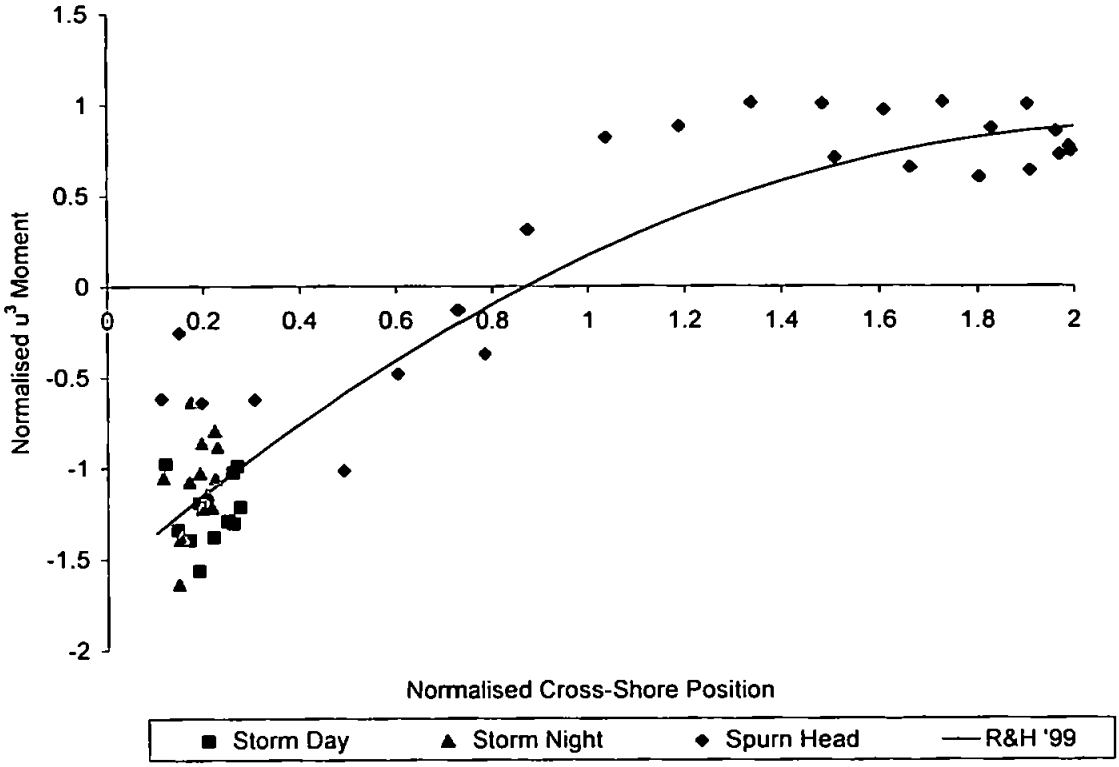

Figure 6.2.1 Normalised bedload moments for B-BAND data used in this analysis, plus Russell and Huntley (1999)'s shape function.

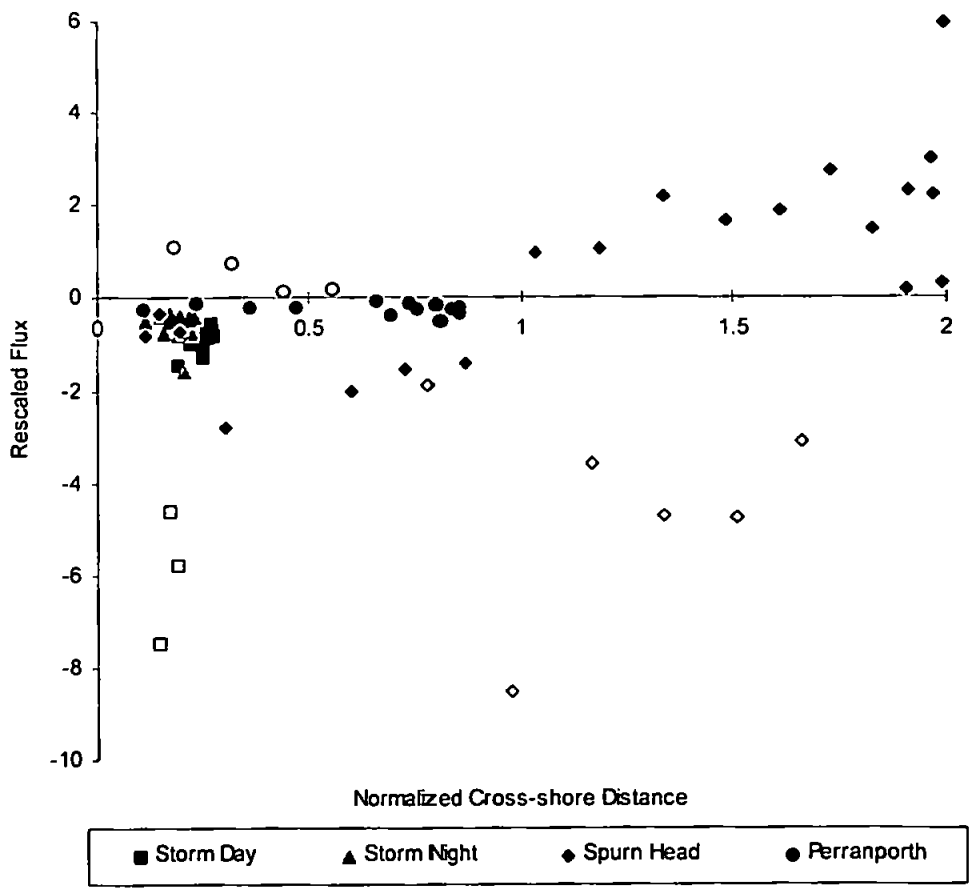

Figure 6.2.2 Rescaled sediment fluxes versus normalised cross-shore distance. Unfilled symbols indicate possible changes in bed response.

6.2.1 Variations in sediment flux at Llangennith

Figure 6.2.3a-c shows sediment fluxes calculated from the Llangennith dataset in more detail. In figure 6.2.3a the overall fluxes from the Storm Day and Storm Night runs are illustrated, with the unfilled symbols denoting runs on the ebb tide. Whilst flux values remain relatively similar and offshore directed for the Storm Night runs, on the Storm Day ebb tide an increasing amount of sediment is transported with decreasing depth at the instruments. The flux values are observed to be particularly large for Storm Day runs 9-11. In figures 6.2.3b and 6.2.3c further comparisons of the contribution to the sediment flux made by the oscillatory versus the mean components, and the infragravity versus incident frequency oscillatory components (as calculated following the method in section 4.3), are shown for Storm Day. Whilst over the whole suite of runs the major flux of sediment is seen to be due to transport by the offshore directed mean current, on the ebb tide during runs 9-11 the largest contribution is seen to come from flux associated with the oscillatory components. These latter fluxes are dominated by the infragravity frequencies.

The mechanisms involved in producing the oscillatory component fluxes are seen in more detail in cross-spectral analyses of c versus u. Figures 6.2.4 and 6.2.5 compare the results from Storm Day runs 3 and 10. A particular feature of the diagrams from these runs is the reversal in the direction of sediment transport between the lowest infragravity frequencies (offshore) and frequencies higher in the infragravity band (onshore). This may be seen in the co-spectra, and is manifested in the phase spectra as a shift through $-\pi/2$ radians. Hence whilst suspended sediments are seen to be transported by an onshore directed velocity from the higher infragravity oscillations, at lower frequencies suspended sediments are transported offshore by currents from the free infragravity wave field. In general both these components provide a larger flux than that at incident frequencies, but for the runs around high water the former two are in opposition and generally cancel each other out. Hence in run 3 the oscillatory contribution to transport is near zero. Late in the ebb tide however, the lowest frequency infragravity component becomes increasingly dominant (e.g run 10, figure 6.2.5), and suspension events take an infragravity duration associated with the offshore directed velocity. This leads to a large offshore directed transport.

In a comparison between the observed flux and the moment, this large increase in sediment transport for the SD9-11 runs is not mirrored in the behaviour of the moment for these runs (figure 6.2.6). To explain briefly, figure 6.2.6 shows the total (non-normalised) moment and flux as line plots; the four terms suggested by Russell and Huntley (1999) as

dominating the total moment in a dissipative surf zone are plotted as columns. Using the Russell and Huntley (1999) scheme these are term 1 (mean current skewness), term 3 (infragravity wave skewness), term 4 (interaction between incident wave stirring and mean current transport) and term 5 (interaction between infragravity wave stirring and mean current transport). High water corresponds to run 4, and therefore run pairs of 4 and 5, 3 and 6, 2 and 7, and 1 and 8 see the instruments in similar depths of water. A comparison between the total moment and flux observations for these run pairs shows similar flux values for a given moment. Over the tide between run 1 and 8 the total moment and flux values also behave in a qualitatively similar fashion, with flux decreasing as moment decreases. However, for the SD9-11 runs the flux shows a dramatic increase where the total moment magnitude decreases.

In figure 6.2.2 this coincides with a change in the terms making up the total moment, observed in runs 8-11. For most of the runs in the tide, the total moment value is dominated by a combination of terms 1, 4 and 5, suggesting flux to be dominated by stirring by the combined oscillatory velocity field interacting with the mean current. For the latter runs (8-11) however, a dramatic increase is observed in the value of term 3 (the infragravity wave skewness). This increase in negative skewness for the infragravity component has been observed by other authors (e.g. Osborne and Rooker, 1997) and appears to be associated with shoaling of the infragravity waves. Corresponding to the increase in infragravity energy, runs 8-11 show that term 5 remains high despite the decrease in the mean component near to shore (see Appendix I).

The increases in the infragravity terms making up the moment in runs SD9-11 also ties in with a change in the character of sediment suspension near to shore. Prior to these runs, sediment suspension events were observed having solely incident duration, but during SD9-11 the largest low frequency events increased not only in scale, but also took on infragravity duration (e.g. Storm Day run 10, figure 6.1.8). These events occurred in association with the offshore phase of the infragravity waves in combination with the mean flow. This suggests therefore that in the SD9-11 runs, the observed flux will be particularly sensitive to the infragravity wave velocity component rather than the total moment predictor.

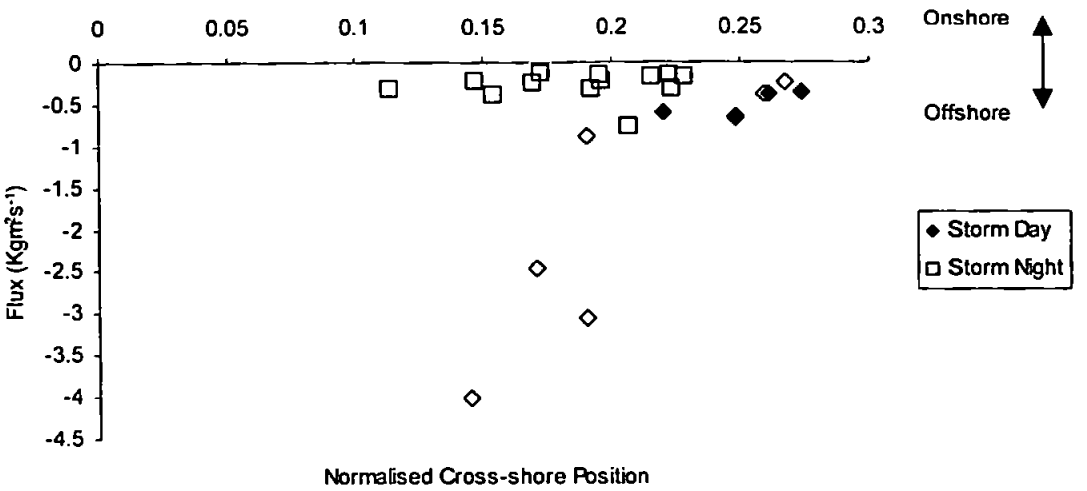

Figure 6.2.3a Sediment fluxes from Llangennith runs versus normalised cross-shore position. Unfilled symbols signify the ebb tide runs.

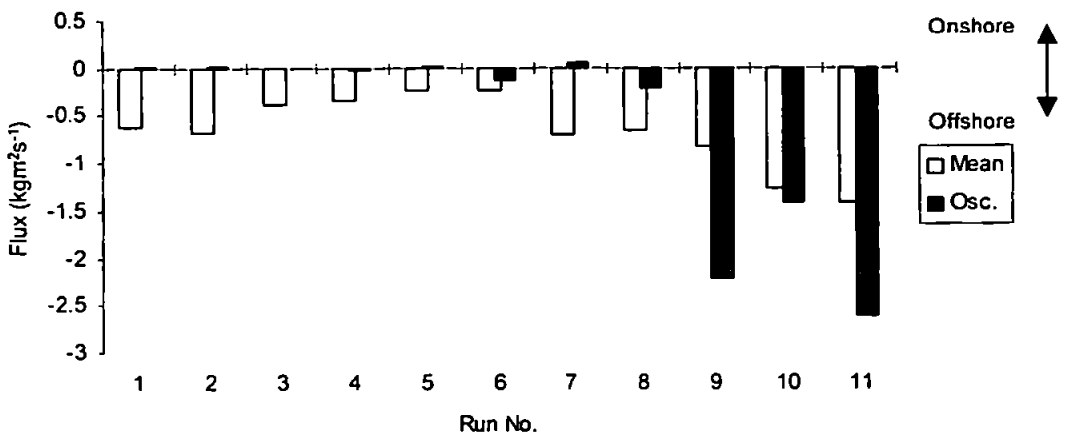

Figure 6.2.3b Temporal variation of mean and oscillatory contributions to sediment flux for Storm Day.

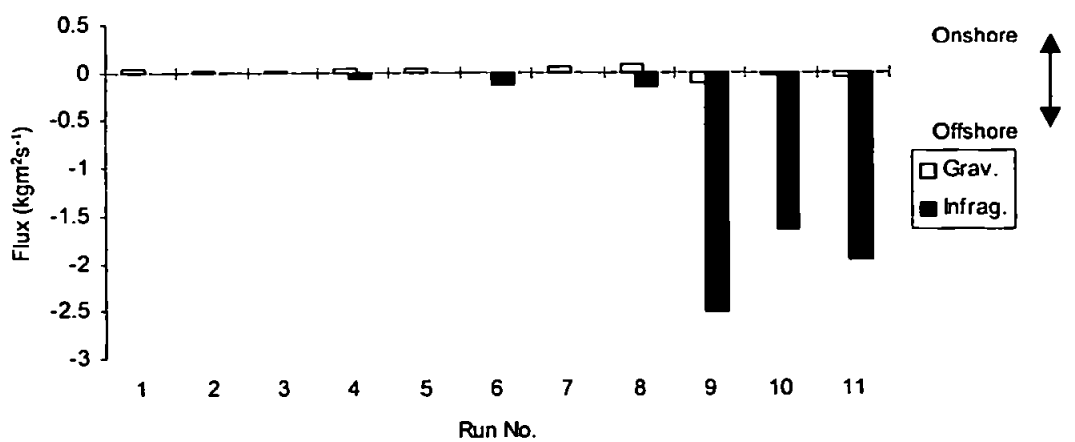

Figure 6.2.3c Temporal variation of incident and infragravity frequency oscillatory contributions to sediment flux for Storm Day.

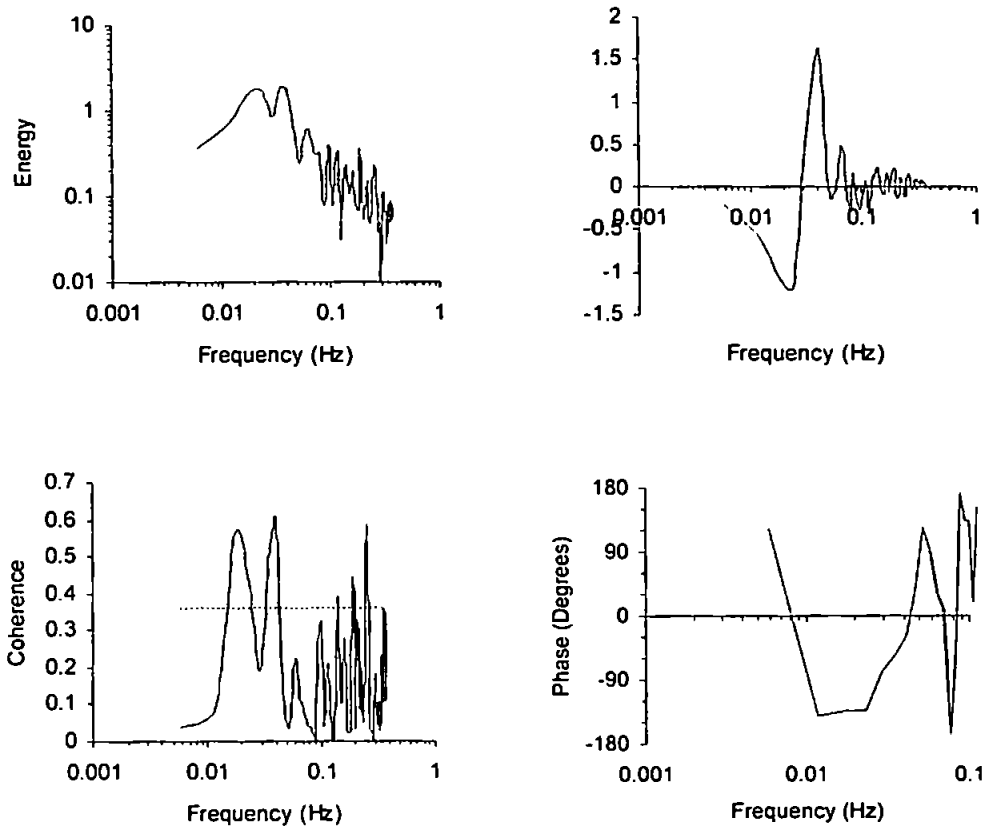

Figure 6.2.4 Storm Day run 3 (h=1.01m) cross-spectra for c versus u, clockwise from top left; cross-spectrum, co-spectrum, phase spectrum, coherence.

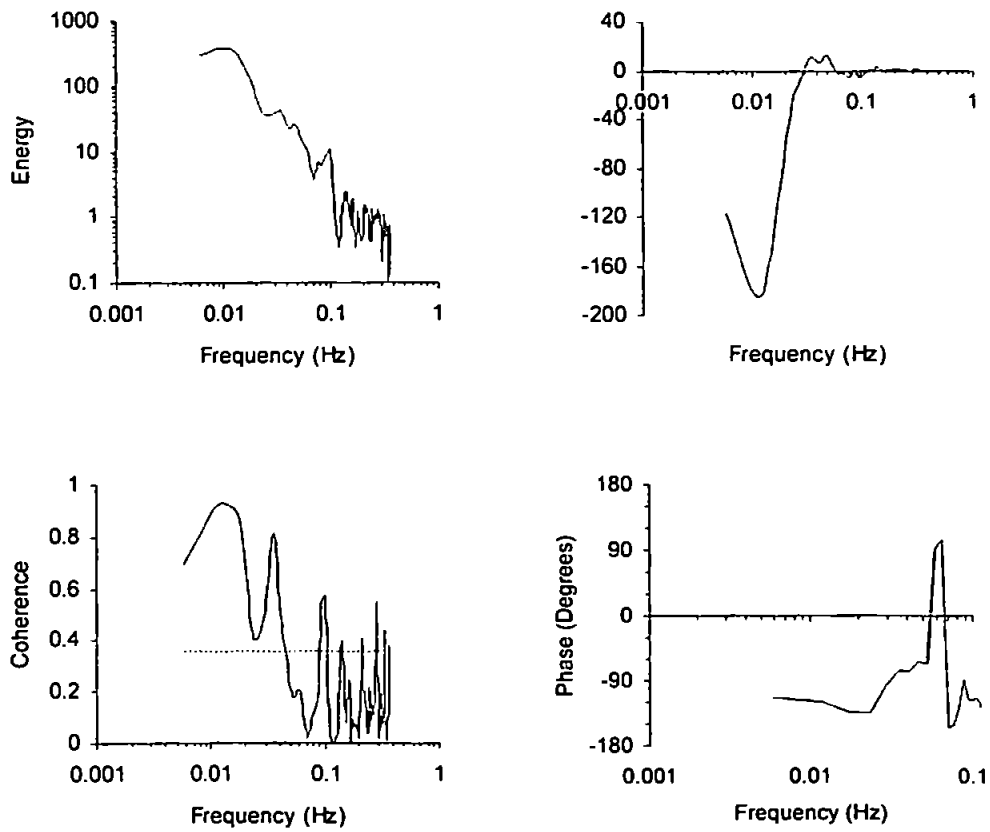

Figure 6.2.5 Storm Day run 10 (h=0.66m) cross-spectra for c versus u.

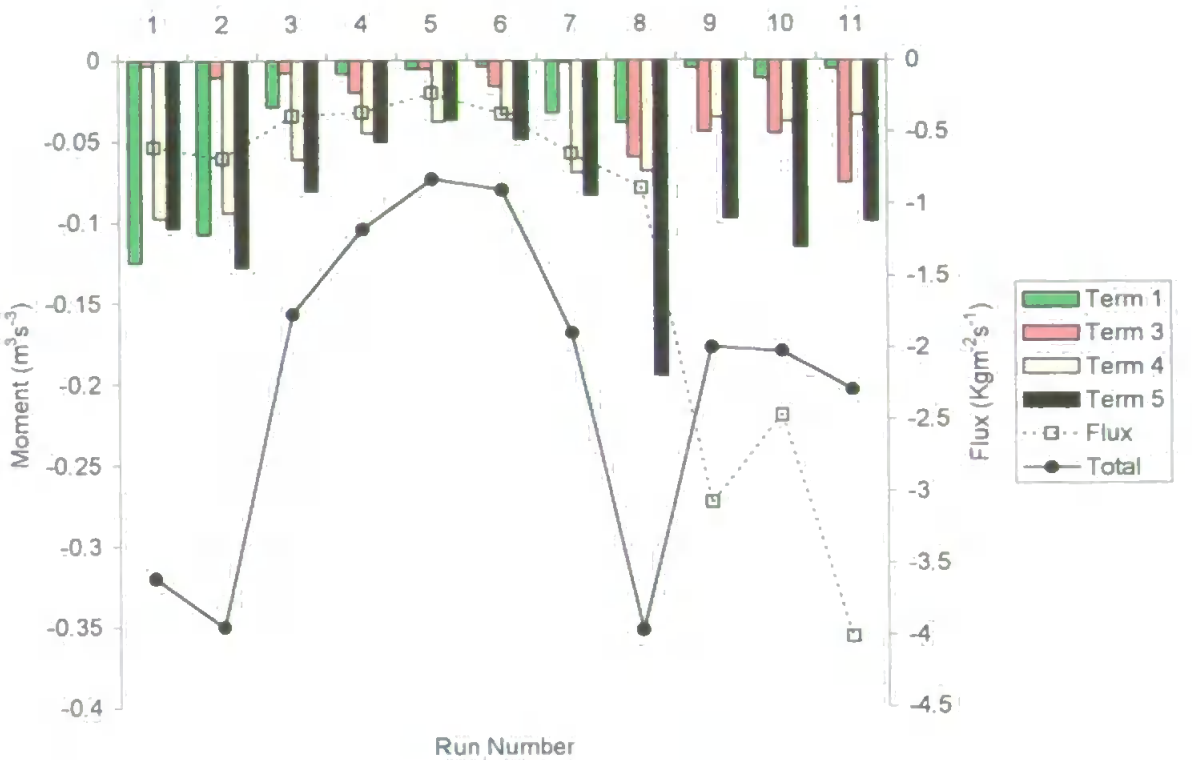

Figure 6.2.6 Comparison between moment terms and fluxes for Storm Day runs. Lines indicate total moment and (point) flux values, whilst moment terms 1,3,4 and 5 are plotted in column form.

6.2.2 Variations in sediment flux at Perranporth

Total flux at Perranporth is onshore directed for the earliest runs on the flood tide, but small and offshore directed otherwise (figure 6.2.7a). Correspondingly, the oscillatory flux of sediment is seen to dominate overall transport for runs Perran1-4 (figure 6.2.7b), when the instruments are near to shore on the flood tide. For these runs, infragravity and incident frequency contributions are of a similar order and are both onshore directed (figure 6.2.7c). However for the later runs (5-18), the offshore directed mean component provides a much larger proportion of the flux.

Figures 6.2.8 and 6.2.9 show a cross-spectral analysis of suspended sediment concentration versus cross-shore velocity for Perranporth runs 1 and 9 respectively. Run 1 comprises observations made with the instruments close to shore (h=0.47m), whilst the run 9 measurements were made at high water (h=2.19m). The main differences between the runs may be seen in the cross spectra and co-spectra. A drop in spectral energy is seen between the run 1 cross spectrum and that from run 9 following the decrease in peak suspended sediment concentrations. Furthermore, the co-spectra for the runs change from being dominated by an onshore directed flux at infragravity frequencies (run 1), to exhibiting a rather smaller peak associated with flux at the main incident wave frequency in run 9. Although an onshore directed flux is seen at this frequency, the co-spectrum from run 9 is dominated by offshore directed peaks associated with the harmonic and higher infragravity frequency bins, leading to an offshore directed flux due to the oscillatory components.

So far the behaviour of the observed fluxes in Perranporth runs 1-4 have been considered as anomalous under the criteria of a wave stirring-mean transport model. Adopting this approach, the observed onshore transport in these runs is the opposite of that expected, since throughout the inner surf zone mean current is offshore directed. However in a consideration of the velocity moments for Perranporth (figure 6.2.10) a rather different situation is observed. In this case, since mean flow is of a low value, the oscillatory components will dominate the velocity field, and because at Perranporth the main velocity component is attributed to the incident frequency breakers, oscillatory skewness tends to be onshore directed. Hence for the majority of runs at Perranporth the velocity moment is onshore directed, rather than offshore directed as has been observed elsewhere in the dataset. Nevertheless for a number of runs where an onshore directed moment is observed (runs 5-12), flux is still offshore directed.

Again the reason for the differences between the moments prediction and observed transport may be seen in an examination of suspended sediment concentrations versus instantaneous velocities. For the Perranporth runs up until run 4 sediment was observed in section 6.1 to be easily suspended by high velocities observed on the onshore phase (e.g. figure 6.1.6). Consequently onshore transport for these runs is high, but after run 4, whilst the oscillatory velocity field remained onshore skewed, sediment was more consistently suspended (albeit at low concentrations) for transport on the offshore phase of flow (e.g. figure 6.1.3). This might lead to a small offshore directed flux. The effect however, is not directly related to any low frequency changes in the hydrodynamics.

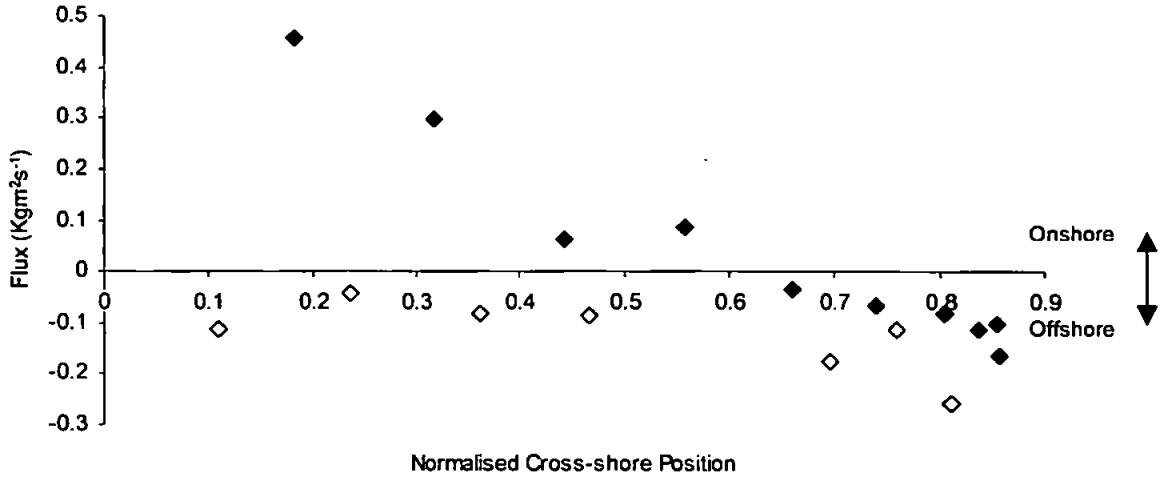

Figure 6.2.7a Sediment fluxes from Perranporth runs versus normalised cross-shore position. Unfilled symbols signify the ebb tide runs.

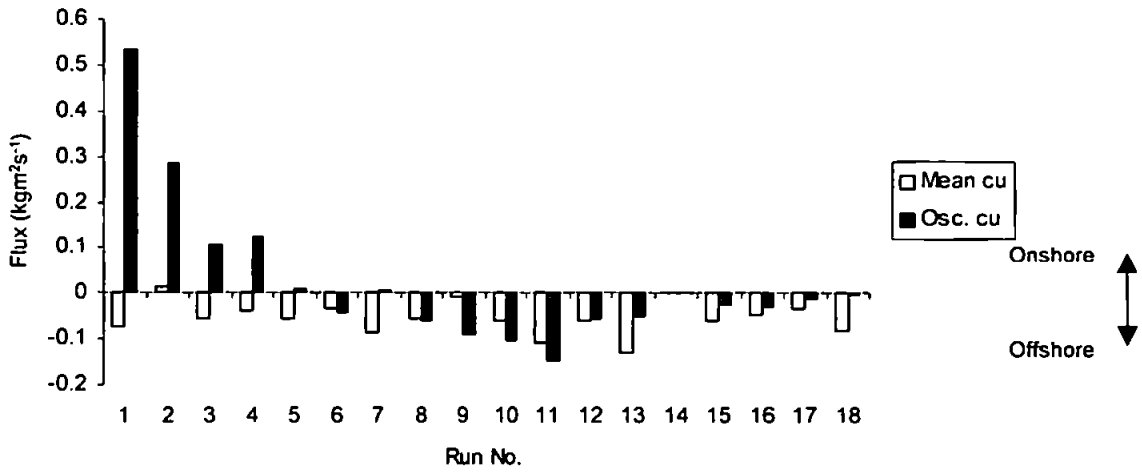

Figure 6.2.7b Perranporth temporal distribution of mean and oscillatory sediment fluxes.

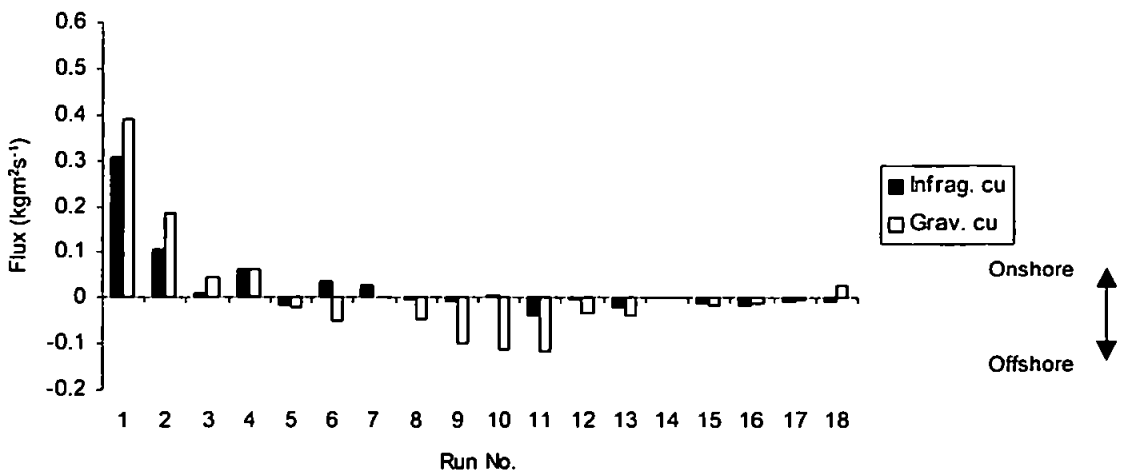

Figure 6.2.7c Perranporth temporal distribution of incident and infragravity frequency oscillatory sediment fluxes.

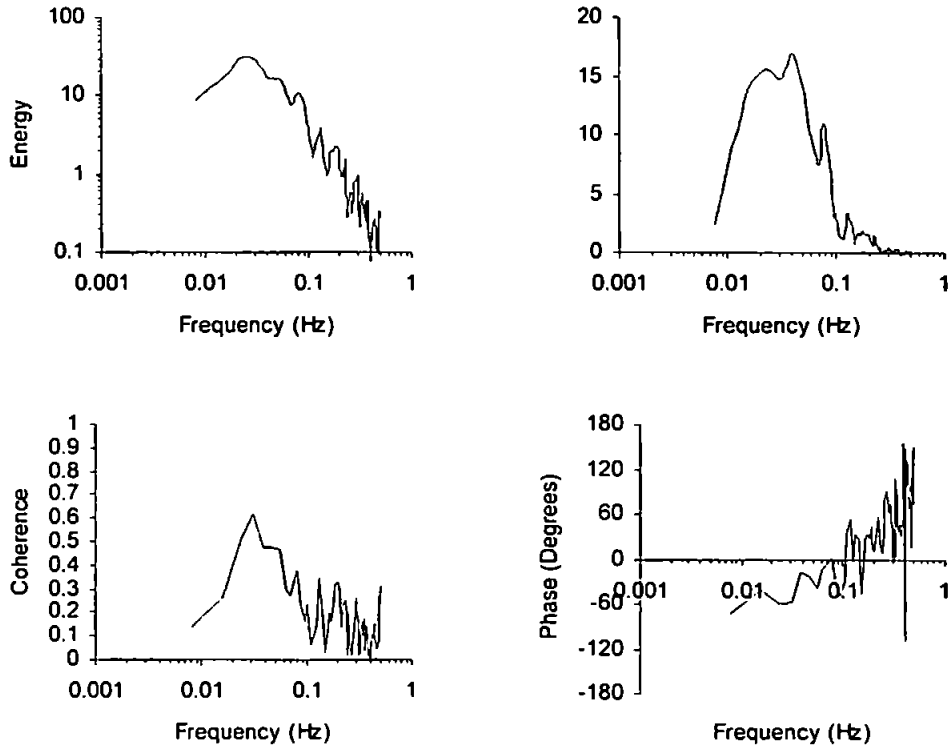

Figure 6.2.8 Perranporth run 1 (h=0.47m) cross-spectra for c versus u, clockwise from top left, cross-spectrum, co-spectrum, phase spectrum, coherence.

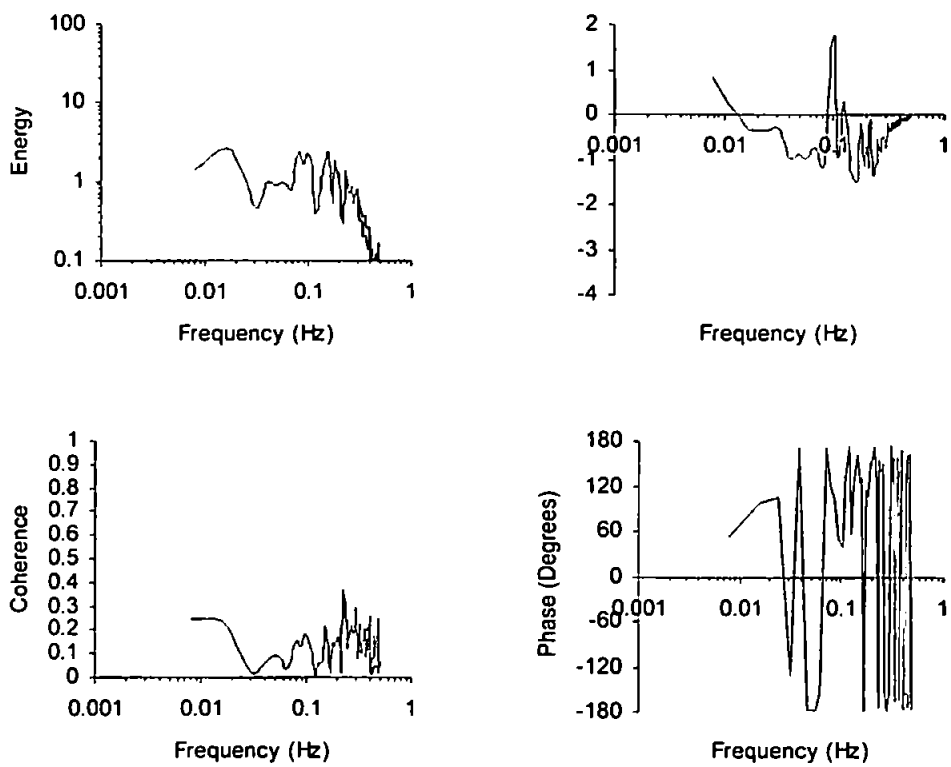

Figure 6.2.9 Perranporth run 9 (h=2.19m) cross-spectra for c versus u.

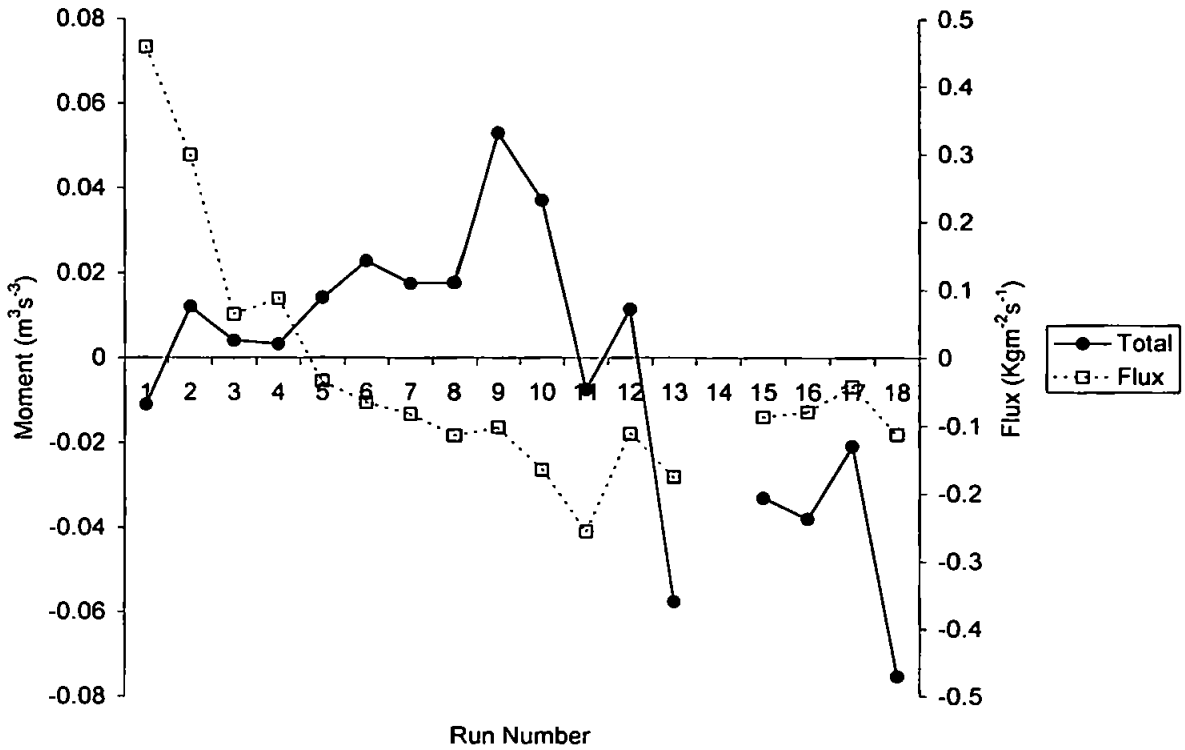

Figure 6.2.10 Comparison between moment and (point) fluxes for Perranporth runs.

6.2.3 Variations in sediment flux at Spurn Head

At Spurn Head the majority of calculated flux values conform to the ideas of both the wave stirring-mean current type model and the shape function (figure 6.2.11a). Figures 6.2.11b and 6.2.11c show contributions to cross-shore sediment flux made by the oscillatory and mean components and infragravity and incident frequency oscillatory components. In general the mean current provides the main contribution to flux which is either offshore/onshore directed inside/outside the surf zone respectively (figure 6.2.11b). The contribution made by the oscillatory component of flux is seen to be of secondary importance in most of the runs (figure 6.2.11b), and is dominated by the incident frequency contribution, which yields an onshore directed oscillatory flux (figure 6.2.11c). The contribution to flux from this component is however seen to change dramatically in Spurn Head runs 24 and 25. For these runs figures 6.2.11b and 6.2.11c show a large offshore directed transport associated with the incident frequency waves. Correspondingly this starts a sequence of four runs where flux is directed in an opposite sense to what would be expected.

Foote (1994), in examining the same result described how the fluxes in the SH24-29 runs were directed in the opposite sense to the moment predictors, and concluded that this behaviour could be put down to the presence of bedforms and their effect on suspended sediment concentration-velocity phase. However, a cursory examination of the suspended sediment concentration and cross-shore velocity time-series from all of the runs in the shoaling zone prior to run 24 (e.g. run 11, figure 6.1.1) seems to conflict with both the moment and resultant oscillatory flux for these runs. Whilst moment, flux and velocity maximum are onshore biased for these runs, the largest sediment suspension events are nevertheless associated with maximum offshore streaming in figure 6.1.1. In looking more closely at the suspended sediment concentration versus cross-shore velocity scatterplot in the figure however, the fluxes can be related to the gradient in scatter during the onshore phase of velocity. In figure 6.1.1 suspension increases almost linearly with increasing onshore velocity, whilst for most events associated with offshore directed velocities, suspension remains low for low velocities, but increases quickly near to the maxima values. Thus despite the largest concentrations being seen on the offshore phase of velocity the majority of sediment is still transported during the onshore phase of the waves, leading to a small onshore oscillatory transport overall.

For run 24 however, the balance is in favour of the larger suspension events associated with the offshore phase of the largest waves (figure 6.1.18). Hence the oscillatory transport reverses. Qualitatively then, numerous runs in the Spurn Head data show a similar scatterplot result to that in run 24, where the largest suspension events are associated with offshore directed velocity whilst the majority of transport events are associated with the onshore flow. A further similarity between runs prior to run 24, and run 24 can be found in the analysis of mobility number made in section 6.1.4 (figure 6.1.17), which suggested that ripples may well have been present for most runs. Consequently the difference between run 24 and the preceding runs is liable to be due to the few wave groups seen in that run which consistently achieved high enough velocities to mobilise the sediment in the ripples.

The inference from this result is that a moments approach in low velocity situations may still produce a qualitatively good prediction of sediment flux even with a rippled bed, although this is likely to depend upon ripple scale. However for velocities associated with transitional mobility numbers, low frequency variations in suspension and resultant transport mean that moment predictors will likely be inappropriate. In the case described here, it is suggested that the observed transport direction was changed (and contradicted the predictor) only when several large wave groups forced the bed enough to destroy a ripple field.

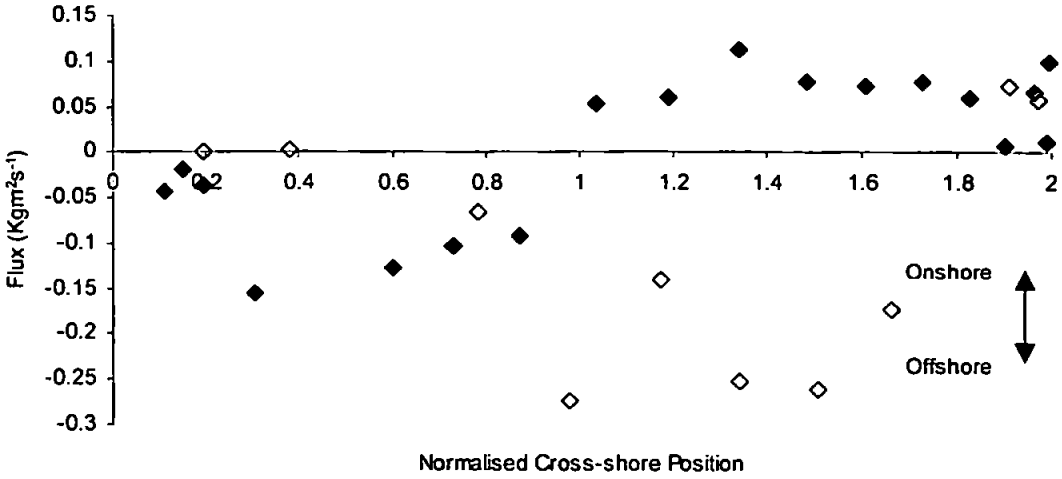

Figure 6.2.11a Sediment fluxes from Spurn Head runs versus depth. Unfilled symbols signify the ebb tide runs.

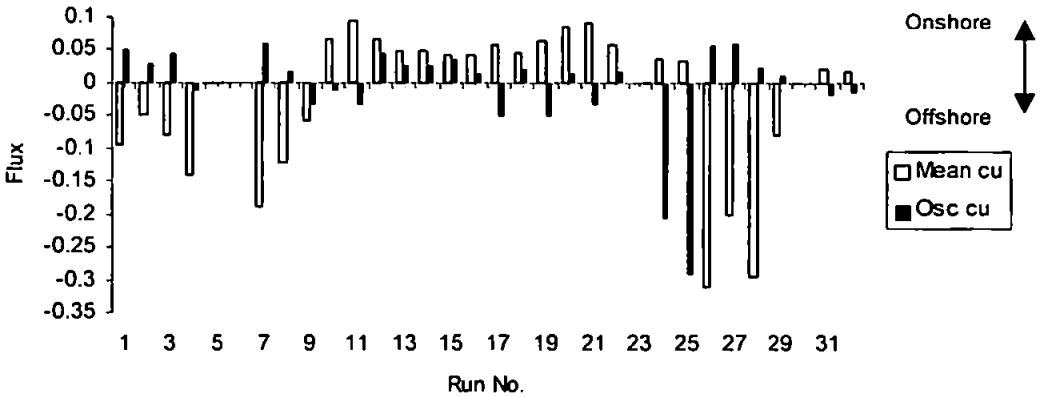

Figure 6.2.11b Spurn Head temporal distribution of mean and oscillatory sediment fluxes calculated from bottom sensors on rig A2.

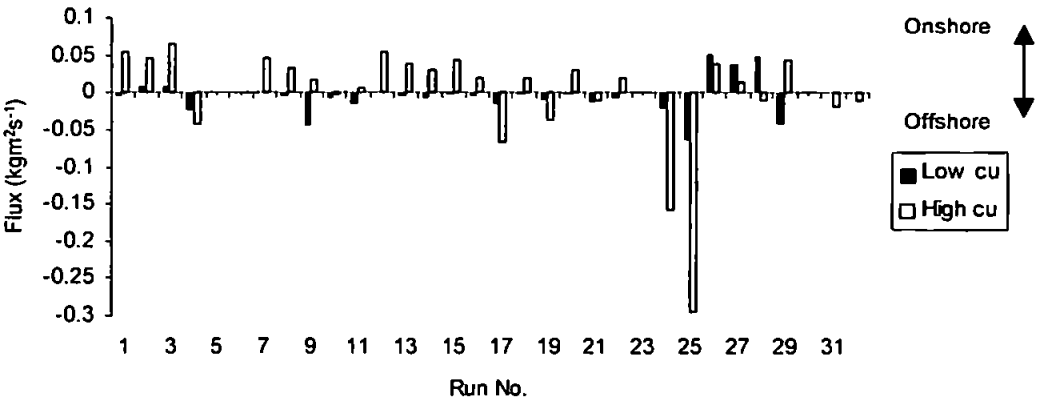

Figure 6.2.11c Spurn Head temporal distribution of incident and infragravity frequency oscillatory sediment fluxes calculated from bottom sensors on rig A2.

6.2.4 Summary: Effects of infragravity frequency variations on sediment transport

In this section observations of sediment flux were compared qualitatively with predictions made following a (time-averaged) velocity moments approach. On a number of occasions the predictors and observations did not agree. These runs were further investigated from the standpoint that low frequency variations in transport might be responsible for the disparity between measurements and model.

The results demonstrate that where observed flux and predictors disagreed, this was probably due to a change in bed response to the hydrodynamic forcing. Two particular cases were observed where this could be tied into low frequency changes in the forcing regime. In the inner surf zone (Storm Day), when sediment became suspended for infragravity duration in association with energetic infragravity waves, offshore flux was increased, despite a decrease in the total velocity moment. In the shoaling zone (Spurn Head), observed fluxes were in the opposite direction to predicted flux when it was suggested that several large wave groups started to destroy a ripple field. Both instances relate a dramatic change in transport to a change in the way that sediment is mobilised as a result of some threshold for sediment motion being exceeded on a low frequency basis by the forcing hydrodynamics.

6.3 Infragravity frequency contributions to flux through the nearshore

Section 6.2 showed that the prediction of sediment flux by energetics type models is highly dependent upon the response of the bed to hydrodynamic forcing. In the instances of the Storm Day and Spurn Head tides, the total amount of sediment in suspension changed as a result of low frequency changes in the forcing. This subsection examines the distribution of the infragravity frequency contribution to flux through the nearshore at the three sites.

Figure 6.3.1 illustrates the infragravity contribution to oscillatory flux plotted versus normalised cross-shore distance. For this plot, the y-axis values

$$\frac{Flux_{ig}}{Flux_{osc}} = \frac{|Flux_{ig}|}{|Flux_g| + |Flux_{ig}|}, \tag{6.8}$$

where the subscripts g and ig respectively, denote the incident (gravity) and infragravity parts of the frequency spectrum. Fluxes are computed from the area under the suspended sediment concentration versus cross-shore velocity co-spectrum. The data shows a lot of scatter, and in order to explain the data the nearshore has been divided into a number of zones (solid lines in figure 6.3.1).

In the shoaling zone the infragravity contribution to the oscillatory component of flux is less than 20%, but near to the breaker line the value jumps to between 50-90%. This sudden increase is most likely associated with the large increase in suspension expected with the onset of wave breaking. At Spurn Head the infragravity waves are still bound to the largest incident waves at the onset of breaking, and therefore sediment suspended by the largest breakers will be transported offshore by the infragravity waves. The width of the zone at which the high infragravity contribution to oscillatory flux values are noted is suggestive of a wide breaker zone occurring at Spurn Head rather than a sharply defined breakpoint.

In the surf zone, for values of normalised cross-shore distance between approximately 0.3-0.8, Spurn Head $Flux_{ig}/Flux_{osc}$ values are again low. The Perranporth data however, shows significantly larger values. The difference between the two datasets is perhaps suggestive that at Perranporth the largest suspension events are more likely to result from a coupling between incident and infragravity components than at Spurn Head. In the latter data the strongest sediment responses were to a flow reversal of the incident frequency waves, and therefore it would seem reasonable that this component might dominate transport. Conversely, in the saturated surf zone at Perranporth, the largest suspension events were

observed in section 6.1.2 to generally be associated with an infragravity wave peak, and will therefore be in phase with a transporting velocity at infragravity frequency.

In the nearest third of the surf zone to shore, values of $Flux_{ig}/Flux_{osc}$ are extremely scattered. The data in this region is a mix of Spurn Head, Perranporth and Llangennith data, and thus sees wide variations in incident and infragravity wave energy and phase. An explanation for the scatter in $Flux_{ig}/Flux_{osc}$ may be found however, in an examination of the suspended sediment versus cross-shore velocity co-spectra from the three sites. Figures 6.3.2-6.3.5 show respectively the co-spectrum from Spurn Head run 1 (SH1), Storm Day run 3 (SD3), Perranporth run 1 (Per1) and Storm Day run 10 (SD10). These runs are indicated in figure 6.3.1 and show an increasing dominance by the infragravity component of the oscillatory flux. The lowest value of $Flux_{ig}/Flux_{osc}$ is for the Spurn Head run, and figure 6.3.2 shows lower and higher infragravity frequencies acting in opposition to each other, such that overall infragravity flux will be small. A similar behaviour is shown in figure 6.3.3 (Storm Day run 3) and again the contribution from the infragravity frequencies to transport is small (<30%). However, Perranporth run 7 (figure 6.3.4) finds the higher infragravity frequencies dominating the infragravity part of the co-spectrum and with this the infragravity contribution to total oscillatory transport increases. A further increase occurs for Storm Day run 10. In figure 6.3.5 flux of sediment still reverses between the higher and lower infragravity frequencies, but the co-spectrum is completely dominated by the lowest frequencies. The reversal of transport direction over the infragravity frequency band noted here was also observed by Beach and Sternberg (1991). It would seem therefore, that high infragravity contributions to sediment flux occur when either the lower or higher infragravity frequencies are dominant or in phase with the largest suspensions, rather than when both components are significant.

The importance of phase to the observed fluxes can be further illustrated when figure 6.3.1 is compared with figure 6.1.11, which showed the behaviour of the infragravity contribution to sediment suspension. In the latter figure the data collapsed together well when represented in terms of cross-shore distance and energy, and suggested that a reasonably simple relationship could be found to derive the low frequency contribution to sediment suspension through the nearshore. However, figure 6.3.1 shows that for the same data, the infragravity contributions to the resultant fluxes are highly variable. The suggestion is that this difference between the two plots comes as a result of changes in phase between suspended sediment concentrations and velocity observed at lower and higher infragravity frequencies in the cross-spectrum. If the difference of phase at these

frequencies means that transport directions at lower and higher infragravity frequencies are in opposition, this can lead to reduced flux from the infragravity band as a whole, even though the infragravity contribution to sediment suspension is high.

Figure 6.3.1 Contribution to oscillatory flux made by the infragravity component plotted versus normalised cross-shore distance for runs from Storm Day, Storm Night, Perranporth and Spurn Head.

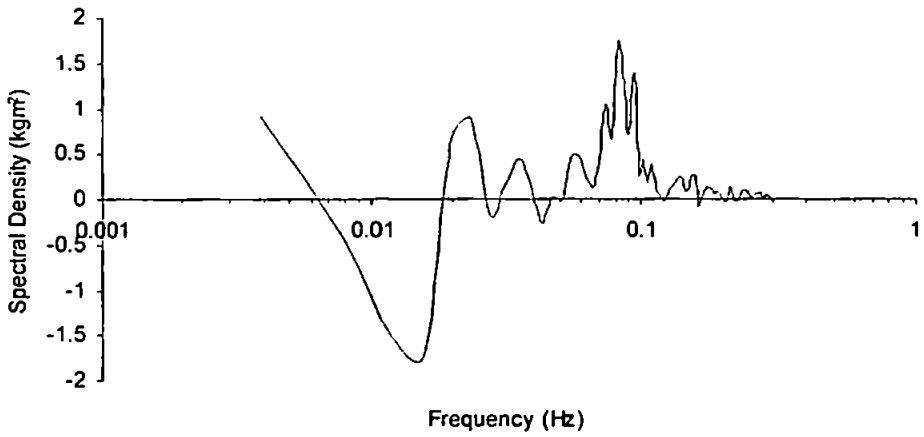

Figure 6.3.2 Suspended sediment concentration versus cross-shore velocity co-spectrum for Spurn Head run 1 (h=0.17m).

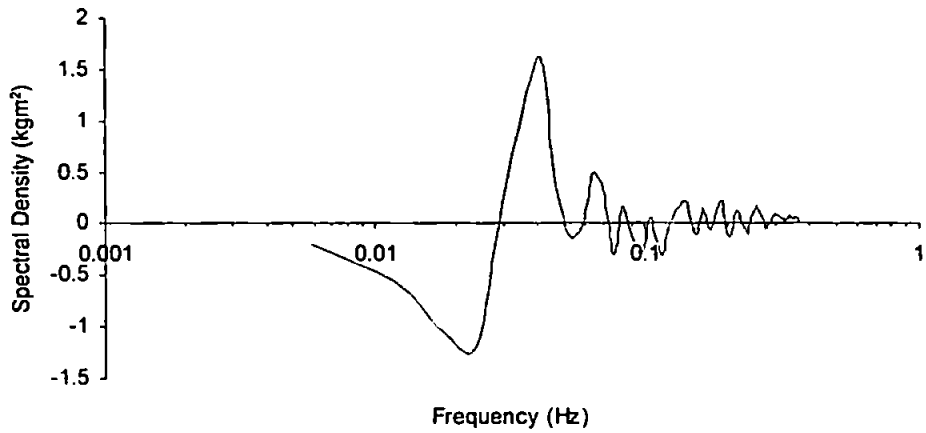

Figure 6.3.3 Suspended sediment concentration versus cross-shore velocity co-spectrum for Storm Day run 3 (h=1.01m).

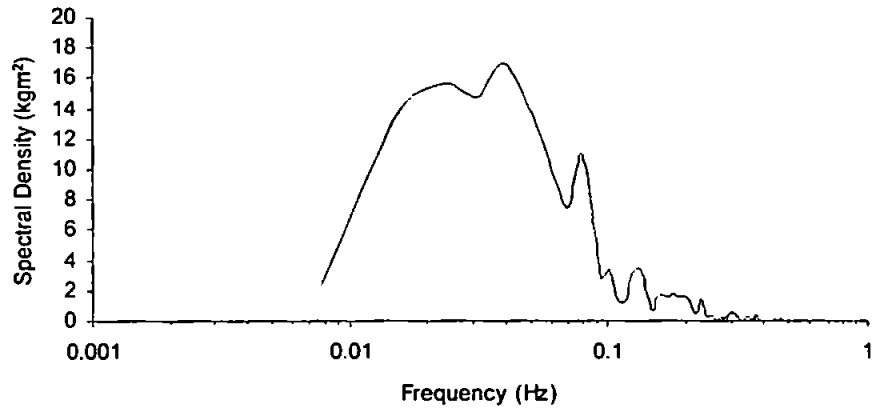

Figure 6.3.4 Suspended sediment concentration versus cross-shore velocity co-spectrum for Perranporth run 1 (h=0.47m).

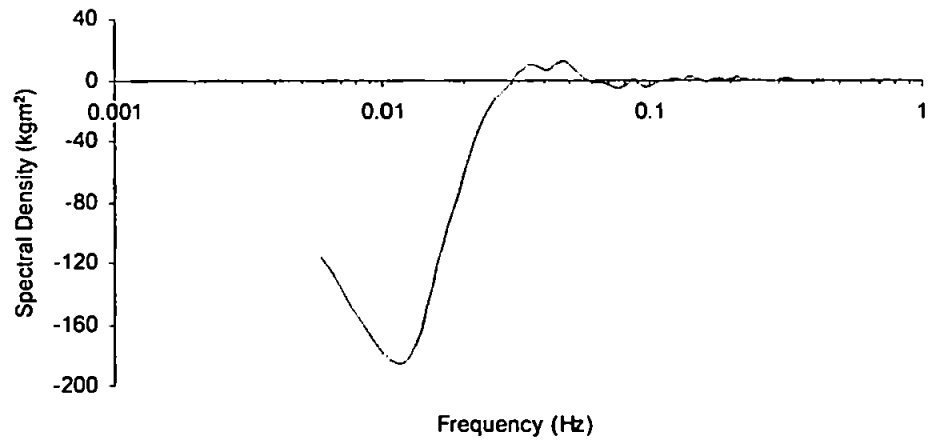

Figure 6.3.5 Suspended sediment concentration versus cross-shore velocity co-spectrum for Storm Day run 10 (h=0.66m).

6.4 Summary: Sediment Dynamics

In suspended sediment concentration time-series from throughout the region of observation, maximum concentrations varied not only at incident banded frequencies, but also at frequencies falling into the infragravity band. These latter variations were observed as being larger than usual concentrations occurring at infragravity periods. The character of these events also varied dependent on the position of observation in the cross-shore, and the relative energy between the incident and infragravity hydrodynamic components. For the majority of cases the largest suspended sediment concentrations were seen in association with the velocity maxima.

In the shoaling zone, the largest suspension events had an incident banded duration, and occurred as sets of two or three consecutive events. These periods coincided with the passage of the highest waves in the shoaling incident frequency wave groups. Maximum concentrations were observed in association with the weaker offshore phase of velocity, and it was suggested that this occurred as a result of the advection of sediment suspended at flow reversal from underlying ripples onto the instruments. Analysis of the data also suggested that a 'tidal asymmetry' in suspension whereby more sediment was suspended on the ebb tide than on the flood be due to destruction of this ripple field by several groups of large waves.

In the surf zone, events of incident band duration were observed, but generally as isolated large suspensions. For these suspension events to occur, generally an in phase combination of incident, infragravity and mean velocity was required. This was as opposed to any individual component being able to stimulate high suspension on its own. In the particularly energetic conditions observed during the Storm Day dataset, the infragravity waves became significantly shoaled enough, that with the addition of the mean component, the cross-shore velocity exceeded the threshold for mobilising sediment for infragravity banded periods. As a consequence the time-series in a number of runs from Storm Day were dominated by extremely large suspension events which had infragravity duration.

The result of both this latter change in the sediment dynamics and the destruction of the ripple field at Spurn Head was to give a qualitative change in the way sediment flux behaved versus velocity moments predictors. The inference from this result is that when thresholds for sediment motion are exceeded on a low frequency basis the character of the resultant transport may change dramatically. However, the infragravity frequency

contribution to transport was observed to be highly variable through the nearshore. This result indicates that in terms of sediment flux, the phase relationship between waves and suspension is as important as the energy of the waves. Phase variations in the infragravity band meant that lower infragravity frequencies were associated with offshore flux of sediment, whilst higher infragravity frequencies were associated with an onshore directed flux.

Chapter 7: Discussion of results

This thesis has been motivated by the idea that infragravity frequency variations in sediment transport may significantly affect total sediment flux, and furthermore, that these variations are not well represented by simple linear modelling approaches. To this end, the results in the previous chapter have demonstrated that low frequency driven transport could yield a qualitatively different type of transport to that predicted using a relatively simple energetics approach (Russell and Huntley, 1999). Two particular cases were identified.

The first case showed infragravity waves energetic enough (when combined with a strong mean flow) to mobilise large quantities of sediment over infragravity duration. This latter behaviour was observed close to shore, but elsewhere in the surf zone, large sediment suspension events were also observed occurring at infragravity frequencies as a result of the combination between the mean and incident and infragravity oscillatory components. For much of the surf zone therefore, infragravity frequency suspension of sediment occurs through a combination of components. Consequently it is imperative to describe accurately not only the behaviour of infragravity waves, but also mean current magnitude through the surf zone and the distribution of incident wave heights and their phase with respect to the infragravity component. This will be discussed further in section 7.1.

The second case for a qualitative change between observed transport and the velocity moment predictor occurred when it was hypothesised that sediment response to wave forcing increased dramatically as a result of a number of large wave groups passing over a ripple field. This behaviour showed changes not only in forcing but also in bed response affecting transport. Without particularly relating to the low frequency problem, a 'tidal asymmetry' in sediment response was also noted at Perranporth. The ramifications of such temporal changes in bed behaviour for energetics type models is noted as part of section 7.2.

7.1 Low frequency hydrodynamics in the surf zone

Infragravity frequency sediment transport in the surf zone can be seen from the results to be a product not only of the relative strengths of the oscillatory components, but also of their phase. Additionally, for the majority of the data, sediment suspension could be linked to instantaneous velocity, and therefore the mean component is equally important. For example, at Perranporth, where the mean current was near zero and higher infragravity frequencies dominated, the largest infragravity suspensions coincided with the onshore phase of velocity (e.g. figure 6.1.6). Conversely, at Llangennith, where a strong offshore directed mean current was observed, the largest events were associated with the offshore phase. In some of the Storm Day runs (e.g. run 10, figure 6.1.8), infragravity duration suspension events could be associated with offshore infragravity wave velocities combined with the mean current, whilst smaller incident duration events occurred when a large breaker coincided with an infragravity wave peak and overcame the mean flow.

In order to accurately characterise sediment suspension in the surf zone therefore, mean current and the incident and infragravity oscillatory components must all be described correctly. For the case of the oscillatory hydrodynamics, previous models (e.g. List, 1992) have made simplifying assumptions whereby in the surf zone;

- Infragravity waves are not broad banded, or in the case of a barred beach, a certain frequency is 'favoured' (e.g. Symonds and Bowen, 1984).
- Infragravity wave energy is fully reflected and forms a standing wave structure in the cross-shore.
- Breaker heights are depth limited.

The results from this data show however, that;

- Infragravity energy is broad banded and that rather different behaviour may be observed in the surf zone between lower and higher infragravity frequencies.
- Infragravity energy is not fully reflected dependent upon frequency and beach slope.
- Incident wave heights (broken and unbroken) remain modulated in the surf zone.

7.1.1 Infragravity wave behaviour

The effect of the broad banded nature of infragravity energy in the surf zone on sediment transport was noted in the suspended sediment concentration versus velocity cross-spectra shown in section 6.3. In these examples a reversal in the transport direction was observed between the higher and lower infragravity frequencies, and when neither was dominant meant that the overall infragravity contribution to transport was small. Both Beach and Sternberg (1991) and Aagaard and Greenwood (1993) saw a similar effect in the surf zones from their experiments. Furthermore, this dataset and the other two experiments show a relationship whereby offshore directed transport is associated with the lower infragravity frequencies and onshore directed transport is associated with the higher infragravity frequencies.

For high energy conditions, at instrument positions close to the swash zone, the data in this work and that of Beach and Sternberg (1991) also show that the lower infragravity frequency offshore directed transport of sediment dominates. This is not particularly surprising given the behaviour of the higher and lower infragravity components through the surf zone. The results throughout chapter 5 suggest that on dissipative beaches near to shore, higher infragravity frequency energy will be dissipated both during the waves shoreward transition and also through reflection. Lower infragravity frequencies on the other hand, show an increase in energy toward shore and have their energy more fully reflected.

The dissipation of higher infragravity energy is perhaps illustrated most clearly in a comparison of the behaviour of the incoming infragravity energy from the Storm Day and Perranporth tides. On Storm Day, when lower infragravity frequency energy dominated the spectrum, infragravity significant wave heights shoaled following a free wave relationship (figure 5.2.6a). However, wave heights from Perranporth did not increase through the surf zone (figure 5.2.13) and this suggested that energy was being dissipated close to shore. A similar result was observed by Ruessink (1998) on the beach at Terschelling (Netherlands), where infragravity energy very close to shore was found to be less than that further offshore in the surf zone.

The reason for energy dissipation from the higher infragravity band might be found in the results of the bispectral analysis presented in section 5.4. In an analysis of the bispectrum of shoaling incident frequency waves a pattern may be seen, in both this data and that of

Doering and Bowen (1995). The shoaling process gives rise to a bispectral peak indicating a sum interaction at the primary frequency forcing a harmonic, a further sum interaction between the primary and harmonic, and a difference interaction whereby the incident frequencies force an infragravity wave. Figures 5.4.5 and 5.4.6 suggested that in the surf zone this pattern would be repeated for the higher infragravity frequencies as the infragravity waves continued to shoal in this region of the nearshore. However, whilst at these frequencies the difference interaction reinforces the lower infragravity frequency waves, the primary-harmonic sum interaction may lead to energy from the higher infragravity frequencies being redistributed to frequencies in the incident band, and hence dissipated. Damping of infragravity energy under breaking conditions has been cited in Boussinesq model results from both Eldeberky and Battjes (1996) and Madsen *et al.* (1997). Furthermore, Madsen *et al.* (1997) noted that in their model breaking incident waves could have an increased dissipative effect on the infragravity component when the difference in frequencies is reduced. In other words, dissipative nonlinear interactions were most likely to occur between the highest infragravity and incident frequencies.

The results further suggest that not only is little energy lost from the lowest infragravity frequencies, but also that the continuing difference interactions that contribute to energy at this end of the spectrum may cause a strong negative skewness in the lower infragravity frequency waves. This is important in providing the dominant offshore directed infragravity frequency transport observed on the ebb phase of the Storm Day tide. In addition to this data, similar negative skewness of the infragravity component near to shore has been cited by a number of authors making measurements in high energy conditions (e.g. Beach and Sternberg, 1991; Aagaard and Greenwood, 1994; Osborne and Rooker, 1997). The observations of these authors were also connected to large offshore directed flux of sediment near to or in the swash zone.

Analysis of infragravity wave reflection showed frequency dependence, but additionally a dependence upon beach slope at the reflection point (section 5.2.4). In figure 5.2.24 this dependency was illustrated by comparing reflection coefficient with the Irribarren number. This comparison is analogous to numerous studies which examined this relationship for incident frequency waves (e.g. Giminez-Curto, 1979; Seelig and Ahrens, 1981; Hughes and Fowler, 1991; Mason *et al.*, 1997; Miles 1997). Whilst these studies investigated reflection coefficients for incident waves reflected from steep beaches or breakwaters, the work in this thesis dealt with lower frequency waves, but incident on a shallower slope reflector. Therefore the Irribarren numbers in the results from this work exist at the higher

end of the scale of values found in the work of the above authors. However, whilst an analogy may be drawn between this and other studies, a direct comparison should not be made, since the Iribarren numbers derived in this work were generated for component frequencies, whilst the aforementioned authors used Iribarren numbers which characterised the entire incident wave band. Nonetheless, a relationship between reflection coefficient and Irribarren number based on that suggested by Giminez-Curto (1979) gave a reasonable approximation to the thesis data.

Using the Spurn Head data allowed for a comparison between reflection on a dissipative slope low tide terrace ($\tan\beta$=0.0235) and reflection from a steep high tide beach ($\tan\beta$=0.1). On a dissipative beach slope the data found approximately 50-80% of lower infragravity frequency energy would be reflected, but less than 50% of higher infragravity frequency energy would be returned. As a consequence, whilst lower infragravity frequency energy may take a partially standing form on a dissipative beach, the higher infragravity frequency waves may behave in a more progressive manner. When reflection occurred on the steeper beach slope reflection coefficients suggested that between 60% and 100% of the incoming wave energy would be reflected for all the infragravity frequencies, and thus standing or partially standing structures might be expected to form. However, on macrotidal beaches such as those in this study, Davidson (1991) speculated that the formation of standing waves might be further hindered since the (shoreline) reflection point will migrate quickly over the beachface with the tide.

Again the difference in behaviour between higher and lower infragravity frequencies might be seen simply as showing continuity of behaviour of waves through the frequency domain. On a dissipative beach therefore, incident frequency waves will be fully dissipated, higher infragravity waves may be partially dissipated and reflected, and lower infragravity waves may not be dissipated and may have more of their energy reflected than the higher infragravity component. A ramification of this behaviour is that for a given set of incident wave conditions the character of the inner surf zone may be highly dependent upon the nature of the incoming infragravity waves. For example, conditions where the incident wave field consists mainly of an energetic long period swell are likely to be associated with an energetic lower infragravity frequency component. Correspondingly, the inner surf zone is more likely to be infragravity wave dominated than for conditions where the incoming infragravity wave field was dominated by higher infragravity frequencies. This latter case might include storm events where the incident wave field was made up of 'local sea' waves, such as the one observed at Perranporth. The study made by

Ruessink (1998) which shows a similar type of behaviour to Perranporth was also conducted in an environment dominated by a wind-driven local sea. The Llangennith data and that of Beach and Sternberg (1991) on the other hand, corresponded to a swell dominated storm event. Speculating further, such conditions could be more likely to see the largest contribution to infragravity energy in the surf zone coming from waves that in deep water made up the bound long wave component.

7.1.2 Incident wave modulation and phase versus infragravity waves

The majority of the surf zone will not be wholly infragravity dominated. In attempting to simulate the instantaneous velocity field in this region, knowledge of the degree of incident wave (broken or unbroken) wave height modulation and the phase between the largest waves and the infragravity component are essential. For example, in the data for much of the surf zone, the largest low frequency suspension events tended to result from the combination between large incident waves and an infragravity wave peak or trough dependent upon the nature of the mean current (e.g. figures 6.1.2 and 6.1.3).

In the non-saturated surf zone at Spurn Head incident frequency waves remained modulated since some broke whilst others continued to shoal. Wave height modulation was also noted in inner surf zone data from Spurn Head, Llangennith and Perranporth, although breaker index values from all the sites remained near constant through this part of the surf zone. This latter behaviour is used to define a surf zone as saturated, and suggests that the breaking wave heights are depth limited. Such an assumption is used in a model such as List's (1992) to determine wave heights at any given point in the surf zone. However, if such a model simply employs a mean water depth, breaker heights at a point will be uniform. This is contradicted by the observations from this work.

For breaker heights to be modulated in the saturated surf zone, one suggestion is that a level of modulation may be transmitted into this region from the non-saturated surf zone, but that subsequently circumstances are such that the breaker index remains constant. Alternatively, Nelson and Gonsalves (1992) suggested that infragravity wave fluctuations in sea surface might influence breaker heights. Raubenheimer and Guza (1996) produced a model that demonstrated that the presence of infragravity waves should not significantly alter the breaker index.

If modulations in broken wave heights could be linked to infragravity wave behaviour then constructing a modulated breaker-infragravity wave height phase relationship could be quite simple. However, figure 5.3.10 showed that little direct correlation between the largest breakers and the infragravity waves could be observed for the majority of the surf zone. Instead a bound long wave type relationship was observed outside of the surf zone whilst a significant correlation was also observed between breaker heights and the infragravity waves very close to shore (normalised cross-shore distance less than 0.3). In this latter region the positive correlation linked the largest breakers to infragravity wave

peaks. The suggestion is therefore that infragravity waves may only force breaker heights close to shore and when infragravity energy dominates the wave spectrum. Under such conditions the infragravity waves may also dominate the forcing driving sediment transport (e.g. Storm Day run 10). Nelson and Gonsalves (1992) argued that variations in breaker heights observed at a given point might be determined by the 'history' of depths through which the waves have propagated, possibly as an effect of a standing wave structure through the nearshore, rather than the instantaneous depths observed. However, in the data from Perranporth, well-established standing wave structures may not necessarily be formed due to a combination of low reflection coefficients and tidal motion of the reflection point.

Being unable to establish a deterministic phase relationship between the modulated incident waves and the infragravity component for much of the surf zone is a problem for examining the contribution made by large low frequency suspension events to sediment transport in this region. Certainly inspection of the velocity time-series shown in section 6.1.2 yields examples of large incident waves coincident with both infragravity wave peaks and troughs. More work is required on this, particularly bearing in mind the reversal in direction observed between transport at lower and higher infragravity frequencies observed in both this data (e.g. figures 6.3.2-5) and that of others (e.g. Beach and Sternberg, 1991). Such common behaviour suggests that a causal relationship may exist for the evolution of phase between all these components through the nearshore.

In the data from this thesis phase can be established with a level of mathematical confidence both outside the breaker zone and close to the shoreline. Furthermore, it should be possible to simulate the behaviour of the infragravity components as described in this work. Thus the question to be posed regarding incident-infragravity frequency wave phase in the surf zone is how are incident wave height modulations transformed between the onset of breaking and close to the shoreline? Following this, a suggestion for further work from this thesis is to attempt to measure the transformation of a wave group through the breaker line and into the inner surf zone. This might be done by the use of a video system coupled with a cross-shore array of instruments.

Alternatively, for modelling purposes the combination between large incident waves and the infragravity component might be assumed to take on a random form in the surf zone, and thus the effect of infragravity frequency suspension of sediment could be tested using a statistical distribution for incident wave heights. Thornton and Guza (1983) demonstrated that the deep water Rayleigh distribution of wave height H,

$$p(H) = \frac{2H}{H_{rms}^2} \exp\left[-\left(\frac{H}{H_{rms}} \right)^2 \right], \tag{7.1}$$

where H_{rms} is root mean square wave height gave a reasonable description of wave height distribution right up to the outer surf zone. For this data the distribution of wave heights was also tested versus the Rayleigh distribution for all the runs in the dataset using a Chi-squared test, with a confidence level of 95%. Figure 7.1.1 shows the results of this test. In the figure the List (1991) groupiness factor has been plotted against the parameter

$$\frac{h}{h_b} \frac{E_g}{E_{ig}}. \tag{7.2}$$

This parameter has been chosen as the x-axis in order to illustrate the increasing infragravity contribution to wave energy near to shore in addition to the cross-shore position at which the measurements were made. Where the observed distribution of wave heights fits the Rayleigh distribution the symbols are filled. In the figure the majority of runs show a distribution of wave heights which fit the Rayleigh distribution when the List (1991) groupiness factor has some of its highest values. The Rayleigh distribution is not applicable for most of the surf zone however, and the GF takes a minimum. Close to shore GF increases, since breaker modulation does not decrease as quickly as breaker height. Interestingly, along with the increase in GF, when infragravity waves dominate the run distribution of wave heights again show a good fit to the Rayleigh distribution.

Thornton and Guza (1983) also suggested a weighting function that could be applied to the Rayleigh distribution in order to give the distribution of breaker heights in the outer surf zone. The function was given as

$$\left(\frac{H_{rms}}{\gamma h} \right)^n \left\{ 1 - \exp\left[-\left(\frac{H}{\gamma h} \right)^2 \right] \right\}, \tag{7.3}$$

where γ is the breaker index, and Thornton and Guza (1983) suggested values of γ=0.42 and n=2. It should be noted that the application of this weighting function no longer yields a proper probability distribution however. In figure 7.1.2 a distribution of observed wave heights taken inside the surf zone (from Spurn head run 8) is shown against both the Rayleigh distribution and a scaled version of the weighted Rayleigh function. This latter distribution shows a good fit to the observed data.

Thus by employing these types of statistical distributions of wave height, and with a knowledge of incident wave period and infragravity wave behaviour it should be possible

to simulate time-averaged values for the type of forcing and transport observed in the surf zones in this dataset.

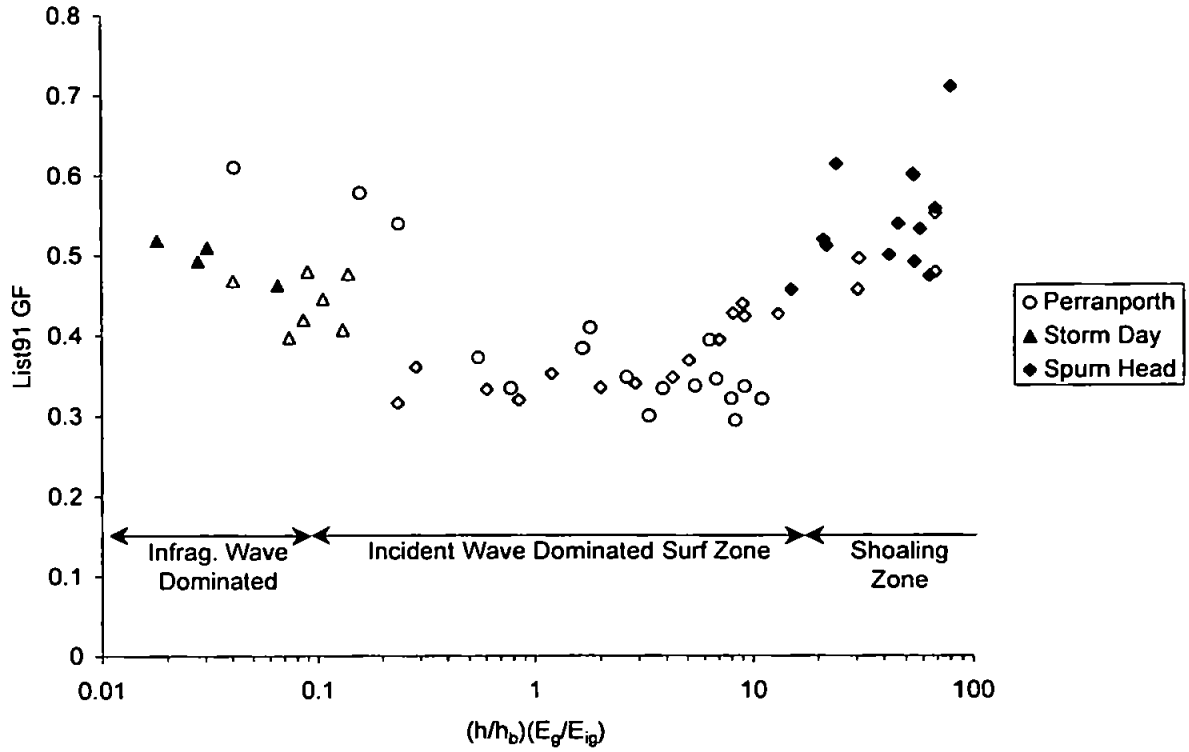

Figure 7.1.1 Distribution of List (1991) groupiness factor in distance-energy space. The filled symbols indicate where observed incident wave height distributions fit a Rayleigh probability density function.

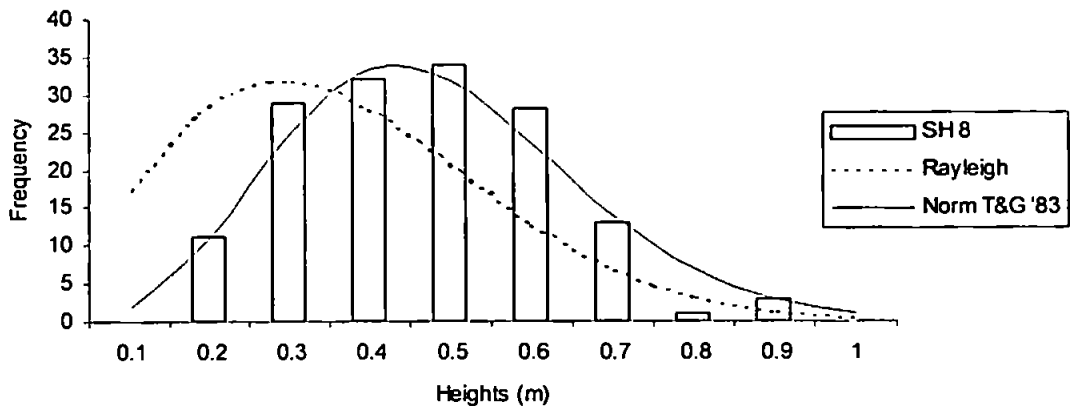

Figure 7.1.2 Comparison between an observed incident wave height distribution, a Rayleigh distribution and a scaled version of Thornton and Guza's (1983) weighted Rayleigh function. Spurn Head run 8, outer surf zone (h=1.09m).

7.2 Observations of sediment response to forcing versus an energetics approach

The results in section 6.1 found that under energetic conditions sediment suspension is generally driven by instantaneous velocity in the nearshore, since maxima in suspended sediment concentrations were observed in association with the cross-shore velocity maxima. This would suggest that an energetics approach such as the one proposed by Russell and Huntley (1999) might provide an appropriate model for nearshore sediment transport, as it employs a total u^3 velocity moment. This is coupled with an efficiency factor to generate the transport prediction. An advantage of Russell and Huntley's (1999) formulation is that since field data was used to generate the shape function, the model should contain much of the necessary velocity phase information discussed in the previous section. However, several features of the results in this work suggest that the use of a simple constant efficiency factor in an energetics model might be inappropriate:

- Sediment transport response to forcing does not simply follow velocity magnitude, but instead may show a relationship to the duration of forcing.
- A degree of asymmetry in sediment response may be observed between the onshore and offshore directed phases of velocity as a result of bedforms.
- The sediment response exhibits temporal variations ('tidal asymmetry').

The most obvious example of the change in sediment transport response to the forcing duration comes from Storm Day runs 9-11, where suspension of sediment took on infragravity duration (e.g. figure 6.1.8). This was a result of a combination of extremely energetic negatively skewed infragravity waves combined with an offshore directed mean current, which meant that the threshold for suspension was exceeded for infragravity periods of time. In this situation offshore sediment flux increased dramatically, although compared to previous runs during the Storm Day tide no similar increase in velocity moment was observed (figure 6.2.6). Thus where sediment was suspended for long periods, the observed (point) flux appeared to be rather more efficient with respect to the velocity moment. This type of result suggests that when using an energetics approach it might be worth employing an efficiency factor which is modified in relation to the duration for which velocity moment exceeds some critical threshold (i.e. long duration suspension events would have an increased efficiency factor).

On an incident timescale a similar effect may well have been observed at Perranporth, where runs during the high water period (runs 5-10, figure 6.2.10) showed a reversal between the observed flux direction (offshore) and the velocity moment predictor

(onshore). The velocity moment took an onshore value as a result of the combination of onshore skewness of the broken incident waves and shoaling of the dominant higher infragravity frequency waves. During these runs however, an analysis of suspended sediment concentration-velocity scatter (e.g. figures 6.1.3 and 6.1.4) showed that although suspension maxima might be observed with the strongest velocities during the onshore phase, a majority of sediment suspension occurred during the offshore phase. Consequently, more sediment transport was directed offshore than onshore. It was suggested that this was a result of the substantially longer duration for which offshore directed velocities might exceed a threshold velocity for suspension (e.g. figure 6.1.12).

Whilst these two tides observed asymmetry in suspended sediment concentration-velocity scatter, both found suspension maxima associated with the velocity maximum. In the outer surf zone and shoaling zone at Spurn Head however, far higher suspension maxima were consistently observed on the weaker offshore phase of velocity than on the stronger onshore phase (e.g. figures 6.1.1, 6.1.2 and 6.1.18). In this situation it was hypothesised that the 'phase asymmetry' in these results was a consequence of the formation of bed ripples. These bedforms cause suspension maxima and velocity to be 180° out of phase since large quantities of sediment will be suspended via a vortex shedding mechanism at the flow reversal from the strongest to weakest phase of velocity (Sleath, 1984). This result suggested that whilst the velocity moment was biased onshore in the Spurn Head data in the shoaling zone, the actual sediment flux in this region saw a disproportionately large contribution from the offshore phase.

Nevertheless, for a majority of runs at Spurn Head the velocity moment predicted the direction of sediment flux correctly. Instead it was only during Spurn Head runs 24-29 that the observed flux became offshore directed whilst the moment was onshore directed (figure 6.2.2). During these runs, it was suggested that several large wave groups were responsible for causing exceptionally large suspension events to occur in association with an offshore directed velocity, resulting in a time-averaged offshore flux. Davidson *et al.* (1993) suggested that these events might tie in with destruction of the ripple field, and analysis using the mobility number suggested by Dingler and Inman (1976) may support this. Hanes *et al.* (1997) suggested that ripple fields could be destroyed by a wave group but then reform quickly under slightly lower wave conditions.

Davidson *et al.* (1993) labelled this behaviour at Spurn Head a 'tidal asymmetry' in sediment transport, and the results here point to this being an effect of a change in bed

response resulting from a number of waves exceeding some threshold for behaviour of the bed. However, a 'tidal asymmetry' was also observed at Perranporth, although it was hypothesised that this was simply a result of a variation in bed response over the tidal cycle. In this case material appeared to be rather more readily suspended during the first few runs than for the remainder of the tide. Again relating this behaviour to an energetics approach it would appear necessary to consider such temporal variations in bed response when designing an efficiency factor for use with velocity moments in future modelling work.

Unfortunately in this data, it remains difficult to draw firm conclusions about the measurements without knowledge of the bed's behaviour, particularly in the Spurn Head case where it has been presumed that bedforms are present. From this perspective the University of Plymouth is currently involved in a multi-institute study, 'Quantification of sediment entrainment in the coastal zone' (COSMOD), which aims to shed further light on the role of bedforms in sediment transport. Along with model and laboratory studies, this project also includes a field programme where measurements similar to the ones in this work are supplemented by sector scanning sonar images of the bed near the instruments and altimeter measurements of the variation in bed height.

7.3 Discussion summary

This chapter has highlighted several features of the results that require further investigation and incorporation into nearshore models. Firstly the surf zone hydrodynamic regime has been shown to consist of modulated incident frequency waves and an infragravity component. The infragravity wave behaviour in this region may however be characterised by the degree to which higher or lower infragravity frequencies dominate the wave field. Higher frequency infragravity waves may have their energy dissipated near to shore on low gradient beaches, possibly as a result of energy cascading toward the incident band during shoaling, and may only have their energy substantially reflected when the shoreline slope is steep. Lower infragravity frequency waves are less prone to this type of dissipation and should also be reflected better from low gradient beaches. Furthermore, the lowest infragravity frequencies may be reinforced in the surf zone by difference interactions due to shoaling of the higher infragravity frequency waves. This might well be responsible for the increase in negative skewness observed in the lower infragravity frequencies near to shore.

For much of the surf zone no single hydrodynamic component was observed to be capable of mobilising sediment unless in phase with the others. Therefore, the phase between the incident and higher and lower infragravity frequency waves, along with the mean current magnitude and direction, is important in determining low frequency suspension and transport for the majority of the surf zone. In the data here however, no clear deterministic relationship between these components was observed. This should be a particular focus in future work on the surf zone transport problem.

Near to the swash zone in energetic conditions, where negatively skewed lower infragravity frequency waves dominate the spectrum, sediment may be mobilised by this component combined with the mean current. In the results from this work, under these conditions the oscillatory contribution to transport was dominated by the lower infragravity frequency component. This behaviour coincided with sediment suspension events having infragravity duration, as a mobilisation threshold was exceeded for an infragravity period, and also corresponded with a large increase in overall sediment transport

A dramatic change in the sediment dynamics was also noted in the data when at Spurn Head a number of wave groups become large enough to change the sediment response to forcing – here hypothesised as due to the destruction of a ripple field. The change in

transport was linked to a threshold for sediment motion being exceeded at an infragravity period. A change in bed response was also suggested as being responsible for a 'tidal asymmetry' in sediment dynamics at Perranporth. These effects were linked to discrepancies in a comparison between observed sediment flux and velocity moments predictors for flux. Therefore, it is suggested that the concepts of sediment motion thresholds and temporal changes in bed response should be incorporated into current energetics modelling approaches such as that of Russell and Huntley (1999).

Chapter 8: Conclusions

Thesis aims and dataset

The motivation behind this work was to compare observations of infragravity frequency effects on sediment transport with the underlying theories behind models that described the role of such components simply. In the past these models have been employed using assumptions such as;

- Incident frequency waves provide a stirring component, with mean flow and the infragravity wave associated current providing a 'drift' velocity for transport of sediment (e.g. Bowen, 1980).
- Incident wave breaker heights are depth limited in the surf zone (e.g. List, 1992).
- The infragravity component propagates through the surf zone without dissipation, and is fully reflected from the shoreline (e.g. List, 1992).

This thesis demonstrates that such simple treatments of low frequency hydrodynamics do not provide an accurate description of the real processes, and moreover that, variations in the velocity field at infragravity frequency can have an important impact on sediment suspension and transport.

Results stemming from the University of Plymouth's involvement in the B-BAND programme, and supplemented by a further study carried out in March 1998 at Perranporth (Cornwall, UK), make up the dataset for this study. The main proviso in selecting the data to be analysed was that wave conditions be sufficiently energetic for a significant infragravity frequency component to be likely to be present. After this, the hydrodynamics at each of the beach sites differ significantly. At Llangennith high swell waves (significant wave height up to 3m) were observed incident on a dissipative beach; the measurements taken from this site show the instruments in a saturated surf zone, where infragravity frequency energy was dominant. The swell observed at the intermediate beach at Spurn Head was rather smaller (significant wave height 1.5m), and led to a non-saturated surf zone dominated by incident wave energy. In energy terms the Perranporth data falls somewhere between these two datasets, in that the locally generated wind wave heights were around 2m and led to a saturated surf zone on the dissipative beach, but dominated in the main by incident frequency energy.

Spatially the data covers regions of the nearshore from the incident frequency wave shoaling zone (Spurn Head) shoreward until the edge of the swash zone (Llangennith,

Perranporth and Spurn Head). Much of the data shows waves incident on low gradient beaches typical of an energetic macrotidal environment, but some data observes more reflective circumstances, where the shoreline occurs on a steep high tide beach (Spurn Head data). Sediment at each of the three beaches is relatively similar, with median grain sizes corresponding to a medium-fine sand at the instrument location.

The fact that a study based on results taken over such a range of spatial and energetic conditions could be compiled in a relatively short period proves the worth of establishing and processing collated data from databases such as that in the B-BAND programme. With developments in information technology this type of data archiving has become an essential feature of most of the large-scale experiments conceived in the last few years (e.g. the EU MASTIII COAST3D project, Soulsby, 1998).

The main analysis for the thesis focused on describing the processes underlying infragravity frequency variations in the velocity field and the effect of low frequency variations in suspended sediment concentration on sediment transport. These variations were defined as larger than usual suspension events occurring at infragravity banded intervals. In the following paragraphs conclusions from analysis of the thesis dataset are presented with respect to the aims (**H.1-H.4** and **S.1-S.3**) set out at the end of chapter 1.

Hydrodynamics

H.1 Examine the evolution of infragravity wave energy through the nearshore, whether these waves are forced or free, and the extent to which infragravity energy may be dissipated.

> In the shoaling zone bispectral analysis of the wave field shows infragravity waves being forced by groupy incident waves, i.e. the infragravity waves have a bound long wave form. In this region of the nearshore, the infragravity wave-incident group phase does not adhere to the theoretical deep water bound long wave phase value suggested by Longuet-Higgins and Stewart (1964). Nonetheless, because of the increasing levels of radiation stress produced by the incident wave shoaling process, which results in a larger differential in wave heights than would be observed in deeper water, forcing of the infragravity wave component still tends to a maximum at the breaker line.

Bound infragravity wave energy is released from the wave groups just after the onset of breaking. However, the nature of the 'free wave' behaviour in the surf zone appears to be dependent on the frequencies of the main components making up the infragravity wave field. More explicitly, on beaches of low slope, higher frequency energy in the infragravity band (>0.02Hz) tends to be dissipated near to shore, whilst the lower frequency waves (<0.02Hz) continue to shoal. Thus, near to shore, lower infragravity frequency waves make an increased contribution to the overall wave spectrum. The lowest infragravity frequencies are associated with an offshore directed skewness, possibly as a result of non-linear forcing related to shoaling of incident waves outside the surf zone, and higher infragravity frequency waves in the surf zone.

H.2 Examine infragravity wave reflection and the possible formation of standing waves.

Infragravity wave energy is not fully reflected from dissipative beaches, but reflection does occur very close to the shoreline. A comparison between infragravity wave reflection coefficients, derived using a Principal Component Analysis technique, and the Irribarren number shows that infragravity wave reflection is dependent upon frequency and the beach slope at the reflection point (figure 5.2.24). For the dissipative conditions in this dataset the reflection process acts as a filter for higher infragravity frequency energy. In these instances, observed reflection coefficients show that for higher infragravity frequencies less than 50% of the incoming wave energy is reflected, as opposed to between 50-80% for the lower infragravity frequency waves. As a result of the increased dissipation of energy at higher infragravity frequencies in the surf zone, the degree to which infragravity energy takes a standing or progressive form in this region of the nearshore depends upon how energy is distributed through the infragravity band in the incoming waves, and the local beach slope at the shoreline.

H.3 Examine the nature of low frequency modulation of incident wave heights through the nearshore.

In the shoaling zone the incident frequency waves retain the deep water 'groupy' form up to the breakpoint. From this point up to the shoreline however, the form of the modulation of wave heights undergoes a change from being an ordered progression of low then high waves, to a seemingly more 'random' form as waves

start breaking in the outer surf zone. In the inner surf zone, broken wave height modulation may still be observed, although comparatively high waves occur simply as individual events. This is despite breaker index remaining constant and suggesting that breaker heights are depth limited. In the inner surf zone under infragravity dominated conditions a calculated 'groupiness factor' (List, 1991), which compares the level of wave height modulation with wave height, increases. Thus in this region of the surf zone broken wave heights decrease more quickly than their level of modulation.

H.4 Examine the phase relationship between modulated incident and infragravity waves, particularly as a result of any interactions between the two components.

In the shoaling zone, although the infragravity waves remain bound to incident wave groups, near to the breaker line they exhibit a phase shift away from the 180° relationship predicted in deep water (Longuet-Higgins and Stewart, 1964). Observations show a phase relationship of approximately 120-150°, which indicates that the infragravity wave trough lags slightly behind the largest incident waves ('positive-negative' form). In the inner surf zone close to the shoreline, incident wave height modulations become significantly correlated with infragravity waves following a 'negative-positive' form, i.e. the largest breakers are in phase with infragravity wave crests. Correspondingly, bispectral analysis suggests that close to shore an increased amount of inter-frequency interaction occurs between infragravity and incident waves. For much of the surf zone however, the phase between modulated incident waves and the free infragravity waves could not be derived with any mathematical confidence.

Sediment Dynamics

S.1 Establish whether sediment suspension is velocity or acceleration driven, and identify the main hydrodynamic components underlying the largest suspension events at a given point in the cross-shore.

For the majority of cases the suspension of sediment could be directly linked to onshore or offshore directed velocity maxima. In the shoaling zone the main source of low frequency variations in suspended sediment concentration is the effect of the groupiness in the incident frequency wave heights. For much of the surf zone, the

velocity maxima stimulating the largest suspension events are (generally) a result of a combination of mean, and incident and infragravity oscillatory components. This indicates that the instantaneous velocity at the bed is responsible for mobilising sediment, and therefore that the infragravity component must be thought of as having a role in 'stirring' sediment and does not simply act as a 'drift velocity'. In the highly energetic inner surf zone at Llangennith, on the Storm Day ebb tide, the infragravity component dominates to such an extent that the resulting suspension events take on an infragravity timescale.

S.2 Examine the contribution to suspension and transport attributable to the infragravity frequency component.

When sediment is suspended over infragravity rather than incident duration, the overall level of suspension increases dramatically. Similar 'tidal asymmetries' in suspended sediment concentration may also occur due to a change in the bed conditions (e.g. the hypothesised destruction of ripples at Spurn Head, or transport of swash material at Perranporth). Nonetheless, the infragravity contribution to suspended sediment concentration remains similar, independent of the absolute concentration, and does not fall below approximately 30%. This value increases substantially near to shore for conditions where infragravity energy is dominant, results here showing the infragravity contribution to be up to 90% of the overall suspended sediment concentration variance (figure 6.1.11).

The infragravity contribution to transport through the nearshore cannot be expressed simply in terms of either nearshore position or an energy parameter, but instead is found to be highly variable throughout the surf zone. This results from a reversal of transport direction occurring between the higher and lower infragravity frequencies, which means that unless one or other component dominates, the overall infragravity contribution to transport is small. This emphasises the need to properly describe phase between the modulated incident and higher and lower infragravity components throughout the nearshore.

S.3 Identify cases where a change in the low frequency hydrodynamics results in sediment flux qualitatively different to that expected when assuming a more simplistic scenario.

Changes in the overall levels of suspension coincide with a qualitative change in the way observations of sediment flux compare with a prediction derived using an energetics approach. In this data, two cases are identified, where infragravity frequency changes in forcing are deemed responsible. In the energetic inner surf zone at Llangennith, negatively skewed infragravity waves, coupled with the mean current, cause suspension events to take on infragravity duration. As a consequence, a large offshore flux occurs without a similar change in the u^3 moment derived from instantaneous velocity. This suggests that the duration for which a threshold for mobilising sediment is exceeded is important in modelling sediment transport and that consideration be given to the efficiency factors used in the energetics model.

In the second case, it is surmised that several large wave groups, the arrival of which at the instrument position occurs on a low frequency timescale, exceed a threshold for the destruction of a ripple field (following the results of Dingler and Inman, 1976). The resulting change in sediment response leads to a reversal of the transport direction observed earlier in the tide. This suggests that models may also need to be sensitive to temporal changes in bed response to forcing.

In closing, it is hoped that this work has emphasised the importance of low frequency effects on sediment transport. Hydrodynamically it is necessary to accurately describe the make up of the infragravity wave field and phase between the modulated incident and higher and lower infragravity components. This applies in particular to shallow water depths in the inner surf zone. Wave period apart, this region of the nearshore should see similar incident wave conditions independent of offshore wave height, i.e. so long as wave breaking is saturated, wave heights at a given depth will be the same whether offshore wave heights are 1m or 5m. The hydrodynamic character of the inner surf zone close to shore will therefore be defined by the nature of the infragravity and mean components associated with a storm event. Elsewhere in the nearshore, low frequency variations in sediment dynamics will take on an increased importance when sediment suspension/transport threshold conditions are exceeded at, or for, infragravity periods. Factors, such as the duration for which a threshold velocity is exceeded and temporal

variations in sediment 'pick-up' (e.g. due to the presence or deformation of bedforms), must be considered in model design, particularly when sediment transport is to be calculated on a time-averaged basis.

Appendix I: Summary tables for cross-shore velocity statistics and autospectral analysis

Cross-shore velocity summary statistics

Run No.	Depth (m)	Mean u	u_{max} on	u_{max} off	Infrag u_{sig}	Incident u_{sig}
1	0.85	**-0.500**	0.667	-1.486	1.068	1.032
2	0.95	-0.475	0.809	-1.669	1.059	1.058
3	1.01	-0.307	0.887	-1.274	1.046	1.046
4	**1.06**	-0.203	1.218	-1.438	1.137	1.073
5	1.03	-0.175	1.014	-1.283	0.878	**1.158**
6	1.00	-0.155	1.127	-1.308	1.130	1.103
7	0.96	-0.320	1.061	-1.588	1.105	1.092
8	0.73	-0.338	1.116	-2.309	1.507	1.085
9	0.73	-0.172	1.336	-1.891	1.596	1.124
10	0.66	-0.223	**1.368**	-1.957	**1.746**	1.048
11	0.56	-0.174	1.226	**-2.021**	1.631	1.039

Table i *u* statistics for Storm Day, values in ms^{-1}. Peak values are in **bold**.

Run No.	Depth (m)	Mean u	u_{max} on	u_{max} off	Inf u_{sig}	Incident u_{sig}
1	0.37	**-0.226**	1.250	-1.580	**2.090**	0.964
2	0.47	-0.162	1.059	**-2.120**	1.860	0.922
3	0.54	-0.175	1.309	-1.508	1.581	0.907
4	0.63	-0.203	1.093	-1.457	1.364	0.915
5	0.49	-0.329	0.862	-1.433	1.213	0.948
6	0.62	-0.124	1.167	-1.141	1.087	0.906
7	0.69	-0.151	0.929	-1.238	1.002	0.863
8	**0.73**	-0.129	1.042	-1.338	1.104	**0.976**
9	0.71	-0.123	1.061	-0.974	1.092	0.820
10	0.72	-0.145	0.997	-1.463	1.175	0.891
11	0.66	-0.120	**1.445**	-1.792	1.749	0.897
12	0.61	-0.122	1.084	-1.648	1.280	0.895
13	0.55	-0.088	1.211	-1.122	1.292	0.898
14	0.48	-0.176	1.088	-1.730	1.626	0.828

Table ii *u* statistics for Storm Night, values in ms^{-1}. Peak values are in **bold**.

Run No.	Depth (m)	Mean u	u_{max} on	u_{max} off	Infrag u_{sig}	Incident u_{sig}
1	0.17	-0.068	1.058	-1.280	0.853	1.012
2	0.22	-0.038	1.233	-1.111	**0.962**	1.082
3	0.30	-0.080	1.221	-1.255	0.722	1.063
4	0.46	-0.085	0.970	-1.286	0.837	1.157
5						
6	0.74	**-0.206**	1.521	**-1.368**	0.821	1.294
7	0.90	-0.110	1.321	-1.111	0.720	1.332
8	1.09	-0.072	1.296	-1.192	0.698	1.383
9	1.31	-0.029	**1.615**	-1.042	0.602	1.394
10	*1.56*	*0.038*	*1.327*	*-0.785*	*0.434*	*1.379*
11	*1.79*	*0.040*	*1.409*	*-0.773*	*0.454*	*1.304*
12	*2.01*	*0.050*	*1.471*	*-0.835*	*0.436*	*1.320*
13	*2.23*	*0.040*	*1.258*	*-0.760*	*0.239*	*1.236*
14	*2.42*	*0.047*	*1.271*	*-0.710*	*0.278*	*1.189*
15	*2.60*	***0.049***	*1.195*	*-0.678*	*0.247*	*1.009*
16	*2.74*	*0.041*	*1.384*	*-0.760*	*0.265*	*1.240*
17	*2.86*	*0.041*	*1.409*	*-0.773*	*0.201*	*1.230*
18	*2.95*	*0.040*	*0.976*	*-0.509*	*0.198*	*1.032*
19	*2.99*	*0.028*	*1.202*	*-0.672*	*0.183*	*1.204*
20	***2.99***	*0.026*	*0.989*	*-0.578*	*0.148*	*0.877*
21	*2.96*	*0.024*	*1.020*	*-0.685*	*0.173*	*1.024*
22	*2.87*	*0.021*	*1.007*	*-0.653*	*0.207*	*1.118*
23	*2.71*	*0.016*	*1.227*	*-0.773*	*0.210*	*1.345*
24	*2.50*	*0.023*	*1.496*	*-1.061*	*0.190*	*1.401*
25	*2.27*	*0.014*	*1.503*	*-0.798*	*0.296*	***1.464***
26	2.01	-0.139	1.127	-1.017	0.547	1.209
27	1.76	-0.065	1.070	-0.904	0.593	1.067
28	1.47	-0.081	1.258	-0.823	0.619	0.954
29	1.18	-0.039	0.857	-0.917	0.643	0.969
30	0.86					
31	0.57	0.021	1.427	-0.798	0.232	1.432
32	0.29	0.013	1.528	-0.804	0.327	1.358

Table iii Spurn Head *u* statistics for bottom EMCM rig A2, values in ms^{-1}. Shoaling zone runs are in *italics*, peak values in **bold**.

Run No.	Depth (m)	Mean u	u_{max} on	u_{max} off	Infrag u_{sig}	Incident u_{sig}
1	0.47	-0.025	1.34	-1.126	1.258	1.113
2	0.81	0.007	1.292	-1.028	1.032	1.193
3	1.13	-0.028	1.283	-0.93	0.763	1.371
4	1.43	-0.017	1.311	-1.056	0.751	1.498
5	1.69	-0.038	1.513	-1.066	0.652	1.673
6	1.89	-0.022	**1.686**	-1.025	0.769	1.745
7	2.06	-0.066	1.591	-1.041	0.732	1.856
8	2.14	-0.053	1.558	-1.027	0.570	1.798
9	2.19	-0.007	1.498	-0.956	0.594	1.818
10	**2.20**	-0.043	1.555	-1.052	0.546	**1.935**
11	2.08	-0.085	1.55	-1.247	0.762	1.894
12	1.95	-0.051	1.667	-1.238	0.737	1.774
13	1.78	**-0.151**	1.361	-1.184	0.747	1.729
14						
15	1.20	-0.119	1.185	-0.977	0.683	1.427
16	0.93	-0.111	1.129	-1.141	0.859	1.190
17	0.61	-0.094	1.009	-0.942	0.972	1.006
18	0.28	-0.090	1.418	**-1.711**	**1.424**	0.897

Table iv *u* statistics for Perranporth runs, values in ms^{-1}. Peak values are given in **bold**.

Autospectrum results summary

		Main Peak(s) (Hz)		Variance (m^2)	
Run No.	Depth (m)	Infragravity	Incident	Infragravity	Incident
1	0.85	0.02930	0.07031	0.00847	0.01507
2	0.95	0.04102	0.07031	0.01407	0.01520
3	1.01	0.03516	0.07617	0.01217	0.01530
4	**1.06**	0.02344	0.07031	0.00932	0.01604
5	1.03	0.03516	0.07617	0.01041	0.01935
6	1.00	0.02344	0.07617	0.01364	0.01659
7	0.96	0.01172	0.07031	0.01474	0.01450
8	0.73	0.00586	0.06445	0.01539	0.01328
9	0.73	0.00586	0.06445	0.01668	0.01131
10	0.66	0.00586	0.07617	0.00917	0.00659
11	0.56	0.00586	0.07617	0.00918	0.00457
12	0.46	0.00586	0.07617	0.01248	0.00246

Table v Features of the Storm Day η autospectra.

		Main Peak(s) (Hz)		Variance (m^2s^{-2})	
Run No.	Depth (m)	Infragravity	Incident	Infragravity	Incident
1	0.85	0.00586	0.07031	0.07130	0.06662
2	0.95	0.03516	0.07617	0.07003	0.06992
3	1.01	0.03516	0.07617	0.06836	0.06841
4	**1.06**	0.00586	0.07031	0.08074	0.07192
5	1.03	0.00586	0.07617	0.04820	0.08377
6	1.00	0.00586	0.07617	0.07974	0.07604
7	0.96	0.01172	0.06445	0.07625	0.07448
8	0.73	0.00586	0.07617	0.14190	0.07360
9	0.73	0.01172	0.06445	0.15920	0.07890
10	0.66	0.01172	0.07617	0.19060	0.06862
11	0.56	0.01172	0.07617	0.16630	0.06750

Table vi Features of the Storm Day u autospectra.

		Main Peak(s) (Hz)		Variance (g^2l^{-2})	
Run No.	Depth (m)	Infragravity	Incident	Infragravity	Incident
1	0.85	0.02930	0.06445	0.04	0.14
2	0.95	0.03516	0.07617	0.17	0.33
3	1.01	0.02344	0.08789	0.07	0.17
4	**1.06**	0.00586	0.07031	0.88	1.35
5	1.03	0.01172	0.07031	0.08	0.17
6	1.00	0.00586	0.08203	0.79	0.52
7	0.96	0.01172	0.07617	1.70	1.57
8	0.73	0.01172	0.09961	4.78	1.60
9	0.73	0.00586	0.05273	77.29	24.79
10	0.66	0.01172	0.07031	105.90	32.41
11	0.56	0.01172	0.06445	117.80	25.62

Table vii Features of Storm Day *c* autospectra.

		Main Peak(s) (Hz)		Variance (m^2)	
Run No.	Depth (m)	Infragravity	Incident	Infragravity	Incident
1	0.37	0.00586	0.05859	0.00640	0.00200
2	0.47	0.02344	0.08203	0.00525	0.00255
3	0.54	0.01172	0.08203	0.00526	0.00296
4	0.63	0.02930	0.07031	0.00551	0.00373
5	0.49	0.02344	0.08203	0.00766	0.00463
6	0.62	0.02930	0.07031	0.00526	0.00473
7	0.69	0.02344	0.07617	0.00529	0.00466
8	**0.73**	0.02344	0.05859	0.00648	0.00661
9	0.71	0.03516	0.08789	0.00519	0.00442
10	0.72	0.03516	0.08203	0.00745	0.00448
11	0.66	0.01172	0.05859	0.00539	0.00375
12	0.61	0.01758	0.08789	0.00473	0.00301
13	0.55	0.01758	0.05273	0.00444	0.00269
14	0.48	0.01758	0.07031	0.00424	0.00156

Table viii Features of the Storm Night η autospectra.

		Main Peak(s) (Hz)		Variance (m^2s^{-2})	
Run No.	Depth (m)	Infragravity	Incident	Infragravity	Incident
1	0.37	0.01172	0.05859	0.27290	0.05810
2	0.47	0.01172	0.08203	0.21610	0.05309
3	0.54	0.01172	0.07031	0.15620	0.05146
4	0.63	0.01172	0.07031	0.11630	0.05228
5	0.49	0.02344	0.08203	0.09189	0.05616
6	0.62	0.01172	0.07031	0.07387	0.05125
7	0.69	0.02344	0.07617	0.06280	0.04658
8	**0.73**	0.02344	0.05859	0.07622	0.05956
9	0.71	0.00586	0.08789	0.07450	0.04204
10	0.72	0.00586	0.07617	0.08628	0.04962
11	0.66	0.01172	0.09375	0.19110	0.05033
12	0.61	0.01172	0.08789	0.10240	0.05006
13	0.55	0.01172	0.05273	0.10440	0.05042
14	0.48	0.01758	0.05273	0.16530	0.04285

Table ix Features of the Storm Night *u* autospectra.

		Main Peak(s) (Hz)		Variance (g^2l^{-2})	
Run No.	Depth (m)	Infragravity	Incident	Infragravity	Incident
1	0.37	0.01172	0.09961	10.94	2.46
2	0.47	0.01172	0.08789	0.90	0.52
3	0.54	0.00586	0.07617	0.42	0.23
4	0.63	0.01172	0.19920	0.13	0.13
5	0.49	0.00586	0.05273	0.05	0.12
6	0.62	0.00586	0.11130	0.04	0.06
7	0.69	0.00586	0.17580	0.01	0.06
8	0.73	0.02344	0.05859	0.08	0.16
9	0.71	0.01172	0.06445	0.04	0.06
10	0.72	0.01172	0.12300	0.95	0.23
11	0.66	0.01758	0.05859	10.86	2.19
12	0.61	0.01172	0.16990	0.92	0.41
13	0.55	0.01172	0.06445	0.43	0.52

Table x Features of Storm Night *c* autospectra.

		Main Peak(s) (Hz)			Variance (m^2)	
Run No.	Depth (m)	Infragravity		Incident	Infragravity	Incident
1	0.17	0.01172	0.02344	0.08984	0.00157	0.00334
2	0.22	0.00781	0.02734	0.09375	0.00221	0.00426
3	0.30	0.00781	0.02734	0.08594	0.00150	0.00462
4	0.46	0.00781	0.02734	0.08984	0.00281	0.00782
5						
6	0.74	0.01172	0.03125	0.09375	0.00372	0.01512
7	0.90	0.00391	0.02734	0.09766	0.00259	0.01841
8	1.09	0.00391	0.02734	0.08984	0.00300	0.02102
9	1.31	0.01172	0.03125	0.09766	0.00246	0.02302
10	1.56	0.00781	0.03125	0.09375	0.00271	0.02371
11	1.79	0.00781	0.03516	0.10160	0.00211	0.02340
12	2.01	0.01172	0.03516	0.09766	0.00179	0.02846
13	2.23	0.01172	0.03516	0.10160	0.00133	0.02787
14	2.42	0.00781		0.10940	0.00081	0.02774
15	2.60	0.00781	0.03516	0.10550	0.00151	0.02133
16	2.74	0.00781	0.03516	0.10550	0.00126	0.03236
17	2.86	0.00781	0.01953	0.10940	0.00079	0.03354
18	2.95	0.00391	0.04297	0.09375	0.00071	0.02508
19	2.99	0.01172	0.03906	0.08984	0.00088	0.03050
20	**2.99**	0.00781	0.04297	0.10550	0.00066	0.01820
21	2.96	0.01172	0.03906	0.09766	0.00082	0.02291
22	2.87	0.00781	0.03125	0.09766	0.00080	0.02706
23	2.71	0.00781	0.01562	0.09375	0.00084	0.03203
24	2.50	0.00781	0.03906	0.10160	0.00098	0.03471
25	2.27	0.01172	0.03906	0.09375	0.00111	0.03138
26	2.01	0.01562	0.03125	0.10550	0.00108	0.02478
27	1.76	0.00781	0.03125	0.10160	0.00136	0.02562
28	1.47	0.00781	0.03125	0.10160	0.00131	0.02035
29	1.18	0.01172	0.03516	0.09375	0.00165	0.01941
30	0.86	0.00781	0.03125	0.09375	0.00115	0.01429
31	0.57	0.00781	0.03516	0.09375	0.00112	0.00846
32	0.29	0.00391	0.02344	0.08594	0.00073	0.00457

Table xi Features of Spurn Head rig A2 η autospectra.

		Main Peak(s) (Hz)			Variance (m^2s^{-2})	
Run No.	Depth (m)	Infragravity		Incident	Infragravity	Incident
1	0.17	0.01562	0.03516	0.05469	0.04550	0.06401
2	0.22	0.00781	0.03906	0.08984	0.05783	0.07317
3	0.30	0.01172	0.03516	0.08594	0.03254	0.07062
4	0.46	0.01172	0.04297	0.08984	0.04383	0.08367
5						
6	0.74	0.01562	0.04688	0.08984	0.04214	0.10465
7	0.90	0.00781	0.02344	0.09375	0.03237	0.11089
8	1.09	0.01172		0.08984	0.03041	0.11954
9	1.31	0.01172		0.09766	0.02265	0.12145
10	1.56	0.01562		0.08984	0.01179	0.11885
11	1.79	0.01953		0.10160	0.01289	0.10628
12	2.01	0.01172		0.09766	0.01189	0.10890
13	2.23	0.01562		0.10160	0.00356	0.09548
14	2.42	0.01562		0.09766	0.00482	0.08836
15	2.60	0.01172		0.09766	0.00380	0.06363
16	2.74	0.01562		0.10550	0.00440	0.09610
17	2.86	0.01953		0.09375	0.00253	0.09456
18	2.95	0.01953		0.09375	0.00246	0.06656
19	2.99	0.01562		0.09375	0.00208	0.09060
20	**2.99**	0.02344		0.09375	0.00137	0.04805
21	2.96	0.01172		0.09375	0.00187	0.06554
22	2.87	0.02344		0.09766	0.00268	0.07812
23	2.71	0.01562	0.02344	0.09375	0.00276	0.11306
24	2.50	0.01562	0.02734	0.10160	0.00226	0.12268
25	2.27	0.01953		0.09375	0.00547	0.13396
26	2.01	0.01562	0.04297	0.08203	0.01870	0.09136
27	1.76	0.01562	0.04297	0.08203	0.02197	0.07116
28	1.47	0.01172	0.04297	0.09375	0.02391	0.05688
29	1.18	0.01172	0.03125	0.08203	0.02584	0.05870
30	0.86					
31	0.57	0.01953		0.08984	0.00335	0.12816
32	0.29	0.01562	0.03125	0.08984	0.00670	0.11526

Table xii Features of Spurn Head rig A2 bottom EMCM *u* autospectra.

		Main Peak(s) (Hz)			Variance (g^2l^{-2})	
Run No.	Depth (m)	Infragravity		Incident	Infragravity	Incident
1	0.17	0.00391	0.02734	0.09375	0.38390	0.52190
2	0.22	0.00781	0.01562	0.08594	0.41940	0.86610
3	0.30	0.00781	0.03125	0.08594	0.32850	0.79820
4	0.46	0.00391	0.03125	0.08594	0.64940	2.25100
5						
6	0.74					
7	0.90	0.01172	0.03516	0.09375	0.36280	0.84590
8	1.09	0.01172	0.02344	0.05859	0.91600	1.02900
9	1.31	0.01172		0.12110	0.35080	0.65040
10	1.56	0.00391		0.08984	0.25130	0.61140
11	1.79	0.00781		0.11720	0.22170	0.64960
12	2.01	0.00391		0.10550	0.14610	0.34110
13	2.23	0.00391		0.10160	0.11940	0.29480
14	2.42	0.01172		0.10160	0.08191	0.21370
15	2.60	0.00391	0.03906	0.05078	0.04189	0.14630
16	2.74	0.00781	0.02344	0.10550	0.18220	0.36400
17	2.86	0.00391	0.01562	0.10940	0.64880	0.83280
18	2.95	0.00781	0.02734	0.09766	0.14490	0.31510
19	2.99	0.01562	0.03906	0.09375	0.53480	1.10000
20	**2.99**	0.00781		0.01562	0.65800	0.64660
21	2.96	0.00391		0.09375	0.66490	0.74760
22	2.87	0.00391		0.10160	0.24330	0.38930
23	2.71					
24	2.50	0.01172		0.09766	1.19700	1.85400
25	2.27	0.00391		0.09375	2.89100	3.20300
26	2.01	0.00781		0.08984	2.55100	5.24400
27	1.76	0.00781		0.08984	1.80700	2.49000
28	1.47	0.00391		0.09375	2.57000	3.57200
29	1.18	0.01172	0.02344	0.08984	1.66600	2.82100
30	0.86	0.00391		0.08203	0.63560	0.87370
31	0.57	0.01172		0.08203	0.09238	0.28240
32	0.29	0.00781	0.01953	0.08594	0.14440	0.22360

Table xiii Features of the Spurn Head rig A2 bottom OBS *c* autospectra.

		Main Peak(s) (Hz)		Variance (m^2)	
Run No.	Depth (m)	Infragravity	Incident	Infragravity	Incident
1	0.47	0.02344	0.09375	0.00550	0.00676
2	0.81	0.02344	0.07812	0.00502	0.01243
3	1.13	0.03125	0.07812	0.00410	0.02189
4	1.43	0.02344	0.07812	0.00499	0.03348
5	1.69	0.01562	0.07812	0.00614	0.05089
6	1.89	0.03125	0.09375	0.00569	0.05947
7	2.06	0.03125	0.07812	0.00456	0.07422
8	2.14	0.03906	0.07812	0.00472	0.06708
9	2.19	0.01562	0.10160	0.00549	0.07306
10	**2.20**		0.08594	0.00433	0.07926
11	2.08	0.03125	0.07812	0.00695	0.07763
12	1.95	0.03125	0.08594	0.00495	0.06335
13	1.78		0.07812	0.00795	0.05427
14					
15	1.20	0.04688	0.07812	0.00516	0.02826
16	0.93	0.03125	0.07812	0.00495	0.01519
17	0.61	0.03906	0.07812	0.00583	0.00838
18	0.28	0.01562	0.07812	0.00531	0.00282

Table xiv Features of Perranporth η autospectra.

		Main Peak(s) (Hz)			Variance (m^2s^{-2})	
Run No.	Depth(m)	Infragravity		Incident	Infragravity	Incident
1	0.47	0.02344	0.05469	0.09375	0.09886	0.07741
2	0.81	0.02344		0.07812	0.06654	0.08902
3	1.13	0.01562	0.03125	0.07812	0.03641	0.11740
4	1.43	0.00781	0.04688	0.07812	0.03523	0.14020
5	1.69	0.01562	0.04688	0.07812	0.02658	0.17500
6	1.89			0.09375	0.03696	0.19030
7	2.06		0.02344	0.07812	0.03352	0.21520
8	2.14	0.01562	0.03906	0.07812	0.02033	0.20210
9	2.19	0.01562	0.03906	0.10160	0.02206	0.20650
10	**2.20**	0.01562		0.08594	0.01860	0.23410
11	2.08	0.03125		0.08594	0.03629	0.22430
12	1.95	0.01562		0.07812	0.03392	0.19680
13	1.78	0.01562		0.07812	0.03489	0.18680
14						
15	1.20	0.01562	0.04688	0.07812	0.02917	0.12730
16	0.93	0.01562	0.04688	0.07812	0.04607	0.08857
17	0.61	0.02344	0.03906	0.07812	0.05902	0.06323
18	0.28	0.01562		0.06250	0.12680	0.05031

Table xv Features of Perranporth u autospectra.

	Main Peak (Hz)		Variance ($g^2 l^{-2}$)	
Run No.	Infragravity	Incident	Infragravity	Incident
1	0.03125	0.07812	5.78	11.70
2	0.01562	0.07812	1.98	7.37
3	0.02344	0.08594	1.43	3.76
4	0.01562	0.07031	1.50	3.79
5	0.02344	0.08594	0.59	2.06
6	0.01562	0.18750	2.55	3.43
7	0.01562	0.09375	0.74	2.29
8	0.02344	0.09375	0.42	1.43
9	0.01562	0.06250	0.41	1.38
10	0.03906	0.07812	0.47	1.27
11	0.02344	0.11720	0.49	1.03
12	0.01562	0.11720	0.47	1.19
13	0.02344	0.09375	0.18	0.34
14				
15	0.01562	0.07812	0.07	0.14
16	0.01562	0.11720	0.04	0.08
17	0.00781	0.10940	0.03	0.05

Table xvi Features of the Perranporth *c* autospectra.

References

Aagaard T., 1990. Infragravity waves and nearshore bars in protected, storm-dominated coastal environments. *Marine Geology,* **94**, 181-203.

Aagaard T. and Greenwood B.,1994. Suspended sediment transport and the role of infragravity waves in a barred surf zone. *Marine Geology,* **118,** 23-48.

Abdelrahman, S.M. and Thornton, E.B., 1987. Changes in the short wave amplitude and wavenumber due to the presence of infragravity waves. *Proc. Coastal Hydrodynamics*, ASCE, 458-478.

Aubrey, D.G. and Trowbridge, J.H., 1985. Kinematic and dynamic estimates from electromagnetic current meter data. *Journal of Geophysical Research*, **90**(C5), 9137-9146.

Bagnold, R.A., 1963. Mechanics of marine sedimentation. In: *The Sea, Ideas and Observations*, Volume 3. Wiley-Interscience Publishers, New York, **3**, 507-528.

Bagnold, R.A., 1966. An approach to the sediment transport problem from general physics. *U.S. Geological Survey Professional Paper*, **444-I**, 37pp.

Baillard, J.A., 1981. An energetics total load sediment transport model for a plane sloping beach. *Journal of Geophysical Research*, **86**, 10938-10954.

Baldock, T.E. and Swan, C., 1996. Extreme waves in shallow and intermediate water depths. *Coastal Engineering*, **27**, 21-46.

Baldock, T.E., Holmes, P. and Horn, D.P., 1997. Low frequency swash motion induced by wave grouping. *Coastal Engineering*, **32**, 197-222.

Baquerizo, A., Losada, M.A., McKee Smith, J. and Kobayashi, N., 1997. Cross-shore variation of wave reflection from beaches. *Journal of Waterway, Port, Coastal and Ocean Engineering*, **123**(5), 274-279.

Basinski, T., 1989. Field studies on sand movement in the coastal zone. *Institute of Hydroengineering Report*, Gdansk, 298p.

Battjes, J.A., 1974. Surf similarity. *Proc. 14th Coastal Engineering Conference*, ASCE, 466-479.

Bauer, B.O. and Greenwood, B., 1990. Modification of a linear bar-trough system by a standing edge wave. *Marine Geology,* **92**, 177-204.

Beach, R.A. and Sternberg, R.W., 1988. Suspended sediment transport in the surf zone: response to cross-shore infragravity motion. *Marine Geology,* **80**, 61-79.

Beach, R.A. and Sternberg, R.W., 1991. Infragravity driven suspended sediment transport in the swash, inner and outer-surf zone. *Proc. Coastal Sediments '91,* ASCE, 114-128.

Beach, R.A. and Sternberg, R.W., 1996. Suspended-sediment transport in the surf zone: response to breaking waves. *Continental Shelf Research*, **16**(15), 1989-2003.

Bowen, A.J., 1980. A simple model of nearshore sedimentation: beach profiles and longshore bars. In: *The Coastline of Canada*. S.B. McCann (Editor), Geological Survey of Canada, Ottawa, 1-11.

Bowen, A.J. and Guza, R.T., 1976. Resonant Interactions for waves breaking on a beach. *Proc. 15th Conference on Coastal Engineering*, ASCE, 560-579.

Broker-Hedegaard, I., Roelvink, J.A., Southgate, H.N., Pechon, P., Nicholson, J. and Hamm, L., 1992. Intercomparison of coastal profile models. *Proc. 23rd International Conference on Coastal Engineering*, ASCE, 2108-2121.

Buller, A.J. and Mcmanus, J., 1979. Sediment sampling and analysis. In: *Estuarine Hydrography and Sedimentation*, K.R. Dyer (Ed.). Cambridge University Press, 230pp.

Butt, T. and Russell, P.E., 1999. Hydrodynamics and sediment transport in the swash zone of natural beaches: a review. *Journal of Coastal Research*, accepted for publication.

Chatfield, C., 1989. *The Analysis of Time-Series, an Introduction (Fourth Edition)*. Chapman and Hall, 241pp.

Chen, Y., Guza, R.T. and Elgar, S., 1987. Modelling spectra of breaking surface waves in shallow water. *Journal of Geophysical Research*, **102**(11), 25035-25046.

Dally, W.R. and Dean, G., 1984. Suspended Sediment Transport and Beach Profile Evolution. *Journal of Waterway, Port, Coastal and Ocean Engineering*, **110**, 15-33.

Davidson, M.A., 1991. Field investigations of infragravity oscillations on a high energy dissipative beach (Llangennith, S. Wales, U.K.). Unpublished Ph.D. Thesis, University of Wales, 322p.

Davidson, M.A., 1992. Implementation of linear wave theory in the frequency domain for the conversion of sea bed pressure to surface elevation. *School of Civil Engineering Internal Report No. 93/001*, University of Plymouth, 24p.

Davidson, M.A., Bird, P.A., Bullock, G.N. and Huntley, D.A., 1993. An analytical solution for standing, shallow water waves over a multiple component, sloping sea bed. *School of Civil Engineering Internal Report No. 92/008*, University of Plymouth, 19p.

Davidson, M.A., Russell, P.E., Huntley, D.A. and Hardisty, J., 1993. Tidal asymmetry in suspended sand transport on a macrotidal intermediate beach. *Marine Geology*, **110**, 333-335.

Davies A.G., 1983. Wave interactions with rippled sand beds. . In: *Physical Oceanography of Coastal and Shelf Seas*, B. Johns (Ed.). Elsevier, 470pp.

Davies, R.A., 1964. A morphogenic approach to world shorelines. *Zeitschrift fur Geomorphology*, **8**, Mortensen Sonderheft, 127-142.

Deigaard, R., 1993. A note on the three-dimensional shear stress distribution in a surf zone. *Coastal Engineering*, **20**, 157-171.

Dingler, J.R. and Inman, D.L., 1976. Wave-formed ripples in near-shore sands. *Proc. 15th Conference on Coastal Engineering*, ASCE, 2109-2126.

Doering, J.R.C. and Bowen, A.J., 1988. Wave-induced flow and nearshore suspended sediment. *Proceedings of the 21st International Conference on Coastal Engineering*, ASCE, 1452-1463.

Doering, J.C. and Bowen, A.J., 1995. Parametrization of orbital velocity asymmetries of shoaling and breaking waves using bispectral analysis. *Coastal Engineering*, **26**, 15-33.

Downing, J.P., Sternberg, R.W. and Lister, C.R.B., 1981. New instrumentation for the investigation of sediment suspension processes in the shallow marine environment. *Marine Geology*, **42**, 19-34.

Dyer, K., 1986. *Coastal and Estuarine Sediment Dynamics*. John Wiley and sons, 342pp.

Dyhr-Nielsen and M., Sorensen, T., 1970. Some sand transport phenomena on coasts with bars. *Proc., 12th International Conference on Coastal Engineering*, ASCE, 855-866.

Eckart, C., 1951. Surface waves on water of variable depth. *Wave Report 100*, Scripps, 99pp.

Eldeberky, Y. and Battjes, J.A., 1996. Spectral modelling of wave breaking: application to Boussinesq equations. *Journal of Geophysical Research*, **101**(1), 1253-1264.

Elgar S.L. and Guza, R.T., 1985. Observations of bispectra of shoaling surface gravity waves. *Journal of Fluid Mechanics*, **161**, 425-448.

Elgar, S., Herbers, T.H.C., Okihiro, M., Oltman-Shay, J. and Guza, R.T., 1992. Observations of infragravity waves. *Journal of Geophysical Research*, **97**(C10), 15,573-15,577.

Elgar, S., Herbers, T.H.C. and Guza, R.T., 1994. Reflection of Ocean Surface Gravity Waves from a Natural Beach. *Journal of Physical Oceanography*, **24**, 1503-1511.

Evans, O.F., 1940. The low and ball of the eastern shore of Lake Michigan. *Journal of Geology*, **48**, 476-511.

Falques, A., Coco, G. and Huntley, D., 1999. A mechanism for the generation of wave driven rhythmic patterns in the surf zone. *Journal of Geophysical Research*, Under Review.

Flick, R.E., Guza, R.T. and Inman, D.L., 1981. Elevation and velocity measurements of laboratory shoaling waves. *Journal of Geophysical Research*, **86**, 4149-4160.

Foote, Y.L.M., 1994. Waves, currents and sand transport predictors on a macro-tidal beach. Unpublished Ph.D. Thesis, University of Plymouth, 257p.

Foote, Y.L.M., Russell, P.E., Huntley, D.A. and Sims, P., 1998. Energetics prediction of frequency-dependent suspended sand transport rates on a macrotidal beach. Earth Surface Processes and Landforms, **23**, 927-941.

Friedrichs, K.O., 1948. Water waves on a shallow sloping beach. *Communications in Pure and Applied Mathematics,* **1**, 109-134.

Galvin, C.J., 1972. Wave breaking in shallow water. In: *Waves on Beaches*, Meyer, R.E. (Ed.). Academic Press, NY, 413-456.

Garrett, C.J.R. and Toulany, B., 1981. Variability of the flow through the Strait of Belle Isle. *Journal of Marine Research*, **39**, 163-189.

Giminez-Curto, L.A., 1979. Behaviour of rubble mound breakwaters under wave action. Unpublished Ph.D. Thesis, University of Santander, Spain.

Goodman N.R.,1957. On the joint estimation of the spectrum, co-spectrum and quadrature spectrum of a two-dimensional stationary Gaussian process. Scientific Paper 10, Engineering Statistics Laboratory, New York University.

Guza, R.T., 1988. Comment on "Kinematic and dynamic estimates from electromagnetic current meter data" by D.G. Aubrey and J.H. Trowbridge. *Journal of Geophysical Research*, **93**, 1337-1343.

Guza, R.T. and Thornton, E.B., 1980. Local and shoaled comparisons of sea surface elevations, pressures and velocities. *Journal of Geophysical Research*, **85**(C3), 1524-1530.

Guza, R.T. and Thornton, E.B., 1982. Swash oscillations on a natural beach. *Journal of Geophysical Research*, **86**(C5), 4133-4137.

Guza, R.T., Thornton, E.B. and Holman, R.A., 1984. Swash on steep and shallow beaches. *Proc. 19th Coastal Engineering Conference*, ASCE, 708-723.

Guza, R.T. and Thornton, E.B., 1985. Observations of Surf Beat. *Journal of Geophysical Research,* **90**(2), 3161-3172.

Hallermeier, R.J., 1980. Sand motion initiation by water waves: two asymptotes. *Journal of Waterway, Port, Coastal and Ocean Engineering*, **106**(3), 299-318.

Hallermeier, R.J., 1981. A profile zonation for seasonal sand beaches from wave climate. *Coastal Engineering*, **4**, 253-277.

Hanes, D.M. and Huntley, D.A., 1986. Continuous measurements of suspended sand concentration in a wave dominated nearshore environment. *Continental Shelf Research,* **6**(4), 585-596.

Hanes, D.M., Jette, C.D., Thosteson, E.D., and Vincent, C.E., 1997. Field observations of nearshore, wave seabed interactions. *Proc. Coastal Dynamics '97*, ASCE, 11-18.

Hardisty, J., 1990. *Beaches: form and process*. Unwin Hyman, London, 324pp.

Hasselmann, K., 1962. On the non-linear energy in a gravity wave spectrum. Part 1. General theory. *Journal of Fluid Mechanics*, **15**, 385-398.

Hasselmann, K., Munk, W. and MacDonald, G., 1963. Bispectra of ocean waves. In: *Time Series Analysis*, Rosenblatt M. (Editor). Wiley, New York, 125-139.

Heathershaw, A.D. and Simpson, J.M., 1978. The sampling variability of the Reynolds stress and its relation to boundary shear stress and drag coefficient measurements. *Estuarine and Coastal Marine Science*, **6**, 263-274.

Heathershaw, A.D., 1988. Sediment transport in the sea, on beaches and in rivers: Part I - fundamental principles. *Journal of Natural Science*, **14**(3), 154-170.

Heathershaw, A.D., 1988. Sediment transport in the sea, on beaches and in rivers: Part II - sediment movement. *Journal of Natural Science*, **14**(4), 221-234.

Herbers, T.H.C., Elgar, S. and Guza, R.T., 1994. Infragravity-Frequency (0.005-0.05 Hz) Motions on the Shelf. Part I: Forced Waves. *Journal of Physical Oceanography,* **24**, 917-927.

Herbers, T.H.C., Elgar, S., Guza, R.T. and O'Reilly, W.C., 1995. Infragravity-Frequency (0.005-0.05 Hz) Motions on the Shelf. Part II: Free Waves. *Journal of Physical Oceanography,* **25**, 1063-1079.

Hjulstrom, F., 1939. Transportation of detritus by moving water. In: *Recent marine sediments*, P.D. Toask (Ed.). Thos. Murphy, London, 5-31.

Holman, R.A. and Bowen, A.J., 1982. Bars, Bumps, and Holes: Models for the Generation of Complex Beach Topography. *Journal of Geophysical Research,* **87**(1), 457-468.

Holman, R.A. and Sallenger, A.H., 1985. Setup and swash on a natural beach. *Journal of Geophysical Research*, **90**(C1), 945-953.

Horikawa, K. and Kuo, C.-T., 1966. A study of wave transformation inside the surf zone. *Proc. 10th Coastal Engineering Conference*, ASCE, 217-233.

Horikawa, K. and Hattori, M., 1987. The Nearshore Environment Research Centre project. *Proc. Coastal Sediments '87*, ASCE, 756-771.

Hotta, S., Mizuguchi, M., and Isobe, M., 1981. Observations of long period waves in the nearshore zone. *Coastal Engineering in Japan*, **24**, 41-76.

Howd, P.A., Oltman-Shay, J. and Holman, R.A., 1991. Wave Variance Partitioning in the Trough of a Barred Beach. *Journal of Geophysical Research,* **96**(7), 12781-12795.

Howd, P.A., Bowen, A.J. and Holman, R.A., 1992. Edge Waves in the Presence of Strong Longshore Currents. *Journal of Geophysical Research,* **97**(7), 11357-11371.

Hughes, S.A. and Fowler, J.E., 1995. Estimating wave induced kinematics at sloping structures. *Journal of Waterway, Port, Coastal and Ocean Engineering*, **121**, 209-215.

Huntley, D.A., Guza, R.T. and Bowen, A.J., 1977. A Universal Form for Run-Up Spectra? *Journal of Geophysical Research,* **82**(18), 2577-2581.

Huntley, D.A., Guza, R.T. and Thornton, E.B., 1981. Field Observations of Surf Beat 1. Progressive Edge Waves. *Journal of Geophysical Research,* **86**(7), 6451-6466

Huntley, D.A. and Kim, C-S., 1984. Is surf beat forced or free? *Proc. 19th Conference on Coastal Engineering*, ASCE, 1659-1676.

Huntley, D.A. and Hanes, D.M., 1987. Direct Measurement of Suspended Sediment Transport. *Proc. Coastal Sediments '87,* ASCE, 723-737.

Huntley, D.A., 1988. Evidence for Phase Coupling Between Edge Wave Modes. *Journal of Geophysical Research,* **93**(10), 12393-12408.

Huntley, D.A., Davidson, M.A., Russell, P.E., Foote, Y. and Hardisty, J., 1993. Long waves and sediment movement on beaches: recent observations and implications for modelling. *Journal of Coastal Research*, **15**, 215-229.

Huntley, D.A. and Simmonds, D.J., 1994. Testing the validity of the principal component analysis method for reducing the influence of noise on frequency-dependent reflection coefficients. University of Plymouth Internal Report, 9p.

Huntley, D.A., Simmonds, D.J. and Davidson, M.A., 1995. Estimation of frequency-dependent reflection coefficients using current and elevation sensors. *Proc. Coastal Dynamics '95*, ASCE, 57-68.

Hwang, C.-H., Tsai, L.-H., Lin, P.-C. and Tsai, C.-C., 1996. Studies on the suspended concentration in the surf zone. *Proc. Coastal Engineering '96*, 4088-4097.

Ippen, A.T. and Kulin, G., 1954. The shoaling and breaking of the solitary wave. *Proc. 5th Coastal Engineering Conference*, ASCE, 27-49.

Irribarren, C.R. and Nogales, C., 1949. Protection des ports. *Section II, Comm. 4, XVIIth International Navigation Congress*, Lisbon, 31-80.

Jaffe, B.E., Sternberg, R.W. and Sallenger, A.H., 1984. The role of suspended sediment in shore-normal beach profile changes. *Proc. 13th International Conference on Coastal Engineering*, ASCE, 1155-1171.

Jenkins, G.M. and Watts, D.G., 1968. *Spectral Analysis and its Applications*. Holden Day, San Francisco, 525pp.

Jonsson, I.G., 1978. A new approach to oscillatory rough turbulent boundary layers. *Technical University of Denmark, Institute of Hydrodynamics and Hydraulic Engineering, Series Paper*, No. 17, 87pp. (Also published in *Ocean Engineering*, **7**, 1980, 109-152).

Kaminsky, G. and Kraus, N.C., 1993. Evaluation of depth-limited wave breaking criteria. *Waves '93*, ASCE, 180-193.

Kim, Y.C. and Powers, E.J., 1979. Digital bispectral analysis and its applications to non-linear wave interactions. *IEEE Trans. Plasma Science*, **1**, 120-131.

King, C.A.M., 1972. *Beaches and Coasts*. Arnold, London, 570pp.

Kinsman, B., 1965. *Wind Waves (Their Generation and Propagation on the Ocean Surface)*. Dover, New York, 676pp.

Kirby, J.T., Dalrymple, R.A. and Liu, P.L-F., 1981. Modification of edge waves by a barred beach topography. *Coastal Engineering*, **5**, 35-49.

Kishi, T. and Saeki, H., 1966. The shoaling, breaking and runup of the solitary wave on impermeable rough slopes. *Proc. 10th Coastal Engineering Conference*, ASCE, 322-348.

Komar, P.D., 1998. *Beach processes and sedimentation. 2nd edition*. Prentice Hall, 544pp (1st Edition 1976).

Kostense, J.K., 1985. Measurements of surf beat and set-down beneath wave groups. *Proc. 19th International Conference on Coastal Engineering*, ASCE, 497-511.

Kriebel, D.L. and Dean, R.G., 1984. Beach and Dune response to severe storms. *Proc. 19th International Conference on Coastal Engineering*, ASCE, pp1584-1599.

Lamb, H., 1932. *Hydrodynamics*. Dover, New York, 738pp.

Larson, M., 1988. Quantification of beach profile change. Ph.D. Thesis (Report No., 1008), Lund University, Sweden.

Lippmann, T.C. and Holman, R.A., 1990. The Spatial and Temporal Variability of Sand Bar Morphology. *Journal of Geophysical Research*, **95**(7), 11575-11590.

Lippmann, T.C., Holman, R.A. and Bowen, A.J., 1997. Generation of edge waves in shallow water. *Journal of Geophysical Research*, **102**(C4), 8663-8679.

List, J.H., 1987. Wave groupiness as a source of nearshore long waves. *Proc. 20th International Conference on Coastal Engineering*, ASCE, 497-511.

List, J.H., 1991. Wave groupiness variations in the nearshore. *Coastal Engineering*, **15**, 475-496

List, J.H., 1992. A Model for the Generation of Two-Dimensional Surf Beat. *Journal of Geophysical Research*, **97**(4), 5623-5635.

Longuet-Higgins, M.S., 1952. On the joint distribution of the periods and amplitudes of sea waves. *Journal of Geophysical Research*, **57**, 2688-2694.

Longuet-Higgins, M.S., 1970. Longshore currents generated by obliquely incident sea waves. *Journal of Geophysical Research*, **75(33)**, 6790-6801.

Longuet-Higgins, M.S. and Stewart, R.W., 1962. Radiation stress and mass transport in gravity waves, with application to "surf beats". *Journal of Fluid Mechanics*, **13**, 481-504.

Longuet-Higgins, M.S. and Stewart, R.W., 1964. Radiation stresses in water waves; A physical discussion, with applications. *Deep-Sea Research,* **11**, 529-562.

Madsen, P.A., Sorensen, O.R. and Schaffer, H.A., 1997. Surf zone dynamics simulated by a Boussinesq type model. Par II: surf beat and swash oscillations for wave groups and irregular waves. *Coastal Engineering*, **32**, 289-319.

Martens, D.E. and Thornton, E.W., 1987. Nearshore zone monitoring system. *Proc. Coastal Hydrodynamics*, ASCE, 579-588.

Mason, T., Voulgaris, G., Simmonds, D.J. and Collins, M.B., 1997. Hydrodynamics and sediment transport on composite (mixed sand/shingle) and sand beaches: a comparison. *Proc. Coastal Dynamics '97*, ASCE, 48-57.

Masselink, G., 1993. Simulating the Effects of Tides on Beach Morphodynamics. *Journal of Coastal Research,* **15**, 180-197.

Masselink, G. and Short, A.D., 1993. The Effect of Tide Range on Beach Morphodynamics and Morphology: A Conceptual Beach Model. *Journal of Coastal Research,* **9**(3), 785-800.

Masselink, G., 1995. Group bound long waves as a source of infragravity energy in the surf zone. *Continental Shelf Research,* **15**(13), 1525-1547.

Matlab Reference Manual, 1992.

Miche, A., 1951. Exposes a l'action de la houle. *Ann. Ponts Chaussees*, **121**, 285-319.

Miles, J.R., 1997. Enhanced sediment transport near seawalls and reflective beaches. Unpublished Ph.D. Thesis, University of Plymouth, 192p.

Munk, W.H., 1948. *Rev. Sci. Instrum.*, **19**, 654.

Munk, W.H., Snodgrass, P.E. and Gilbert, F., 1964. Long waves on the continental shelf: An experiment to separate trapped and leaky modes. *Journal of Fluid Mechanics,* **20**, 529-554.

Nearshore Processes Workshop, 1990. *Report on the State of Nearshore Processes Research*, Report No. OSU-CO-90-6, Oregon State University, 25pp.

Nelson, R.C. and Gonsalves, J., 1992. Surf zone transformation of wave height to water depth ratios. *Coastal Engineering,* **17**, 49-70.

Nielsen, P., 1979. Some basic concepts of wave sediment transport. *Series Paper 20*, Inst. Hydrodyn. Hydraul. Eng., Technical University of Denmark, 160p.

Nielsen, P., 1988. Three simple models of wave sediment transport. *Coastal Engineering,* **12**, 43-62.

Nishimura, H. and Sunamura, T., 1986. Numerical simulation of beach profile changes. *Proc. 20th International Conference on Coastal Engineering*, Taipei, ASCE, New York, Vol. 2, 1444-1455.

Norheim, C.A., Herbers, T.H.C. and Elgar, S., 1998. Nonlinear evolution of surface wave spectra on a beach. *Journal of Physical Oceanography*, **28**, 1534-1551.

Nuttall, A.N., 1971. Spectral estimation by means of overlapped Fast Fourier Transforms of windowed data. NUSC Report No.4169, Dep. Navy, USA.

O'Hare, T.J. and Huntley, D.A., 1994. Bar formation due to wave groups and associated long waves. *Marine Geology*, **116**, 313-325.

O'Hare, T.J., 1994. The role of long waves in sand bar formation – a model exploration. *Proc. International Conference on the Role of Large Scale Experiments in Coastal Research*, ASCE, 74-88.

Okazaki, S. and Sunamura, T., 1991. Re-examination of breaker-type classification on uniformly inclined laboratory beaches. *Journal of Coastal Research*, **7**, 559-564.

Okihiro, M., Guza, R.T. and Seymour, R.J., 1992. Bound infragravity waves. *Journal of Geophysical Research*, **97**, 11453-11469.

Okihiro, M. and Guza, R.T., 1995. Infragravity energy modulation by tides. *Journal of Geophysical Research,* **100**(8), 16143-16148.

Oltman-Shay, J and Howd, P.A., 1989. Shear Instabilities of the Mean Longshore Current 2. Field Observations. *Journal of Geophysical Research,* **94**(12), 18031-18042.

Osborne, P.D., 1990. Suspended sediment transport on barred and non-barred beaches. Unpublished Ph.D. Thesis, University of Toronto, Canada, 196p.

Osborne, P.D. and Greenwood, B., 1992. Frequency dependent cross-shore suspended sediment transport 1. A non-barred shoreface. *Marine Geology,* **106**, 1-24.

Osborne, P.D. and Greenwood, B., 1992. Frequency dependent cross-shore suspended sediment transport 2. A barred shoreface. *Marine Geology,* **106**, 25-51.

Osborne, P.D. and Greenwood, B., 1993. Sediment suspension under waves and currents: time scales and vertical structure. *Sedimentology,* **40**, 599-622.

Osborne, P.D. and Rooker, G.A., 1997. Surf zone and swash zone sediment dynamics on high energy beaches: West Auckland, New Zealand. *Proc. Coastal Dynamics '97*, ASCE, 814-823.

Ottesen-Hansen, N-E., Sand, S.E., Lundgren, H., Sorensen, T., and Gravesen, H., 1981. Correct reproduction of group-induced long waves. *Proc. 17th International Conference on Coastal Engineering*, ASCE, 784-800.

Press, W.H., Flannery, B.P., Teulosky, S.A. and Vetterling, W.T., 1986. Fourier transform spectral methods. In: *Numerical Recipes*. Cambridge University Press, 818pp.

Raubenheimer, B. and Guza, R.T., 1996. Observations and predictions of run-up. *Journal of Geophysical Research*, **101**(C10), 25575-25587.

Reineck, H.E. and Singh, I.B., 1980. Depositional sedimentary environment with reference to terrigenous clastics. Springer Verlag, Berlin, 2nd Edition.

Roelvink, J.A., 1993. Surf beat and its effect on cross-shore profiles. Ph.D. Thesis, Technical University of Delft.

Roelvink, J.A. and Broker, I., 1993. Cross-shore profile models. *Coastal Engineering,* **21**, 163-191.

Ruessink, B.G., 1998. The temporal and spatial variability of infragravity energy in a barred nearshore zone. *Continental Shelf Research*, **18**, 585-605.

Ruessink, B.G., 1998. Bound and free infragravity waves in the nearshore zone under breaking and nonbreaking conditions. *Journal of Geophysical Research*, **103**(C6), 12795-12805.

Russell, P.E., 1990. Field studies of suspended sand transport on a high energy dissipative beach. Unpublished Ph.D. Thesis, University of Wales, 318p.

Russell, P.E., Davidson, M., Huntley, D.A., Cramp, A., Hardisty, J. and Lloyd, G., 1991. The British Beach and Nearshore Dynamics (B-BAND) Programme. *Proc. Coastal Sediments '91,* ASCE, 371-384.

Russell, P.E., 1993. Mechanisms for beach erosion during storms. *Continental Shelf Research,* **13**(11), 1243-1265.

Russell, P.E. and Huntley, D.A., 1999. A cross-shore sediment transport 'shape function' for high energy beaches. *Journal of coastal Research,* in press.

Sallenger, A.H. and Holman, R.A., 1987. Infragravity Waves Over a Natural Barred Profile. *Journal of Geophysical Research,* **92**(9), 9531-9540.

Sallenger, A.H. and Howd, P.A., 1989. Nearshore Bars and the Break-Point Hypothesis. *Coastal Engineering,* **12**, 301-313.

Schaffer, H.A. and Jonsson, I.G., 1992. Edge waves revisited. *Coastal Engineering,* **16**, 349-368.

Schaffer, H.A., 1993. Infragravity waves induced by short-wave groups. *Journal of Fluid Mechanics,* **217**, 551-588.

Schoones, J.S. and Theron, A.K., 1995. Evaluation of 10 cross-shore sediment transport/morphological models. *Coastal Engineering*, **25**, 1-41.

Schonfeldt, H., 1995. On the modification of edge waves by longshore currents. *Continental Shelf Research,* **15**(10), 1213-1220.

Seelig, W.N. and Ahrens, J.P., 1981. Estimation of wave reflection coefficient and energy dissipation for beaches, revetments and breakwaters. CERC Technical paper 81-1, Fort Belvoir, US Army Engineer Waterways Coastal Experiment Station, Vicksburg, Miss., 40pp.

Seymour, R.J., 1987. An assessment of the Nearshore Sediment Transport Study (NSTS). *Proc. Coastal Sediments '87*, ASCE, 642-651.

Shibayama, T., 1984. Sediment transport mechanism and two dimensional beach transformation due to waves. Dept. Engineering Thesis, University of Tokyo.

Shields, A., 1936. Anwendung der ahnlichkertsmechanik und der turbulenztorshung, aut doe geschrebebewegung. *Preuss Versuchsanstalt fur Wasserbau und Schittbau*, Berlin, Mitt 26, 26p.

Short, A.D., 1975. Multiple offshore bars and standing waves. *Journal of Geophysical Research*, **80**(7), 3838-3840.

Short, A.D., 1991. Macro-Meso Tidal Beach Morphodynamics - An Overview. *Journal of Coastal Research,* 7(2), 417-436.

Short, A.D. and Aagaard, T., 1993. Single and Multi-Bar Beach Change Models. *Journal of Coastal Research,* **15**, 141-157

Sleath, J.F.A., 1984. Sea bed mechanics. John Wiley and Sons, England.

Soulsby, R.L., 1983. The bottom boundary layer of shelf seas. In B. Johns (Ed.), *Physical Oceanography of Coastal and Shelf Seas*, Elsevier, 470pp.

Soulsby, R.L., 1998. Coastal sediment transport: the COAST3D project. *Proc. 26th International Conference on Coastal Engineering*, ASCE.

Staub, C., Jonsson, I.G. and Svendsen, I.A., 1996. Sediment suspension in oscillatory flow: measurements of concentration at high shear. *Coastal Engineering*, **27**, 67-96.

Steetzel, H.J., 1987. A model for beach and dune profile changes near dune revetments. *Proc. Coastal Sediments '87*, ASCE, 87-97.

Sternberg, R.W., 1968. Friction factors in tidal channels with differing bed roughness. *Marine Geology*, **6**, 243-260.

Sternberg, R.W., Kineke, G.C. and Johnson, R., 1990. An instrument for profiling suspended sediment, fluid, and flow conditions in shallow marine environments. *Continental Shelf Research*, **11**(2), 109-122.

Suhayda, J.N., 1974. Standing Waves on Beaches. *Journal of Geophysical Research,* **79**(21), 3065-3071.

Svendsen, I.A., 1987. Analysis of surf zone turbulence. *Journal of Geophysical Research,* **92**(C5), 5115-5124.

Symonds, G., Huntley, D.A. and Bowen, A.J., 1982. Two-Dimensional Surf Beat: Long Wave Generation by a Time-Varying Breakpoint., *Journal of Geophysical Research,* **87**(1), 492-498.

Symonds, G. and Bowen, A.J., 1984. Interactions of Nearshore Bars with Incoming Wave Groups., *J. Geophysical Research,* **89**(2), 1953-1959.

Tatavarti, R.V.S.N., Huntley, D.A. and Bowen A.J., 1988. Incomign and outgoing wave interactions on beaches. *Proc. 21st Conference on Coastal Engineering*, ASCE, 1104-1120.

Tatavarti, R.V.S.N., 1989. The reflection of waves on natural beaches. Unpublished Ph.D. Thesis, Dalhousie University, Halifax, Nova Scotia, Canada.

Thornton, E.B. and Guza, R.T., 1983. Transformation of wave height distribution. *Journal of geophysical research*, **88**, 5925-5938.

Thornton, E.B. and Kim, C.S., 1993. Longshore Current and Wave Height Modulation at Tidal Frequency Inside the Surf Zone. *Journal of Geophysical Research,* **98**(9), 16509-16519.

Thornton, E.B., Swayne, J.L. and Dingler, J.R., 1998. Small-scale morphology across the surf zone. *Marine Geology*, **145**, 173-196.

Trouw, K., Williams, J.J. and Rose, C.P., 1999. Modelling sand resuspension by waves over a rippled bed. *ECSS Special Issue*, Wolanski (Editor), 18pp.

Tucker, M.J., 1950. Surf beats: sea waves of 1 to 5 minute period. *Proceedings of the Royal Society London,* **202**, 565-573.

Ursell, F., 1952. Edge waves on a sloping beach. . *Proceedings of the Royal Society London,* **214,** 79-97.

Valeport Ltd., 1998. Synchronised Logger for Investigation of Transport of Sediment (SLOT) Manual.

Voulgaris, G., Wallbridge, S., Tomlinson, B.N. and Collins, M.B., 1995. Laboratory investigations into wave period effects on sand bed erodibility, under the combined action of waves and currents. *Coastal Engineering*, **26**, 117-134.

Weggel, J.R., 1972. Maximum Breaker Height. *Proc. ASCE Waterways, Port, Coastal and Ocean Engineering,* **98**(4), 529-548.

Welch, P.D., 1967. The use of the Fast Fourier Transform for the estimation of power spectra: A method based on time averaging over short, modified periodograms. *IEEE Trans. on Audio and Electroacoustics*, Vol.AU-15(2), 70-73.

Wells, D.R., 1967. Beach equilibrium and second-order wave theory. *Journal of Geophysical Research*, **72**, 497-504.

Willis, D.H., 1987. The Canadian Coastal Sediment Study: an overview. *Proc. Coastal Sediments '87*, ASCE, 682-693.

Wright, D., Guza, R.T. and Short, A.D., 1982. Dynamics of a High-Energy Dissipative Surf Zone. *Marine Geology,* **45**, 41-62.

Wright, L.D. and Short, A.D., 1983. Morphodynamics of beaches and surf zones in Australia. In: *CRC Handbook of coastal processes and erosion*, Komar, P.D., (Ed.). CRS Press, Bocaraton, Fla., 35-64.

Wright, D. and Short, A.D., 1984. Morphodynamic variability of surf zones and beaches: a synthesis. *Marine Geology,* **56**, 93-118.

You, Z.-J., 1998. Initial motion of sediment in oscillatory flow. *Journal of Waterway, Port, Coastal and Ocean Engineering*, March/April, 68-72.